# LINEAR THERMO-VISCO-ELASTIC WAVE PROPAGATION INCLUDING STRESS RELAXATION: A GENERAL FRAMEWORK AND CANONICAL PROBLEMS

A thesis submitted to the University of Manchester
for the degree of Doctor of Philosophy
in the Faculty of Engineering and Physical Sciences

2022

**Erik García Neefjes**
School of Natural Sciences
Department of Mathematics

# Contents

Word count 50023

# The University of Manchester

**Erik García Neefjes**
**Doctor of Philosophy**
**Linear Thermo-Visco-Elastic wave propagation including stress relaxation: a general framework and canonical problems**
**March 9, 2022**

This thesis is focused around the theoretical study of attenuation of acoustic and elastic waves due to viscous and thermal effects. The initial focus is on fluid acoustic media, where we employ the well known theory of linear thermo-visco-acoustics (TVA) to study the influence of boundary layer effects on the propagation of sound in narrow channels filled by air and water. In the latter case, the effects of fluid-structure interaction are taken into account by assuming the neighbouring solid is elastic, but only *acoustically hard* solids are analysed. On an attempt to generalise the type of media in consideration, the possible advantages arising from the development of a theory for thermo-visco-elasticity (TVE) in this context are noticed.

We propose a TVE framework which incorporates more general material behaviour such as creep and stress relaxation, and can be reduced to several other physically relevant theories like TVA for Newtonian fluids, in a way that we can accurately study a diverse class of materials ranging from metals and polymers to air and water in a large number of conditions. As for TVA fluids, TVE media accept three families of modes in free-space, namely two coupled thermo-compressional waves and a shear wave whose phase speed and attenuation differ significantly depending on the specific material. Accurate asymptotic approximations to thermo-compressional coupling are provided which highly simplify the initial expressions for the wavenumbers. We consider a canonical scattering problem consisting of a compressional plane wave incident on two TVE half–spaces in perfect contact, where the thermo-viscous effects on reflection/transmissions and conveniences of the developed framework as opposed to standard approaches in the literature are highlighted.

We make use of the above framework to extend the initial study by examining fluid-filled slits within soft viscoelastic media, which we find gives rise to very different results to those obtained for hard solids in the initial work. We show that this can partly be attributed to the properties of the *Scholte* mode which propagates in the interface of a fluid-solid half-space and is analysed thoroughly. Particular emphasis is put on how the stress relaxation effects can influence the results, which we find to be significant under certain conditions that are discussed in detail. Furthermore, given the generality of the framework, we can analyse the problem of fluid-loaded viscoelastic plates under the same set of dispersion equations obtained for the slit. In particular, we find that for sufficiently soft media so that the phase speed of the symmetric *coupled plate-Scholte* mode becomes dispersive, the mode experiences a global maximum in attenuation which may be of physical interest, particularly if stress relaxation can be exploited.

# Declaration

No portion of the work referred to in the thesis has been submitted in support of an application for another degree or qualification of this or any other university or other institute of learning.

# Copyright Statement

**i.** The author of this thesis (including any appendices and/or schedules to this thesis) owns certain copyright or related rights in it (the "Copyright") and s/he has given The University of Manchester certain rights to use such Copyright, including for administrative purposes.

**ii.** Copies of this thesis, either in full or in extracts and whether in hard or electronic copy, may be made **only** in accordance with the Copyright, Designs and Patents Act 1988 (as amended) and regulations issued under it or, where appropriate, in accordance with licensing agreements which the University has from time to time. This page must form part of any such copies made.

**iii.** The ownership of certain Copyright, patents, designs, trade marks and other intellectual property (the "Intellectual Property") and any reproductions of copyright works in the thesis, for example graphs and tables ("Reproductions"), which may be described in this thesis, may not be owned by the author and may be owned by third parties. Such Intellectual Property and Reproductions cannot and must not be made available for use without the prior written permission of the owner(s) of the relevant Intellectual Property and/or Reproductions.

**iv.** Further information on the conditions under which disclosure, publication and commercialisation of this thesis, the Copyright and any Intellectual Property and/or Reproductions described in it may take place is available in the University IP Policy (see http://documents.manchester.ac.uk/DocuInfo.aspx?DocID=487), in any relevant Thesis restriction declarations deposited in the University Library, The University Library's regulations (see http://www.manchester.ac.uk/library/aboutus/regulations) and in The University's Policy on Presentation of Theses.

# Acknowledgements

Firstly, my thanks go to EPSRC and Thales UK for funding via a KTN Industrial CASE PhD Studentship for making this project possible. I feel very fortunate to have been able to work with several people throughout these 4 years who I admire, and from whom I have learned significantly. In particular I want to thank Will Parnell for your guidance, being an excellent supervisor and giving me the opportunity to explore and develop my research interests, including the chance to spend some time with fellow research groups in France and Australia. David Nigro, thanks for always taking the time to talk and for constantly expressing your interest in this work. During certain periods of this project we communicated on a daily basis and I cannot thank you enough for all the invaluable discussions (many of which via iMessage!). I am grateful to Raphaël Assier for the support since the beginning and continuous technical suggestions. Art Gower, many thanks for acting as an informal supervisor, the technical help in Chapter 3 of this thesis and making this collaboration a joyful working experience.

Further, I would like to thank Phil Cotterill for the useful discussions at the beginning of my PhD. Mike Simon, thanks for acting as a great mentor during the final year of my undergraduate degree, and introducing me to Will Parnell and the MWM research group. I wish to show gratitude to my past officemates Will R, Rob, Amy, Mary, Matt, Georgia and James for showing me the ropes as well as Eleanor, Valentin and Tom who joined after me. I also want to acknowledge all the members of MWM for their hard work, especially Naomi. More generally, to everyone that I had regular contact with in the Alan Turing Building and the University of Manchester, thanks for contributing towards making this a nice environment to work in.

I want to express my gratitude to my friends, family and girlfriend for having been there every step of the way. Mum, Dad and Kai thanks for being the best role models I could ever ask for and your unconditional love and support. The pandemic hit our family with some horrible events including the passing of our *lieve Oma* who is greatly missed, but the silver lining was getting to spend this period together at home in Gran Canaria with Sunny, Liefje and Chispa. Martha, thanks for your support and making the last 3 years a lot of fun, and to the Casey family thank you for taking care of me during the first major lockdown.

Finally, I would like to thank my examiners Prof. Vincent Pagneux and Dr. Gareth Wyn Jones for their time spent going through this thesis, the enjoyable viva and the resulting feedback. It was a pleasure discussing my work with such talented scientists.

# Chapter 1

# Background

In this chapter, we aim to provide the reader with the necessary physical context that motivates this project and introduce the well established mathematical models that underpin the original work developed in the subsequent chapters.

## 1.1 Introduction

Waves are manifested in many different ways in the world that surrounds us, and they allow us to encapsulate extremely diverse physical phenomena such as oscillations observed in oceans, light, radio, sound, vibrations and even gravity under the same category. Due to their omnipresence, the understanding of how some of these waves behave under different conditions has been a focus of study for centuries, with early work on optics dating back to Da Vinci in the fifteenth century. As a result, enough knowledge has been obtained in order to find various applications in sensing, non-destructive testing, material characterisation, energy harvesting, noise reduction (and enhancement) just to name a few. Nevertheless, many phenomena associated with wave propagation in many complex materials (both natural and synthetic) are not fully understood. Furthermore, significant interest lies in the development of *new* materials that can manipulate waves in novel ways. This field of study is known as the science of *metamaterials*, which we will discuss shortly. The design of these materials will help us improve existing technologies that will be necessary in order to tackle our current and upcoming problems as a civilization.

Acoustic and elastic transmission consist of three fundamental elements: the source,

the propagation medium and the receiver. For a homogeneous medium in the absence of any external disturbance or forcing, increasing the distance between the source and the receiver, not only results in a natural time lag dictated by the finiteness of the wave speed of the medium in consideration, but it also yields a drop of the intensity of the signal as the source-receiver distance increases which is besides that of geometric spreading. This energy loss is predominantly due to *viscous* and *thermal phenomena*. As the wave propagates in a *fluid* medium, the difference in the motion of adjacent fluid particles gives rise to reaction forces that oppose the displacements resulting in an overall damping of the wave. Furthermore, acoustic wave motion is longitudinal which creates regions of compression where many particles become closely packed, and regions of rarefaction, where the particles are distributed more sparsely. This creates a variation in the temperature of the fluid which induces heat transfer from the 'hotter' to the 'colder' region. Despite this, for many common materials under regimes of interest, the values of energy losses are so small that they are approximated by adding a small imaginary part to the expression of the wave speed, or completely ignored. From a modelling perspective, this is particularly convenient since the governing equations reduce to a scalar wave equation, which is the regime of 'classical acoustics' which has been studied extensively.

The presence of boundaries in the fluid medium leads to thin regions in which viscosity and thermal dissipation become important, and in these regions the classical acoustics approximation fails to fully characterize the fluid's motion. These regions are denoted as *boundary layers* and in particular it is easily observable that the dissipation associated with these regions is significantly superior to the losses in the absence of boundaries. This was demonstrated over one hundred and fifty years ago when Kirchhoff [1868] proposed a theory for sound propagation in gases based on the Navier-Stokes equations and Fourier's equation of heat conduction. He discussed the effect of attenuation for plane waves and spherical outgoing waves in the absence of boundaries and for guided waves along the axis of a rigid cylindrical duct. The presence of boundary layer regions on the duct walls that gives rise to interesting effects and motivated several posterior studies [Rayleigh, 1896, Zwikker and Kosten, 1949, Tijdeman, 1975, Bruneau et al., 1989, Stinson, 1991, Bruneau, 2006] which have resulted in a vast general theoretical understanding of visco-thermal attenuation of

sound in gas-filled waveguides both from the analytical and numerical perspectives [Bossart et al., 2003, Kampinga et al., 2011, Cutanda-Henríquez and Juhl, 2013].

A class of materials that has received significant attention across most disciplines of wave motion during the last few decades is that of metamaterials and metasurfaces. Although there is no particular consensus, according to Prof. Vicent Romero-García (*Metagenierie 2019*) the following definition captures most of the essence: "Metamaterials are artificial heterogeneous devices that present new responses that could not occur in the constitutive resonant elements alone because of physical constraints". The reliance on *resonances* distinguishes them from more traditional fields of composite materials as well as photonic and phononic crystals, although today these are also considered metamaterials for many researchers [Ma and Sheng, 2016]. The constituent scatterers in metamaterials are often periodically arranged, and for wavelengths much larger than the scatterers size and relative distances, it is well known that this type of heterogeneous media can be characterized as homogeneous with effective properties that depend on the scatterers' resonances. This widely used technique is known as *homogenisation* [Parnell, 2004]. In the realm of acoustics, the responses exhibited by resonances in metamaterials allow to extend the traditional regime where the structure's *effective* bulk modulus $K_{\text{eff}}$ and mass density $\rho_{\text{eff}}$ are positive, into regions of parameter space where these quantities become near zero [Fleury and Alù, 2013], and even negative, both individually [Yang et al., 2008, Lemoult et al., 2016] and simultaneously [Lee et al., 2010]. As waves propagate through such media, these regimes allow the effective wave speed $c_{\text{eff}} = \sqrt{K_{\text{eff}}/\rho_{\text{eff}}}$ to be manipulated in order to achieve exotic behaviour such as perfect absorption [Romero-García et al., 2016]. These types of structures generally consist of very small length scales, and the combination of resonances with the intrinsic thermo-viscous losses are key elements of their response, and therefore the classical acoustics theory discussed above is generally not sufficiently accurate. In fact, modelling of many proposed metamaterial structures in the absence of losses has led to contradicting results. In Cutanda Henríquez et al. [2017] it was recently shown that a design theoretically presented in Graciá-Salgado et al. [2013] as a near-zero and negative mass density metamaterial at certain frequencies, has actually always positive mass density when thermo-viscous losses are taken into account, which was further validated experimentally. As a consequence, the resulting *perfect*

*transmission* initially proposed in Graciá-Salgado et al. [2013] is nonexistent in practice and the losses are so strong that it is noted in Cutanda Henríquez et al. [2017] that the structure would perform better as an absorber. As such, losses are often considered to complicate the possibility of achieving certain exotic effects, but in other instances they are considered advantageous since they provide an additional tunability mechanism to achieve a particular phenomenon [Li et al., 2017, Fernández-Marín et al., 2019, Gerard and Jing, 2020].

Most of the discussion thus far has been focused on the *in-air* 'acoustic' context. Some acoustic metamaterial devices such as membrane-type media have used resonant constituents made of very soft media such as aerogels in order to further damp noise [Fernández-Marín et al., 2019]. Nevertheless, for the most part, the low density of air is such that the majority of boundaries can be considered as *acoustically rigid*. This is not the case however for acoustic propagation in heavier fluids such as water. In this instance, it is generally important to account for the energy that gets radiated into the solid material and, unlike for gases, in most cases this cannot be simply approximated by means of a boundary condition. This phenomenon is referred to as *fluid-structure interaction* (FSI) and is one of the key reasons why 'in-air' structures such as those encountered in acoustic metamaterials generally cannot perform well underwater (UW) and alternative designs must be proposed [Meng et al., 2012, Sharma et al., 2019]. Many of these UW designs rely on the presence of soft polymeric media which are highly *viscoelastic*.

As opposed to fluids, *solid* media have a capacity to store energy. Deformations of viscoelastic media are particularly sensitive to the time scales involved in the applied forces, as well as temperature. This leads to important physical behaviour such as *stress relaxation* and *creep*, that are related to the dissipation of mechanical energy. Naturally, this material behaviour largely affects the way waves propagate in such media which, following the discussion presented above, is clearly of significant interest for acoustic applications. Nevertheless, applications of viscoelastic media extend across many other important areas in biology and engineering [Lakes, 2017].

Despite the significant inherent differences between the ways fluids and solids deform, in the regime of small deformations and temperature differences, the equations governing wave propagation including losses in these media obtain very similar forms.

It turns out that this occurrence is particularly convenient for the types of problems that will be discussed in this thesis.

### 1.1.1 Structure and work presented in this thesis

In this PhD thesis, we are concerned with the modelling of attenuation of linear wave motion across a vast range of homogeneous continua ranging from (Newtonian) fluids including gases and liquids, to solids which are capable of both storing and dissipating energy such as rubbery-type media and metals. We are particularly interested in the behaviour of waves around interfaces bounding fluid-solid media where FSI is important. In order to aid this analysis, we will introduce a framework for wave propagation in linear thermo-visco-elasticity (TVE) that will allow us to simultaneously analyze the role of viscous and thermal dissipation in all such media. In particular this generalizes existing approaches in the literature for modelling visco-thermal dissipation in fluids and solids e.g. Karlsen and Bruus [2015]. The framework is then applied to study wave propagation in some canonical problems involving fluid-filled slits and fluid-loaded plates. We show that the role of stress relaxation can give rise to interesting dispersive effects that cannot be captured with commonly used viscoelastic models.

In the remaining sections of this chapter, we aim to introduce the necessary concepts that are used throughout the thesis in order to formulate problems of our interest, and obtain their respective solutions. Section 1.2 describes the characterization of fluid media, and in particular the assumptions that must be made in order to arrive at the governing equations that describe their motion as well as associated types of boundary conditions. This is firstly done for *ideal* fluids for which dissipative mechanisms are not taken into account (Section 1.2.1) and subsequently for visco-thermal fluids which dissipate energy via viscous and thermal effects in Section 1.2.2. The latter model is put into practice in Section 1.3, where we consider an introductory scattering problem consisting of a thermo-visco-acoustic (TVA) half–space residing on top of a rigid substrate. From this problem we are able to identify a regime (namely when the boundary layers are very narrow compared to the exterior domain) in which the governing equations can generally be simplified significantly. This regime is discussed from first principles since it is often used in the associated literature. We then move

onto the characterization of solid media in Section 1.4 with focus on the idealized media in Section 1.4.1, and the addition of viscoelastic and thermoelastic effects (separately) in Section 1.4.2. Finally, we discuss the approach taken in this thesis to analyse *dispersion relations*, and in particular their visualization and the obtention of their roots which are of high interest since they (can) correspond to particular solutions to the governing equations. As we will see, various dispersion relations of different physical significance are considered in this thesis, particularly in Chapters 2 and 4. We therefore finish the current chapter with a classical example consisting of the *Rayleigh dispersion equation* in elasticity, which will be extended upon in subsequent chapters.

Chapter 2 focuses on the study of acoustic propagation in the narrow slit regime (within infinite media), where boundary layer effects become notable and can greatly alter the phase speed and attenuation of the corresponding acoustic mode. The study is focused on air and water, and their differences are noted throughout. Despite it being well known, it is highlighted how for standard water-metal interfaces the presence of fluid-structure interaction effects (FSI) must be taken into account for a correct description of the acoustic field, which is nevertheless unnecessary for air where the boundaries can assumed to be rigid. The elastic effects of the metal are introduced by considering a medium obeying the equations of linear elasticity from Section 1.4.1. The physical consequences, particularly on the reduction of phase speed and dispersion are discussed extensively. This work is presented in terms of a journal article, namely Cotterill et al. [2018] which was published during the second year of this PhD project. In Section 2.3 we briefly comment on the significant differences in the obtained FSI results that can arise when the *hard* (metal) interfaces considered in the paper are replaced by *softer* media such as those consisting of rubbery materials and plastics. We note that although some of these differences can be explained with the linear elastic theory employed, in reality soft media experience internal damping as a result of viscoelastic effects, due to large molecular rearrangements which lead to stress relaxation and creep. In order to incorporate these extra physical mechanisms, we must include far more general modelling assumptions, which are introduced in Chapter 3, and subsequently applied in Chapter 4.

Chapter 3 is devoted to the development of a framework for linear *thermo-viscoelasticity* (TVE). Although frequently addressed in the literature due to the natural

physical significance, it was noted that unlike in the case of TVA, the literature seemed to lack a consistent set of equations for the study of general linear TVE with clear assumptions of the underlying theory that is readily available for the consideration of dynamic problems. This is attempted in this work, where convenient asymptotic approximations to the thermo-compressional wavenumbers appearing in the resulting governing equations are provided. We further discuss the possibility to arrive at the equations of TVA for Newtonian fluids introduced in Section 1.2.2 which is convenient for FSI problems, as well as other useful limits from the theory which are discussed in detail. Since these limits are well behaved, this allows for the study of wave propagation in a diverse range of media without prior specification. This is put into practice for the canonical problem of two TVE half–spaces in perfect contact where results for air, water, steel and rubber are included, and in the last of these stress relaxation is highlighted. In Section 3.3 we give an additional example to showcase how the TVE model can be used for the study of TVA fluids with rigid boundaries and further show the validity of the asymptotic approximations previously obtained by providing direct comparisons with solutions from Section 2.2.

Chapter 4 makes use of the TVE framework to focus on boundary layer effects, together with stress relaxation effects on three related canonical problems: namely two half–spaces, narrow slits (as in Chapter 2) and loaded plates. The study is performed in the absence of thermal effects since the physical interest is in water–solid interfaces, and both hard and soft solids are considered in order to emphasize their differences. The half–space problem is relevant to the other two, since it constitutes their geometrical limit in the short wavelength regime, and this fact is used to identify the starting point of the numerical root finding technique. Physically, it gives rise to *Scholte* and *Leaky Rayleigh* modes on the fluid–solid interface. It is the former of these two which is mainly analysed in this paper, since it is present for *any* fluid/solid pair and is truly localized to the interface and as a result is of high interest in sensing and *non-destructive testing* (NDT). For the slit, this solution turns into a 'coupled duct–Scholte mode' whereas for the loaded plates the mode becomes a 'coupled plate–Scholte mode'. In both instances it is shown how high values of attenuation can be obtained when the moduli of the solid are close to *glass transition*. For the symmetric coupled plate–Scholte mode in soft viscoelastic plates we find the presence

of a global maximum in attenuation with respect to plate thickness which could be of particular physical significance.

Finally, in Chapter 5 we summarise the work presented and discuss possible direct continuations for future studies.

### 1.1.2 A note on notation

In this introductory chapter, we will interchangeably refer to the different fields in both vector (tensor) or index notation, where in the former vectors/tensors are represented in bold whereas for index notation we use light italic with indices as subscripts, and repeated suffices indicate summation over these indices. Overbars are used throughout this chapter to represent dimensional quantities.

We note that since this thesis is presented in alternative format, the main bodies of work in Chapters 2, 3 and 4 are introduced as individual papers involving studies in various contexts, so that different sets of notation have inevitably been employed. Furthermore, there is duplication of the equation numbers between the main thesis body and some of the individual chapters. In order to avoid confusion, when an equation from one of the papers is referenced in the main thesis body, the chapter in which it is found will be emphasized.

## 1.2 Modelling Fluids

In what follows we are assuming fluids follow the *continuum hypothesis* such that the concept of a 'material particle' can be defined (see e.g. Marsden and Hughes [1994]). The corresponding dimensions of these particles are large enough so that molecular scales need not be considered, but smaller than any other relevant physical dimension. We can apply the fundamental laws of classical physics to a finite volume of these fluid particles in order to obtain relevant equations for fluid flow, which are mathematically expressed in integral form. If we further make the common assumption that fluid properties are continuous and their derivatives exist, we can take an appropriate limit so that the governing equations become purely differential, and therefore particularly convenient to tackle with mathematical machinery.

### 1.2.1 Linear Acoustics

We commence by deriving the equations governing classical linear acoustics from conservation laws in the absence of any form of dissipation, and in particular emphasize the key thermodynamic assumptions that lead to this classical theory. We state this level of detail here for notational consistency and to underpin the work that follows. Similar treatments to this introductory section can be found in most fluid mechanics or wave motion textbooks such as Landau and Lifshitz [1959], Morse and Ingard [1986], and Pierce et al. [1981].

#### Governing Equations

In general, *compressible* fluids experience overall changes in volume when deformed due to a particular force. The time rate of change is governed by the physical requirement of *conservation of mass*, namely

$$\frac{\partial \bar{\rho}}{\partial \bar{t}} + \bar{\nabla} \cdot (\bar{\rho}\bar{\mathbf{v}}) = 0, \tag{1.1}$$

where the scalar field $\bar{\rho}(\bar{\mathbf{x}}, \bar{t})$ denotes the fluid's mass density at a particular position within the fluid at a given instant of time, $\bar{\mathbf{v}}(\bar{\mathbf{x}}, \bar{t})$ represents the associated (vectorial) velocity field, and the independent variables of space and time are given by $\bar{\mathbf{x}} \equiv \bar{x}_i = (\bar{x}_1, \bar{x}_2, \bar{x}_3)$ and $\bar{t}$ respectively. We note here that the overbar notation is used from here onwards to refer to dimensional quantities.

The fluid's behaviour in response to applied stresses is incorporated into the model through the *conservation of momentum* equations, namely

$$\bar{\rho}\left(\frac{\partial \bar{\mathbf{v}}}{\partial \bar{t}} + \bar{\mathbf{v}} \cdot \bar{\nabla}\bar{\mathbf{v}}\right) = \bar{\nabla} \cdot \bar{\boldsymbol{\sigma}}, \tag{1.2}$$

in the absence of external *body forces*, where $\bar{\boldsymbol{\sigma}}(\bar{\mathbf{x}}, \bar{t})$ denotes the *Cauchy stress tensor*. For an inviscid fluid, the only internal force acting is that of *hydrostatic pressure* which results in the constitutive equation

$$\bar{\boldsymbol{\sigma}} = -\bar{p}\mathbf{I}, \tag{1.3}$$

where $\bar{p}(\bar{\mathbf{x}}, \bar{t})$ denotes the pressure which is a force per unit area, and $\mathbf{I}$ is the identity tensor. Direct substitution of (1.3) into (1.2) yields *Euler's equations*, i.e.

$$\bar{\rho}\left(\frac{\partial \bar{\mathbf{v}}}{\partial \bar{t}} + \bar{\mathbf{v}} \cdot \bar{\nabla}\bar{\mathbf{v}}\right) = -\bar{\nabla}\bar{p}, \tag{1.4}$$

which is a vectorial manifestation of the ubiquitous *Newton's second law* ($F = ma$) per unit volume, with the negative pressure gradient term on the right of (1.4) acting as the only force $F$ and the term on the left hand side representing mass times acceleration $ma$. At this stage, we notice that for the 5 unknown quantities (in the 3D case) introduced so far $(\bar{\rho}, \bar{p}, \bar{\mathbf{v}})$ we only have 4 independent equations, namely (1.1), (1.4). In order to obtain a closure condition, it is customary to specify an equation of state of the form

$$\bar{p} = \bar{p}(\bar{\rho}), \tag{1.5}$$

which implies the fluid is *barotropic*, i.e. its pressure only varies with density (and vice versa). Implicit in this assumption is the fact that the fluid is regarded as being in local *thermodynamic equilibrium*[1] (sometimes referred to as Stokes' hypothesis [Rienstra and Hirschberg, 2004]) so that there is an equation of state that relates the fluid's thermodynamic variables which as a result are not independent. Naturally, in order to analyse thermodynamic processes and a given systems state, we must first introduce the fluid's (absolute) *temperature* field $\bar{T}$, and *entropy* (per unit mass) $\bar{h}$ which satisfies $\mathrm{d}\bar{h} = \delta\bar{Q}/\bar{T}$, with $\bar{Q}$ representing the quantity of heat[2] per unit of mass. Except in some very specific cases (e.g. ideal gases and Van der Waals gases) equations of state are unknown, but significant progress can be achieved by admitting nothing else than their existence, and the fact that the thermodynamic variables are therefore not all independent. The *first law of thermodynamics* can be invoked by considering entropy a function of *internal energy* and volume per unit mass $\bar{\mathcal{E}}$, $1/\bar{\rho}$ respectively, i.e. $\bar{h} = \bar{h}(\bar{\mathcal{E}}, \bar{\rho}^{-1})$, whose differential is given by

$$\bar{T}\,\mathrm{d}\bar{h} = \mathrm{d}\bar{\mathcal{E}} + \bar{p}\,\mathrm{d}\left(\frac{1}{\bar{\rho}}\right), \tag{1.6}$$

indicating that the change of internal energy $\mathrm{d}\bar{\mathcal{E}}$ of a quasi-static system can only occur due to heat $\bar{T}\,\mathrm{d}\bar{h}$ (by definition of entropy) and work, represented by $\bar{p}\,\mathrm{d}\bar{\rho}^{-1}$ for an inviscid fluid [Wilson, 1960]. Equation (1.6) is particularly useful, since we observe that temperature $\bar{T}$ and pressure $\bar{p}$ can also be seen as functions of $\bar{\mathcal{E}}$, $\bar{\rho}^{-1}$. We can therefore interpret the entropy as a function of any *two* of the state variables $\bar{\mathcal{E}}$, $\bar{\rho}$, $\bar{p}$,

[1] This is considered valid for quasi-static processes i.e. low frequency disturbances with little spatial variation (as we are considering here) as explained in detail in Pierce et al. [1981].

[2] Its differential is represented by the symbol $\delta$ since heat (and work) does not describe the state of a system.

$\bar{T}$, as suggested above due to thermodynamic equilibrium. In particular, this implies that we can write

$$\bar{p} = \bar{p}(\bar{\rho}, \bar{h}), \tag{1.7}$$

which generalises the barotropic relation (1.5). In order to find out under which conditions (1.5) can be applied rather than (1.7) we must understand the variation of entropy in the processes in consideration, which we shall discuss next. The differential equation of total energy in a fluid particle can be written as [Pierce et al., 1981]

$$\bar{\rho}\left(\frac{\partial}{\partial \bar{t}} + \bar{\mathbf{v}} \cdot \bar{\nabla}\right)\left(\frac{1}{2}|\bar{\mathbf{v}}|^2 + \bar{\mathcal{E}}\right) = \bar{\nabla} \cdot (\bar{\boldsymbol{\sigma}}\bar{\mathbf{v}}) - \bar{\nabla} \cdot \bar{\mathbf{q}}, \tag{1.8}$$

where in index notation $\bar{\nabla} \cdot (\bar{\boldsymbol{\sigma}}\bar{\mathbf{v}}) = \partial(\bar{\sigma}_{ij}\bar{v}_i)/\partial \bar{x}_j$ and $\bar{\mathbf{q}}$ represents the (inward) heat-flux vector which commonly follows *Fourier's law* so that $\bar{\mathbf{q}} = -\bar{\mathcal{K}}\bar{\nabla}\bar{T}$ where $\bar{\mathcal{K}} > 0$ represents the *coefficient of thermal conductivity* which we assume to be constant. If we further substitute the ideal inviscid fluid relation (1.3), after some algebraic manipulation using (1.6) we can obtain

$$\bar{\rho}\bar{T}\left(\frac{\partial \bar{h}}{\partial \bar{t}} + \bar{\mathbf{v}} \cdot \bar{\nabla}\bar{h}\right) = \bar{\mathcal{K}}\bar{\nabla}^2\bar{T}, \tag{1.9}$$

which gives the time evolution of the entropy $\bar{h}$. Interestingly, in the early stages it was unclear whether sound was best modelled as an *isothermal* process where temperature remains constant, or as an *adiabatic* process where there is no heat flow [Stokes, 1851]. These two cases are represented by whether heat conduction dominates (RHS term in (1.9) is predominant) or is negligible (LHS term in (1.9) predominates). Experimental results confirmed that for standard acoustic scenarios in fluids, the adiabatic approximation is much better[3] (see Pierce et al. [1981] Section 1.10) and therefore (1.9) can be approximated by

$$\frac{\partial \bar{h}}{\partial \bar{t}} + \bar{\mathbf{v}} \cdot \bar{\nabla}\bar{h} = 0. \tag{1.10}$$

In particular, if we ignore the (non-linear) advective term in (1.10) we observe that if the medium is initially *isentropic* (so that $\bar{h}$ is the same everywhere), and since the fluid is *homogeneous* (so that each fluid particle has same equation of state), the barotropic assumption (1.5) is a direct consequence of (1.7) and (1.10). This argument will be made precise next once some extra assumptions are considered.

[3]Nevertheless, as we will see later this assumption is not particularly accurate in regions near boundaries.

We further suppose that the fluid is homogeneous and has ambient quantities $\bar{\mathbf{v}} = \mathbf{0}$, $\bar{p} = \bar{p}_0$, $\bar{\rho} = \bar{\rho}_0$, $\bar{T} = \bar{T}_0$, $\bar{h} = \bar{h}_0$ and is perturbed by a small amplitude motion so that we can represent the relevant fields as

$$\bar{\mathbf{v}} = \epsilon\bar{\mathbf{V}}(\bar{\mathbf{x}}, \bar{t}) + O(\epsilon^2), \tag{1.11a}$$

$$\bar{p} = \bar{p}_0 + \epsilon\bar{P}(\bar{\mathbf{x}}, \bar{t}) + O(\epsilon^2), \tag{1.11b}$$

$$\bar{\rho} = \bar{\rho}_0 + \epsilon\bar{\varrho}(\bar{\mathbf{x}}, \bar{t}) + O(\epsilon^2), \tag{1.11c}$$

$$\bar{T} = \bar{T}_0 + \epsilon\bar{\mathcal{T}}(\bar{\mathbf{x}}, \bar{t}) + O(\epsilon^2), \tag{1.11d}$$

$$\bar{h} = \bar{h}_0 + \epsilon\bar{H}(\bar{\mathbf{x}}, \bar{t}) + O(\epsilon^2), \tag{1.11e}$$

where $\epsilon \ll 1$ is a small, non-dimensional parameter representing the fact that we are dealing with small amplitude perturbations from an equilibrium state, so that the linear approximation (1.11) is adequate. The subscript "0" has been used to denote the equilibrium value of the various quantities which we assume to be independent of space and time (i.e. constant). Direct substitution of (1.11) into (1.1), (1.4) gives at $O(\epsilon)$

$$\frac{\partial\bar{\varrho}}{\partial\bar{t}} = -\bar{\rho}_0\bar{\nabla}\cdot\bar{\mathbf{V}}, \tag{1.12}$$

$$\bar{\rho}_0\frac{\partial\bar{\mathbf{V}}}{\partial\bar{t}} = -\bar{\nabla}\bar{P}, \tag{1.13}$$

so that we have neglected quadratic and higher order terms due to their smallness given that $\epsilon \ll 1$. Furthermore, substitution of (1.11e) into the approximate entropy evolution equation (1.10) gives at $O(\epsilon)$ that $\bar{H}$ must in fact be zero and therefore $\bar{h} = \bar{h}_0$ at any given time[4], and the barotropic assumption (1.5) is valid in this regime. We therefore continue by performing a Taylor expansion about the ambient state $\bar{p}_0 = \bar{p}(\bar{\rho}_0) = \bar{p}(\bar{\rho}_0, \bar{h}_0)$ in order to arrive at the first order approximation

$$\bar{P} = \left(\frac{\partial\bar{p}}{\partial\bar{\rho}}\right)_{\bar{\rho}_0,\bar{h}_0}\bar{\varrho}, \tag{1.14}$$

where[5]

$$\left(\frac{\partial\bar{p}}{\partial\bar{\rho}}\right)_{\bar{\rho}_0,\bar{h}_0} = \bar{c}_{\mathrm{A}}^2 = \frac{\bar{K}_{\mathrm{A}}}{\bar{\rho}_0}, \tag{1.15}$$

[4]Since we are considering homogenous fluids.

[5]The subscript $(\bar{\rho}_0, \bar{h}_0)$ indicates that the derivatives are evaluated at constant entropy, and with density subsequently set to $\bar{\rho}_0$.

and $\bar{c}_{\mathrm{A}}^2$ is in fact the (square of the) adiabatic[6] speed of sound, and $\bar{K}_{\mathrm{A}}$ the (adiabatic) bulk modulus, which are both $O(1)$ constant following the expansion. In the case of an ideal gas for which (1.5) is explicitly known, it can be shown that $\bar{c}_{\mathrm{A}}^2 = \sqrt{\frac{\gamma\bar{p}_0}{\bar{\rho}_0}}$ where $\gamma$ represents the *ratio of specific heats* [Bruneau, 2006]. Equations (1.12), (1.13) and (1.14) constitute what are commonly known as the *linear acoustics equations* after using the *acoustic approximation* since we have omitted $O(\epsilon^2)$ terms. Further, if we take the divergence of (1.13) and subtract it from the time derivative of (1.12) whilst substituting (1.14) we obtain

$$\bar{c}_{\mathrm{A}}^2 \bar{\nabla}^2 \bar{P} = \frac{\partial^2 \bar{P}}{\partial \bar{t}^2}, \tag{1.16}$$

which is a linear, homogeneous *hyperbolic* Partial Differential Equation (PDE) commonly known as the (linear) *wave equation*. From a physical point of view, (1.16) implies that linear acoustics is governed by compressional (stress) waves. As an observation, we further note that despite being commonly ignored due to the uncoupling of the entropy equation (1.9) under the adiabatic approximation, this model can also yield an associated temperature perturbation. Indeed, if we further consider $\bar{T} = \bar{T}(\bar{p}, \bar{h})$ and substitute (1.11b), (1.11e) together with the fact that the entropy is a constant, we obtain at $O(\epsilon)$

$$\bar{\mathcal{T}} = \left(\frac{\partial \bar{T}}{\partial \bar{p}}\right)_{\bar{p}_0, \bar{h}_0} \bar{P}, \tag{1.17}$$

after performing a Taylor expansions over the equilibrium state $\bar{T}_0 = \bar{T}(\bar{p}_0, \bar{h}_0)$, where the term in brackets in (1.17) is a constant as a result of the expansion. Further, a thermodynamic identity[7] allows us to write this term in brackets in terms of well tabulated physical quantities, namely

$$\left(\frac{\partial \bar{T}}{\partial \bar{p}}\right)_{\bar{p}_0, \bar{h}_0} = \frac{\bar{\alpha}\bar{T}_0}{\bar{\rho}_0 \bar{c}_p}, \tag{1.18}$$

where further

$$\bar{\alpha} = \bar{\rho}\left(\frac{\partial \bar{\rho}^{-1}}{\partial \bar{T}}\right)_{\bar{p}_0}, \quad \bar{c}_p = \bar{T}\left(\frac{\partial \bar{h}}{\partial \bar{T}}\right)_{\bar{p}_0}, \tag{1.19}$$

correspond to the coefficient of volumetric *thermal expansion* $\bar{\alpha}$ and *specific heat* at constant pressure $\bar{c}_p$. Equation (1.17) together with the linearity of (1.16) and the adiabatic approximation used in (1.9), (1.10) implies that $\bar{\mathcal{T}}$ satisfies the same standard

[6] Or isentropic since as we have seen adiabaticity is a consequence of an isentropic process.

[7] The derivation of this identity is straightforward by using a *Maxwell* relation, see e.g. page 17 of Pierce et al. [1981].

wave equation (1.16) in this model (which is the reason why temperature is usually not mentioned in classical acoustics).

Finally, substitution of (1.3) with Fourier's law into the energy equation (1.8) and linearising following (1.11) gives, after writing the (linearised) internal energy in terms of pressure using (1.6) with $\mathrm{d}\bar{h} = 0$ and (1.15)

$$\frac{\partial \bar{\mathcal{U}}}{\partial \bar{t}} + \bar{\nabla} \cdot \bar{\mathbf{J}} = 0, \quad \text{with} \quad \bar{\mathcal{U}} = \frac{1}{2}\left(\bar{\rho}_0 |\bar{\mathbf{V}}|^2 + \frac{\bar{P}^2}{\bar{\rho}_0 \bar{c}_\mathrm{A}^2}\right) \quad \text{and} \quad \bar{\mathbf{J}} = \bar{P}\bar{\mathbf{V}}, \tag{1.20}$$

which we note is an $O(\epsilon^2)$ equation relating the total acoustic energy density $\bar{\mathcal{U}}$, and the intensity (or energy flux vector) $\bar{\mathbf{J}}$ respectively. The interpretation of (1.20) becomes clear when integrating it over a fixed closed volume. Letting $V$ be a fixed volume, and $S$ its corresponding enclosing surface we can write, (using the *divergence theorem* on the second term)

$$\frac{\mathrm{d}}{\mathrm{d}\bar{t}} \iiint_V \bar{\mathcal{U}} \, \mathrm{d}V + \oiint_S \bar{\mathbf{J}} \cdot \mathbf{n} \, \mathrm{d}A = 0. \tag{1.21}$$

with $\mathbf{n}$ representing the outward unit normal from $S$ (parametrized by the differential element $\mathrm{d}A$). This shows that the rate of change of energy on a (fixed) volume particle is solely due to the work done on it by the surface forces (as expected for an ideal fluid). The fact that (1.20) can be derived from the leading order equations (1.12), (1.13) and (1.14) (not shown) implies that it is in fact a *Corollary*, and hence need not be discussed to obtain the solution to the linear acoustic mathematical problem. Nevertheless, its physical importance can be very helpful in specific scenarios, as we will observe later.

### The Helmholtz Equation

Given the linearity of the wave equation (1.16), its *Fourier transform* [Stein and Weiss, 1971] transforms the directly observable time domain problem into an associated frequency domain problem. In this space we can look for steady, time-harmonic solutions to (1.16) in the form[8] $\bar{P}(\bar{\mathbf{x}}, \bar{t}) = \mathrm{Re}\left\{\hat{\bar{P}}(\bar{\mathbf{x}})\mathrm{e}^{-\mathrm{i}\bar{\omega}\bar{t}}\right\}$ with angular frequency $\bar{\omega}$, so that (1.16) reduces to the unforced *Helmholtz equation*

$$\left(\bar{\nabla}^2 + \bar{k}^2\right)\hat{\bar{P}} = 0, \tag{1.22}$$

[8] Equivalently, the time factor $\mathrm{e}^{\mathrm{i}\omega t}$ is often chosen in the literature. The choice adopted here is merely due to the author's preference.

where $\bar{k} = \bar{\omega}/\bar{c}_{\mathrm{A}} = 2\pi/\bar{\lambda}_W$ denotes the acoustic wavenumber and $\bar{\lambda}_W$ the acoustic wavelength (Figure 1.1). Given a solution to (1.22), the associated (time harmonic) velocity $\hat{\bar{\mathbf{V}}}$ and density $\hat{\bar{\varrho}}$ are directly obtained via (1.13), (1.12), which written in the frequency domain become

$$\mathrm{i}\bar{\omega}\bar{\rho}_0\hat{\bar{\mathbf{V}}} = \bar{\nabla}\hat{\bar{P}}, \tag{1.23}$$

$$\mathrm{i}\bar{\omega}\hat{\bar{\varrho}} = \bar{\rho}_0\bar{\nabla}\cdot\hat{\bar{\mathbf{V}}}, \tag{1.24}$$

where $\bar{\mathbf{V}}(\bar{\mathbf{x}},\bar{t}) = \mathrm{Re}\,\{\hat{\bar{\mathbf{V}}}(\bar{\mathbf{x}})\mathrm{e}^{-\mathrm{i}\bar{\omega}\bar{t}}\}$, and $\bar{\varrho}(\bar{\mathbf{x}},\bar{t}) = \mathrm{Re}\,\{\hat{\bar{\varrho}}(\bar{\mathbf{x}})\mathrm{e}^{-\mathrm{i}\bar{\omega}\bar{t}}\}$. In principle, when obtaining the solution to the steady state problem governed by (1.22) it is possible (under certain conditions [Stein and Weiss, 1971]) to recover the full time-dependent solution by taking the *inverse Fourier transform*. For this reason time-harmonic problems are of high interest, and in fact the majority of problems in this thesis are set-up in this regime. Furthermore, from direct substitution into (1.22) we note that plane-wave solutions of the type

$$\hat{\bar{P}} = \bar{A}_1\mathrm{e}^{-\mathrm{i}\bar{\mathbf{k}}\cdot\bar{\mathbf{x}}} + \bar{A}_2\mathrm{e}^{+\mathrm{i}\bar{\mathbf{k}}\cdot\bar{\mathbf{x}}} \tag{1.25}$$

where $\bar{\mathbf{k}} = (\bar{k}_1,\bar{k}_2,\bar{k}_3)$ are solutions to the Helmholtz equation provided $\bar{\mathbf{k}}\cdot\bar{\mathbf{k}} = ||\bar{\mathbf{k}}|| = \bar{k}^2$. $\bar{A}_1,\bar{A}_2$ are arbitrary constant amplitudes of waves travelling in opposite directions. The fact that the wave propagates in the direction of $\bar{\mathbf{k}}$ with associated wavelength[9] $\bar{\lambda}_W = 2\pi/||\bar{\mathbf{k}}||$ is illustrated in Figure 1.1. Furthermore, direct substitution of (1.25) into (1.23) shows that the associated velocity field is parallel to $\bar{\mathbf{k}}$, and therefore to the direction of propagation[10]. As we will see this is not always the case in other physical systems and for this reason pressure ('P') waves are also called *longitudinal* waves.

A very large class of problems of much interest are associated to *wave scattering* which encompass waves in its many manifestations e.g. light, vibrations, radio, etc. In the current acoustic context these can be formulated by using the linearity of the Helmholtz equation to write e.g.

$$\hat{\bar{P}}_{\mathrm{tot}} = \hat{\bar{P}}_{\mathrm{in}} + \hat{\bar{P}}_{\mathrm{sc}}, \tag{1.26}$$

where $\hat{\bar{P}}_{\mathrm{in}}$ is the *incident* field and $\hat{\bar{P}}_{\mathrm{sc}}$ the *scattered* field arising from the presence of a given *scatterer* representing a certain obstacle in the otherwise acoustic medium

[9] The $2\pi$ factor arises naturally due to the periodicity of the trigonometric functions that compose the complex exponential function.

[10] This in turn implies that the motion is *irrotational*, which can be seen from taking the curl of (1.23).

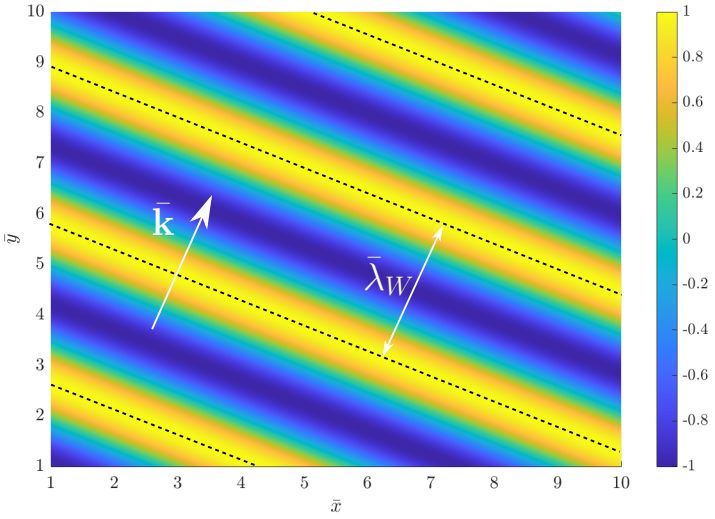


Figure 1.1: Heatmap of travelling plane wave solution to the Helmholtz equation (1.25) ($\text{Re}\{\hat{\bar{P}}\}$) with $\bar{A}_1 = 0$, $\bar{A}_2 = 1$ and $\bar{\mathbf{k}} = (1, 2)$ m$^{-1}$ with associated wavelength $\bar{\lambda}_W = 2\pi/||\bar{\mathbf{k}}||$. The dotted lines indicate the contours of maximum pressure.

where certain conditions must apply (see section "Boundary Conditions" below). In general the functional form of $\hat{\bar{P}}_{\text{in}}$ is known a priori, and therefore the task is to find $\hat{\bar{P}}_{\text{sc}}$ which can be interpreted as the 'response' of the scatterer to the incident forcing.

### Boundary Conditions (BCs)

Having obtained the governing equation to solve in the domain of interest (1.22), for finite domains it is important to accurately specify the fluid's behaviour around the boundary regions. Depending on the type of media bounding the acoustic medium of interest, we can distinguish two main different scenarios.

#### - Interface conditions between neighbouring acoustic media

When two distinct acoustic media occupying regions $D_1$, $D_2$ with associated pressure and velocity fields $\{\hat{\bar{P}}_1, \hat{\bar{\mathbf{V}}}_1\}$, $\{\hat{\bar{P}}_2, \hat{\bar{\mathbf{V}}}_2\}$ are in perfect contact, the physical requirement of *continuity of pressure* and *continuity of normal velocity* at the boundary between these two domains is given by

$$\hat{\bar{P}}_1 = \hat{\bar{P}}_2 \qquad \text{on} \quad \partial D, \tag{1.27}$$

$$\hat{\bar{\mathbf{V}}}_1 \cdot \mathbf{n} = \hat{\bar{\mathbf{V}}}_2 \cdot \mathbf{n} \qquad \text{on} \quad \partial D, \tag{1.28}$$

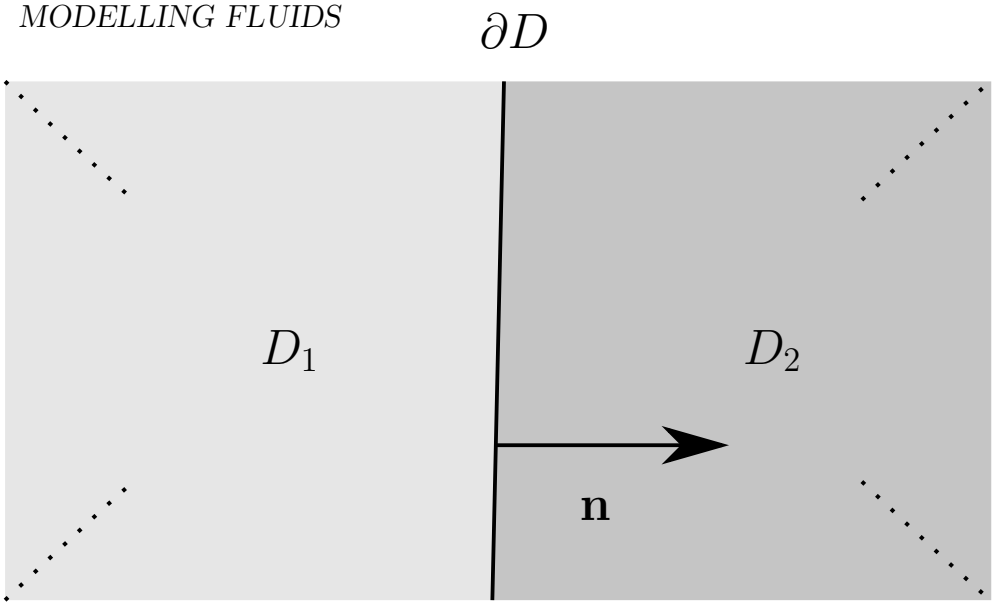


Figure 1.2: Schematic representation of two acoustic media occupying regions $D_1$, $D_2$ and the region of intersection denoted by $\partial D$ with (unit) normal $\mathbf{n}$ where the boundary conditions apply. For the Neumann, Dirichlet and Robin conditions we assume $D_1$ is the acoustic region of interest and make different assumptions of the medium in $D_2$ that lead to (1.30), (1.31) and (1.34).

where $\partial D$ denotes the boundary between $D_1$ and $D_2$ and $\mathbf{n}$ denotes the outer unit normal to $\partial D$ (see Figure 1.2). We may also write (1.28) in terms of pressure using the linearised equation (1.23) so that it becomes

$$\frac{1}{\bar{\rho}_1}\bar{\nabla}\hat{\bar{P}}_1 \cdot \mathbf{n} = \frac{1}{\bar{\rho}_2}\bar{\nabla}\hat{\bar{P}}_2 \cdot \mathbf{n} \qquad \text{on} \quad \partial D, \tag{1.29}$$

where $\bar{\rho}_1$ denotes the background density in medium 1 i.e. $\bar{\rho}_{1_0}$, where the subscript "0" has been suppressed for convenience, and similarly with $\bar{\rho}_2$.

**- Neumann, Dirichlet and Robin Conditions**

When a fluid encounters an impenetrable, *rigid* body that cannot support acoustic waves, the interface conditions (1.27), (1.28) must be revisited. We define a surface to be 'sound hard' whenever the normal gradient of the acoustic pressure field vanishes at its boundary, that is

$$\bar{\nabla}\hat{\bar{P}}_1 \cdot \mathbf{n} = 0 \qquad \text{on} \quad \partial D, \tag{1.30}$$

where $D_2$ is now occupied by the (rigid) solid substrate following the notation in Figure 1.2 above. We refer to (1.30) as the sound hard *Neumann* boundary condition. It is particularly relevant for gas-solid interfaces e.g. air-metal, since the density contrast between the two media does not allow the acoustic energy from the fluid to transmit

into the solid. This can be seen from letting $\bar{\rho}_1 \ll \bar{\rho}_2$ in (1.29) which approximates (1.30). On the other hand the 'sound soft' or *Dirichlet* BC is given by the requirement of the pressure field vanishing on the interface such that

$$\hat{\bar{P}}_1 = 0 \qquad \text{on} \quad \partial D. \tag{1.31}$$

Intuitively, this BC is often employed when the acoustic medium $D_1$ has a much higher density[11] than that of the material occupying $D_2$ which can for example occur in a fluid-gas interface, with the fluid ($D_1$) being the acoustic medium of interest (e.g. water-air).

Further, it turns out that in order to characterize the acoustic behaviour of many physically relevant materials including *porous* and *lossy* media, it is convenient to define the *acoustic impedance* (per unit area) $\bar{\mathcal{Z}}$ of a surface, which is given (assuming the surface is not moving) by the ratio of the surrounding fluid's pressure divided by the inward normal component (into the surface, see Figure 1.2) of the fluid velocity, namely

$$\bar{\mathcal{Z}} = \frac{\hat{\bar{P}}_1}{\hat{\bar{\mathbf{V}}}_1 \cdot \mathbf{n}}, \tag{1.32}$$

which can be fully written in terms of pressure via (1.23) to yield

$$\bar{\mathcal{Z}}(\bar{\omega}) = \frac{\mathrm{i}\bar{\omega}\bar{\rho}_0 \hat{\bar{P}}_1}{\bar{\nabla}\hat{\bar{P}}_1 \cdot \mathbf{n}}. \tag{1.33}$$

The acoustic impedance of a surface is generally a function of frequency $\bar{\mathcal{Z}}(\bar{\omega})$ found via experimental means with different techniques often consisting of the study of standing wave patterns in *impedance tubes* [Beranek, 1942]. Further, here we will always be considering $\bar{\mathcal{Z}}(\bar{\omega})$ that is independent of position along the surface. The *impedance* or *Robin* BC is then written as, using (1.33) with $\bar{\omega} = \bar{k}\bar{c}_\mathrm{A}$

$$\bar{\nabla}\hat{\bar{P}}_1 \cdot \mathbf{n} - \mathrm{i}\bar{k}\left(\frac{\bar{\rho}_0\bar{c}_\mathrm{A}}{\bar{\mathcal{Z}}}\right)\hat{\bar{P}}_1 = 0 \qquad \text{on} \quad \partial D, \tag{1.34}$$

where the term in brackets is a useful non-dimensional number (known as the normalised *acoustic admittance* of the material) which weighs the bounding material's acoustic impedance relative to the fluid's characteristic impedance ($\bar{\rho}_0\bar{c}_\mathrm{A}$). In particular, we observe how for $\bar{\mathcal{Z}} \gg \bar{\rho}_0\bar{c}_\mathrm{A}$ (1.34) approaches the sound hard BC (1.30) and conversely the sound soft BC (1.31) is recovered when $\bar{\mathcal{Z}} \ll \bar{\rho}_0\bar{c}_\mathrm{A}$. A more general

[11] This will be made precise shortly, when the acoustic impedance/admittance is introduced.

description of the same concept which includes moving surfaces is given in Bruneau [2006]. From a modelling perspective the possibility of characterizing complex acoustic media via $\bar{\mathcal{Z}}(\bar{\omega})$ is attractive, since it can possibly reduce a multi-domain problem into a single domain $(D_1)$ for the pressure $\hat{\bar{P}}_1$ with a more complex boundary condition that encapsulates the bounding medium's $(D_2)$ behaviour.

Finally, for physically sensible solutions to wave-scattering problems of the form (1.26) taking place in infinite domains, it must also be ensured that the scattered (outgoing) field solutions are not increasing as you move away from the scatterer. Formally, this can be written in terms of the *Sommerfeld radiation condition* [Sommerfeld, 1949].

### 1.2.2 Thermo-Visco Acoustics (TVA)

Building from the derivation yielding the linear acoustic model presented in Section 1.2.1, following Pierce et al. [1981] (Chapter 10) we introduce the extra modelling assumptions that must be considered which lead to the governing equations of linear thermo-visco acoustics in *Newtonian* fluids, and discuss the form of common types of associated boundary conditions. *Molecular relaxation* effects are not hereby considered for simplicity, although their importance in the prediction of attenuation at certain frequency ranges is noted[12]. Models including molecular relaxation are further discussed in standard acoustics textbooks by Pierce et al. [1981], and Bruneau [2006] with emphasis on *air*.

#### Governing Equations

We again consider a small amplitude sinusoidal motion in an otherwise still compressible, homogeneous thermo-viscous fluid. In order to characterize the resulting fluid behaviour, we propose a linear expansion analogous to (1.11) to be substituted in the relevant governing equations which we revisit next. The first major difference with the acoustic case is the more general constitutive relation for a compressible, viscous,

[12] More specifically, they become particularly important when the *relaxation time* $\tau$ (representing the molecule's vibration reaction time to an excitation) is close to the period of the wave so that $\omega\tau \approx 1$ [Bruneau, 2006].

heat conducting fluid which in component form is given by

$$\bar{\sigma}_{ij} = (-\bar{p} + \bar{\eta}'\bar{\nabla}\cdot\bar{\mathbf{v}})\boldsymbol{I} + \bar{\eta}(\bar{\nabla}\bar{\mathbf{v}} + \bar{\nabla}\bar{\mathbf{v}}^T) \tag{1.35a}$$

$$= -\bar{p}_0\delta_{ij} + \epsilon\left[\left(-\bar{P} + \bar{\eta}'\frac{\partial \bar{V}_j}{\partial \bar{x}_j}\right)\delta_{ij} + \bar{\eta}\left(\frac{\partial \bar{V}_i}{\partial \bar{x}_j} + \frac{\partial \bar{V}_j}{\partial \bar{x}_i}\right)\right] + O(\epsilon^2), \tag{1.35b}$$

with (1.35b) following from the linear expansion (1.11), where $\bar{\eta}$ is the classical shear viscosity representing the fluid's resistance to shear forces and $\bar{\eta}' = \bar{\eta}_K - 2\bar{\eta}/3$ where $\bar{\eta}_K > 0$ denotes the bulk/second viscosity associated with hydrostatic compression (which is often ignored in liquids due to their lower compressibility). Note that despite thermal effects not arising explicitly in (1.35b), they are contained in the pressure field $\bar{P}$ and their particular dependence is given by the equations of state[13] which we discuss shortly. Substitution of (1.35b) into conservation of momentum (1.2) yields at first order $O(\epsilon)$ the linearised *Navier-Stokes equations* for a compressible fluid, namely

$$\bar{\rho}_0\frac{\partial \bar{\mathbf{V}}}{\partial \bar{t}} = -\bar{\nabla}\bar{P} + \bar{\eta}\bar{\nabla}^2\bar{\mathbf{V}} + (\bar{\eta} + \bar{\eta}')\bar{\nabla}\left(\bar{\nabla}\cdot\bar{\mathbf{V}}\right). \tag{1.36}$$

On the other hand, the continuity of mass equation (1.1) remains identical in the same form, (since it is independent of the particular *rheology*) which after substituting (1.11) becomes (1.12) at $O(\epsilon)$. With regards to the corresponding equation for entropy, starting from (1.8) with the current expression for the Cauchy stress (1.35a) we can obtain in component form (details are omitted for brevity, but see Pierce et al. [1981] Section 10.1)

$$\bar{\rho}\bar{T}\left(\frac{\partial \bar{h}}{\partial \bar{t}} + \bar{v}_i\frac{\partial \bar{h}}{\partial \bar{x}_i}\right) = \frac{\bar{\eta}}{2}\bar{M}_{ij}\bar{M}_{ij} + \bar{\eta}_K\left(\frac{\partial \bar{v}_i}{\partial \bar{x}_i}\right)^2 + \bar{\mathcal{K}}\frac{\partial^2\bar{T}}{\partial \bar{x}_i\partial \bar{x}_i}, \tag{1.37}$$

where $\bar{M}_{ij} = \frac{\partial \bar{v}_i}{\partial \bar{x}_j} + \frac{\partial \bar{v}_j}{\partial \bar{x}_i} - \frac{2}{3}\left(\frac{\partial \bar{v}_k}{\partial \bar{x}_k}\right)\delta_{ij}$. Direct comparisons with (1.9) shows how all the extra terms in (1.37) arise due to the influence of fluid viscosity. Nevertheless, after linearising via (1.11) yields at $O(\epsilon)$

$$\bar{\rho}_0\bar{T}_0\frac{\partial \bar{H}}{\partial \bar{t}} = \bar{\mathcal{K}}\bar{\nabla}^2\bar{\mathcal{T}}, \tag{1.38}$$

observing that all viscous effects no longer appear in (1.38) since they are $O(\epsilon^2)$. Importantly, here we no longer make the adiabatic approximation (from which it can be concluded that $\bar{h} = \bar{h}_0$) which in turn implies that equations of state such

[13] Recall that in the purely acoustic case this is given by (1.17).

as the barotropic (1.5) are no longer valid and the more general form[14] (1.7) must be considered. In particular, note that (1.6) still applies since we are in the quasi-static regime with thermodynamic equilibrium. Consequently letting $\bar{\rho} = \bar{\rho}(\bar{p}, \bar{h})$, $\bar{T} = \bar{T}(\bar{p}, \bar{h})$ and substituting (1.11) we obtain at $O(\epsilon)$,

$$\bar{\varrho} = \left(\frac{\partial \bar{\rho}}{\partial \bar{p}}\right)_{\bar{p}_0, \bar{h}_0} \bar{P} + \left(\frac{\partial \bar{\rho}}{\partial \bar{h}}\right)_{\bar{p}_0, \bar{h}_0} \bar{H}, \tag{1.39a}$$

$$\bar{\mathcal{T}} = \left(\frac{\partial \bar{T}}{\partial \bar{p}}\right)_{\bar{p}_0, \bar{h}_0} \bar{P} + \left(\frac{\partial \bar{T}}{\partial \bar{h}}\right)_{\bar{p}_0, \bar{h}_0} \bar{H}, \tag{1.39b}$$

after performing two Taylor expansions over the equilibrium states $\bar{\rho}_0 = \bar{\rho}(\bar{p}_0, \bar{h}_0)$, and $\bar{T}_0 = \bar{T}(\bar{p}_0, \bar{h}_0)$ respectively. We note that (1.39) are more general versions of (1.14), (1.17). The terms in brackets in (1.39) are assumed to be $O(1)$ constants. We can relate them to common physical quantities by making use of (1.18) and the (linearised) thermodynamic identity

$$\left(\frac{\partial \bar{\rho}}{\partial \bar{h}}\right)_{\bar{p}_0, \bar{h}_0} = -\frac{\bar{\rho}_0 \alpha \bar{T}_0}{\bar{c}_p}, \tag{1.40}$$

where $\bar{\alpha}$, and $\bar{c}_p$ are defined in (1.19), whence (1.39) become

$$\bar{\varrho} = \frac{1}{\bar{c}_{\mathrm{A}}^2} \bar{P} - \frac{\bar{\rho}_0 \bar{T}_0 \bar{\alpha}}{\bar{c}_p} \bar{H}, \tag{1.41a}$$

$$\bar{\mathcal{T}} = \frac{\bar{T}_0 \bar{\alpha}}{\bar{\rho}_0 \bar{c}_p} \bar{P} - \frac{\bar{T}_0}{\bar{c}_p} \bar{H}, \tag{1.41b}$$

after having further used (1.15). We note that if instead, we let e.g. $\bar{\varrho} = \bar{\varrho}(\bar{p}, \bar{T})$ we can similarly define an *isothermal* speed of sound

$$\bar{c}_{\mathrm{Iso}}^2 = \left(\frac{\partial \bar{p}}{\partial \bar{\rho}}\right)_{\bar{T}_0}, \tag{1.42}$$

which is related to the adiabatic speed of sound via the *ratio of specific heats* $\gamma$ such that

$$\gamma = \frac{\bar{c}_p}{\bar{c}_v} = \frac{\bar{c}_{\mathrm{A}}^2}{\bar{c}_{\mathrm{Iso}}^2}, \tag{1.43}$$

where $\bar{c}_v^2 = \bar{T}\left(\frac{\partial \bar{h}}{\partial \bar{T}}\right)_{\bar{\rho}_0}$ denotes the *specific heat* at constant volume. As we will observe later, the value of $\gamma$ (and hence the difference between isothermal and adiabatic speeds of sound) is significantly higher in gases than in liquids (and solids) which has important implications in the influence of thermal effects in acoustic propagation. These

[14] Bruneau [2006] refers to this notion as the *bivariance* of the fluid.

quantities are related by the thermodynamic identity

$$\gamma - 1 = \frac{\bar{\alpha}^2 \bar{T}_0 \bar{c}_{\mathrm{A}}^2}{\bar{c}_p}. \tag{1.44}$$

Equations (1.12), (1.36) and (1.38) together with the thermodynamic relations in (1.41) constitute the governing equations for (coupled) *linear thermo-visco acoustics* and a strategy for their decomposition will be discussed shortly.

The current model also allows for a useful expression for the energy of a fluid particle in a similar manner to (1.21) for the purely acoustic case. Indeed, algebraic manipulation of (1.12), (1.36), (1.38), (1.41) yield an equation of the form (see Pierce et al. [1981] Sections 10.2.2, 10.8.2)

$$\frac{\partial \bar{\mathcal{U}}}{\partial \bar{t}} + \bar{\nabla} \cdot \bar{\mathbf{J}} = -\bar{\mathcal{D}}, \tag{1.45}$$

with

$$\bar{\mathcal{U}} = \frac{1}{2}\left(\bar{\rho}_0 |\bar{\mathbf{V}}|^2 + \frac{\bar{P}^2}{\bar{\rho}_0 \bar{c}_{\mathrm{A}}^2} + \frac{\bar{\rho}_0 \bar{T}_0}{\bar{c}_p} \bar{H}^2\right), \tag{1.46a}$$

$$\bar{\mathbf{J}} = \bar{P}\bar{\mathbf{V}} - \bar{\eta}_K \bar{\mathbf{V}}(\bar{\nabla} \cdot \bar{\mathbf{V}}) - \bar{\eta}\bar{\mathbf{V}}\bar{\boldsymbol{M}} - \frac{\bar{\mathcal{K}}}{\bar{T}_0}\bar{\mathcal{T}}\bar{\nabla}\bar{\mathcal{T}}, \tag{1.46b}$$

$$\bar{\mathcal{D}} = \bar{\eta}_K (\bar{\nabla} \cdot \bar{\mathbf{V}})^2 + \frac{\bar{\eta}}{2}\bar{\boldsymbol{M}} : \bar{\boldsymbol{M}} + \frac{\bar{\mathcal{K}}}{\bar{T}_0}(\bar{\nabla}\bar{\mathcal{T}})^2, \tag{1.46c}$$

where $\bar{\boldsymbol{M}} \equiv \bar{M}_{ij}$ is defined just under (1.37) and $\bar{\boldsymbol{M}} : \bar{\boldsymbol{M}} = \bar{M}_{ij}\bar{M}_{ij} > 0$. Direct comparison with (1.20) shows the extra terms included into the total acoustic energy density $\bar{\mathcal{U}}$ and energy flux vectors $\bar{\mathbf{J}}$ as well as an extra term $\bar{\mathcal{D}} > 0$ discussed shortly. If we integrate (1.45) over a fixed close volume $V$ with corresponding enclosing surface $S$ we obtain

$$\frac{\mathrm{d}}{\mathrm{d}\bar{t}} \iiint_V \bar{\mathcal{U}} \, \mathrm{d}V + \oiint_S \bar{\mathbf{J}} \cdot \mathbf{n} \, \mathrm{d}A = -\iiint_V \bar{\mathcal{D}} \, \mathrm{d}V, \tag{1.47}$$

after employing the divergence theorem on the divergence term to obtain the closed surface integral term, and $\mathbf{n}$ representing the outward unit normal from $S$. From (1.47) it becomes clear that for a thermo-viscous fluid, the rate of total energy of a fluid particle has an additional contribution 'leaving' the fixed volume (since $\bar{\mathcal{D}} > 0$), and therefore we this term represents the rate of energy dissipation due to visco-thermal effects. Naturally, if we neglect all visco-thermal effects in (1.46) (i.e. let $\bar{\eta}, \bar{\eta}_K, \bar{\mathcal{K}} \to 0$) (1.45) becomes identical to (1.20) and consequently (1.47) becomes (1.21) so that $\bar{\mathcal{D}} \to 0$.

### Non-dimensionalisation

Before continuing with the decomposition of the governing equations obtained above, it will be useful to non-dimensionalise the system of equations. Introducing a (problem specific) length-scale $\bar{\mathcal{L}}$ we can scale the physical independent variables to non-dimensional variables via

$$\mathbf{x} = \frac{\bar{\mathbf{x}}}{\bar{\mathcal{L}}}, \qquad t = \frac{\bar{c}_\mathrm{A}}{\bar{\mathcal{L}}}\bar{t}, \tag{1.48}$$

noting that we have dropped the overbar for non-dimensional terms. The first of (1.48) further implies that $\nabla = \bar{\mathcal{L}}\bar{\nabla}$. Similarly the non-dimensional visco-thermal (constant) parameters become

$$(\eta, \eta', \eta_K) = \frac{(\bar{\eta}, \bar{\eta}', \bar{\eta}_K)}{\bar{\rho}_0 \bar{c}_\mathrm{A} \bar{\mathcal{L}}}, \tag{1.49a}$$

$$\mathcal{K} = \frac{\bar{T}_0}{\bar{\rho}_0 \bar{c}_\mathrm{A}^3 \bar{\mathcal{L}}}\bar{\mathcal{K}}, \tag{1.49b}$$

$$(c_p, c_v) = \frac{\bar{T}_0}{\bar{c}_\mathrm{A}^2}(\bar{c}_p, \bar{c}_v), \tag{1.49c}$$

$$\alpha = \bar{\alpha}\bar{T}_0, \tag{1.49d}$$

$$\mathcal{C} = \frac{\mathcal{K}}{c_p}. \tag{1.49e}$$

Furthermore, the relevant non-dimensional fields (1.11) become

$$\mathbf{v} = \frac{\bar{\mathbf{v}}}{\bar{c}_\mathrm{A}} = \frac{\epsilon\bar{\mathbf{V}}}{\bar{c}_\mathrm{A}}, \tag{1.50a}$$

$$p = \frac{\bar{p} - \bar{p}_0}{\bar{\rho}_0 \bar{c}_\mathrm{A}^2} = \frac{\epsilon\bar{P}}{\bar{\rho}_0 \bar{c}_\mathrm{A}^2}, \tag{1.50b}$$

$$\theta = \frac{\bar{T} - \bar{T}_0}{\bar{T}_0} = \frac{\epsilon\bar{\mathcal{T}}}{\bar{T}_0}, \tag{1.50c}$$

$$s = \frac{\bar{\rho} - \bar{\rho}_0}{\bar{\rho}_0} = \frac{\epsilon\bar{\varrho}}{\bar{\rho}_0}, \tag{1.50d}$$

$$h = \frac{\bar{T}_0}{\bar{c}_\mathrm{A}^2}(\bar{h} - \bar{h}_0) = \frac{\bar{T}_0}{\bar{c}_\mathrm{A}^2}\epsilon\bar{H}. \tag{1.50e}$$

It follows directly from (1.48)-(1.50) and (1.35b) that this choice further implies that the non-dimensional Cauchy stress becomes

$$\boldsymbol{\sigma} = (\bar{\boldsymbol{\sigma}} + \bar{p}_0\boldsymbol{I})/\bar{\rho}_0\bar{c}_\mathrm{A}^2 = (-p + \eta'\nabla\cdot\mathbf{v})\,\mathbf{I} + \eta\left(\nabla\mathbf{v} + \nabla\mathbf{v}^T\right). \tag{1.51}$$

Using (1.48)-(1.50) we can summarize our governing equations (1.12), (1.36), (1.38) and (1.41) in non-dimensional form as

$$\frac{\partial s}{\partial t} = -\nabla \cdot \mathbf{v}, \tag{1.52}$$

$$\frac{\partial \mathbf{v}}{\partial t} = -\nabla p + \eta \nabla^2 \mathbf{v} + (\eta + \eta')\nabla \left(\nabla \cdot \mathbf{v}\right), \tag{1.53}$$

$$-\frac{\alpha}{c_p}\frac{\partial p}{\partial t} = \left(\mathcal{C}\nabla^2 - \frac{\partial}{\partial t}\right)\theta, \tag{1.54}$$

$$s = p - \frac{\alpha}{c_p}h, \quad \theta = \frac{1}{c_p}\left(\alpha p + h\right), \tag{1.55}$$

where we have used (1.41b) to write the entropy fluctuations in terms of pressure and temperature in (1.38) in order to arrive at (1.54). From (1.52)-(1.55) we directly observe that (in three dimensional space) our model consists of seven equations for seven unknowns $\{s, \mathbf{v}, p, \theta, h\}$. The process of non-dimensionalisation allows one to solve a particular problem on a convenient domain with fewer parameters, and use this solution for corresponding physical problems via the scales in (1.48)-(1.50). Hence, unless otherwise stated, from here onwards we will only consider non-dimensional quantities.

### Decomposition into thermo-compressional and vorticity fields

Following Beltman [1999], we will now focus on the decomposition of (1.52)-(1.55) in order to arrive at uncoupled equations which are more convenient for the consideration of physical problems. As we show next, in the frequency domain this will lead to three individual Helmholtz equations for the thermo-compressional fields $\Theta_1, \Theta_2$ and vorticity $\mathbf{\Omega}$ which couple through the boundary conditions.

Applying the curl of (1.53), with $\mathbf{\Omega} = \nabla \times \mathbf{v}$ where ($\mathbf{\Omega} = \bar{\mathcal{L}}\bar{\mathbf{\Omega}}/\bar{c}_{\mathrm{A}}$) corresponding to the fluid *vorticity*, directly gives the *diffusion equation*

$$\frac{\partial \mathbf{\Omega}}{\partial t} = \eta \nabla^2 \mathbf{\Omega}. \tag{1.56}$$

Further, using (1.55) in order to rewrite $p$ in terms of $s$ and $\theta$, substituting in (1.53) and (1.54) gives, recalling (1.44)

$$\frac{\partial \mathbf{v}}{\partial t} = -\frac{1}{\gamma}\left\{\nabla s + \alpha \nabla \theta\right\} + \eta \nabla^2 \mathbf{v} + (\eta + \eta')\nabla \left(\nabla \cdot \mathbf{v}\right), \tag{1.57a}$$

$$\frac{\alpha}{c_p}\frac{\partial s}{\partial t} = \left(\frac{\partial}{\partial t} - \gamma \mathcal{C}\nabla^2\right)\theta. \tag{1.57b}$$

In order to eliminate $\mathbf{v}$ from the equations, we take the divergence of (1.57a) and use continuity of mass (1.52) to yield

$$\frac{\partial^2 s}{\partial t^2} = \frac{1}{\gamma}\left\{\alpha\nabla^2\theta + \left(1 + \zeta\gamma\frac{\partial}{\partial t}\right)\nabla^2 s\right\}, \tag{1.58}$$

where we have introduced the viscous quantity $\zeta = 2\eta + \eta'$ and made use of the vector identity

$$\nabla^2\mathbf{f} = \nabla\left(\nabla\cdot\mathbf{f}\right) - \nabla\times\nabla\times\mathbf{f}, \tag{1.59}$$

valid for any sufficiently smooth vector field $\mathbf{f}$. We now note that (1.57b), (1.58) form a system of coupled partial differential equations for $\{s, \theta\}$ from which, as we shall show next, together with (1.56) all the remaining quantities can be obtained. As we did to obtain the Helmholtz equation (1.22) in the acoustic case, at this stage we assume time harmonicity of the dynamic fields in the form $\mathrm{e}^{-\mathrm{i}\omega t}$, where $\omega = \bar{\mathcal{L}}\bar{\omega}/\bar{c}_{\mathrm{A}}$ is the non-dimensional frequency of the oscillation so we write

$$\{s, \mathbf{v}, p, \theta, h, \boldsymbol{\sigma}\} = \mathrm{Re}\{\{\hat{s}, \hat{\mathbf{v}}, \hat{p}, \hat{\theta}, \hat{h}, \hat{\boldsymbol{\sigma}}\}(\mathbf{x}, \omega)\mathrm{e}^{-\mathrm{i}\omega t}\}, \tag{1.60}$$

which results in $\partial/\partial t \equiv -\mathrm{i}\omega$ and the time factor $\mathrm{e}^{-\mathrm{i}\omega t}$ will be suppressed from here onwards, noting that we can still recover the evolution of these signals in time via Fourier Transforms. In particular, we can now combine (1.57b), (1.58) into a single fourth order equation for $\hat{\theta}$ which can be rearranged into

$$\left((1 - \mathrm{i}\omega\zeta\gamma)\mathcal{C}\nabla^4 + \mathrm{i}\omega\left[1 - \mathrm{i}\omega(\zeta + \gamma\mathcal{C})\right]\nabla^2 + \mathrm{i}\omega^3\right)\hat{\theta} = 0, \tag{1.61}$$

or, equivalently

$$\left(\nabla^2 + \kappa_1^2\right)\left(\nabla^2 + \kappa_2^2\right)\hat{\theta} = 0, \tag{1.62}$$

where

$$\kappa_1^2 = \mathrm{i}\omega\frac{\left[1 - \mathrm{i}\omega(\zeta + \gamma\mathcal{C})\right] + \mathcal{S}(\omega)}{2(1 - \mathrm{i}\omega\zeta\gamma)\mathcal{C}}, \quad \text{and} \quad \kappa_2^2 = \mathrm{i}\omega\frac{\left[1 - \mathrm{i}\omega(\zeta + \gamma\mathcal{C})\right] - \mathcal{S}(\omega)}{2(1 - \mathrm{i}\omega\zeta\gamma)\mathcal{C}}, \tag{1.63}$$

with

$$\mathcal{S}(\omega) = \sqrt{\left[1 - \mathrm{i}\omega(\zeta - \gamma\mathcal{C})\right]^2 - 4\mathrm{i}\omega\mathcal{C}(\gamma - 1)}. \tag{1.64}$$

Bruneau [2006] (Section 2.5) shows how in the time-domain an equation of the form of (1.62) can be obtained via an integro-differential operator. Next, we adopt the

split into thermo-compressional fields $\hat{\theta}(\mathbf{x},\omega) = \hat{\Theta}_1(\mathbf{x},\omega) + \hat{\Theta}_2(\mathbf{x},\omega)$ such that each component satisfies

$$\left(\nabla^2 + \kappa_1^2\right)\hat{\Theta}_1(\mathbf{x},\omega) = 0, \qquad \left(\nabla^2 + \kappa_2^2\right)\hat{\Theta}_2(\mathbf{x},\omega) = 0. \tag{1.65}$$

Despite (1.65) clearly being a sufficient condition to satisfy (1.62), we must ensure that we are not overlooking the presence of other solutions with different functional form. It turns out that all solutions have this linear structure provided $\kappa_1^2 \neq \kappa_2^2$ [Wu, 1956, Courant, 2011, Pierce et al., 1981]. In the frequency domain, the fluid vorticity equation (1.56) becomes

$$\left(\nabla^2 + k_\Omega^2\right)\hat{\mathbf{\Omega}} = 0, \qquad \text{where} \quad k_\Omega^2 = \frac{\mathrm{i}\omega}{\eta}. \tag{1.66}$$

Importantly, equations (1.65), (1.66) are the uncoupled governing equations to be solved for linear TVA propagation (in the absence of any external sources). We note that although these are all Helmholtz equations as in (1.22), their respective wavenumbers $(\kappa_1, \kappa_2, k_\Omega)$ are very different[15] in nature which implies the respective plane wave type solutions (1.25) will vary significantly for each mode of propagation.

In practice, we are interested in solving problems in domains consisting of different types of geometries and interfaces where boundary conditions apply. As illustrated for the inviscid case, these BCs are often written in terms of the velocity field (and pressure). The extra BCs for TVA are discussed shortly, but in order to apply them we must first relate the physical fields to $\{\hat{\Theta}_1, \hat{\Theta}_2, \hat{\mathbf{\Omega}}\}$.

Applying (1.59) to $\mathbf{v}$, using (1.52) and substituting onto (1.57a) gives

$$\frac{\partial \mathbf{v}}{\partial t} = -\frac{1}{\gamma}\left\{\alpha\nabla\theta + \left(1 + \zeta\gamma\frac{\partial}{\partial t}\right)\nabla s\right\} - \eta\nabla\times\hat{\mathbf{\Omega}}, \tag{1.67}$$

which, in the frequency domain, using (1.57b) to eliminate $s$, (1.63) and their respective PDEs (1.65) to introduce $\hat{\Theta}_1, \hat{\Theta}_2$ finally yields

$$\mathrm{i}\omega\hat{\mathbf{v}} = \frac{c_p}{2\alpha}\left\{[1 - \mathrm{i}\omega(\zeta - \gamma\mathcal{C}) - \mathcal{S}]\nabla\hat{\Theta}_1 + [1 - \mathrm{i}\omega(\zeta - \gamma\mathcal{C}) + \mathcal{S}]\nabla\hat{\Theta}_2\right\} + \eta\nabla\times\hat{\mathbf{\Omega}}. \tag{1.68}$$

Repeating this same last step on (1.57b) and the equation of state for pressure[16]

[15] It is difficult to physically appreciate the distinction between $\kappa_1, \kappa_2$ via (1.63) but it will become clear in (1.73) after some approximations.

[16] This equation is directly obtained by eliminating entropy in (1.55)

$\gamma p = s + \alpha\theta$ respectively, gives

$$\hat{s} = \frac{c_p}{\alpha}\left\{\left(1 + \mathrm{i}\frac{\gamma\mathcal{C}\kappa_1^2}{\omega}\right)\hat{\Theta}_1 + \left(1 + \mathrm{i}\frac{\gamma\mathcal{C}\kappa_2^2}{\omega}\right)\hat{\Theta}_2\right\}, \tag{1.69a}$$

$$\hat{p} = \frac{c_p}{\alpha}\left\{\left(1 + \mathrm{i}\frac{\mathcal{C}\kappa_1^2}{\omega}\right)\hat{\Theta}_1 + \left(1 + \mathrm{i}\frac{\mathcal{C}\kappa_2^2}{\omega}\right)\hat{\Theta}_2\right\}, \tag{1.69b}$$

and similarly for entropy (not shown). Equations (1.68), (1.69) confirm the above claim that once $\{\hat{\Theta}_1, \hat{\Theta}_2, \hat{\boldsymbol{\Omega}}\}$ are known all the relevant physical fields can be obtained, and all the coupling occurs in the boundaries. Prior to analysing the extra BCs to consider, at this stage it is useful to have a physical idea of the magnitude of some of the parameters in question.

### Approximations for air and water

Although as we have mentioned above, the model is valid for a general Newtonian fluid, we show that for a large class of fluids and frequencies of interest we can further simplify the model. Due to their fundamental importance as well as intrinsic differences, we focus on air and water.

Using Table 1 from Section 2.2 we find that, for air at 27° Celsius

$$\omega\mathcal{C} = \frac{\bar{\omega}\bar{\mathcal{K}}}{\bar{\rho}_0\bar{c}_0^2\bar{c}_p} \approx (1.865 \times 10^{-10}\mathrm{s})\bar{\omega}, \quad \omega\zeta = \frac{\bar{\omega}\bar{\zeta}}{\bar{\rho}_0\bar{c}_0^2} \approx (7.914 \times 10^{-11}\mathrm{s})\bar{\omega}, \quad \gamma \approx 1.390, \tag{1.70}$$

whereas for water at 10° Celsius

$$\omega\mathcal{C} \approx (6.415 \times 10^{-14}\mathrm{s})\bar{\omega}, \quad \omega\zeta \approx (1.354 \times 10^{-12}\mathrm{s})\bar{\omega}, \quad \gamma \approx 1.001, \tag{1.71}$$

recalling that $\bar{\omega}$ denotes the dimensional frequency of oscillation in rad/s. For example, at a frequency of 1 MHz we still have $\omega\mathcal{C} = O(10^{-3})$, $\omega\zeta = O(10^{-4})$ for air, whereas for water $\omega\mathcal{C} = O(10^{-7})$, $\omega\zeta = O(10^{-6})$. Hence, for these fluids (and indeed most other common fluids) and frequencies of interest, we have that $\gamma = O(1)$, $\omega\mathcal{C} \ll 1$, and $\omega\zeta \ll 1$ which can give accurate useful approximations to the full theory as we show next. Indeed, we commence by noting that $\mathcal{S}(\omega)$ defined in (1.64) can be approximated by

$$\mathcal{S} = 1 - \mathrm{i}\omega[\zeta + \mathcal{C}(\gamma - 2)] + O((\omega\zeta)^2, (\omega\mathcal{C})^2), \tag{1.72}$$

and direct substitution into (1.63) gives

$$\kappa_1^2 = \frac{\mathrm{i}\omega}{\mathcal{C}}\left\{1 + \mathrm{i}\omega(\gamma-1)[\zeta - \mathcal{C}] + O((\omega\zeta)^2, (\omega\mathcal{C})^2)\right\}, \tag{1.73a}$$

$$\kappa_2^2 = \omega^2\left\{1 + \mathrm{i}\omega[\zeta + \mathcal{C}(\gamma-1)] + O((\omega\zeta)^2, (\omega\mathcal{C})^2), \right\}, \tag{1.73b}$$

where, since the magnitudes of $\zeta, \mathcal{C}$ vary depending on the fluid by $O((\omega\zeta)^2, (\omega\mathcal{C})^2)$ we simply refer to the larger contribution of the two terms in each case. Given the plane-wave solutions of the Helmholtz equation (1.25), observation of the leading order terms in (1.73a), (1.73b) directly dictates the *propagative* nature of $\hat{\Theta}_2$ (which resembles the purely acoustic compressional field), as opposed to the *diffusive* highly attenuated behaviour of $\hat{\Theta}_1$, which is similar to that of $\hat{\mathbf{\Omega}}$ in (1.66). This fundamental fact of TVA propagation is depicted in Figure 1.3. For this reason some authors [Bruneau, 2006] denote $\hat{\Theta}_1$ as the "entropic" contribution to temperature and $\hat{\Theta}_2$ as the "acoustic" temperature. Using (1.73) in (1.68)-(1.69) we can obtain similar approximations for the pressure, velocity and condensation. For the pressure, we have

$$\hat{p} \approx \frac{c_p}{\alpha}\left[-\mathrm{i}\omega(\gamma-1)[\zeta-\mathcal{C}]\hat{\Theta}_1 + (1-\mathrm{i}\omega\mathcal{C})\hat{\Theta}_2\right] = \hat{p}_1 + \hat{p}_2, \tag{1.74}$$

with

$$\hat{p}_1 = -\mathrm{i}\omega\frac{c_p}{\alpha}(\gamma-1)[\zeta-\mathcal{C}]\hat{\Theta}_1, \tag{1.75a}$$

$$\hat{p}_2 = \frac{c_p}{\alpha}(1-\mathrm{i}\omega\mathcal{C})\hat{\Theta}_2, \tag{1.75b}$$

are the entropic and acoustic pressure fields respectively, and we can observe from (1.75a), (1.75b), that we have $|\hat{p}_2| \gg |\hat{p}_1|$, since $\omega\mathcal{C}, \omega\zeta \ll 1$. For the velocity component $\hat{\mathbf{v}}$ we obtain

$$\mathrm{i}\omega\hat{\mathbf{v}} \approx \frac{c_p}{\alpha}\left\{\mathrm{i}\omega(\gamma-1)\mathcal{C}\nabla\hat{\Theta}_1 + [1-\mathrm{i}\omega(\zeta-\mathcal{C})]\nabla\hat{\Theta}_2\right\} + \eta\nabla\times\hat{\mathbf{\Omega}}, \tag{1.76}$$

which may be decomposed as

$$\hat{\mathbf{v}} = \hat{\mathbf{v}}_1 + \hat{\mathbf{v}}_2 + \hat{\mathbf{v}}_\Omega, \tag{1.77}$$

where

$$\hat{\mathbf{v}}_1 = \frac{c_p}{\alpha}(\gamma-1)\mathcal{C}\nabla\hat{\Theta}_1, \tag{1.78a}$$

$$\mathrm{i}\omega\hat{\mathbf{v}}_2 = \frac{c_p}{\alpha}[1-\mathrm{i}\omega(\zeta-\mathcal{C})]\nabla\hat{\Theta}_2, \tag{1.78b}$$

$$\mathrm{i}\omega\hat{\mathbf{v}}_\Omega = \eta\nabla\times\hat{\mathbf{\Omega}}, \tag{1.78c}$$

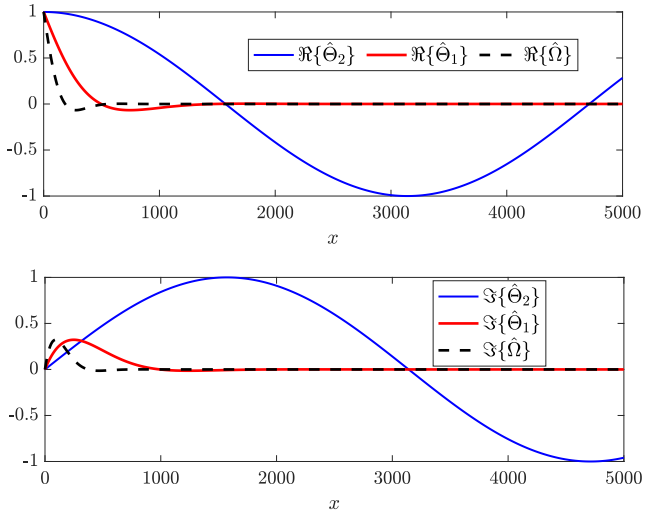


Figure 1.3: Comparisons between (unit amplitude) 1D free-space plane wave solutions ($\mathrm{e}^{\mathrm{i}kx}$) to the Helmholtz equations with wavenumber $k$ according to the different modes of propagation $\{\hat{\Theta}_1, \hat{\Theta}_2, \hat{\boldsymbol{\Omega}}\}$ given by (1.73) and (1.66) respectively, plotted with respect to their direction of propagation. The top and bottom plots show the real and imaginary parts respectively. Hypothetical non-dimensional parameters are given by: $\omega = 10^{-3}, \mathcal{C} = 50, \eta = 7$. The propagative nature of $\hat{\Theta}_2$ is noted, as opposed to $\hat{\Theta}_1, \hat{\Omega}$ which decay much quicker with distance.

are sometimes denoted as the "laminar entropic", "laminar acoustic" and "vortical" velocities respectively [Bruneau, 2006]. We further observe that (1.78a), (1.78b) are similar in functional form to (1.23), which implies that for general plane waves of the type $\hat{\Theta}_m = \mathrm{e}^{\mathrm{i}\boldsymbol{\kappa_m}\cdot\mathbf{x}}$ $(m = 1, 2)$, the associated velocity field (and hence motion) will have the same direction of propagation as $\boldsymbol{\kappa_m}$ (see discussion below (1.25)). For this reason we have denoted $\hat{\Theta}_m$ as compressional, with the prefix '*thermo*' to further indicate that in TVA there is an associated thermal coupling. On the other hand for a plane wave solution of the particular type $\hat{\boldsymbol{\Omega}} = \mathrm{e}^{\mathrm{i}\boldsymbol{\kappa}_\Omega\cdot\mathbf{x}}\mathbf{e_z}$ (with $\mathbf{e_z}$ representing a unit vector along the $z$ direction), all the associated motion from (1.78c) will in fact be confined to the $(x, y)$ plane and hence orthogonal to $\mathbf{e_z}$ (by definition of the curl operator) suggesting that vorticity modes are *transverse* or shear ('S') waves. This distinction will be further considered in more detail when we discuss wave propagation in elastic solids, where we fill further make a distinction between two different types of shear waves, namely 'SV' and 'SH'.

### Boundary Conditions

We have seen above the equations governing a linear, dissipative, thermo-viscous fluid in free space in the absence of sources and body forces (1.65), (1.66). Conveniently, these equations have no coupling between the fields, and their individual solutions are in principle well known in (orthogonal) coordinate systems. Nevertheless, all the coupling between the different quantities lies in the boundary conditions which are briefly discussed next, and applied in subsequent sections.

#### - Interface conditions between neighbouring TVA media

Contrary to the ideal acoustic media from Section 1.2.1, in the case of thermo-visco-acoustic fluids we cannot neglect the specification of the fluid temperature at the interface with a neighbouring TVA medium, since there exists a heat flux as a result of their interaction. For this discussion we refer to a situation similar to Figure 1.2, although here we replace the subscripts '$1, 2$' with '$A, B$' to avoid confusion with the notation introduced in (1.74), (1.76), so two TVA media occupy $D_A$, $D_B$ and their respective associated quantities are labelled with subscripts '$A$' and '$B$'. At the interface these media must satisfy *continuity of temperature*, as well as *continuity of temperature flux* which yields

$$\hat{\theta}_A = \hat{\theta}_B, \qquad \text{on} \quad \partial D, \tag{1.79}$$

$$\mathcal{K}_A \nabla\hat{\theta}_A \cdot \mathbf{n} = \mathcal{K}_B \nabla\hat{\theta}_B \cdot \mathbf{n} \qquad \text{on} \quad \partial D, \tag{1.80}$$

where (1.80) represents continuity of heat flux since we are assuming that the heat flux vector follows Fourier's law (see (1.8) and discussion just below). We also note that in writing (1.79) the background temperature ($\bar{T}_0$ in (1.50c)) in $D_A$ and $D_B$ is equal.

As opposed to Euler's equations (1.4), the Navier-Stokes equations (1.36) contain second order spatial derivatives. One of the direct consequences is that the requirement of continuity of normal velocity (1.28) is not sufficient to guarantee unique solutions. From a physical perspective, the presence of viscosity puts an extra restriction on the tangential component of the velocity field at the interface with another medium, [Shapiro, 1961]. We therefore replace (1.28) by the more restrictive condition

$$\hat{\mathbf{v}}_A = \hat{\mathbf{v}}_B \qquad \text{on} \quad \partial D. \tag{1.81}$$

Finally, in accordance with Newton's *third law* we must ensure that the *traction* $\hat{t}_i = \hat{\sigma}_{ij} n_j$ i.e. force per unit area on a surface with normal $\mathbf{n}$ is also continuous, which we write in component form as

$$\hat{\sigma}^A_{ij} n_j = \hat{\sigma}^B_{ij} n_j \qquad \text{on} \quad \partial D, \tag{1.82}$$

noting that we have used a superscript '$A$' ('$B$') to refer to the Cauchy stress in medium $D_A$ ($D_B$) in order to avoid confusion with the indices. We note that the continuity of pressure BC (1.27) is equivalent to (1.82) when substituting the ideal fluid constitutive relation (1.3).

**- Thermal Neumann, Dirichlet and Robin Conditions**

We now assume that $D_B$ is occupied by a solid medium. In this case, the fluid will still 'stick' to the surface, so that the no-slip condition (1.81) is still applicable. In the special case in which the solid is *stationary* (i.e. $\hat{\mathbf{v}}_B = \mathbf{0}$) we obtain after using (1.77)

$$\hat{\mathbf{v}}^A_2 = -\hat{\mathbf{v}}^A_1 - \hat{\mathbf{v}}^A_\Omega \qquad \text{on} \quad \partial D, \tag{1.83}$$

which comprises the fluid-solid interface (where again we have used superscripts to avoid confusion).

Even if *thermoelastic coupling* is ignored (so that in this approximation the solid body conducts heat but does not deform when doing so, see Section 1.4), we must ensure that we account for the heat transfer between the fluid and the solid. From a general perspective, in this case we must ensure that (1.79), (1.80) are satisfied, as well as the diffusion equation governing the heat conduction in the solid. On this basis, if we assume the heat flow parallel to the interface is negligible (due to the relatively small temperature gradient in this direction) one can incorporate this thermal flux into the solid via a Robin type boundary condition as in (1.34) but for temperature [Bruneau, 2006][17]. For a geometry such as that of Figure 1.2, assuming e.g. $\mathbf{n} = \mathbf{e}_\perp$ so that the direction orthogonal to the interface $\partial D$ is given by the $x_\perp$ coordinate, we can write

$$\left(1 + L_T \frac{\partial}{\partial x_\perp}\right) \hat{\theta} = 0, \qquad \text{on} \quad \partial D, \tag{1.84}$$

[17] The derivation is performed in the frequency domain.

where $L_T = O(\mathcal{C}/\sqrt{\omega \mathcal{C}_B})$, and $\mathcal{C}_B$ denotes the (non-dimensional) thermal conductivity of the wall. It so happens that for rigid substrates the thermal conductivity is generally much larger than that of the fluid, such that $\sqrt{\mathcal{C}_B} \gg \mathcal{C}$, and hence for most frequencies of interest $|L_T| \ll 1$ so that (1.84) can be approximated by the Dirichlet BC

$$\hat{\Theta}_2 = -\hat{\Theta}_1 \qquad \text{on} \quad \partial D, \tag{1.85}$$

after using $\hat{\theta} = \hat{\Theta}_1 + \hat{\Theta}_2$. Despite being less physically relevant in standard fluid-solid conditions of interest, in a situation in which $|L_T| \gg 1$, (1.84) becomes approximately

$$\frac{\partial \hat{\theta}}{\partial x_\perp} = 0, \qquad \text{on} \quad \partial D, \tag{1.86}$$

i.e. a Neumann type BC. The *isothermal* condition (1.85) is commonly used in the thermo-visco-acoustic literature, which as aforementioned has mostly been focused on the study of gases. In Section 1.3 we will quantify the impact upon reflection between the Dirichlet and Neumann BCs for a forced semi-infinite TVA medium in contact with a rigid half-space. We also make comparisons between these two opposing BCs in Section 2.2 for TVA propagation in narrow slits, where experimental data from Ward et al. [2015] is further included (FIG 2). As we shall see, the isothermal BC (1.85) is in fact a better approximation for most channel widths.

From (1.85) we can conclude that thermal modes $\hat{\Theta}_1$ should not be ignored near boundaries (since the magnitude is in fact equal to that of the compressional mode $\hat{\Theta}_2$ on the interface), as opposed to within the bulk of the fluid, where normally $\hat{\Theta}_1$, $\hat{\mathbf{\Omega}}$ can be neglected when compared to $\hat{\Theta}_2$ to a very good approximation. Intuitively, this can be seen from Figure 1.3 for plane waves where the hypothetical boundary is located at $x = 0$ (where $\hat{\Theta}_1 = \hat{\Theta}_2 = \hat{\Omega} = 1$ is imposed). For this reason, a question of high interest is, how far from the boundary must we move so that ignoring shear and thermal mode effects is a valid approximation for the correct description of the acoustic field? These characteristic lengths are denoted by *boundary layers*, which are frequently addressed in this thesis due to their physical inherence. Furthermore, as we will see in Section 1.3 for the particular case of a rigid half-space, in some instances we can take advantage of this localization of thermo-viscous effects near solid boundaries in order to obtain highly accurate approximate solutions of much simpler form.

## 1.3 TVA scattering

We very briefly introduced the set-up of a scattering problem in the case of an acoustic medium satisfying the Helmholtz equation (1.22) via (1.26), and how in these scenarios it must be ensured that respective solutions do not grow as we move away from the scatterer. Having discussed a framework to study sound propagation in thermo-viscous fluids in Section 1.2.2, here we want to consider a canonical scattering problem to put the theory into practice. Before this, it is convenient to reconsider the energy flux from (1.45).

### 1.3.1 Energy flux partition into different modes

As we will illustrate shortly for the half-space problem, it is advantageous for many problems to know the contributions of each existing mode to the overall energy balance in order to quantify visco-thermal effects. In non-dimensional form, the energy balance equation (1.45) with (1.46) becomes

$$\frac{\partial \mathcal{U}}{\partial t} + \nabla \cdot \mathbf{J} = -\mathcal{D}, \tag{1.87}$$

with $\bar{\mathcal{U}} = \bar{\rho}_0 \bar{c}_\mathrm{A}^2 \mathcal{U}$, $\bar{\mathbf{J}} = \bar{\rho}_0 \bar{c}_\mathrm{A}^3 \mathbf{J}$, $\bar{\mathcal{D}} = (\bar{\rho}_0 \bar{c}_\mathrm{A}^3 / \bar{\mathcal{L}}) \mathcal{D}$ so that

$$\mathcal{U} = \frac{1}{2}\left(|\mathbf{v}|^2 + p^2 + h^2\right), \tag{1.88a}$$

$$\mathbf{J} = p\mathbf{v} - \eta_K \mathbf{v}(\nabla \cdot \mathbf{v}) - \eta \mathbf{v}\boldsymbol{M} - \mathcal{K}\theta\nabla\theta = -(\boldsymbol{\sigma}\mathbf{v} + \mathcal{K}\theta\nabla\theta), \tag{1.88b}$$

$$\mathcal{D} = \eta_K (\nabla \cdot \mathbf{v})^2 + \frac{\eta}{2}\boldsymbol{M} : \boldsymbol{M} + \mathcal{K}(\nabla\theta)^2. \tag{1.88c}$$

In component form we can write the energy flux vector $\mathbf{J}$ as

$$J_i = -\left(\sigma_{ij} v_j + \mathcal{K}\theta \frac{\partial \theta}{\partial x_i}\right), \tag{1.88b revisited}$$

with $\sigma_{ij}$ given in (1.51). Since in our decomposition we have assumed the steady-state condition (1.60), it is helpful to consider the time-average over a period of the energy flux vector (1.88b) which becomes

$$\langle \mathbf{J} \rangle = -\frac{1}{2} \mathrm{Re}\{\boldsymbol{\sigma}\mathbf{v}^* + \mathcal{K}\theta\nabla\theta^*\}, \tag{1.89}$$

since the time-average over a period ($T = 2\pi/\omega$) of the energy flux vector is given by

$$\langle \mathbf{J} \rangle = \frac{1}{T}\int_t^{t+T} \mathbf{J}\, \mathrm{d}s, \tag{1.90}$$

and we have used the result that for two general time harmonic signals $F = F_0 \mathrm{e}^{-\mathrm{i}(\omega t+\gamma_1)}$ $f = f_0 \mathrm{e}^{-\mathrm{i}(\omega t+\gamma_2)}$, ($\gamma_1$, $\gamma_2$ represent arbitrary phase shifts) we have

$$\langle \mathrm{Re}\{F\} \times \mathrm{Re}\{f\} \rangle = \frac{1}{2} \mathrm{Re}\{F f^*\}, \tag{1.91}$$

where asterisk $^*$ denotes complex conjugate [Achenbach, 2012]. As we have discussed above, both the fluid velocity and Cauchy stress are linear combinations of $\{\hat{\Theta}_1, \hat{\Theta}_2, \hat{\boldsymbol{\Omega}}\}$ and we can therefore decompose $\langle \mathbf{J} \rangle$ accordingly.

For example, consider a 1D disturbance in the $x$-direction consisting of the two thermo-compressional fields such that

$$\Theta_1 = \mathrm{Re}\{\hat{\Theta}_1 \mathrm{e}^{-\mathrm{i}\omega t}\} = \mathrm{Re}\{\mathrm{e}^{\mathrm{i}\kappa_1 x - \mathrm{i}\omega t}\}, \tag{1.92a}$$

$$\Theta_2 = \mathrm{Re}\{\hat{\Theta}_2 \mathrm{e}^{-\mathrm{i}\omega t}\} = \mathrm{Re}\{\mathrm{e}^{\mathrm{i}\kappa_2 x - \mathrm{i}\omega t}\}. \tag{1.92b}$$

It is clear that (1.92) satisfy the governing equations (1.65). Then, using (1.68) the resultant velocity component due to $\hat{\Theta}_2$ (which we denote $\hat{v}_x^{\Theta_2}$) is given by

$$\mathrm{i}\omega \hat{v}_x^{\Theta_2} = \frac{c_p}{2\alpha}[1 - \mathrm{i}\omega(\zeta - \gamma\mathcal{C}) + \mathcal{S}]\mathrm{i}\kappa_2 \hat{\Theta}_2, \tag{1.93}$$

and the (only non-zero contribution) to the non-dimensional stress (1.51) due to $\hat{\Theta}_2$, namely $\hat{\sigma}_{xx}^{\Theta_2}$ is given by

$$\hat{\sigma}_{xx}^{\Theta_2} = \frac{c_p}{\alpha}\left[\left(1 + \frac{\mathrm{i}\mathcal{C}\kappa_2^2}{\omega}\right) - \frac{\mathrm{i}(3\eta + \eta')\kappa_2}{\omega}(1 - \mathrm{i}\omega(\zeta - \gamma\mathcal{C}) + \mathcal{S})\right]\hat{\Theta}_2, \tag{1.94}$$

where we used (1.69b) in order to write the pressure fields in terms of $\hat{\Theta}_2$ as well as (1.65) to simplify slightly. Finally, by definition the temperature and its gradient due to $\hat{\Theta}_2$ alone gives

$$\hat{\theta}^{\Theta_2} = \hat{\Theta}_2, \quad \nabla\hat{\theta}^{\Theta_2} = \frac{\partial \hat{\Theta}_2}{\partial x} = \mathrm{i}\kappa_2 \hat{\Theta}_2. \tag{1.95}$$

Hence, the contribution to the energy flux (averaged over a period) due to $\hat{\Theta}_2$ exclusively $\langle \mathbf{J}_{\Theta_2} \rangle$ is given by (from (1.89))

$$\begin{aligned}\langle \mathbf{J}_{\Theta_2} \rangle &= -\frac{1}{2}\mathrm{Re}\{\hat{\sigma}_{xx}^{\Theta_2}\mathrm{e}^{-\mathrm{i}\omega t}\left(\hat{v}_x^{\Theta_2}\mathrm{e}^{-\mathrm{i}\omega t}\right)^* + \mathcal{K}\hat{\theta}^{\Theta_2}\mathrm{e}^{-\mathrm{i}\omega t}\left(\nabla\hat{\theta}^{\Theta_2}\mathrm{e}^{-\mathrm{i}\omega t}\right)^*\} \\ &= \frac{1}{2}\mathrm{Re}\{\hat{\sigma}_{xx}^{\Theta_2}(\hat{v}_x^{\Theta_2})^* + \mathcal{K}\hat{\theta}^{\Theta_2}\left(\nabla\hat{\theta}^{\Theta_2}\right)^*\},\end{aligned} \tag{1.96}$$

with[18] (1.93), (1.94), (1.95) which we note is a scalar field only since we are in 1D (for simplicity). As expected, the time dependence is no longer present in (1.96). We

[18] Note that we used the *distributivity* over multiplication of complex number conjugation to arrive at (1.96).

can perform the same calculation with the remaining field in (1.92) to obtain $\langle \mathbf{J}_{\Theta_1} \rangle$. Furthermore, there is also a non-zero contribution to the power due to *interaction* between different modes, that is e.g. the stress field of $\Theta_1$ interacting with the velocity field of $\Theta_2$ which we will denote as

$$\langle \mathbf{J}_{\Theta_1\Theta_2} \rangle = -\frac{1}{2} \mathrm{Re}\{\hat{\sigma}_{xx}^{\Theta_2} (\hat{v}_x^{\Theta_1})^* + \mathcal{K}\hat{\theta}^{\Theta_2} \left(\nabla \hat{\theta}^{\Theta_1}\right)^*\} \tag{1.97}$$

where we note that the order of the subscript is important since it indicates whether the particular mode is being applied to the stress or the velocity (temperature or temperature gradient). It can be shown that the overall contributions to the energy flux due to these cross terms are characteristic of *lossy* media only, see e.g. Chapter 5 of Borcherdt [1973]. For a free-space TVA medium in the absence of boundaries, as in this case, there are therefore two (distinct) contributions due to interactions, namely

$$\langle \mathbf{J}_{\Theta_1\Theta_2} \rangle, \quad \langle \mathbf{J}_{\Theta_2\Theta_1} \rangle. \tag{1.98}$$

If we consider a plane orthogonal to the direction of propagation, say at $x = 0$, the evaluation of $\langle \mathbf{J}_{\Theta_1} \rangle$, $\langle \mathbf{J}_{\Theta_2} \rangle$, together with (1.98) allows us to understand the *energy flux* through this plane (which can be thought of as a "fictitious" boundary). As we will show next, this is particularly relevant for situations involving physical boundaries.

### 1.3.2 Reflection from a rigid half–space in a TVA medium

We will next apply the model presented in Section 1.2.2 to the simplest possible scatterer, namely a two dimensional stationary, rigid half-space such that there is no mechanical coupling between the fluid and the solid. Above the solid resides a TVA fluid medium satisfying (1.65), (1.66). In reality it is expected that any source of energy driving the motion in this setting will induce the three fields $\hat{\Theta}_1, \hat{\Theta}_2, \hat{\mathbf{\Omega}}$. However, as we have discussed and seen in Figure 1.3, $\hat{\Theta}_2$ is the only propagative field in nature. We therefore assume that the source is sufficiently far[19], such that the incident field is comprised only of a plane wave of this type, impinging the surface at an angle $\psi$ (measured anticlockwise from the positive $x$-axis) which we label $\hat{\Theta}_{2I}$. The boundary of the half-space is confined to be $y = 0$. Since we are considering the wall to be rigid

[19]This argument can be found in the literature as it is a very good approximation, see e.g. Bruneau [2006], Scharstein and Davis [2007].

and uniform, we must impose (1.83) and we study both (1.85), (1.86) on $y = 0$, as illustrated in Figure 1.4.

Given this set-up we want to understand how the boundary conditions lead to the corresponding reflected (scattered) fields, and in particular quantify the effect of visco-thermal effects on the resulting behaviour compared to the (idealized) much simpler case of a purely acoustic medium from Section 1.2.1. As we will show next, under certain circumstances we can use approximations to the full theory in order to obtain an expression for the acoustic impedance which conveniently allows the problem to be written in a purely acoustic setting through a Robin condition (1.34) which encapsulates the visco-thermal losses with high accuracy. Similar analytical discussion of this approach to solve the problem in consideration are provided in several classical books e.g. Morse and Ingard [1986], Pierce et al. [1981], Bruneau [2006]. Here we will further give some exact solutions to the full problem for values of common fluids in standard scenarios, aiming to provide the reader with some extra physical intuition. Furthermore, in order to aid physical interpretation we will obtain a useful conservation equation that follows from the BCs and the discussion in Section 1.3.1.

We assume the incident field has the form

$$\hat{\Theta}_{2I} = \mathrm{e}^{-\mathrm{i}\kappa_2(x\cos\psi + y\sin\psi)}, \quad \psi \in [0, \pi] \tag{1.99}$$

and given the translational invariance of the problem in the $x$ direction, we expect the thermo-compressional and vorticity potentials to behave like[20]

$$\Theta_1(\omega, x, y) = \Theta_{1R}(\omega, y)\mathrm{e}^{-\mathrm{i}\kappa_2 x\cos\psi}, \tag{1.100a}$$

$$\hat{\Theta}_2(\omega, x, y) = \hat{\Theta}_{2I} + \Theta_{2R}(\omega, y)\mathrm{e}^{-\mathrm{i}\kappa_2 x\cos\psi}, \tag{1.100b}$$

$$\hat{\Omega}(\omega, x, y) = \Omega_R(\omega, y)\mathrm{e}^{-\mathrm{i}\kappa_2 x\cos\psi}, \tag{1.100c}$$

where we note that, since this problem is considered in the $(x, y)$ plane, the vectorial vorticity field becomes a scalar in the out of plane direction, i.e. $\hat{\boldsymbol{\Omega}} = \hat{\Omega}\mathbf{e_z}$ with $\mathbf{e_z}$ being a unit normal vector pointing outwards from the plane, and the subscripts $(I, R)$ are labels denoting 'incident' and 'reflected' respectively. Furthermore, given the symmetry of the problem it is sufficient to study incident angles in the first quadrant $\psi \in [0, \pi/2]$.

[20] This particular $x$ dependence follows since the BCs must be satisfied everywhere along $y = 0$ and is sometimes called the *phase matching condition* [Achenbach, 2012].

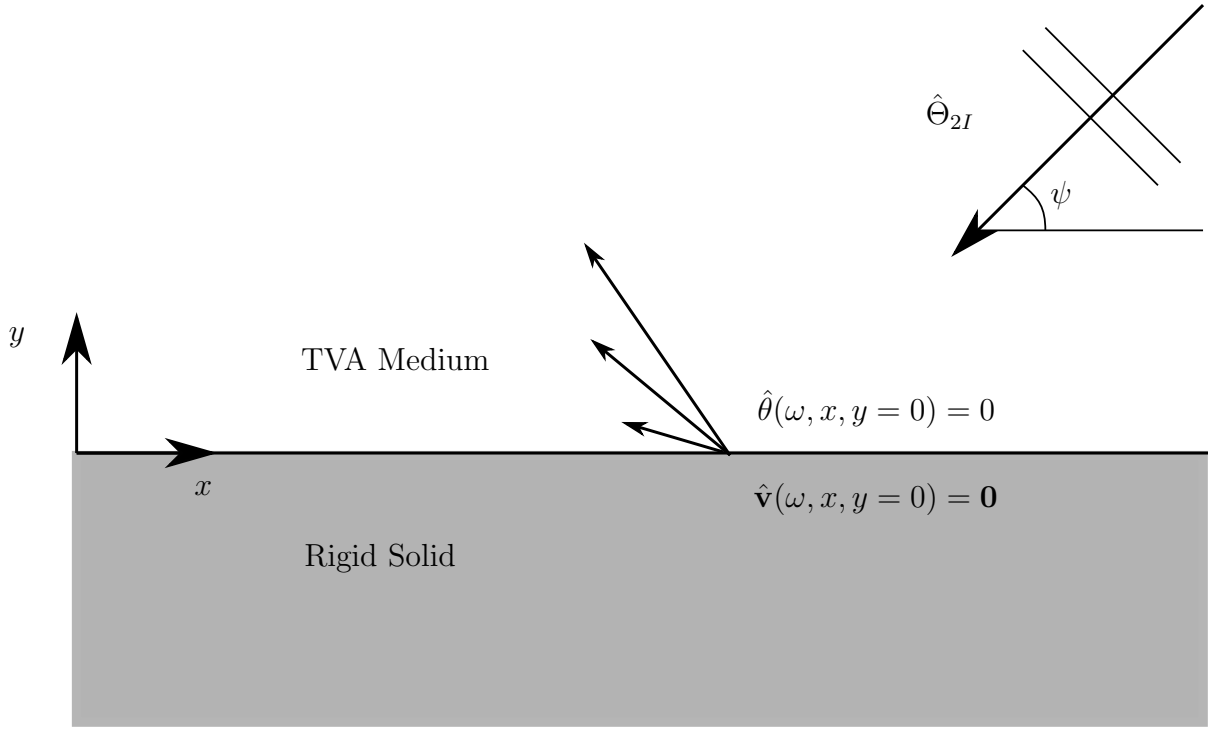


Figure 1.4: Schematic representation of the configuration of the rigid half-space problem for a visco-thermal fluid. An incident $\hat{\Theta}_{2I}$ mode at an angle $\psi$ (measured anticlockwise from the positive $x$-axis) impinges onto the $y = 0$ surface, giving rise to reflected thermo-compressional and vortical modes $\hat{\Theta}_{1R}$, $\hat{\Theta}_{2R}$ and $\hat{\Omega}_R$. The boundary conditions on $y = 0$ explicitly written correspond to the no-slip (1.83) and isothermal (1.85), but the adiabatic (1.86) is also considered.

Direct substitution of (1.100a)-(1.100c) into their respective governing PDEs (1.65), (1.66) gives three one-dimensional Helmholtz equations with straightforward solutions

$$\Theta_{1R} = C_{\Theta_1} \mathrm{e}^{\mathrm{i}y\sqrt{\kappa_1^2 - \kappa_2^2 \cos^2\psi}}, \tag{1.101a}$$

$$\Theta_{2R} = C_{\Theta_2} \mathrm{e}^{\mathrm{i}\kappa_2 \sin\psi y}, \tag{1.101b}$$

$$\Omega_R = C_{\Omega} \mathrm{e}^{\mathrm{i}y\sqrt{k_\Omega^2 - \kappa_2^2 \cos^2\psi}}, \tag{1.101c}$$

where the choice of roots made is consistent with the physical requirement of boundedness of the scattered field

$$\mathrm{Im}\left\{\sqrt{\kappa_1^2 - \kappa_2^2\cos^2\psi}\right\}, \mathrm{Im}\left\{\sqrt{k_\Omega^2 - \kappa_2^2\cos^2\psi}\right\} \geq 0, \tag{1.102}$$

such that solutions decay away from the boundary, and the fact that scattered waves must be outgoing in $y \geq 0$. The fact that (1.102) is satisfied can be directly verified when approximating the wavenumbers by (1.73a), (1.73b). The task therefore reduces to obtaining the complex valued amplitudes $\{C_{\Theta_1}, C_{\Theta_2}, C_{\Theta_\Omega}\}$, which come from the BCs. Applying the no-slip condition (1.83) yields explicitly

$$0 = \frac{c_p}{2\alpha}\kappa_2 \cos\psi[MC_{\Theta_1} + N(1 + C_{\Theta_2})] - C_\Omega \eta\sqrt{k_\Omega^2 - \kappa_2^2\cos^2\psi}, \tag{1.103a}$$

$$0 = \frac{c_p}{2\alpha}[M\sqrt{\kappa_1^2 - \kappa_2^2\cos^2\psi}C_{\Theta_1} + N\kappa_2(C_{\Theta_2} - 1)\sin\psi] + C_\Omega\eta\kappa_2\cos\psi, \tag{1.103b}$$

after using (1.68), where $M(\omega) = [1 - \mathrm{i}\omega(\zeta - \gamma\mathcal{C}) - \mathcal{S}]$ and $N(\omega) = [1 - \mathrm{i}\omega(\zeta - \gamma\mathcal{C}) + \mathcal{S}]$. Before we specify the thermal boundary condition, it is useful to consider the energy flux at the interface $y = 0$.

### Energy flux conservation at the boundary

In Section 1.3.1 we briefly described the different terms contributing to the overall energy flux in a one-dimensional example in the absence of boundaries. In this problem, since a rigid substrate occupies $y \leq 0$ we must have that the energy flux satisfies

$$\langle \mathbf{J} \rangle \cdot \mathbf{e_y} = 0 \qquad \text{on} \quad y = 0, \tag{1.104}$$

which follows from the definition (1.89) and the BCs (noting that it holds for either thermal BC) and $\mathbf{e_y}$ represents the unit normal to the boundary, since we have motion in the entire $(x, y)$ plane so that $\langle \mathbf{J} \rangle$ is a vector field. Given the decomposition (1.100),

we must also take into account the presence of *interaction terms* arising from the coupling between the incident and reflected modes, as well as distinct reflected modes. This results in seven extra terms to be accounted for (compared to the free space case from Section 1.3.1), so that we decompose $\langle \mathbf{J} \rangle$ as

$$\langle \mathbf{J} \rangle = \langle \mathbf{J}_{\mathrm{NI}} \rangle + \langle \mathbf{J}_{\mathrm{IRR}} \rangle + \langle \mathbf{J}_{\mathrm{IRI}} \rangle, \tag{1.105}$$

where $\langle \mathbf{J}_{\mathrm{NI}} \rangle$, $\langle \mathbf{J}_{\mathrm{IRR}} \rangle$, $\langle \mathbf{J}_{\mathrm{IRI}} \rangle$ denote the contribution to the power due to "Non-Interacting", "Interacting Reflected" and "Interacting between Reflected and Incident" modes respectively. These are specifically given by

$$\langle \mathbf{J}_{\mathrm{NI}} \rangle = \langle \mathbf{J}_{\Theta_{2I}} \rangle + \langle \mathbf{J}_{\Theta_{1R}} \rangle + \langle \mathbf{J}_{\Theta_{2R}} \rangle + \langle \mathbf{J}_{\Omega_R} \rangle, \tag{1.106a}$$

$$\langle \mathbf{J}_{\mathrm{IRR}} \rangle = \langle \mathbf{J}_{\Theta_{1R}\Theta_{2R}} \rangle + \langle \mathbf{J}_{\Theta_{2R}\Theta_{1R}} \rangle + \langle \mathbf{J}_{\Theta_{1R}\Omega_R} \rangle + \langle \mathbf{J}_{\Omega_R\Theta_{1R}} \rangle + \langle \mathbf{J}_{\Theta_{2R}\Omega_R} \rangle + \langle \mathbf{J}_{\Omega_R\Theta_{2R}} \rangle, \tag{1.106b}$$

$$\langle \mathbf{J}_{\mathrm{IRI}} \rangle = \langle \mathbf{J}_{\Theta_{2I}\Theta_{1R}} \rangle + \langle \mathbf{J}_{\Theta_{1R}\Theta_{2I}} \rangle + \langle \mathbf{J}_{\Theta_{2I}\Theta_{2R}} \rangle + \langle \mathbf{J}_{\Theta_{2R}\Theta_{2I}} \rangle + \langle \mathbf{J}_{\Theta_{2I}\Omega_R} \rangle + \langle \mathbf{J}_{\Omega_R\Theta_{2I}} \rangle, \tag{1.106c}$$

remembering that for interacting terms, the order in the subscripts is important. We can therefore rewrite (1.104) as

$$(\langle \mathbf{J}_{\Theta_{2I}} \rangle + \langle \mathbf{J}_{\Theta_{1R}} \rangle + \langle \mathbf{J}_{\Theta_{2R}} \rangle + \langle \mathbf{J}_{\Omega_R} \rangle + \langle \mathbf{J}_{\mathrm{IRR}} \rangle + \langle \mathbf{J}_{\mathrm{IRI}} \rangle) \cdot \mathbf{e_y} = 0, \tag{1.107}$$

after using (1.106). We can now define the *energy reflection coefficients* $R$ and *interaction-reflected coefficients* $IR$ such that

$$R_{\Theta_1} = -\frac{\langle \mathbf{J}_{\Theta_{1R}} \rangle \cdot \mathbf{e_y}}{\langle \mathbf{J}_{\Theta_{2I}} \rangle \cdot \mathbf{e_y}}, \quad R_{\Theta_2} = -\frac{\langle \mathbf{J}_{\Theta_{2R}} \rangle \cdot \mathbf{e_y}}{\langle \mathbf{J}_{\Theta_{2I}} \rangle \cdot \mathbf{e_y}}, \quad R_{\Omega} = -\frac{\langle \mathbf{J}_{\Omega_R} \rangle \cdot \mathbf{e_y}}{\langle \mathbf{J}_{\Theta_{2I}} \rangle \cdot \mathbf{e_y}}, \tag{1.108a}$$

$$IR_{RR} = -\frac{\langle \mathbf{J}_{\mathrm{IRR}} \rangle \cdot \mathbf{e_y}}{\langle \mathbf{J}_{\Theta_{2I}} \rangle \cdot \mathbf{e_y}}, \quad IR_{IR} = -\frac{\langle \mathbf{J}_{\mathrm{IRI}} \rangle \cdot \mathbf{e_y}}{\langle \mathbf{J}_{\Theta_{2I}} \rangle \cdot \mathbf{e_y}}, \tag{1.108b}$$

so that finally (1.107) becomes

$$R_{\Theta_1} + R_{\Theta_2} + R_{\Omega} + IR_{RR} + IR_{IR} = 1, \tag{1.109}$$

which represents conservation of energy and hence provides a physical interpretation to the various coefficient in terms of energetic principles. In order to calculate these different quantities we must first determine the complex amplitudes $(C_{\Theta_1}, C_{\Theta_2}, C_{\Omega})$. We will continue by calculating them for the isothermal boundary condition, followed by the adiabatic.

### Isothermal BC

In the (physically relevant) case of an isothermal boundary condition (1.85) at $y = 0$ we obtain

$$C_{\Theta_1} + 1 + C_{\Theta_2} = 0, \tag{1.110}$$

to be solved together with (1.103), which in matrix form reads

$$\begin{pmatrix} -c_p\kappa_2 M(\omega)\cos\psi & -c_p\kappa_2 N(\omega)\cos\psi & 2\alpha\eta d_\Omega \\ c_p d_1 M(\omega) & c_p\kappa_2 N(\omega)\sin\psi & 2\alpha\kappa_2\eta\cos\psi \\ 1 & 1 & 0 \end{pmatrix} \cdot \begin{pmatrix} C_{\Theta_1} \\ C_{\Theta_2} \\ C_\Omega \end{pmatrix} = \begin{pmatrix} c_p\kappa_2 N(\omega)\cos\psi \\ c_p\kappa_2 N(\omega)\sin\psi \\ -1 \end{pmatrix}, \tag{1.111}$$

where, for brevity, we have introduced $d_1 = \sqrt{\kappa_1^2 - \kappa_2^2\cos^2\psi}$ and $d_\Omega = \sqrt{k_\Omega^2 - \kappa_2^2\cos^2\psi}$. The solution to this system can be written as

$$\begin{pmatrix} C_{\Theta_1} \\ C_{\Theta_2} \\ C_\Omega \end{pmatrix} = \begin{pmatrix} \frac{2d_\Omega\mathcal{A}}{\cos^2\psi - d_\Omega(\mathcal{A}-\mathcal{D})} \\ \frac{-\cos^2\psi - d_\Omega(\mathcal{A}+\mathcal{D})}{\cos^2\psi - d_\Omega(\mathcal{A}-\mathcal{D})} \\ \frac{\sin 2\psi\mathcal{W}}{\cos^2\psi - d_\Omega(\mathcal{A}-\mathcal{D})} \end{pmatrix}, \tag{1.112}$$

where

$$\mathcal{A} = \frac{N(\omega)\sin\psi}{\kappa_2(M(\omega) - N(\omega))}, \qquad \mathcal{D} = \frac{d_1 M(\omega)}{\kappa_2^2(M(\omega) - N(\omega))}, \qquad \mathcal{W} = \frac{c_p N(\omega)}{2\alpha\eta}. \tag{1.113}$$

### Adiabatic BC

In this case, we must naturally still satisfy (1.103) as well as $\frac{\partial\hat{\theta}}{\partial y} = 0$ on $y = 0$ which implies that the scattering system becomes

$$\begin{pmatrix} -c_p\kappa_2 M(\omega)\cos\psi & -c_p\kappa_2 N(\omega)\cos\psi & 2\alpha\eta d_\Omega \\ c_p d_1 M(\omega) & c_p\kappa_2 N(\omega)\sin\psi & 2\alpha\kappa_2\eta\cos\psi \\ d_1 & k_2\sin\psi & 0 \end{pmatrix} \cdot \begin{pmatrix} C_{\Theta_1} \\ C_{\Theta_2} \\ C_\Omega \end{pmatrix} = \begin{pmatrix} c_p\kappa_2 N(\omega)\cos\psi \\ c_p\kappa_2 N(\omega)\sin\psi \\ k_2\sin\psi \end{pmatrix}, \tag{1.114}$$

where we note that only the last row of the system has changed from the isothermal scattering system (1.111). The solution to (1.114) is given by

$$\begin{pmatrix} C_{\Theta_1} \\ C_{\Theta_2} \\ C_\Omega \end{pmatrix} = \begin{pmatrix} \frac{-2\mathcal{G}\sin\psi\cos^2\psi}{\cos^2\psi + d_\Omega(\mathcal{F}-\mathcal{G})\sin\psi}\frac{\kappa_2^2}{d_1} \\ 1 + \frac{2\mathcal{G}\cos^2\psi}{\cos^2\psi + d_\Omega(\mathcal{F}-\mathcal{G})\sin\psi}\kappa_2 \\ \frac{(\mathcal{F}-\mathcal{G})\mathcal{W}\sin 2\psi}{\cos^2\psi + d_\Omega(\mathcal{F}-\mathcal{G})\sin\psi}\kappa_2 \end{pmatrix}, \tag{1.115}$$

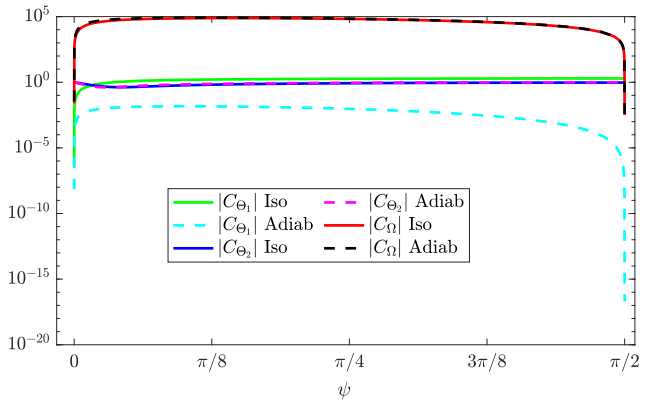


Figure 1.5: Comparison of absolute value of complex amplitudes for the TVA rigid half–space between the isothermal (1.112) and adiabatic (1.115) cases as a function of incident angle. The material parameters used for air are given in Table A.1 of Appendix A and the incident frequency is 10MHz. The large variation in the scale of the $y$ axis is noted.

where

$$\mathcal{F} = \frac{d_1 M(\omega)}{\kappa_2(\kappa_2 M(\omega)\sin\psi - d_1 N(\omega))}, \qquad \mathcal{G} = \frac{d_1 N(\omega)}{\kappa_2(\kappa_2 M(\omega)\sin\psi - d_1 N(\omega))}. \tag{1.116}$$

A comparison between the magnitude of the complex amplitudes isothermal and adiabatic solutions (1.112), (1.115) for air is given in Figure 1.5. We can observe that the (absolute values of the) pressure dominated mode and the vortical mode $|C_{\Theta_2}|, |C_{\Omega}|$ behave very similarly with the two different boundary conditions. For $|C_{\Theta_1}|$ the adiabatic and isothermal solutions are significantly different and seems to suggest that the coupling with thermal effects is stronger in the isothermal case, noting that in the adiabatic case $|C_{\Theta_1}| \to 0$ as $\psi \to \pi/2$ i.e. towards normal incidence. Nevertheless, we note that since the incident mode is pressure dominated (with unit amplitude) (1.99), the respective reflected pressure dominated mode $\Theta_{2R}$ is directly comparable, but this is not the case for $\Theta_{1R}, \Omega_R$ as can be seen from the large variation in the values of the vertical axis, which makes the physical interpretation unclear. In order to understand this better, it is convenient to analyse the different energy reflection coefficients in (1.109). This is done in Figure 1.6, which consists of the different energy reflection coefficients from (1.108a) for the same input parameters of those in Figure 1.5. The analytical expressions for these terms are not provided here[21] and have been obtained using symbolic computations in *Wolfram Mathematica 12.0* confirming

[21] A consequence of this computation nevertheless is that $R_{\Theta_2} = |C_{\Theta_2}|^2$ due to the similarity between (1.99) and (1.101b).

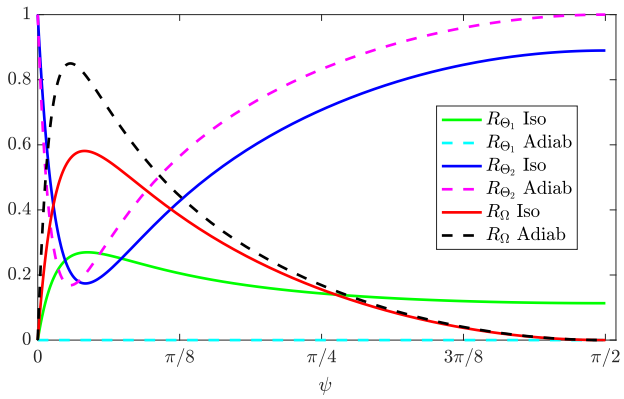


Figure 1.6: Comparison of energy reflection coefficients for the TVA-rigid half–space (1.108a) between the isothermal (1.112) and adiabatic (1.115) cases as a function of incident angle. The material parameters used for air are those given in Table A.1 of Appendix A and the incident frequency is 10MHz.

in each case that (1.109) is always satisfied. Furthermore, the only distinction between the different $R_s$ and $IR_s$ for the isothermal and adiabatic boundary condition lies in the complex amplitudes (1.112), (1.115).

In Figure 1.6 the normalization of values allows for direct comparisons between the various curves. Indeed as Figure 1.5 suggested, the isothermal BC leads to significant thermal coupling as seen from $R_{\Theta_1}$ which in turn offsets the maximum value of $R_\Omega$ (near grazing incidence) which is much higher in the adiabatic case. For $R_{\Theta_2}$ (and $R_{\Theta_1}$) we note that differences between BCs are noted in the entire interval. We must note that in Figures 1.5, 1.6 the driving frequency given by 10 MHz which is considered very high in most instances. In order to see the consequence of the incident frequency on these results, we consider 10 kHz in Figure 1.7 which we note lies in the audible regime. We observe that this leads to a much different overall behaviour upon reflection with the various turning points having been shifted[22] very close to grazing incidence ($\psi \to 0$). At larger angles for both cases of BCs, the majority of the energy gets converted into the pressure dominated mode. For completeness, in Figure 1.8 we finally give the sum of the remaining terms that contribute to the energy balance (1.109), noting that in the absence of dissipation these terms add up to zero. We observe that this is almost the case at 10 kHz for either BC, whereas at 10 MHz there is a larger magnitude in the isothermal case.

[22]The particular scaling describing this shift with frequency will be discussed shortly.

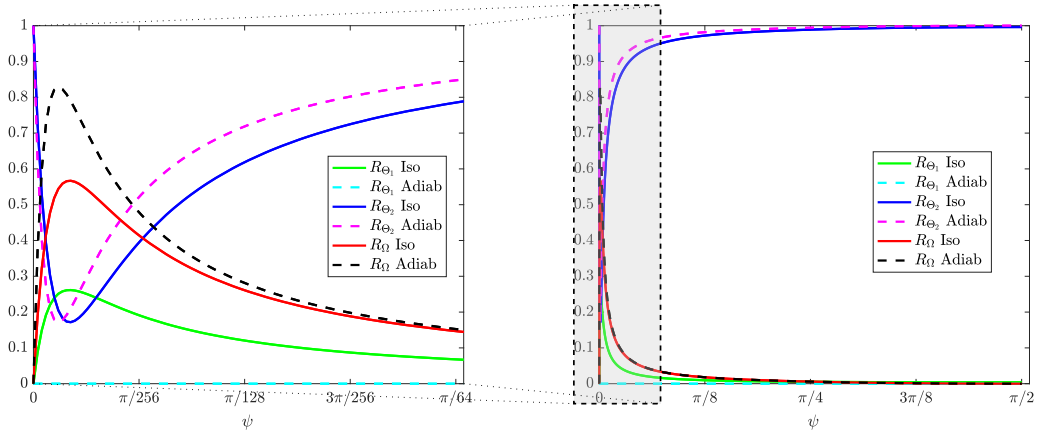


Figure 1.7: Comparison of reflection coefficients for the TVA rigid half–space (1.108a) between the isothermal (1.112) and adiabatic (1.115) cases as a function of incident angle. The plot on the left is the same as that on the right, but for a shorter range of angles closer to incidence, as indicated by the grey region and the dotted lines. The material parameters used for air are those given in Table A.1 of Appendix A and the incident frequency is 10kHz.

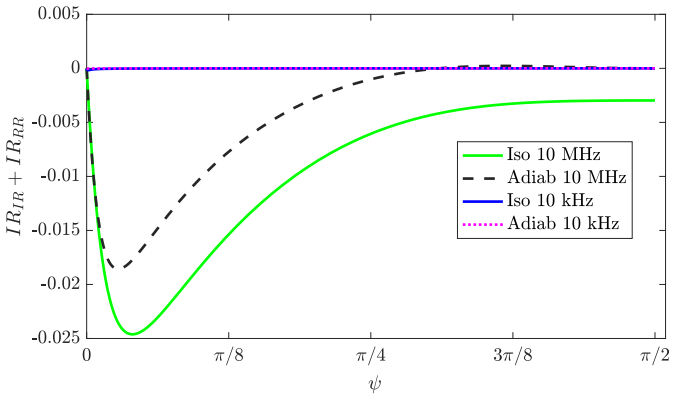


Figure 1.8: Comparison of the sum of interaction coefficients for the TVA rigid halfspace (1.109) between the isothermal and adiabatic solutions as a function of incident angle. The material parameters used for air are those shown in Table A.1 of Appendix A.

**Obtaining the acoustic admittance of the surface**

We next show an alternative approach to the solution of the isothermal TVA rigid half–space problem from above. We first observe that (1.103), (1.112) can be combined into a single equation for $C_{\Theta_2}$, namely

$$\begin{aligned} &-(1+C_{\Theta_2})M(\omega)\left[\kappa_2^2\cos^2\psi+\sqrt{k_\Omega^2-\kappa_2^2\cos^2\psi}\sqrt{\kappa_1^2-\kappa_2^2\cos^2\psi}\right] \\ &=N(\omega)\left[(1-C_{\Theta_2})\kappa_2\sin\psi\sqrt{k_\Omega^2-\kappa_2^2\cos^2\psi}-(1+C_{\Theta_2})\kappa_2^2\cos^2\psi\right], \end{aligned} \tag{1.117}$$

or equivalently, using the definitions for $d_1$, $d_\Omega$ just below (1.111)

$$\kappa_2\sin\psi\frac{1-C_{\Theta_2}}{1+C_{\Theta_2}}=\frac{1}{d_\Omega}\left[\frac{-M}{N}\left(\kappa_2^2\cos^2\psi+d_\Omega d_1\right)+\kappa_2^2\cos^2\psi\right] \tag{1.118}$$

which can be simplified by using equation[23] (1.72), as well as (1.73a), (1.73b) with $\omega\mathcal{C}$, $\omega\zeta\ll 1$ so that

$$M\approx \mathrm{i}\omega(\gamma-1)\mathcal{C},\qquad N\approx 1-\mathrm{i}\omega(\zeta-\mathcal{C}), \tag{1.119a}$$

$$\begin{aligned} d_1=\sqrt{\kappa_1^2-\kappa_2^2\cos^2\psi}&=\sqrt{\frac{\mathrm{i}\omega}{\mathcal{C}}\left(1+\mathrm{i}\omega(\gamma-1)(\zeta-\mathcal{C})\right)-\omega^2\cos^2\psi(1+\mathrm{i}\omega(\zeta+\mathcal{C}(\gamma-1)))} \\ &=\sqrt{\frac{\mathrm{i}\omega}{\mathcal{C}}}\sqrt{1+\mathrm{i}\omega\mathcal{C}\left[(\gamma-1)(\zeta-\mathcal{C})+\cos^2\psi(1+\mathrm{i}\omega(\zeta+\mathcal{C}(\gamma-1)))\right]} \\ &\approx\sqrt{\frac{\mathrm{i}\omega}{\mathcal{C}}}, \end{aligned} \tag{1.119b}$$

$$\begin{aligned} d_\Omega=\sqrt{k_\Omega^2-\kappa_2^2\cos^2\psi}&=\sqrt{\frac{\mathrm{i}\omega}{\eta}-\omega^2\cos^2\psi(1+\mathrm{i}\omega(\zeta+\mathcal{C}(\gamma-1)))} \\ &=\sqrt{\frac{\mathrm{i}\omega}{\eta}}\sqrt{1+\mathrm{i}\omega\eta\cos^2\psi(1+\mathrm{i}\omega(\zeta+\mathcal{C}(\gamma-1)))}\approx\sqrt{\frac{\mathrm{i}\omega}{\eta}}, \end{aligned} \tag{1.119c}$$

where terms of $O(\omega\sqrt{\omega\eta},\omega\sqrt{\omega\mathcal{C}})$ have been neglected. With these approximations (1.118) can then be rearranged into

$$\omega\sin\psi\frac{1-C_{\Theta_2}}{1+C_{\Theta_2}}=\omega^{3/2}\sqrt{-\mathrm{i}}\left((\gamma-1)\sqrt{\mathcal{C}}+\cos^2\psi\sqrt{\eta}\right), \tag{1.120}$$

which we will next show is of great utility since it can be related to the acoustic admittance discussed in (1.34). The non-dimensional acoustic[24] admittance of an arbitrary surface is defined as

$$\frac{1}{\mathcal{Z}}=\frac{\hat{\mathbf{v}}_2\cdot\mathbf{n}}{\hat{p}_2}\quad\text{on the surface,} \tag{1.121}$$

[23] This is equivalent to applying the approximation (1.77) directly as the no-slip condition.

[24] By acoustic here we refer to the contributions to the pressure and velocity due to $\hat{\Theta}_2$ only.

with $\mathbf{n}$ denoting the (unit) outer normal to the fluid (into the surface boundary). In this particular case, $\mathbf{n} = -\mathbf{e_y}$ so we are only interested in the vertical component of the (laminar) acoustic velocity $\hat{\mathbf{v}}_2$. From (1.75b), (1.78b) we directly obtain

$$\begin{aligned}\hat{\mathbf{v}}_2|_{y=0} \cdot \mathbf{n} &= \frac{c_p}{\alpha}\left(\frac{\mathrm{i}}{\omega} + \zeta - \mathcal{C}\right)(\mathrm{i}\kappa_2 \sin\psi)\left[1 - C_{\Theta_2}\right]\mathrm{e}^{-\mathrm{i}\kappa_2 x\cos\psi} \\ &= -\frac{c_p}{\alpha}\sin\psi\left[1 - C_{\Theta_2}\right]\mathrm{e}^{-\mathrm{i}\kappa_2 x\cos\psi} + O(\omega\zeta, \omega\mathcal{C}), \qquad (1.122)\\ \hat{p}_2|_{y=0} &= \frac{c_p}{\alpha}(1 + \mathrm{i}\omega\mathcal{C})\left[1 + C_{\Theta_2}\right]\mathrm{e}^{-\mathrm{i}\kappa_2 x\cos\psi} \\ &= \frac{c_p}{\alpha}\left[1 + C_{\Theta_2}\right]\mathrm{e}^{-\mathrm{i}\kappa_2 x\cos\psi} + O(\omega\mathcal{C}). \qquad (1.123)\end{aligned}$$

Hence the leading order term of (1.121) is given by

$$\frac{1}{\mathcal{Z}} = \frac{\hat{\mathbf{v}}_2|_{y=0} \cdot \mathbf{n}}{\hat{p}_2|_{y=0}} = \sin\psi\frac{1 - C_{\Theta_2}}{1 + C_{\Theta_2}}, \qquad (1.124)$$

which, when using (1.120) becomes

$$\begin{aligned}\frac{1}{\mathcal{Z}} &= \sqrt{-\mathrm{i}\omega}\left((\gamma - 1)\sqrt{\mathcal{C}} + (1 - \sin^2\psi)\sqrt{\eta}\right), \\ &= \mathrm{e}^{\frac{-\mathrm{i}\pi}{4}}\sqrt{\omega}\left((\gamma - 1)\sqrt{\mathcal{C}} + (1 - \sin^2\psi)\sqrt{\eta}\right). \qquad (1.125)\end{aligned}$$

It can be observed that there is a direct dependence on the incident angle $\psi$, as a result, the surface cannot be considered *locally reacting* [Opdam et al., 2014]. Moreover, for a given frequency, grazing incidence $\psi = 0$ maximizes the (shear) viscous effects which also yields the largest real part of the admittance (1.125). Conversely, for normal incident energy ($\psi = \pi/2$) these shear effects are not present and (1.125) becomes minimal. Thermal effects are independent of incident angle. We next note that with (1.125) we may write (1.124) in terms of $C_{\Theta_2}$ to obtain

$$C_{\Theta_2}(\psi, \omega) = \frac{\sin\psi - \frac{1}{\mathcal{Z}}}{\sin\psi + \frac{1}{\mathcal{Z}}} = \frac{\sin\psi - \mathrm{e}^{\frac{-\mathrm{i}\pi}{4}}\sqrt{\omega}\left((\gamma - 1)\sqrt{\mathcal{C}} + \sqrt{\eta}\cos^2\psi\right)}{\sin\psi + \mathrm{e}^{\frac{-\mathrm{i}\pi}{4}}\sqrt{\omega}\left((\gamma - 1)\sqrt{\mathcal{C}} + \sqrt{\eta}\cos^2\psi\right)}. \qquad (1.126)$$

As it will become apparent, this is precisely the complex amplitude arising in the much simpler problem of an acoustic half-space reflection in a non-dissipative fluid as modelled in Section 1.2.1 and governed by (1.22), but still taking into account the loss through the boundary via an impedance condition (1.34). That is (in non-dimensional form so that $k = \omega$),

$$\begin{aligned}&\left(\nabla^2 + \omega^2\right)\hat{p} = 0, \qquad (1.127)\\ &\frac{\partial\hat{p}}{\partial y} + \omega\mathrm{e}^{\frac{\pm\mathrm{i}\pi}{4}}\sqrt{\omega}\left((\gamma - 1)\sqrt{\mathcal{C}} + \sqrt{\eta}\cos^2\psi\right)\hat{p} = 0 \quad \text{on} \quad y = 0, \qquad (1.128)\end{aligned}$$

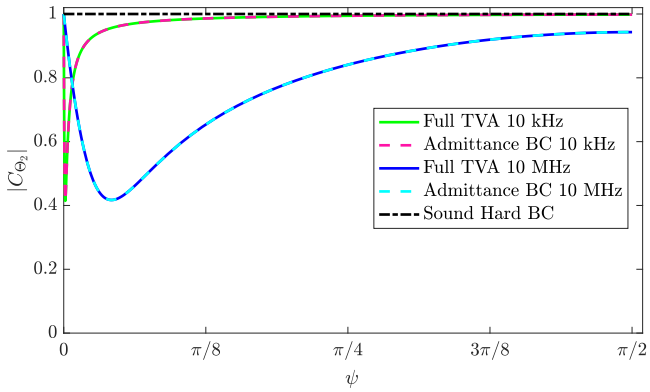


Figure 1.9: Comparison of $|C_{\Theta_2}|$ (isothermal) between the full TVA approach and the approximate solution obtained via the acoustic admittance boundary condition as a function of incident angle. The sound hard (1.30) acoustic solution given by the black dotted line is independent of frequency. The material parameters used for air are taken from Table A.1 of Appendix A.

as well as the radiation condition. The solution of the boundary value problem consisting of (1.127), (1.128) assuming unit amplitude incident pressure is simply written as

$$\hat{p} = \hat{p}_I + \hat{p}_R = \left(\mathrm{e}^{-\mathrm{i}\omega y \sin\psi} + C_{\Theta_2}\mathrm{e}^{\mathrm{i}\omega y \sin\psi}\right)\mathrm{e}^{\mathrm{i}\omega x \cos\psi}, \tag{1.129}$$

where $C_{\Theta_2}$ is found by direct application of (1.128) which yields (1.126). This solution is directly compared to that obtained by solving the full TVA isothermal scattering system (1.112) in Figure 1.9. We can observe an excellent agreement between both solutions at both frequencies showing the accuracy and convenience of the concept of effective admittance for the rigid half-space problem. Although not shown here, the solution seems to break down when reaching GHz frequencies which is expected since the assumptions used to obtain (1.119a)-(1.119c) become no longer applicable. In the bulk of the dissipative fluid (1.73b), visco-thermal effects appear first at $O(\omega\eta, \omega\mathcal{C})$, whereas in the equivalent admittance of the wall (1.125) these damping mechanisms are manifested at $O(\sqrt{\omega\eta}, \sqrt{\omega\mathcal{C}})$, and for frequencies of interest we have $1 \gg \sqrt{\omega\eta}, \sqrt{\omega\mathcal{C}} \gg \omega\eta, \omega\mathcal{C}$, as can be seen from (1.70), (1.71).

The key for the success of the admittance BC to represent visco-thermal losses lies in the fact that these effects are only really confined to boundary layers of very narrow thicknesses compared to the exterior domain of the given problem (which is the reason this argument is particularly suitable for the half-space). For in-air acoustics, these (boundary layer) lengths become increasingly small as the frequency increases, e.g. at

10 MHz they become $O(10^{-7})$ m. Nevertheless, note that the continuum theory we are assuming in this project requires that the relevant length scales must be significantly larger than the *mean free path*[25] of the fluid [Bruneau, 2006]. It turns out that in the case of air the mean free path is $O(10^{-8})$ m [Jennings, 1988] so that the conditions are satisfied (although not by much) indicating that care must be taken at frequencies beyond those considered here.

Outside the boundary layers, the particle velocity induced by visco-thermal effects is negligible. Further, in the boundary layers, shear effects dominate over bulk viscosity effects, which is the reason why (1.125) contains $\eta$, but not $\eta_K$. Also note that with this approach, the thermal field $\hat{\theta}$ cannot be fully described in the domain, as opposed to the full TVA approach. Nevertheless, for most acoustic-engineering applications this is usually not a concern since it is the influence of visco-thermal effects on the propagative acoustic pressure wave that is of principal interest [Beltman, 1999].

### Extending the concept of acoustic admittance

It is further shown in Bruneau [2006] how an expression for the acoustic admittance which generalises (1.125) can be obtained regardless of the nature of the incident wave profile. This extension is key since it allows to approximate thermo-viscous losses in terms of admittance boundary conditions to more complex geometries than the half-space illustrated here. Of particular relevance is the propagation of sound in waveguides which has been extensively studied (and we discuss in Chapter 2) but it can also be applied to classical scattering problems, e.g. spheres under incident plane wave forcing are given explicitly in Bruneau [2006]. For cylindrical waveguides, two distinct non-dimensional quantities are useful to 'partition' the problem into various differing regimes, namely the reduced frequency and a non-dimensional viscous boundary layer parameter [Tijdeman, 1975]. With these parameters, three distinct regimes of studies can be identified [Weston, 1980]: the "Low frequency-narrow tube range", "high frequency-wide tube range" and the "very high frequency-very wide tube range". In the second of these, the boundary layers are localised to the vicinity of the waveguide and the effective admittance BC is valid. The "Low frequency-narrow tube range" is

[25] This is often stated in terms of the *Knudsen number* (dimensionless ratio of mean free path of the fluid to representative physical length scale) being much less than unity.

concerned with *capillary* tubes whose width is (less or) of the order of the boundary layer, so that the 'bulk' region where we were allowed to use the asymptotic approximations (1.119) is no longer valid. Nevertheless, other useful approximations can be made in this regime, such as the "reduced solution" from Zwikker and Kosten [1949].

Using our analysis from Section 2.2, in Section 2.3 we will examine quantitatively the accuracy of the acoustic admittance BC approximation for a 2D rectangular waveguide, as we transition from the "high frequency-wide tube range" into the capillary tubes regime.

## 1.4 Modelling Solids

As for fluids, it is inherently assumed that the solids in consideration here are continua for which the concept of a 'material particle' can be defined, which allows for a convenient mathematical description which is highly accurate in our regime of interest since we are operating at macroscopic lengthscales which are much much larger than the corresponding characteristic atomic lengthscales. Emphasis is put in the development of the ideal lossless theory in the absence of dissipation given in Section 1.4.1, whereas the inclusion of losses via the theories of viscoelasticy (VE) and thermoelasticity (TE) are discussed in Section 1.4.2. Finally, in Section 1.4.3 we suggest the possible conveniences resulting from a theory of thermo-visco-elasticity (TVE).

### 1.4.1 Linear Elasticity

Following the preceding analysis for fluids, we now want to illustrate the different constitutive assumptions that lead to the governing equations for linearly elastic solids, and the respective form of their solutions. Here we will mostly follow Nowacki [2013] and Achenbach [2012], but the author also found useful the classical textbooks by Love [2013], Graff [2012] (for elastic waves) and Sokolnikoff [1956] for a more technical description.

#### Governing Equations

If a solid particle is in equilibrium at a position $\bar{\mathbf{x}}$, and is deformed to a position $\bar{\mathbf{x}}'$, the *displacement* field at time $\bar{t}$ is defined as

$$\bar{\mathbf{u}}(\bar{\mathbf{x}}, \bar{t}) = \bar{\mathbf{x}}'(\bar{\mathbf{x}}, \bar{t}) - \bar{\mathbf{x}}, \tag{1.130}$$

which when differentiated with respect to the initial coordinates gives the *displacement gradient tensor*, namely

$$\frac{\partial \bar{\mathbf{u}}(\bar{\mathbf{x}}, \bar{t})}{\partial \bar{\mathbf{x}}} = \boldsymbol{F} - \boldsymbol{I}, \quad \text{where} \quad \boldsymbol{F} = \frac{\partial \bar{\mathbf{x}}'(\bar{\mathbf{x}}, \bar{t})}{\partial \bar{\mathbf{x}}} \tag{1.131}$$

is known as the *deformation gradient*. In order to develop this linearized theory, we shall assume that displacement gradients are infinitesimal, so that $|\partial \bar{u}_i / \partial \bar{x}_j| \ll 1$ and therefore contains *no* quadratic or higher order terms, so that it can be written as

$$\frac{\partial \bar{u}_i}{\partial \bar{x}_j} = \varepsilon_{ij} + w_{ij}, \tag{1.132}$$

where

$$\varepsilon_{ij} = \frac{1}{2}\left(\frac{\partial \bar{u}_i}{\partial \bar{x}_j} + \frac{\partial \bar{u}_j}{\partial \bar{x}_i}\right), \quad \text{and} \quad w_{ij} = \frac{1}{2}\left(\frac{\partial \bar{u}_i}{\partial \bar{x}_j} - \frac{\partial \bar{u}_j}{\partial \bar{x}_i}\right), \tag{1.133}$$

correspond respectively to the infinitesimal *strain tensor* (which is symmetric) and the *rotation tensor* (which is anti-symmetric). Under the current theory we are therefore assuming both small displacements and small rotations. Of course the displacement further satisfies $\partial \bar{u}_i/\partial \bar{t} = \bar{v}_i$. With these assumptions, the conservation of mass equation (1.1) simply states that $\bar{\rho} = \bar{\rho}_0$ (at leading order) and the linear equation for conservation of momentum (1.2) (in the absence of external body forces) can be written in the current context as

$$\bar{\rho}_0 \frac{\partial^2 \bar{\mathbf{u}}}{\partial \bar{t}^2} = \bar{\nabla} \cdot \bar{\boldsymbol{\sigma}}. \tag{1.134}$$

In linear elasticity, the Cauchy stress tensor is symmetric[26] and is dictated by *Hooke's law*, which may be written in component form as

$$\bar{\sigma}_{ij} = \bar{C}_{ijkl}\varepsilon_{kl}, \tag{1.135}$$

or $\varepsilon_{ij} = \bar{D}_{ijkl}\bar{\sigma}_{kl}$, where the fourth order tensors $\bar{C}_{ijkl}, \bar{D}_{ijkl}$ are the *elastic moduli* and *compliance* tensors. In the particular case in which $\bar{C}_{ijkl}, \bar{D}_{ijkl}$ and $\bar{\rho}_0$ are independent of spatial coordinates, the materials are said to be *homogeneous*. The symmetries of the stress/strain tensor reduce the number of independent coefficients from the apparent $3^4$ to 21, which are in general determined experimentally. Furthermore, in this thesis we will mainly be focusing on *isotropic* media whose material properties have no preferred direction. This assumption further reduces to the simple form

$$\bar{C}_{ijkl} = \bar{\lambda}\delta_{ij}\delta_{kl} + \bar{\mu}(\delta_{ik}\delta_{jl} + \delta_{il}\delta_{jk}), \tag{1.136}$$

so that there are only two physical constants present $\bar{\lambda}, \bar{\mu}$ commonly known as *Lamé constants* which have units of Pascals. Upon substitution of (1.136) into (1.135), Hooke's law simply becomes

$$\bar{\sigma}_{ij} = \bar{\lambda}\delta_{ij}\varepsilon_{kk} + 2\bar{\mu}\varepsilon_{ij} = \bar{K}\delta_{ij}\varepsilon_{kk} + 2\bar{\mu}\left(\varepsilon_{ij} - \frac{1}{3}\delta_{ij}\varepsilon_{kk}\right). \tag{1.137}$$

It is clear that if we let $i = j$, (1.137) becomes

$$\bar{\sigma}_{ii} = (3\bar{\lambda} + 2\bar{\mu})\varepsilon_{ii} = 3\bar{K}\varepsilon_{ii}, \tag{1.138}$$

[26] This can be shown directly by the consideration of *conservation of angular momentum* of a material particle [Marsden and Hughes, 1994].

where $\bar{K}$ is commonly known as the material's bulk modulus. In fact, this can be seen by direct comparison of (1.138) with the ideal fluid relation (1.3) which gives $\bar{p} = -\bar{K}\varepsilon_{ii}$. Since $\varepsilon_{ii}$ represents a volume change (also referred to as the *dilation*), and hydrostatic pressure reduces the volume of a body, we must have[27] $\bar{K} > 0$. On the other hand, by considering a particular state of *simple shear* so that e.g. $\bar{\sigma}_{12} = 2\bar{\mu}\varepsilon_{12}$ is the only non-zero component of stress, experiments confirm that $\bar{\sigma}_{12}$ and $\varepsilon_{12}$ have in fact the same direction and so it is well established that $\bar{\mu} > 0$. This easily measurable quantity is therefore known as the *shear modulus*. Further simple experiments involving simple extension of thin rods can give rise to the (non-dimensional) *Poisson's ratio* $\nu$ and *Young's modulus* $\bar{E} \geq 0$, which often appear in the governing equations due to their straightforward physical interpretation. We can obtain further constraints on $\nu$ by using the relationships from Table 1.1, where we provide useful relationships between the various moduli. Indeed, we note that as $\bar{K} \to \infty$ the Poisson's ratio approaches $\nu \to 0.5$ which in turn implies that the material becomes increasingly incompressible ($\bar{\lambda} \to \infty$) and $\bar{\mu} \to \bar{E}/3$. On the other hand, $\nu \to -1$ results in $\bar{\mu}, \bar{\lambda} \to \infty$, and therefore physical materials are constrained by $-1 < \nu \leq 0.5$. Note that from substituting (1.138) into (1.137) we can write

$$\varepsilon_{ij} = \bar{D}_{ijkl}\bar{\sigma}_{kl} = \frac{1}{2\bar{\mu}}\bar{\sigma}_{ij} - \frac{\bar{\lambda}}{2\bar{\mu}(3\bar{\lambda} + 2\bar{\mu})}\bar{\sigma}_{kk}\delta_{ij}, \tag{1.139}$$

and hence the corresponding isotropic compliance tensor is given by

$$\bar{D}_{ijkl} = \frac{1}{4\bar{\mu}}(\delta_{ik}\delta_{jl} + \delta_{il}\delta_{jk}) - \frac{\bar{\lambda}}{2\bar{\mu}(3\bar{\lambda} + 2\bar{\mu})}\delta_{ij}\delta_{kl}. \tag{1.140}$$

Following the fact obtained above that $(3\bar{\lambda} + 2\bar{\mu}), \bar{\mu} > 0$ it is clear from (1.139) that the strain can be uniquely determined.

Finally, if we substitute the isotropic version of Hooke's law (1.137) into the conservation of momentum equation (1.134) we obtain the (unforced) *Navier-Lamé* equations which governs (isotropic) linear elasticity, namely

$$(\bar{\lambda} + 2\bar{\mu})\bar{\nabla}\left(\bar{\nabla} \cdot \bar{\mathbf{u}}\right) - \bar{\mu}\bar{\nabla} \times \bar{\nabla} \times \bar{\mathbf{u}} = \bar{\rho}_0 \frac{\partial^2 \bar{\mathbf{u}}}{\partial \bar{t}^2}, \tag{1.141}$$

which will be analysed shortly. We note that although often unmentioned, it is implicitly assumed in this theory that heat conduction within the solids in consideration

[27] And trivially $3\bar{K} = 3\bar{\lambda} + 2\bar{\mu} > 0$, which is used later.

| Independent pair | $\bar{E}, \nu$ | $\bar{E}, \bar{\mu}$ | $\bar{\lambda}, \bar{\mu}$ |
|---|---|---|---|
| $\bar{\lambda}$ | $\frac{\bar{E}\nu}{(1+\nu)(1-2\nu)}$ | $\frac{\bar{\mu}(\bar{E}-2\bar{\mu})}{3\bar{\mu}-\bar{E}}$ | $\bar{\lambda}$ |
| $\bar{\mu}$ | $\frac{\bar{E}}{2(1+\nu)}$ | $\bar{\mu}$ | $\bar{\mu}$ |
| $\bar{E}$ | $\bar{E}$ | $\bar{E}$ | $\frac{\bar{\mu}(3\bar{\lambda}+2\bar{\mu})}{\bar{\lambda}+\bar{\mu}}$ |
| $\bar{K}$ | $\frac{\bar{E}}{3(1-2\nu)}$ | $\frac{\bar{\mu}\bar{E}}{3(3\bar{\mu}-\bar{E})}$ | $\bar{\lambda}+\frac{2}{3}\bar{\mu}$ |
| $\nu$ | $\nu$ | $\frac{\bar{E}-2\bar{\mu}}{2\bar{\mu}}$ | $\frac{\bar{\lambda}}{2(\bar{\lambda}+\bar{\mu})}$ |

Table 1.1: Relationships among isotropic elastic coefficients for commonly used independent pairs, following Achenbach [2012].

occurs slowly, so that the motion can be treated as adiabatic (as for ideal fluids). As we have seen, for a linear theory of homogeneous media this in turn implies that the entropy equation (1.10) satisfies $\bar{h} = \bar{h}_0$, i.e. it remains constant and as a result the thermodynamics need not be considered since the equation of energy reduces to $\bar{\nabla}^2\theta = 0$, which is entirely uncoupled (i.e. independent) of the solid's motion [Nowacki, 2013]. As a consequence of this, the material constants arising from the above discussion are measured in an adiabatic state. This distinction is often minimal and can be ignored for solid media, but it can be paramount when employing generalised elastic theories for e.g. fluid media which will be done in this thesis, as will be explained in detail in Chapter 3. The particular relations will become clear once *thermo-elastic* effects are incorporated in Section 1.4.2.

### Non-dimensionalisation

Again choosing a length-scale $\bar{\mathcal{L}}$ and a characteristic (wave) speed $\bar{c}_\square$ (length per unit time), we non-dimensionalise the relevant quantities appearing in our equations via

$$(\mathbf{u}, \mathbf{x}) = \frac{(\bar{\mathbf{u}}, \bar{\mathbf{x}})}{\bar{\mathcal{L}}}, \qquad t = \frac{\bar{c}_\square}{\bar{\mathcal{L}}}\bar{t}, \quad (\boldsymbol{D}, \boldsymbol{C}, \boldsymbol{\sigma}, \lambda, \mu, E, K) = \frac{(\bar{\boldsymbol{D}}, \bar{\boldsymbol{C}}, \bar{\boldsymbol{\sigma}}, \bar{\lambda}, \bar{\mu}, \bar{E}, \bar{K})}{\bar{\rho}_0 \bar{c}_\square^2}, \quad (1.142)$$

which implies that $\nabla = \bar{\mathcal{L}}\bar{\nabla}$ noting that the bars have been dropped in non-dimensional quantities.

### Body waves in isotropic elastic solids

We next show that the Navier-Lamé equations (1.141) can be reduced to a set of two separate wave equations giving rise to compressional and shear waves. We introduce

the *Helmholtz potentials* $\phi, \boldsymbol{\Phi}$ such that $(\phi, \boldsymbol{\Phi}) = (\bar{\phi}, \bar{\boldsymbol{\Phi}})/\bar{\mathcal{L}}^2$ with

$$\mathbf{u} = \nabla\phi + \nabla \times \boldsymbol{\Phi}, \qquad \nabla \cdot \boldsymbol{\Phi} = 0 \tag{1.143}$$

where the choice for the second condition is commonly used [Achenbach, 2012], and the need for an extra condition is to ensure we obtain unique displacements (since e.g. in 3D $\phi, \boldsymbol{\Phi}$ are four components, for the three components of the displacement vector $\mathbf{u}$). Direct substitution of (1.143) into (1.141) then gives

$$\nabla\left\{(\lambda + 2\mu)\nabla^2\phi - \frac{\partial^2\phi}{\partial t^2}\right\} + \nabla \times \left\{\mu\nabla^2\boldsymbol{\Phi} - \frac{\partial^2\boldsymbol{\Phi}}{\partial t^2}\right\} = \mathbf{0}, \tag{1.144}$$

where we have used the identity (1.59) and the fact that $\nabla \cdot \nabla \times \mathbf{u} = \mathbf{0}$. It is clear that if we independently satisfy

$$\left(\frac{\bar{\lambda} + 2\bar{\mu}}{\bar{\rho}_0\bar{c}_\square^2}\right)\nabla^2\phi = \frac{\partial^2\phi}{\partial t^2}, \tag{1.145a}$$

$$\left(\frac{\bar{\mu}}{\bar{\rho}_0\bar{c}_\square^2}\right)\nabla^2\boldsymbol{\Phi} = \frac{\partial^2\boldsymbol{\Phi}}{\partial t^2}, \tag{1.145b}$$

the governing equation (1.144) is also automatically satisfied. In order for the dimensions to agree, it is clear that the quantities in brackets must be a ratio of squares of speeds, so we define the non-dimensional wave-speeds as $(c_\mathrm{L}, c_\mathrm{S}) = (\bar{c}_\mathrm{L}, \bar{c}_\mathrm{S})/\bar{c}_\square$ where

$$\bar{c}_\mathrm{L} = \sqrt{\frac{\bar{\lambda} + 2\bar{\mu}}{\bar{\rho}_0}}, \tag{1.146a}$$

$$\bar{c}_\mathrm{S} = \sqrt{\frac{\bar{\mu}}{\bar{\rho}_0}}, \tag{1.146b}$$

where the subscripts 'L, S' are for *longitudinal* and *shear* respectively. If we assume time harmonicity of the dynamic fields with $\mathrm{e}^{-\mathrm{i}\omega t}$ ($\omega = \bar{\mathcal{L}}\bar{\omega}/\bar{c}_\square$) as we have been doing throughout

$$\{\mathbf{u}, \phi, \boldsymbol{\Phi}, \boldsymbol{\sigma}, \boldsymbol{\varepsilon}\} = \mathrm{Re}\{\{\hat{\mathbf{u}}, \hat{\phi}, \hat{\boldsymbol{\Phi}}, \hat{\boldsymbol{\sigma}}, \hat{\boldsymbol{\varepsilon}}\}(\mathbf{x}, \omega)\mathrm{e}^{-\mathrm{i}\omega t}\}, \tag{1.147}$$

it is clear that the wave equations (1.145) reduce to two Helmholtz equations

$$\left(\nabla^2 + k_\mathrm{L}^2\right)\hat{\phi} = 0 \qquad \left(\nabla^2 + k_\mathrm{S}^2\right)\hat{\boldsymbol{\Phi}} = \mathbf{0} \tag{1.148}$$

where the non-dimensional longitudinal and shear wavenumbers satisfy $(k_\mathrm{L}, k_\mathrm{S}) = \bar{\mathcal{L}}(\bar{k}_\mathrm{L}, \bar{k}_\mathrm{S})$ where

$$\bar{k}_\mathrm{L} = \sqrt{\frac{\bar{\rho}_0\bar{\omega}^2}{\bar{\lambda} + 2\bar{\mu}}} = \frac{\bar{\omega}}{\bar{c}_\mathrm{L}}, \qquad \text{and} \qquad \bar{k}_\mathrm{S} = \sqrt{\frac{\bar{\rho}_0\bar{\omega}^2}{\bar{\mu}}} = \frac{\bar{\omega}}{\bar{c}_\mathrm{S}}. \tag{1.149}$$

By considering plane wave solutions to (1.148) using (1.143) it is easy to see that $\phi$ is associated to 'P' waves (as with $\hat{P}$ in ideal acoustics, and $\hat{\Theta}_1, \hat{\Theta}_2$ in TVA), whereas $\mathbf{\Phi}$ gives rise to 'S' waves (as with $\hat{\mathbf{\Omega}}$ in TVA, which has no analogue in ideal acoustics). Let us consider a hypothetical situation in which time harmonic, plane waves propagate in the $(x, y)$ plane of a linearly isotropic medium, with displacements being independent of the $z$ direction orthogonal to the plane ($\partial/\partial z = 0$). In this case (1.143) gives, noting (1.147) and writing $\hat{\mathbf{\Phi}} = (\hat{\Phi}_x, \hat{\Phi}_y, \hat{\Phi}_z)$

$$\hat{u}_x = \frac{\partial \hat{\phi}}{\partial x} + \frac{\partial \hat{\Phi}_z}{\partial y}, \qquad \hat{u}_y = \frac{\partial \hat{\phi}}{\partial y} - \frac{\partial \hat{\Phi}_z}{\partial x}, \tag{1.150a}$$

$$\hat{u}_z = -\frac{\partial \hat{\Phi}_x}{\partial y} + \frac{\partial \hat{\Phi}_y}{\partial x}, \qquad \frac{\partial \hat{\Phi}_x}{\partial x} + \frac{\partial \hat{\Phi}_y}{\partial y} = 0, \tag{1.150b}$$

where $\hat{\phi}, \hat{\mathbf{\Phi}}$ must satisfy (1.149). We now note from (1.150a) that the 'in-plane' displacements $\hat{u}_x, \hat{u}_y$ only depend upon $\hat{\phi}$ and $\hat{\Phi}_z$ and correspondingly so do the stresses $\hat{\sigma}_{11}, \hat{\sigma}_{22}, \hat{\sigma}_{12}$ (from (1.137)), whereas $\hat{u}_z$ and $\hat{\sigma}_{23}$ ($\hat{\sigma}_{13} = 0$) are dependent only on $\hat{\Phi}_x$, $\hat{\Phi}_y$ (1.150b). Moreover, since $\hat{\phi}, \hat{\Phi}_x, \hat{\Phi}_y, \hat{\Phi}_z$ are each governed by a scalar-valued wave equation (1.149) the motion in consideration can be interpreted as two separate (i.e. uncoupled) wave propagation problems. One constitutes *plane-strain* motion where the 'in-plane' displacements satisfy $\hat{u}_x, \hat{u}_y \neq 0$, but the 'out of plane' displacement vanishes $\hat{u}_z = \partial/\partial z = 0$ which concerns 'P, SV' waves, and an additional complementary situation in which $\hat{u}_z \neq 0$ but $\hat{u}_x = \hat{u}_y = \partial/\partial z = 0$ which focuses on 'SH' waves. More concretely, if we denote the displacement associated to either of these modes by an amplitude vector $\mathbf{A}_\square$ and propagation vector $k_\square \mathbf{n}$ such that

$$\mathbf{u} = \Re\{\mathbf{A}_\square \exp\left(\mathrm{i} k_\square \mathbf{n} \cdot \mathbf{x} - \omega t\right)\}, \qquad \mathbf{n} = n_1 \mathbf{e}_x + n_2 \mathbf{e}_y, \tag{1.151}$$

with $(\mathbf{e}_x, \mathbf{e}_y, \mathbf{e}_z)$ representing unit vectors along the Cartesian axes, the three different types of (body) waves satisfy

$$\text{P Waves} : \mathbf{A}_\square = \mathbf{A}_P, \quad k_\square = k_\mathrm{L}, \quad \mathbf{A}_P \cdot \mathbf{n} = \text{'non-zero constant'} \tag{1.152a}$$

$$\text{SV Waves} : \mathbf{A}_\square = \mathbf{A}_{SV}, \quad k_\square = k_\mathrm{S}, \quad \mathbf{A}_{SV} \cdot \mathbf{n} = 0, \quad \mathbf{A}_{SV} = \mathbf{e}_z \times \mathbf{n}, \tag{1.152b}$$

$$\text{SH Waves} : \mathbf{A}_\square = \mathbf{A}_{SH}, \quad k_\square = k_\mathrm{S}, \quad \mathbf{A}_{SH} \cdot \mathbf{n} = 0, \quad \mathbf{A}_{SH} = \mathbf{e}_z. \tag{1.152c}$$

When 'SH' waves are incident on a boundary, it can be shown that the reflected motion will also be in the form of 'SH' waves [Achenbach, 2012]. On the contrary

when either 'P' or 'SV' waves are incident on a boundary, the reflected field will in general be composed of both 'P' and 'SV' waves, leading to *mode conversion*. This is also the case for TVA fluids, recall that in Section 1.3 we observed that an incident 'P' (dominated) wave $\hat{\Theta}_2$ on a half-space in the $(x, y)$ plane gives rise to a reflected SV wave $\hat{\Omega}\mathbf{e}_z$ (as well as a reflected thermal dominated mode $\hat{\Theta}_1$).

In this thesis we will mainly restrict attention to 2D configurations, and hence it is the 'P-SV' problem that is considered or 'P-T-SV' if we include 'T' for thermal modes (as we saw in Section 1.3 for TVA fluids). In order to do so for solids however, we must first include these effects in our constitutive model, which we briefly discuss in Section 1.4.2 and analyse in more detail in Chapter 3.

As we will see throughout this thesis, under certain circumstances, combinations of these body waves can give rise to *surface* waves that propagate along the interface between two differing media which may be a fluid, a (different) solid or even a vacuum. The latter gives rise to *Rayleigh waves* and their appearance is discussed in Section 1.5.3. Fluid-solid interfaces give rise to *Scholte waves* which will be analysed in detail in Chapters 2, 4.

### Boundary Conditions

The classical associated types of BCs to be satisfied in the boundaries of elastic media are similar to those described for acoustic media in Section 1.2.1. Generally, assuming the boundary of the (finite) elastic region is given by $\partial D$ they can be summarized as

- Dirichlet BCs, where the displacement is prescribed, so that e.g. $\mathbf{u} = \mathbf{u}_0$ on $\partial D$, where $\mathbf{u}_0$ is given. In the special case of $\mathbf{u}_0 = \mathbf{0}$ the boundary is said to be *clamped*.

- Neumann BCs, where the traction vector $t_i = \sigma_{ij} n_j$ is prescribed on the boundary with unit normal $\mathbf{n}$, i.e. $\mathbf{t} = \mathbf{t_0}$ on $\partial D$ where $\mathbf{t_0}$ is known. Note from (1.137) that these conditions are in fact on the spatial derivatives of $\mathbf{u}$ (and hence Neumann). *Traction-free* BCs correspond to the particular case for which $\mathbf{t_0} = \mathbf{0}$.

Naturally, Robin BCs can also be formulated by e.g. considering an elastic bedding, but these are considerably more rare and won't be considered in this thesis. Finally,

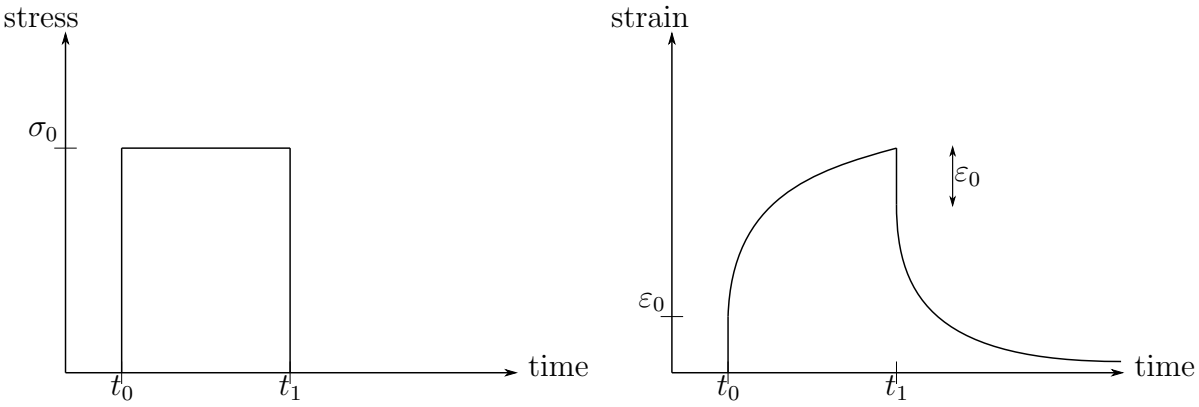


Figure 1.10: Schematic representation of the strain response to a *creep recovery test*. (Left) A sudden loading of the material occurs at $t_0$ and the stress remains constant $\sigma_0$ up until $t_1$. (Right) The resulting strain of the sample as a consequence of the constant stress loading. Of particular interest is the behaviour in the strain for $t > t_1$ which cannot be predicted with an elastic theory.

in the particular case that two elastic solids are in perfect contact, it must be ensured that continuity of displacement *and* traction are satisfied on the boundary.

### 1.4.2 Further physical dissipative effects

Having introduced the equations governing (isotropic) linearly elastic solids and its associated types of wave motion, here we simply suggest with fewer details how these equations are generalised with the consideration of further physical effects. Detailed descriptions of the theory of viscoelasticity are given by Hunter [1976], Christensen [2012], Bland [2016] whereas for thermoelasticity the author found the treatments in Boley and Weiner [2012] and Nowacki [2013] very useful, although the original work dates back to the classical paper from Biot [1956].

#### Viscoelasticity (VE)

Viscoelastic effects are often introduced in terms of one dimensional mechanical models that can be interpreted as different arrangements of springs and dashpots, [Borcherdt, 2009, Bland, 2016]. This gives a clear intuitive understanding of the phenomena of *creep strain* and *stress relaxation* which are the fundamental properties encountered in viscoelastic media. Here we will simply give a brief physical explanation of these terms before providing the general equation that will be used in order to capture these effects in three dimensions.

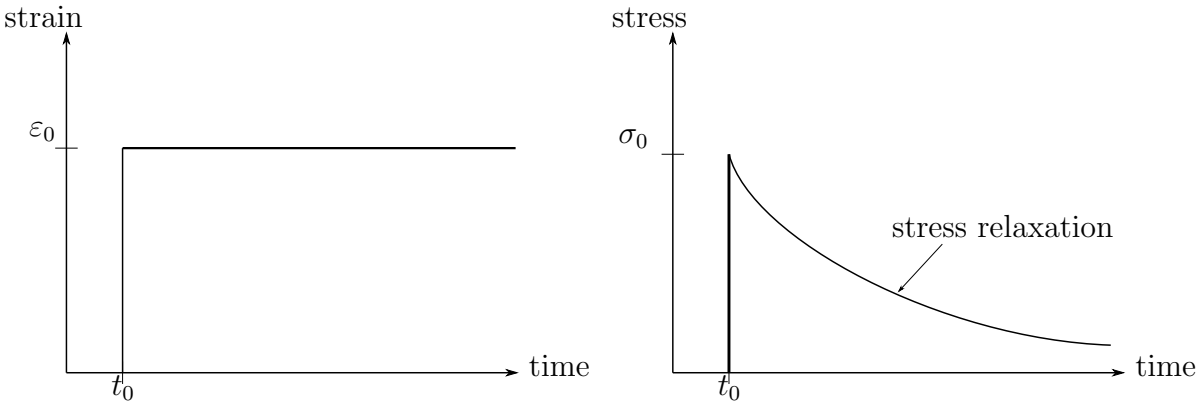


Figure 1.11: Schematic representation of the stress response to a *stress relaxation test*. (Left) A particular material is strained at $t_0$ and is held at that constant value $\varepsilon_0$ over time. (Right) Resulting stress to the constant applied strain. It is observed that the stress required to keep the material at constant strain decreases over time from its initial value $\sigma_0$, from which the term *stress relaxation* originates.

Viscoelastic materials are often characterised through the nature of their response to a 'suddenly applied' uniform distribution of stress or strain in a particular mode of deformation. The former are commonly known as *creep recovery tests* which are depicted in Figure 1.10, noting that depending on the material the 'creeping' behaviour exhibited for $t > t_1$ in the figure tends to a number which may or may not be zero. On the other hand, in *stress relaxation tests* one observes the material's behaviour in stress to a constant applied strain, as illustrated in Figure 1.11. Mathematically, this can be captured in terms of hereditary integrals which span over the past *history* of the deformation thanks to *Boltzmann's superposition principle* [Boltzmann, 1874] which ultimately results in (1.137) being replaced by [Christensen, 2012]

$$\bar{\sigma}_{ij}(\bar{t}) = \int_{-\infty}^{\bar{t}} 2\bar{\mu}(\bar{t}-\bar{\mathfrak{T}})\frac{\partial e_{ij}(\bar{\mathfrak{T}})}{\partial \bar{\mathfrak{T}}}\,\mathrm{d}\bar{\mathfrak{T}} + \left(\int_{-\infty}^{\bar{t}} \bar{K}(\bar{t}-\bar{\mathfrak{T}})\frac{\partial \varepsilon_{kk}(\bar{\mathfrak{T}})}{\partial \bar{\mathfrak{T}}}\,\mathrm{d}\bar{\mathfrak{T}}\right)\delta_{ij}, \tag{1.153}$$

where we have introduced $e_{ij}$ in order to denote the non-diagonal terms of the strain tensor i.e. $e_{ij} = \varepsilon_{ij} - \varepsilon_{kk}\delta_{ij}/3$. Equation (1.153) characterises linear, isothermal, homogeneous, isotropic, viscoelastic solids and we note that the key difference with (1.137) is that the shear and bulk modulus are now in general functions of time and are referred to as *relaxation functions* following the behaviour from Figure 1.11. Indeed, consider a hypothetical (shear like) deformation in which $e_{12}$ is the only non-zero component of strain which follows a *Heaviside* step function $e_{12} = H(\bar{t})$. Direct substitution into (1.153) then yields (by the properties of the delta function) that $\bar{\sigma}_{12} = 2\bar{\mu}(\bar{t})$, so that the associated stress component to this mode of deformation is precisely represented

by $2\bar{\mu}(\bar{t})$ (from which the name 'relaxation function' arises). Naturally, as for linear elastic media, it is also possible to represent strain in terms of stress giving rise to *creep functions* which can be easily related to relaxation functions via *Laplace transforms* [Hunter, 1976]. A formal description on how to obtain (1.153) from first principles including the functional analytic assumptions is given in Christensen [2012].

Note that this theory is attributed to *isothermal* conditions which assume that all deformations satisfy $\bar{T} = \bar{T}_0$ so that the energy balance equation is satisfied, although technically the second law of thermodynamics gives further restrictions on the type of time histories of the moduli [Christensen, 2012]. Assuming the moduli are physical (such as those commonly found in experiments) this theory reduces to the single (vectorial) equation of conservation of momentum which is obtained by simply substituting (1.153) into (1.134). Despite the natural analytic complexities arising from the time dependence in (1.153), under time harmonic conditions it is simple to show that a decomposition equivalent to that of linear elasticity (which led to (1.148), (1.149)) is possible, with the difference being that the elastic moduli become functions of frequency i.e. $\bar{\mu}(\bar{\omega})$, $\bar{\lambda}(\bar{\omega})$ as we will shown in Chapters 3, 4. In fact, this observation leads to the *elastic-viscoelastic correspondence principle* for steady state conditions, which allows the consideration of a viscoelastic problem as an elastic problem with complex valued (frequency dependent) material parameters provided certain conditions are satisfied (see Bland [2016] for a detailed discussion on these conditions).

In practice, the frequency dependence of the moduli is often obtained by fitting experimental results to a particular model (such as the Kelvin-Voigt or Maxwell [Borcherdt, 2009]) with certain fixed parameters, both for homogeneous materials (e.g. Favretto-Anrès [1996] who study synthetic resins) and more complex media such as metamaterials (e.g. Fernández-Marín et al. [2019] for an aerogel-based metasurface). Although this simple characterisation is often sufficient for many works and certainly for 'proof of concept' style studies, the accuracy of some commonly used models is restricted to certain frequency ranges outside of which important effects such as stress relaxation or creep compliance become poorly approximated. In this thesis we shall concentrate on accommodating both the effects of creep compliance and stress relaxation, with emphasis on the latter which is generally predominant in the low frequency range [Liao and Wells, 2006].

In Chapter 3 we shall discuss how to include these effects with more detail and in Chapter 4 we will observe their possible impact on some canonical problems involving slits and plates.

### Thermoelasticity (TE)

Unlike the previously considered theory for viscoelasticity whose derivation is reliant on thermodynamically isothermal conditions, here the coupling between the absolute temperature $\bar{T}$ and the solid's deformation $\bar{\boldsymbol{\sigma}}$ is taken into account.

Together with our geometric linearity assumptions based on the small magnitudes of deformation used in order to derive the linearly elastic theory, here it is assumed that the temperature difference $\bar{T}-\bar{T}_0$ accompanying the deformation is also small i.e. $\theta=(\bar{T}-\bar{T}_0)/\bar{T}_0 \ll 1$ (and of the same order as strain $\varepsilon_{ij}$). Furthermore, the material parameters both elastic (such as the moduli in Table 1.1) and thermal are assumed to be independent of temperature and strain (this is a requirement for a linear theory [Christensen and Naghdi, 1967]). The "point of departure" in comparison with the adiabatic theory from Section 1.4.1 lies in the conservation of energy equation and entropy production i.e. the first and second law of thermodynamics (equivalent to what we saw in order to go from ideal acoustics to TVA in Sections 1.2.1, 1.2.2). By expanding out the divergence term involving stress in the general energy equation (1.8), writing it in terms of displacement and using the symmetries from (1.133) following our linearity assumptions, the energy equation reduces to [Nowacki, 2013]

$$\bar{\rho}_0\frac{\partial\bar{\mathcal{E}}}{\partial\bar{t}}=\bar{\sigma}_{ij}\frac{\partial\varepsilon_{ij}}{\partial\bar{t}}-\frac{\partial\bar{q}_i}{\partial\bar{x}_i}, \tag{1.154}$$

whereas the second law of thermodynamics in this context is often written in terms of the *Clausius-Duhem* inequality which under our assumptions may be written as[28] [Christensen, 2012]

$$\bar{\rho}_0\bar{T}\frac{\partial\bar{h}}{\partial\bar{t}}+\frac{\partial\bar{q}_i}{\partial\bar{x}_i}\geq\left(\bar{q}_i\frac{\partial\bar{T}}{\partial\bar{x}_i}\right)/\bar{T}. \tag{1.155}$$

Following Boley and Weiner [2012], at this stage it is useful to introduce the *Helmholtz*

[28] Note that in the case of TVA fluids, the equations of state are in agreement with the second law [Pierce et al., 1981], so that this inequality need not be considered.

*free energy*[29] (per unit mass) $\bar{\Psi}$

$$\bar{\Psi}(\varepsilon_{ij}, \bar{T}) = \bar{\mathcal{E}} - \bar{T}\bar{h}, \tag{1.156}$$

so that on combining (1.154), (1.155) together with (1.156) we may finally arrive at (in symbolic form)

$$\left(\bar{\boldsymbol{\sigma}} - \bar{\rho}_0 \frac{\partial \bar{\Psi}}{\partial \boldsymbol{\varepsilon}}\right) \frac{\partial \boldsymbol{\varepsilon}}{\partial \bar{t}} - \left(\frac{\partial \bar{\Psi}}{\partial \bar{T}} + \bar{h}\right) \bar{\rho}_0 \frac{\partial \bar{T}}{\partial \bar{t}} - \frac{\bar{\mathbf{q}} \cdot \bar{\nabla} \bar{T}}{\bar{T}} \geq 0, \tag{1.157}$$

which must be satisfied for arbitrary deformations (within the implicit constraints of our linearised theory). Considerations of specific types of deformations as described in detail in e.g. Coleman and Noll [1963] give that for thermoelasticity we must in fact have

$$\bar{\boldsymbol{\sigma}} = \bar{\rho}_0 \frac{\partial \bar{\Psi}}{\partial \boldsymbol{\varepsilon}}, \qquad \text{and} \qquad \bar{h} = -\frac{\partial \bar{\Psi}}{\partial \bar{T}}, \tag{1.158}$$

which together with Fourier's law of heat conduction $\bar{q}_i = -\bar{\mathcal{K}} \partial \bar{T} / \partial \bar{x}_i$ (as for TVA) ensures that (1.157) is always satisfied (since $\bar{\mathcal{K}} > 0$). It is therefore clear from (1.158) that the remaining task is to obtain the functional form of $\bar{\Psi}$ which can be done by expanding it to second order around a constant state of no strain and constant temperature i.e. $\bar{\Psi}(\varepsilon_{ij} = 0, \bar{T} = \bar{T}_0)$. We do not do this explicitly here to avoid repetition since it is discussed in detail in Section 3.2, but the key thing to note is that this expansion is about an *isothermal* state. With this the Cauchy stress and entropy (1.158) become

$$\bar{\sigma}_{ij} = \left(\varepsilon_{kk} - \bar{\alpha}(\bar{T} - \bar{T}_0)\right) \bar{K} \delta_{ij} + 2\bar{\mu} \left(\varepsilon_{ij} - \frac{1}{3}\delta_{ij}\varepsilon_{kk}\right), \tag{1.159a}$$

$$\bar{h} = \bar{h}_0 + \frac{\bar{c}_v}{\bar{T}_0}(\bar{T} - \bar{T}_0) + \frac{\bar{\alpha}\bar{K}}{\bar{\rho}_0}\varepsilon_{kk}, \tag{1.159b}$$

where we note that the extra parameters in (1.159) namely $\bar{\alpha}, \bar{c}_v$ previously defined for fluids (1.19), (1.43) are defined under the current context equivalently as

$$\bar{c}_v = \bar{T}_0 \left(\frac{\partial \bar{h}}{\partial \bar{T}}\right)_{\boldsymbol{\varepsilon}=\mathbf{0}}, \quad \bar{\alpha} = \left(\frac{\partial \varepsilon_{kk}}{\partial \bar{T}}\right)_{\boldsymbol{\varepsilon}=\mathbf{0}}. \tag{1.160}$$

The energy equation (1.154) then reduces to the forced diffusion equation

$$\bar{\mathcal{K}} \bar{\nabla}^2 \theta - \bar{\rho}_0 \bar{c}_v \frac{\partial \theta}{\partial \bar{t}} = \bar{\alpha} \bar{K} \frac{\partial \varepsilon_{kk}}{\partial \bar{t}}, \tag{1.161}$$

[29] The Helmholtz energy is the Legendre transformation of the internal energy $\bar{\mathcal{E}}$, in which temperature replaces entropy as the independent variable. Note that equivalently it may be written in terms of stress or entropy as given explicitly in Lubarda [2004].

similarly to what we observed for TVA (1.54). Equation (1.161) together with the modified Navier-Lamé obtained when (1.159a) is substituted into the conservation of momentum equation (1.134) constitute the governing equations for linear isotropic (coupled) thermoelasticity. The decomposition will not be given here, but we will see later that media governed by these equations support three types of wave motion, two thermo-compressional fields and a shear wave which is independent of thermal effects and purely real valued [Deresiewicz, 1957].

We finally want to show that care must be taken when directly comparing material parameters from the current theory to those obtained earlier in (1.137). Given the derivation above, if we now assume the deformations are adiabatic, by definition we must have $\bar{h} = \bar{h}_0$, which from (1.159b) implies that

$$\bar{T} - \bar{T}_0 = -\frac{\bar{\alpha}\bar{K}\bar{T}_0}{\bar{\rho}_0\bar{c}_v}\varepsilon_{kk}, \tag{1.162}$$

and therefore the Cauchy stress tensor (1.159a) becomes (explicitly labelling the thermodynamic state of the elastic moduli)

$$\bar{\sigma}_{ij} = \left\{\bar{K}_{\text{Iso}}\left(1 + \frac{\bar{\alpha}^2\bar{K}_{\text{Iso}}\bar{T}_0}{\bar{\rho}_0\bar{c}_v}\right)\right\}\varepsilon_{kk}\delta_{ij} + 2\bar{\mu}_{\text{Iso}}\left(\varepsilon_{ij} - \frac{1}{3}\delta_{ij}\varepsilon_{kk}\right). \tag{1.163}$$

Direct comparison then with its adiabatic counterpart (1.137) (labelling its material constants with a subscript 'Adiab' for distinction) gives that

$$\bar{K}_{\text{Adiab}} = \bar{K}_{\text{Iso}}\left(1 + \frac{\bar{\alpha}^2\bar{K}_{\text{Iso}}\bar{T}_0}{\bar{\rho}_0\bar{c}_v}\right), \quad \text{and} \quad \bar{\mu}_{\text{Adiab}} = \bar{\mu}_{\text{Iso}}, \tag{1.164}$$

and it is straightforward to show [Lubarda, 2004] that the quantity in brackets in (1.164) is equal to the ratio of specific heats $\gamma$ as we saw for fluids, which can deviate significantly from unity, implying that $\bar{K}_{\text{Adiab}}$ and $\bar{K}_{\text{Iso}}$ may have very different values.

### 1.4.3 Towards Thermo-Visco-Elasticity (TVE)

Given the two extensions to the linear elasticity theory discussed above including thermal and viscoelastic dissipative effects in each case, one may wonder about the possibility to simultaneously include these two mechanisms of loss, giving rise to a theory for linear thermo-visco-elasticity. This is discussed from first principles in Chapter 3. Furthermore, below we explain how interest in Thermo-Visco-Elasticity can arise by considering the interface of a TVA fluid with a general solid.

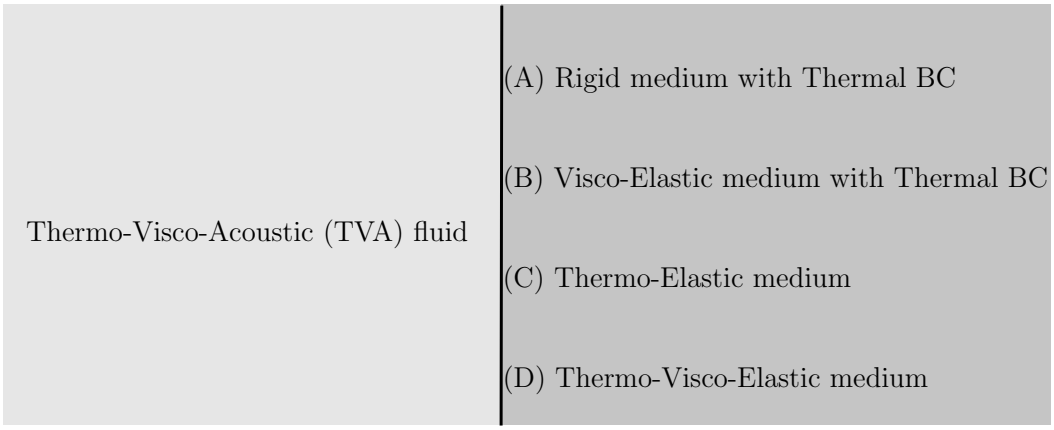


Figure 1.12: Hypothetical interface between a TVA fluid medium as described in Section 1.2.2 (left) and a neighbouring solid medium (right). The letters (A)-(D) represent different possible assumptions on the medium whose 'pros and cons' and described in the text.

As explained in detail in Section 1.2.2, the derivation of the theory of thermo-visco-acoustics (TVA) is based on (Newtonian) fluid media. A direct consequence of this is that it will fail to characterize the wave propagation properties of solid materials since the theory lacks fundamental elastic parameters such as the shear modulus which are not generally present in (Newtonian) fluids. As we have seen, when a TVA fluid is in direct contact with another medium, there will be an energy transfer due to both mechanical and thermal means (1.87), (1.88b). If this neighbouring medium is a solid, BCs can often be applied that capture most of the important effects and highly simplify the problem. This was done for example in Section 1.3.2, where we assumed the solid substrate was 'rigid' and the isothermal BC was applicable (based on the argument just below (1.84)). Although this is a (very) good approximation for e.g. standard air-metal interfaces, the same may not apply to heavier fluids (or lighter solids). It is therefore useful to be able to have the analytical means to avoid these kinds of simplifications. As we show below, this line of thought also gives rise to the consideration of Thermo-Visco-Elasticity (TVE).

We next give some of the key advantages and disadvantages of different modelling options to describe the behaviour of a solid neighbouring a TVA fluid, see Figure 1.12.

(A) Rigid medium with Thermal BC: Although convenient and very accurate for many gases like air, ignoring the motion in the solid medium (i.e. the fluid-structure interaction FSI) is too strong of an assumption for the type of media

we want to consider in this thesis. An example for which this fails under standard conditions is when the TVA fluid is water and the solid is e.g. steel, as we show[30] explicitly in Section 2.2.

(B) Visco-Elastic medium with Thermal BC: In this case FSI effects are taken into account and therefore this will allow to accurately model interfaces with much smaller contrast/impedance. Furthermore, the inclusion of visco-elastic effects implies that the dissipation of the medium due to viscosity is taken into account. Nevertheless, as we have seen the motion in (visco) elastic media is uncoupled from temperature, and therefore thermal dissipation within the solid medium cannot be accounted for.

(C) Thermo-Elastic medium: This gives a much more accurate description of the energy transfer and associated dissipation that can cover a very large range of interfaces. Nevertheless, unlike in (B) losses due to viscosity are not taken into account.

(D) Thermo-Visco-Elastic medium: With such media we would be able to resolve all of the individual nuances of settings (A)-(C). Nevertheless, the issue we encounter at this stage is that, to our surprise, these models have not been as developed as the previously mentioned and general governing equations are not easily found in the literature. We will therefore devote Chapter 3 to their study.

Furthermore, as we will show in Chapter 3, with a fully developed TVE theory for continua, the TVA theory for fluids developed in Section 1.2.2 arises naturally as a special case, which often allows us to avoid specifying the particular type of medium in consideration prior to obtaining the solution to a given problem. For example, the set-up from Figure 1.12 can be replaced by the more general setting of Figure 1.13, which avoids any of the approximations described in (A)-(C) and also generalises (D) to consider e.g. solid-fluid or solid-solid interfaces.

[30] Nevertheless, we will also show that under standard conditions thermal damping is usually negligible in underwater acoustics, which highly simplifies the problem.

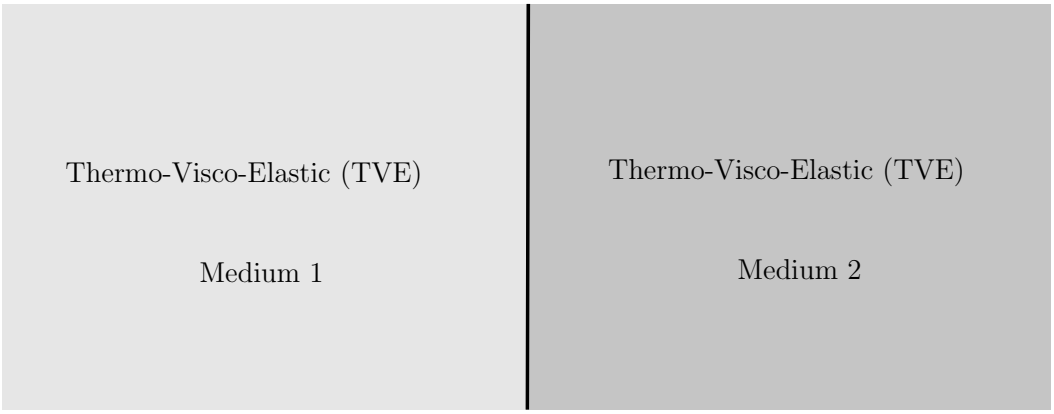


Figure 1.13: Possible generalisation of the set-up in Figure 1.12 with a fully developed TVE theory. At the interface between the two TVE media the standard continuity conditions (1.79)-(1.82) must be satisfied, which avoid any of the approximations introduced with (A)-(C). Furthermore, as we will see, there is no need to define medium 1 as a TVA fluid, instead, this can be specified once the general solution is obtained.

## 1.5 Analysing dispersion relations

It is a common theme in this thesis (particularly in Chapters 2, 4) to analyse the behaviour of *dispersion equations* which are generally non-linear, complex valued equations relating wavenumber with frequency, and encapsulate all the properties of wave–type solutions to a particular system. Due to the complexity of these expressions in some instances, it is convenient to have a visualization tool in order to understand the main features of the functions that lead to these equations such as the zeros that represent the required roots, and the different types of singularities which are usually in the form of poles and branch cuts.

### 1.5.1 Complex function visualisation

These functions are in general of the form $f : \mathbb{C} \to \mathbb{C}$ so that we would require a 4D visualisation, (or 2 3D visualisation for the real and imaginary parts). Instead, following Wegert [2012] we choose a visualisation which assigns a particular (unique) HSV hue to a corresponding complex valued argument, and is implemented in both MATLAB and Mathematica. With this, we are effectively trying to get as much information as we can by simply looking at the phase $\arg(f(z))$, which is often enough to identify the required behaviour. An illustration is given in Figure 1.14, where we show a first order zero ($z = 0$) given by the identity map (left) and a single branch cut from a square

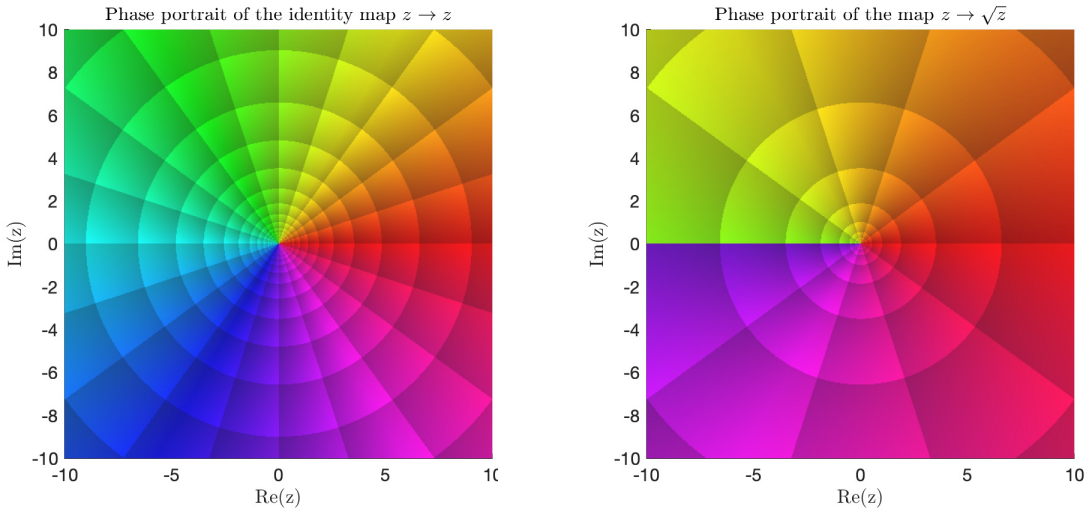


Figure 1.14: Examples of phase portraits for the identity map in the complex plane $z \to z$ (left), and the complex square root function $z \to \sqrt{z}$ (right). In both plots we are assuming the principal branch so that $-\pi \leq \arg(z) < \pi$ and $-\frac{\pi}{2} \leq \arg(\sqrt{z}), < \frac{\pi}{2}$. The various colours indicate different values of the arguments: e.g. red corresponds to a zero argument (real value), cyan corresponds to an argument of $\pm\pi$ and so on.

root function (right). Note that the particular branch definition (Riemann sheet) is important for consistency between the colours, which has physical consequences.

### 1.5.2 Obtaining the roots

Throughout this thesis, the roots of the dispersion equations are generally calculated using the MATLAB [version 9.8.0.556344 (R2017a) and onwards] command *fsolve*, which finds the local zero of a function close to a given starting point specified by the user. Generally there is a wide range of admissible values for the starting point which makes it easy to assign for the user given some basic prior knowledge of the spectrum of the equation in consideration, which is provided by the phase plots (as in Figure 1.14). Note that although this simple method has proved to be successful in all situations encountered in this work, particular care must be taken when two or more roots are close to one another and in the presence of a root near a branch cut. It must also be ensured that the general behaviour of the function away from the root is scaled such that it is significantly greater from the specified *tolerance*, whose default value is given by $10^{-6}$ (further details can be found by simply typing "help fsolve" on the MATLAB command window).

We next focus our attention to a particular example consisting of the physically

relevant *Rayleigh* dispersion equation.

### 1.5.3 Example: The elastic Rayleigh Dispersion Equation

In order to arrive at the Rayleigh dispersion equation (DE) we consider a two-dimensional homogeneous semi-infinite linearly elastic medium occupying the half-space $y \leq 0$, where the boundary at $y = 0$ with unit normal $\mathbf{e}_y$ is subject to a traction-free condition. We assume the motion to be invariant in the $z$ direction, so that we have a plain-strain problem where all the wave motion occurs in the $(x, y)$ plane and correspondingly $u_z, \partial/\partial z = 0$. We will further assume time-harmonicity in the form (1.147) so that the governing equations reduce to solving (1.148) which are both scalar valued since due to our assumptions $\hat{\mathbf{\Phi}} = \hat{\Phi}_z \mathbf{e}_z$, and the associated (non-zero) displacements are given by (1.150a). We therefore seek for travelling plane wave solutions of the form

$$\hat{\phi} = P \exp\{\gamma_{\mathrm{L}} y + \mathrm{i}kx\}, \qquad \hat{\Phi}_z = S \exp\{\gamma_{\mathrm{S}} y + \mathrm{i}kx\}, \tag{1.165}$$

where

$$\gamma_{\mathrm{L}} = (k^2 - k_{\mathrm{L}}^2)^{1/2}, \quad \gamma_{\mathrm{S}} = (k^2 - k_{\mathrm{S}}^2)^{1/2}, \tag{1.166}$$

for some complex amplitudes $P, S$. In order to obtain a physical solution we must ensure that the solutions decay as we move away from the boundary ($y \to -\infty$), which given (1.165) implies that we should have $\mathrm{Re}\{\gamma_{\mathrm{L}}\}, \mathrm{Re}\{\gamma_{\mathrm{S}}\} \geq 0$ and this choice will depend on the branch definitions of the square root functions appearing in (1.166), which are further discussed below. Since the surface is free of tractions, on $y = 0$ we have that $\hat{t}_i = \hat{\sigma}_{i2} n_2 = 0$ which in turn implies that we must satisfy $\hat{\sigma}_{12} = \hat{\sigma}_{22} = 0$ on $y = 0$, which results in

$$\begin{pmatrix} 2ik\gamma_{\mathrm{L}}\mu & \left(2k^2 - {k_{\mathrm{S}}}^2\right)\mu \\ 2k^2\mu - k_{\mathrm{L}}^2(\lambda + 2\mu) & -2ik\gamma_{\mathrm{S}}\mu \end{pmatrix} \cdot \begin{pmatrix} P \\ S \end{pmatrix} = \begin{pmatrix} 0 \\ 0 \end{pmatrix}, \tag{1.167}$$

after using (1.137) recalling (1.133). Setting the determinant of the matrix to zero, the condition for nontrivial solution gives (upon rewriting the elastic constant in terms of wavenumbers using (1.149) and rearranging)

$$(2k^2 - k_{\mathrm{S}}^2)^2 - 4k^2\gamma_{\mathrm{L}}\gamma_{\mathrm{S}} = 0, \tag{1.168}$$

which is the well known Rayleigh DE. It is worth noting how our original problem consisting of two PDE's coupling through the BCs has now reduced to finding the

roots $k$ of a non-linear scalar valued equation, where we will use the simple root finding technique outlined above in Section 1.5.2. However, in order to examine the roots of (1.168) the branches $\gamma_{\mathrm{L}}$, $\gamma_{\mathrm{S}}$ must be defined carefully. In order to illustrate this, let us write the radicals (1.166) in the two following distinct forms

$$\gamma_{\mathrm{L}} = \mathrm{i}\sqrt{k_{\mathrm{L}}^2 - k^2}, \qquad \gamma_{\mathrm{S}} = \mathrm{i}\sqrt{k_{\mathrm{S}}^2 - k^2}, \tag{1.169a}$$

$$\gamma_{\mathrm{L}} = \sqrt{\mathrm{i}(k-k_{\mathrm{L}})}\sqrt{-\mathrm{i}(k+k_{\mathrm{L}})}, \qquad \gamma_{\mathrm{S}} = \sqrt{\mathrm{i}(k-k_{\mathrm{S}})}\sqrt{-\mathrm{i}(k+k_{\mathrm{S}})}, \tag{1.169b}$$

and consider the subsequent effects on (1.168). This is illustrated in Figure 1.15, where we note that MATLAB uses the standard principal branch for the individual square roots (as in the right of Figure 1.14). Due to the $k \to -k$ symmetry of the complex $k$ plane, it is sufficient to analyse the region corresponding to $\mathrm{Re}\{k\} \geq 0$. The branch points corresponding to $k = k_{\mathrm{L}}, k_{\mathrm{S}}$ ($k_{\mathrm{S}} > k_{\mathrm{L}}$) are denoted by the black crosses, from which the branch cuts (dotted lines) emanate. In particular, we observe that the region of the complex plane given by $k_{\mathrm{L}} \leq \mathrm{Re}\{k\} \leq k_{\mathrm{S}}$, and $\mathrm{Im}\{k\} \geq 0$ is completely different in the two cases. In terms of the zeros, we see in both cases the presence of a real valued root $k_{\mathrm{R}}$ say, slightly larger than $k_{\mathrm{S}}$ i.e. satisfying $k_{\mathrm{R}} > k_{\mathrm{S}}$ (denoted by a black circle). In Figure 1.15b) however, we also see the presence of a complex valued root closer to $k_{\mathrm{L}}$, which is not observed in Figure 1.15a) since the root lies in the region of the complex plane where the resulting equation differs as a result of our branch choice.

In order to further investigate this, it is useful to visualize the corresponding motion of the elastic body under these two different solutions, which we obtain numerically as explained above. Substituting (1.165) into (1.150a) then explicitly gives

$$\begin{pmatrix} \hat{u}_x \\ \hat{u}_y \end{pmatrix} = \begin{pmatrix} \mathrm{i}kP\mathrm{e}^{\gamma_{\mathrm{L}}y+\mathrm{i}kx} + \gamma_{\mathrm{S}}S\mathrm{e}^{\gamma_{\mathrm{S}}y+\mathrm{i}kx} \\ \gamma_{\mathrm{L}}P\mathrm{e}^{\gamma_{\mathrm{L}}y+\mathrm{i}kx} - \mathrm{i}kS\mathrm{e}^{\gamma_{\mathrm{S}}y+\mathrm{i}kx} \end{pmatrix}, \tag{1.170}$$

which are illustrated as heatmaps in Figure 1.16 (where we have let $P = S = 1$ in (1.170)). We see that the motion for the real valued root Figure 1.16 a) is confined to the boundary $y = 0$ and decays away in $y < 0$ as originally described by Rayleigh [Rayleigh, 1896], whereas for the root in Figure 1.16 b) the energy seems to flow from the boundary into the solid, with a decay along the $x$-direction but no decrease for $y \ll 0$. As a result, for the latter root we have $\mathrm{Re}\{\gamma_{\mathrm{S}}\} < 0$ and therefore does not meet the criterion of physical *causality*, despite it nevertheless being a mathematical solution

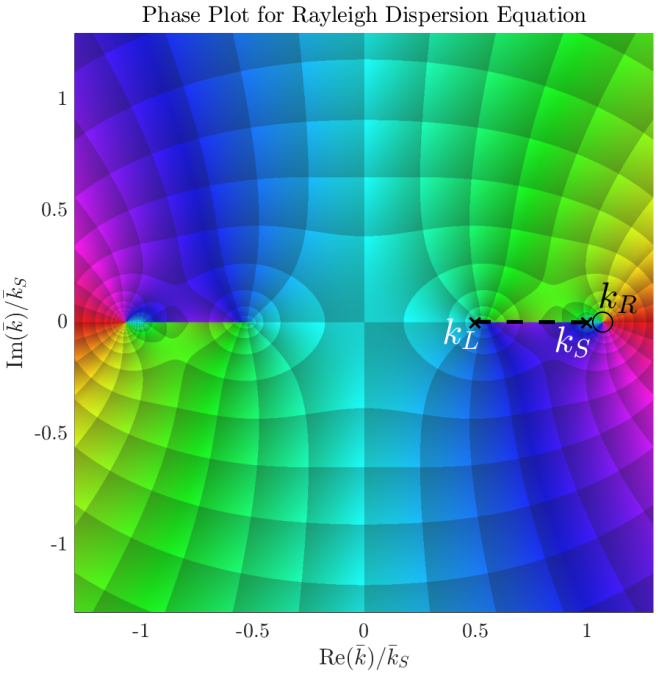


(a) Branches according to (1.169a).

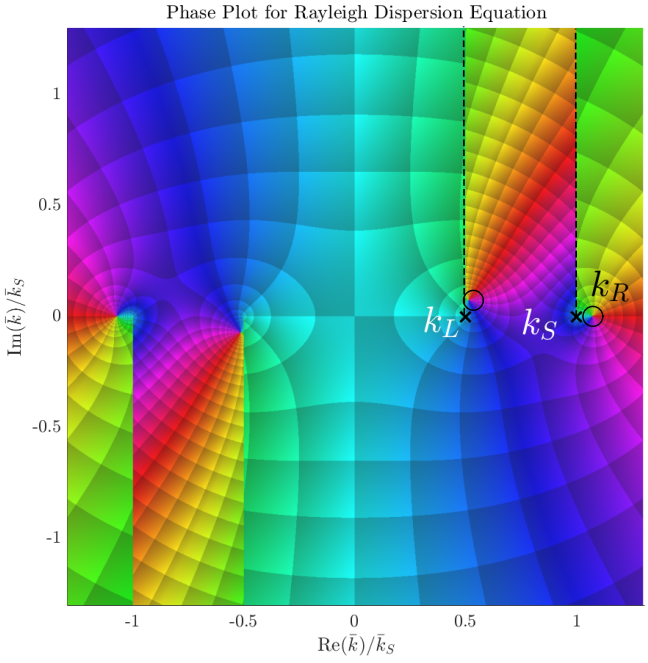


(b) Branches following (1.169b).

Figure 1.15: Phase portraits for the Rayleigh Dispersion Equation (1.168) according to the two different branch definitions, noting the $k \to -k$ symmetry. The superimposed crosses (**x**) correspond to the branch points, the dotted lines (–) represent the branch cuts, and the circles (o) denote the zeros. We observe that for (b) an extra zero arises which is not present in (a).

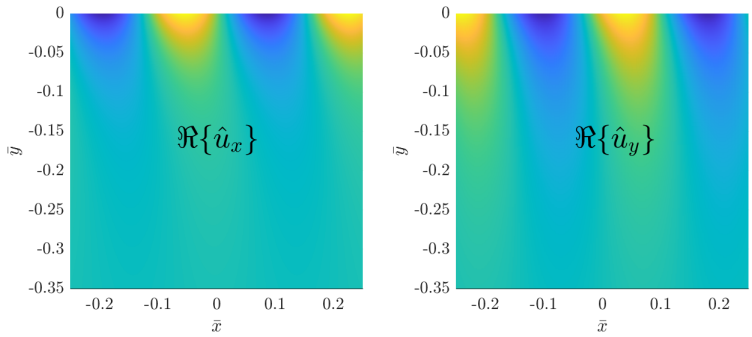


(a) Classical real valued Rayleigh root confined to $y = 0$ appearing in Figures 1.15 a),b).

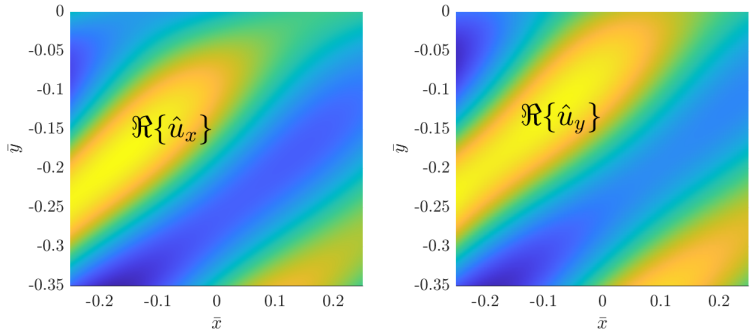


(b) Auxiliary complex valued solution to the Rayleigh DE observed in Figures 1.15 b) only.

Figure 1.16: Heatmaps for the displacement fields (1.170) for the Rayleigh DE, where $k$ is given by the two roots found on Figure (1.15) and the units are arbitrary.

to (1.168). These non-causal roots lying on the various Riemann sheets can play an important role in more complex scattering problems, where the solutions are often formulated as integrals in the complex plane and therefore extra care must be taken in the choice of branches, see e.g. Harris [2001] for a general description and Schröder and Scott Jr [2001], Harris and Achenbach [2002] for a particular case involving the set-up described here but forced by a line source on the surface. It is further shown in Schröder and Scott Jr [2001] that non-causal roots can be physically excited, although under much more specific scenarios.

With regards to the dispersion equations analysed in this thesis, we shall mostly be considering the influence of thermo-visco-elastic effects on well known physical solutions to specific set-ups such as half-spaces (like here), slits and plates. As a result, we must simply ensure that the choice of cuts obeys causality and is such that our root of interest does not jump the given Riemann sheet of choice.

# Chapter 2

# Thermo-viscous damping of acoustic waves in narrow channels: A comparison of effects in air and water

## 2.1 Introduction

This section consists of an application of the model presented in Section 1.2.2 to the study of damping properties in a fluid-filled narrow channel for a number of different physically relevant cases.

This work is included as a published copy of the paper Cotterill et al. [2018], in which Erik García Neefjes is a co-author, together with Phil Cotterill, David Nigro, Ian David Abrahams and William J. Parnell.

This paper provides quantitative answers to questions regarding visco-thermal propagation in Newtonian fluids, with a focus on the differences in attenuation properties between air and water. In the first part of this manuscript, we obtain dispersion relations arising in a thermo-viscous fluid filled rigid channel with different temperature boundary conditions. In the isothermal case, we recover some well known solutions

discussed by classical works such as Attenborough [1983], Stinson [1991] for an infinitely extending two-dimensional slit. Motivated by the study of the same problem for higher density fluids such as water, we incorporate the compliance of the walls by adding fluid structure interaction effects, and analyse the subsequent dispersion relations. We show how this extra coupling between the fluid and the elastic solid can result in a significant reduction in apparent phase speed as well as sound attenuation compared to the rigid case.

Abrahams, Parnell and Cotterill conceived of and designed the outline of the study. Cotterill and Nigro developed the initial theoretical aspects of the paper and initial parameter studies. García Neefjes further developed the theoretical approach specifically in order to better understand certain parameter regimes in the FSI problem (part V from the paper in Section 2.2) and carried out extended parameters studies as well as literature review. All authors contributed to the writing of the manuscript and responded equally to the several queries and comments from the reviewers.

Section 2.2 consists of a copy of Cotterill et al. [2018], and we give some posterior observations in the form of additional comments in Section 2.3. In most instances, it has been intended to keep a consistent notation between the previous chapter and the following manuscript. Nevertheless, there are some important changes which will be introduced accordingly. Some of these include the fluid velocity $\bar{\mathbf{v}} \equiv \bar{\mathbf{u}}$ , the coefficient of thermal expansion $\alpha \equiv \beta$, the ratio of specific heats $\gamma \equiv \mathcal{A}$, and the adiabatic speed of sound $\bar{c}_{\mathrm{A}} \equiv \bar{c}_0$.

## 2.2 Published article: Cotterill, Nigro, Abrahams, García-Neefjes & Parnell (2018)

# Thermo-viscous damping of acoustic waves in narrow channels: A comparison of effects in air and water

Philip A. Cotterill,[1] David Nigro,[2] I. David Abrahams,[3] Erik Garcia-Neefjes,[1] and William J. Parnell[1,a)]

[1]*School of Mathematics, University of Manchester, Oxford Road, Manchester, M13 9PL, United Kingdom*
[2]*Thales United Kingdom, 350 Longwater Avenue Green Park, Reading, RG2 6GF, United Kingdom*
[3]*Isaac Newton Institute, University of Cambridge, Clarkson Road, Cambridge, CB3 0EH, United Kingdom*

(Received 8 March 2018; revised 16 October 2018; accepted 21 October 2018; published online 21 December 2018)

Recent work in the acoustic metamaterial literature has focused on the design of metasurfaces that are capable of absorbing sound almost perfectly in narrow frequency ranges by coupling resonant effects to visco-thermal damping within their microstructure. Understanding acoustic attenuation mechanisms in narrow, viscous-fluid-filled channels is of fundamental importance in such applications. Motivated by recent work on acoustic propagation in narrow, air-filled channels, a theoretical framework is presented that demonstrates the controlling mechanisms of acoustic propagation in arbitrary Newtonian fluids, focusing on attenuation in air and water. For rigid-walled channels, whose widths are on the order of Stokes's boundary layer thickness, attenuation in air at 10 kHz can be over 200 dB $m^{-1}$; in water it is less than 37 dB $m^{-1}$. However, in water, fluid-structure-interaction effects can increase attenuation dramatically to over 77 dB $m^{-1}$ for a steel-walled channel, with a reduction in phase-speed approaching 70%. For rigid-walled channels, approximate analytical expressions for dispersion relations are presented that are in close agreement with exact solutions over a broad range of frequencies, revealing explicitly the relationship between complex phase-speed, frequency and channel width.



https://doi.org/10.1121/1.5078528

[BA] Pages: 3421–3436

## I. INTRODUCTION

Perforations in plates and structures have traditionally been used as a sound manipulation tool (Estrada *et al.*, 2008; Leppington and Levine, 1973; Putra and Thompson, 2010) with a significant breadth of work having been carried out over the years, involving analytical, computational, and experimental approaches. This research has been performed mainly in order to study the influence of microstructure on transmission and reflection of incident acoustic energy. In recent years the term *metasurface* has been coined by the metamaterials community, as a microstructured surface that is capable of almost complete absorption of sound, usually in a very narrowband manner with some of the microstructure proposed being quite *exotic* (Jiménez *et al.*, 2017; Jiménez *et al.*, 2016). A classical related problem, still of great importance and studied with significant interest, is the problem of acoustic propagation through a screen with periodic slits or channels (Christensen *et al.*, 2008). The canonical problem of transmission through a single channel, slit, or duct with rigid walls has been studied widely over the years (Allard and Atalla, 2009; Gomperts and Kihlman, 1967; Gompeters, 1964; Oldham and Zhao, 1993; Stinson and Champoux, 1992; Wilson and Soroka, 1965). It is well-known that resonances are set up within the channel, associated with relations between the wavelength and the length of the slit, save for what are known as *end-corrections*. Although the term has not classically been employed, more recently these resonances have been termed the *Fabry-Perot* resonances, terminology that appears to have crossed over from the electromagnetics community. Christensen *et al.* (2008) provided a model for the emergence of such resonances associated with an inviscid fluid. As pointed out by Ward *et al.* (2015), however, neglecting thermo-viscous effects is a significant assumption, particularly at small lengthscales and the latter authors showed that including attenuation *in-air* results in the phase speed along a narrow duct or channel being substantially reduced, even when the channel width is an order of magnitude greater than the boundary layer parameter $\bar{\delta}_\nu = \sqrt{\bar{\nu}/\bar{\omega}}$. Here $\bar{\nu}$ denotes kinematic viscosity and $\bar{\omega}$ is the radian frequency. In the present analysis, we show that Stokes's boundary layer thickness $\bar{\delta}_s = 2\pi\sqrt{2\bar{\nu}/\bar{\omega}} \approx 9\bar{\delta}_\nu$ is a better indicator than $\bar{\delta}_\nu$ of the extent to which the channel-wall boundary layers disturb the motion of the fluid; $\bar{\delta}_\nu$ underestimates, somewhat, the true extent of the boundary layer.

More generally then, over the years it has been observed that thermo-viscous boundary layer effects can have a significant impact upon the propagation of sound along narrow, rigid-walled channels giving substantial acoustic absorption within the audio frequency range in air. This phenomenon is used routinely in the acoustics industry as a means to *soften*

a)Electronic mail: william.parnell@manchester.ac.uk

boundaries and attenuate unwanted sound. Indeed, the propagation of acoustic waves along channels, ducts, tubes, or slits has been studied extensively over the years, with work dating back to the late nineteenth century. Helmholtz (1863) studied the impact of viscosity and estimated the absorption due to viscous effects. Kundt (1868) tested the theory experimentally and noticed that absorption was higher than expected, presumably due to thermal effects. Kirchhoff (1868) introduced the general theory of thermo-visco acoustics based on the Navier-Stokes equations and the Fourier-law of heat conduction for a perfect gas in a circular tube. He also gave approximate expressions in the case of a *wide* tube, i.e., when the radius is much larger than the viscous/thermal boundary layer thickness. Rayleigh (1896) gave approximate solutions for the *narrow* tube limit, i.e., when the radius is much smaller than the viscous/thermal boundary layer thickness and for the two-dimensional narrow channel case. Zwikker and Kosten (1949) introduced an approximate model for *wide* tubes that allowed for the derivation of a simpler solution in which viscous and thermal effects decoupled. Weston (1953), based on Kirchhoff's model, developed approximations for tubes of various diameters (*narrow*, *wide*, and *very wide*). Tijdeman (1975) rewrote Kirchhoff's model in terms of non-dimensionalized parameters, which allowed him to estimate the relative importance of each term and to show that the two main factors involved are the reduced viscous wavenumber and the reduced acoustic wavenumber. Bruneau *et al.* (1989) presented a general framework for a perfect gas in a bounded domain; a general formula for the dispersion relation with a no-slip boundary condition for the velocity and an isothermal boundary condition for the temperature is obtained and applied to simple geometries. Stinson (1991) analyzed Kirchhoff's original model and showed that Zwikker and Kosten's solution is recovered in the appropriate limit. He also extended Kirchhoff's theory to tubes of arbitrary cross-section. Beltman (1999a) provided an extensive literature review on the various models and approximations developed in thermo-viscous acoustics for a perfect gas. All those models were compared and their domain of validity was assessed. Solutions for canonical problems for each approximate/exact model were also provided. In subsequent work, this theory was then applied to a variety of engineering problems, such as the spherical resonator, the classic circular tube, and a miniaturized acoustic transducer (Beltman, 1999b). The last model is of particular interest as it involved a fluid-structure interaction problem.

It is clear that most, if not all, the literature above is focused on a perfect gas. The study of thermo-viscous acoustic propagation in *narrow water filled channels* or *slits* appears to be lacking although work has been done on the viscous liquid-filled elastic tube, usually having relatively thin walls. This area of research was initiated by Del Grosso (1971) who considered multimode propagation in an inviscid fluid-filled elastic tube. It has been followed up recently with work that includes viscous effects, carried out in a number of papers (Baik *et al.*, 2010; Dokumaci, 2014; Elvira-Segura, 2000; Liangh and Scarton, 2002). We note, however, that the frequency range considered in these works is generally high since the studies are mainly associated with non-destructive evaluation. The low frequency regime appears to be unexplored territory.

The purpose of the analysis presented in this paper is therefore two-fold, first to provide a general framework with which to study thermo-viscous acoustic attenuation in narrow channels that is applicable to an arbitrary Newtonian fluid. In particular, we wish to study the impact of thermo-viscous effects upon dense fluids of low compressibility, for which the *perfect gas* assumption is clearly inappropriate, and to determine the extent to which boundary layer influences are felt throughout the channel both in air and in water. Second, we wish to determine the conditions under which viscous and thermal boundary effects may influence acoustic propagation in water, when account is taken of the coupling between water and a real (elastic) channel wall material. (A pre-requisite to this study is the development of a theoretical framework for a general Newtonian fluid.) In the present study, we restrict our attention to the influence of thermo-viscous effects upon the lowest order symmetric duct mode, as only this mode would propagate along a narrow, rigid-walled tube filled with an inviscid fluid; future studies will consider higher-order modes.

In Sec. II we summarize the equations that arise when Beltman's analysis is extended to an arbitrary Newtonian fluid by using the linearized, quasi-equilibrium equations of state for a viscous fluid presented in Chapter 3 of Dunn *et al.* (2015), thereby enabling the study of the impact of thermo-viscous effects upon sound propagation in water. These equations are then applied to study the propagation of sound in narrow rigid-walled two-dimensional channels in Sec. III, where analytic expressions are derived for the dispersion equations of natural modes incorporating thermo-viscous effects. From this analysis, we are able to determine the conditions under which thermo-viscosity has a significant impact upon the propagation of guided acoustic waves by examining the phase-speed and attenuation of such waves along the channel for two different thermal boundary conditions: insulating and conducting. In particular, we show that the thermal expansion coefficient of the fluid has a significant impact upon the relative influence of viscous and thermal effects.

In Sec. IV we present results associated with propagation in air and in water along rigid-walled channels, and consider the different behavior of these two fluids. We show that their behaviors are captured by simple approximate analytic expressions for the complex phase-speed that are valid up to the MHz frequency range. We also compare our theoretical predictions to the in-air measurements of Ward *et al.* (2015) and find that our results are broadly consistent with their data, thereby confirming our analysis, which should be valid for any simple (Newtonian) fluid. Finally, in Sec. V, we consider acoustic coupling with compliant boundaries. As is known this is particularly important in the water-filled channel, unlike the air-filled case where all boundaries can, in general, be considered rigid. In particular, we show that for narrow, water-filled channels that have widths of the same order of magnitude as Stokes's boundary layer thickness, fluid-structure interaction has a dramatic impact upon the characteristics of the fundamental acoustic mode of propagation. Attenuation is increased by about 40 dB $m^{-1}$ compared to the

rigid-walled assumption and the phase speed is slowed by almost 70%. We offer conclusions in Sec. VI.

Whilst variables and parameters employed herein are defined in the text, where they are first encountered, a notation summary is provided in the Appendix for the convenience of the reader.

## II. GOVERNING EQUATIONS FOR THERMO-VISCOUS ACOUSTICS

In this section, the equations governing linear thermo-viscous acoustics are presented in non-dimensional form. By combining these equations in the manner described by Beltman (1999a), for time-harmonic propagation, the vorticity field is shown to satisfy the Helmholtz equation and fractional temperature fluctuations of the fluid can be described by a pair of Helmholtz equations. From these solutions the velocity and pressure fields can be constructed. The study is restricted to two dimensions, which is appropriate for the models of interest.

### A. Thermo-viscous fluids

Below we state the linearized governing equations for thermo-viscous fluids with dimensional variables and parameters having an over-bar and their non-dimensional counterparts being free of bars. In non-dimensional form then, these equations are (see, e.g., Chapter 3 of Dunn *et al.*, 2015)

$$\frac{\partial s}{\partial t} + \boldsymbol{\nabla}\cdot\boldsymbol{u} = 0, \tag{1}$$

$$\frac{\partial \boldsymbol{u}}{\partial t} = -\boldsymbol{\nabla} p + \eta\nabla^2\boldsymbol{u} + (\eta+\eta')\boldsymbol{\nabla}(\boldsymbol{\nabla}\cdot\boldsymbol{u}), \tag{2}$$

$$\frac{\partial \theta}{\partial t} - \frac{\mathcal{K}}{c_p}\nabla^2\theta - \frac{\beta}{c_p}\frac{\partial p}{\partial t} = 0, \tag{3}$$

$$s = p - \frac{\beta}{c_p}h, \quad \theta = \frac{1}{c_p}(\beta p + h), \tag{4}$$

where boldface symbols are used to denote vector quantities. $h$ denotes non-dimensionalized fluctuations of entropy per unit mass, whilst $p$ is the non-dimensional acoustic pressure. They are defined by

$$p = \frac{\bar{p}-\bar{p}_0}{\bar{\rho}_0\bar{c}_0^2}, \quad h = \frac{\bar{T}_0}{\bar{c}_0^2}(\bar{h}-\bar{h}_0). \tag{5}$$

$s$ and $\theta$ are, respectively, the fractional fluctuations of density and temperature, i.e.,

$$s = \frac{\bar{\rho}-\bar{\rho}_0}{\bar{\rho}_0}, \quad \theta = (\bar{T}-\bar{T}_0)/\bar{T}_0. \tag{6}$$

In the above, $\bar{p}$, $\bar{\rho}$, $\bar{h}$, and $\bar{T}$ denote, respectively, the fluctuating (dimensional) pressure, density, entropy, and absolute temperature of the fluid, with $\bar{p}_0$, $\bar{\rho}_0$, $\bar{h}_0$, and $\bar{T}_0$ being their equilibrium values (taken to be spatially invariant); $\bar{c}_0$ is the barotropic sound speed of the fluid. Other relations between dimensional and non-dimensional variables are those for the fluid particle velocity $\bar{\boldsymbol{u}} = \bar{c}_0\boldsymbol{u} = \bar{c}_0\,(u_x, u_y, 0)$, Cartesian variables $(\bar{x},\bar{y}) = \bar{\mathcal{L}}\,(x,y)$ where $\bar{\mathcal{L}}$ is a problem specific length scale and time $\bar{t} = (\bar{\mathcal{L}}/\bar{c}_0)\,t$. Non-dimensional parameters are also introduced for convenience, in particular the first, or shear, coefficient of viscosity: $\bar{\eta} = \bar{\rho}_0\bar{c}_0\bar{\mathcal{L}}\,\eta$ and second coefficient of viscosity: $\bar{\eta}' = \bar{\rho}_0\bar{c}_0\bar{\mathcal{L}}\,\eta'$, noting that $\bar{\eta}$ and $\bar{\eta}'$ are related to the commonly used bulk viscosity, $\bar{\eta}_B$, through $\bar{\eta}_B = \bar{\eta}' + (2/3)\bar{\eta}$. Furthermore, the thermodynamic coefficients of conductivity $\bar{\mathcal{K}}$, specific heat at constant pressure $\bar{c}_p$, and thermal expansion at constant pressure $\bar{\beta}$ are non-dimensionalized as follows:

$$\mathcal{K} = \frac{\bar{T}_0\,\bar{\mathcal{K}}}{\bar{\rho}_0\bar{c}_0^3\bar{\mathcal{L}}}, \quad c_p = \frac{\bar{T}_0}{\bar{c}_0^2}\,\bar{c}_p, \quad \beta = \bar{\beta}\,\bar{T}_0. \tag{7}$$

Equation (2) is associated with a non-dimensional viscous stress tensor, which, in index form, has an $ij$th component (see, e.g., Chapter 41 of Feynman *et al.*, 1965)

$$\sigma_{ij} = \eta\left(\frac{\partial u_i}{\partial x_j} + \frac{\partial u_j}{\partial x_i}\right) + \eta'\delta_{ij}\frac{\partial u_k}{\partial x_k}, \tag{8}$$

where $u_1 \equiv u_x$, $u_2 \equiv u_y$, $x_1 \equiv x$, $x_2 \equiv y$, $\delta_{ij}$ is the $ij$th component of the Kronecker-delta tensor and we employ the convention that repeated indices are summed over. The dimensional stress is $\bar{\sigma}_{ij} = \bar{\rho}_0\bar{c}_0^2\sigma_{ij}$.

### B. Decomposition into vortex and thermo-compression fields

Beltman (1999a) shows that the governing equations for an ideal gas decouple into a vortex field, $\boldsymbol{\Omega}$, and two thermo-compression fields, $\Theta_1$ and $\Theta_2$. We find this field description to be valid in the more general case of an arbitrary Newtonian fluid whose governing equations were described in the previous section. The decomposition applied to an arbitrary Newtonian fluid within the frequency domain is given next as well as the relationships between $\boldsymbol{\Omega}$, $\Theta_1$, $\Theta_2$, and other variables.

Since the problem here is considered two-dimensional, the vortex field can be written as $\boldsymbol{\Omega} = \boldsymbol{\nabla}\times\boldsymbol{u} = \hat{\boldsymbol{k}}\Omega$, where $\hat{\boldsymbol{k}}$ indicates a unit vector pointing in the $z$-direction, and $\Omega$ is a scalar function. $\Omega$ satisfies the diffusion equation

$$\frac{\partial \Omega}{\partial t} = \eta\nabla^2\Omega, \tag{9}$$

and is decoupled from the thermal and compression field-variables. For harmonic excitation, $\Omega(x,y,t) = \tilde{\Omega}(x,y,\omega)e^{-i\omega t}$, where $\omega = \bar{\omega}\bar{\mathcal{L}}/\bar{c}_0$ is the non-dimensionalized frequency (or equivalently non-dimensionalized acoustic wavenumber), and Eq. (9) becomes the complex Helmholtz equation for $\tilde{\Omega}$, i.e.,

$$\left(\nabla^2 + \frac{i\omega}{\eta}\right)\tilde{\Omega} = 0. \tag{10}$$

In terms of dimensional parameters,

$$\frac{\omega}{\eta} = \left(\frac{\bar{\mathcal{L}}}{\bar{\delta}_\nu}\right)^2, \tag{11}$$

where $\bar{\delta}_\nu$ is the boundary layer parameter of Ward *et al.* (2015) that was referred to in the Introduction.

Similarly, harmonic temperature fluctuations are written as $\theta(x,y,t) = \tilde{\theta}(x,y,\omega)e^{-i\omega t}$, where the following decomposition is used for $\tilde{\theta}$:

$$\tilde{\theta}(x,y,\omega) = \tilde{\Theta}_1(x,y,\omega) + \tilde{\Theta}_2(x,y,\omega). \tag{12}$$

$\tilde{\Theta}_1(x,y,\omega)$ and $\tilde{\Theta}_2(x,y,\omega)$ each satisfy a Helmholtz equation, viz.,

$$(\nabla^2 + \kappa_1^2)\tilde{\Theta}_1 = 0, \quad (\nabla^2 + \kappa_2^2)\tilde{\Theta}_2 = 0, \tag{13}$$

where

$$\kappa_1^2 = i\omega\,\frac{[1 - i\omega(\zeta + \mathcal{AC})] + \mathcal{S}}{2(1 - i\omega\zeta\mathcal{A})\mathcal{C}},$$
$$\kappa_2^2 = i\omega\,\frac{[1 - i\omega(\zeta + \mathcal{AC})] - \mathcal{S}}{2(1 - i\omega\zeta\mathcal{A})\mathcal{C}}, \tag{14}$$

with

$$\mathcal{S} = \sqrt{[1 - i\omega(\zeta - \mathcal{AC})]^2 - 4i\omega\,\mathcal{C}(\mathcal{A} - 1)},$$
$$\mathcal{A} = 1 + \frac{\beta^2}{c_p}, \quad \mathcal{C} = \frac{\mathcal{K}}{c_p}, \tag{15}$$

and $\zeta = 2\eta + \eta' = \eta_B + (4/3)\eta$. $\mathcal{C}$ represents the non-dimensionalized thermal diffusion coefficient. If in Eq. (14) and the first of Eq. (15), $\mathcal{A}$ is replaced by the ratio of specific heats at constant pressure and volume, the solution for an ideal gas is recovered; see, for example, Stinson (1991) and Beltman (1999a).

It is readily shown for harmonic excitation, defining the velocity $\boldsymbol{u}(x,y,t) = \tilde{\boldsymbol{u}}(x,y,\omega)e^{-i\omega t}$, condensation $s(x,y,t) = \tilde{s}(x,y,\omega)e^{-i\omega t}$ and pressure $p(x,y,t) = \tilde{p}(x,y,\omega)e^{-i\omega t}$, that these harmonic variables can be defined in terms of $\tilde{\Omega}, \tilde{\Theta}_1$ and $\tilde{\Theta}_2$ in the forms

$$i\omega\tilde{\boldsymbol{u}} = \frac{c_p}{2\beta}\{[1 - i\omega(\zeta - \mathcal{AC}) - \mathcal{S}]\nabla\tilde{\Theta}_1 + [1 - i\omega(\zeta - \mathcal{AC}) + \mathcal{S}]\nabla\tilde{\Theta}_2\} + \eta\nabla\times\hat{\boldsymbol{k}}\tilde{\Omega}, \tag{16}$$

$$\tilde{s} = \frac{c_p}{\beta}\left[\left(1 + i\frac{\mathcal{AC}\kappa_1^2}{\omega}\right)\tilde{\Theta}_1 + \left(1 + i\frac{\mathcal{AC}\kappa_2^2}{\omega}\right)\tilde{\Theta}_2\right], \tag{17}$$

$$\tilde{p} = \frac{c_p}{\beta}\left[\left(1 + i\frac{\mathcal{C}\kappa_1^2}{\omega}\right)\tilde{\Theta}_1 + \left(1 + i\frac{\mathcal{C}\kappa_2^2}{\omega}\right)\tilde{\Theta}_2\right]. \tag{18}$$

Having summarized the governing equations and relations between dependent field variables, we now move on to defining the problem of interest.

## III. THERMO-VISCOUS ACOUSTIC PROPAGATION IN NARROW CHANNELS WITH RIGID WALLS

In this section and with reference to Fig. 1, we examine the behavior of the natural modes of propagation along an infinitely-long parallel-sided channel, considering the impact of frequency, and channel width in particular, upon phase-speed and attenuation. The channel is aligned with the $x$-direction and lies in $|\bar{y}| \le \bar{L}$. Its width in the $z$-direction is considered to be of infinite extent, and the motion of the fluid is considered to be independent of $\bar{z}$. Hence, the problem is two dimensional, governed by the equations summarized in Sec. II.

We start by setting the characteristic length scale, $\bar{\mathcal{L}} = \bar{L}$, i.e., equal to the half-width of the channel. Thus, in non-dimensional coordinates, the channel lies in $|y| \le 1$ and is aligned along the $x$ direction. Its walls are considered rigid so that

$$\tilde{\boldsymbol{u}}(x, y = \pm 1, \omega) = 0. \tag{19}$$

Solutions are sought with the dependence $e^{ikx}$, where $k$ may be complex [with $\Im(k) \ge 0$] and its permissible values are determined by the boundary conditions on the channel wall. Here we concentrate upon natural modes possessing a symmetric pressure distribution about the centre-line of the channel. This case is of particular interest because, for an inviscid fluid, only the lowest order *symmetric* mode is cut on at channel widths and frequencies of interest; all other modes are evanescent. For symmetric modes, we require $\tilde{p}(x,y,\omega)$ to be an even function of $y$. This requires $\tilde{s}$, $\tilde{\theta}$, and $\tilde{u}_x$ to be even functions of $y$, whilst $\tilde{\Omega}$ and $\tilde{u}_y$ are odd. Hence our basic $k$-space solutions for temperature and vorticity, which we denote by $\hat{\theta}(k,y,\omega) = \hat{\Theta}_1(k,y,\omega) + \hat{\Theta}_2(k,y,\omega)$, and $\hat{\Omega}(k,y,\omega)$, respectively, using the hat symbol to denote a $k$-space function, take the forms

$$\hat{\theta}(k,y,\omega) = B(k,\omega)\cosh(\gamma_1 y) + D(k,\omega)\cosh(\gamma_2 y), \tag{20}$$

$$\hat{\Omega}(k,y,\omega) = E(k,\omega)\sinh(\alpha y), \tag{21}$$

where $\gamma_1 = (k^2 - \kappa_1^2)^{1/2}, \gamma_2 = (k^2 - \kappa_2^2)^{1/2}, \alpha = (k^2 - i\omega/\eta)^{1/2}$. The functional forms of $B$, $D$, and $E$ will clearly depend upon the thermal properties of the channel walls. We now consider two cases: thermally insulating walls and isothermal (perfectly conducting) walls.

In addition to Eq. (19), a *thermally insulating channel wall* must also satisfy

$$\frac{\partial\tilde{\theta}}{\partial y}(x, y = \pm 1, \omega) = 0, \tag{22}$$

or its equivalent form in $k$-space. Imposing the boundary conditions in Eqs. (19) and (22) upon the basic solutions

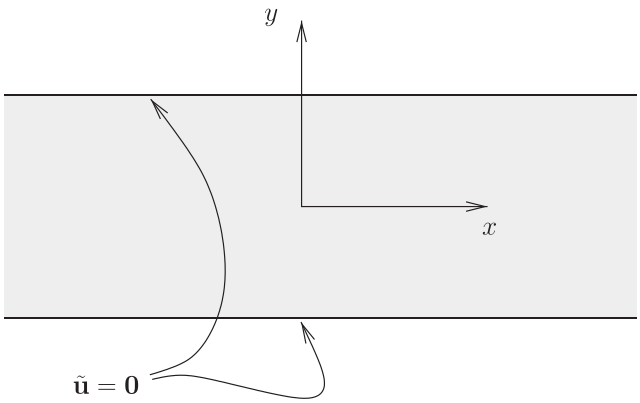


FIG. 1. Thermo-viscous acoustic propagation in a channel, running parallel to the $x$ axis and having rigid walls at $y = \pm 1$.

from Eqs. (20) and (21), noting Eq. (16), requires that for natural modes of propagation along the channel, $k$ must satisfy the following dispersion equation:

$$k^2\tanh(\alpha)\{[1-i\omega(\zeta-\mathcal{AC})-\mathcal{S}]\gamma_2\tanh(\gamma_2) -[1-i\omega(\zeta-\mathcal{AC})+\mathcal{S}]\gamma_1\tanh(\gamma_1)\} +2\alpha\gamma_1\gamma_2\mathcal{S}\tanh(\gamma_1)\tanh(\gamma_2)=0. \quad (23)$$

Temperature fluctuations vanish on a *perfectly conducting channel wall* whose temperature is maintained at the equilibrium temperature of the fluid. Thus, the thermal boundary condition for this case is

$$\tilde{\theta}(x, y=\pm 1, \omega)=0, \quad (24)$$

with the corresponding dispersion equation for *symmetric* modes being

$$\alpha\{[1-i\omega(\zeta-\mathcal{AC})-\mathcal{S}]\gamma_1\tanh(\gamma_1) -[1-i\omega(\zeta-\mathcal{AC})+\mathcal{S}]\gamma_2\tanh(\gamma_2)\} +2k^2\mathcal{S}\tanh(\alpha)=0. \quad (25)$$

### A. The limit of zero thermal expansion

In Sec. IV below, we examine the numerical behavior of the dispersion equation for typical values of the thermo-viscous coefficients applicable to air and water. First, however, it is instructive to consider the limit of vanishingly small thermal expansion, which is of particular relevance to water.

It is clear from Eq. (4) that for a vanishingly small thermal expansion coefficient, pressure and density variations are decoupled from temperature fluctuations. That is as $\beta \to 0$,

$$s \to p, \quad \theta \to \frac{h}{c_p}, \quad (26)$$

and the acoustic (compressional) channel modes become independent of thermal effects but may still be influenced by the viscous boundary layer. In this limit, we see from Eq. (15) that clearly $\mathcal{A}=1+O(\beta^2)$, and $\mathcal{S}\to 1-i\omega(\zeta-\mathcal{C})+O(\beta^2)$, whence Eqs. (23) and (25) acquire the following common form:

$$\mathcal{D}_{vr}=k^2\tanh(\alpha)-\alpha\gamma_2\tanh(\gamma_2)=0. \quad (27)$$

Equation (27) is independent of $\gamma_1$ and hence $\kappa_1$, where in the limit $\beta\to 0$, $\kappa_1$ depends only upon thermal parameters (and fluid density), indeed

$$\kappa_1 \to \sqrt{\frac{i\omega}{\mathcal{C}}}\left[1+O(\beta^2)\right] \quad \text{as } \beta\to 0, \quad (28)$$

whilst

$$\kappa_2 \to \frac{\omega}{\sqrt{1-i\omega\zeta}}\left[1+O(\beta^2)\right] \quad \text{as } \beta\to 0, \quad (29)$$

which depends only upon viscous and acoustic parameters. Furthermore, as $\beta\to 0$, Eqs. (16) to (18) acquire the following forms:

$$i\omega\tilde{\boldsymbol{u}} \to \frac{c_p}{\beta}[1-i\omega(\zeta-\mathcal{C})]\boldsymbol{\nabla}\tilde{\Theta}_2+\eta\boldsymbol{\nabla}\times\boldsymbol{k}\tilde{\Omega}, \quad (30)$$

$$\tilde{s}\to\tilde{p}\to\frac{c_p}{\beta}\left[\frac{1-i\omega(\zeta-\mathcal{C})}{1-i\omega\zeta}\right]\tilde{\Theta}_2. \quad (31)$$

Clearly as $\beta\to 0$, $\tilde{\Theta}_2/\beta$ must remain bounded and $\tilde{\Theta}_2$ must vanish, if the physical variables $\tilde{\boldsymbol{u}}$, $\tilde{s}$ and $\tilde{p}$ are to remain finite, whence from Eq. (12), $\tilde{\theta}\to\tilde{\Theta}_1$. Finally, using Eq. (31) to eliminate $\tilde{\Theta}_2$ from Eq. (30), we see that

$$i\omega\tilde{\boldsymbol{u}} \to (1-i\omega\zeta)\boldsymbol{\nabla}\tilde{p}+\eta\boldsymbol{\nabla}\times\boldsymbol{k}\tilde{\Omega}, \quad (32)$$

which, if $\beta$ is set to zero at the outset, follows directly from Eqs. (1), (2), the first of Eq. (4), and the definition of $\Omega$ [given just prior to Eq. (9)]. And we note that $\tilde{p}$ now satisfies

$$\left(\nabla^2+\frac{\omega^2}{1-i\omega\zeta}\right)\tilde{p}=0. \quad (33)$$

In this limit, the visco-acoustic and thermal problems appear to decouple completely, which of course cannot be the case because viscous *losses* in the former problem cause thermal heating of the fluid. This anomaly arises because non-linear terms associated with viscous stresses were neglected in the energy/heat equation [Eq. (3)]. In most circumstances, this is perfectly acceptable, but in the limit $\beta\to 0$, these non-linear terms become the dominant source term of the heat equation. Thus, in the limit $\beta\to 0$, the visco-acoustic problem can be solved without reference to thermal effects and the viscous stresses from its solution lead to known, non-linear, source terms in the thermal problem. We note, however, that if non-linear effects are significant in the energy equation, it may be necessary to revisit the form of the equations of state; see, for example, Pierce (1978).

## IV. IMPLEMENTATION FOR AIR AND WATER FILLED CHANNELS

The theory is now implemented in the case of air and water filled channels. Relevant parameters are listed in Table I, taken from Dunn *et al.* (2015), and assumed independent of frequency.

In Sec. IV A, we evaluate the phase speed and attenuation of acoustic waves propagating along air-filled and water-filled channels, by finding the lowest order roots of the dispersion equations derived in Sec. III. The results are presented as a function of the channel width, $\bar{W}=2\bar{L}$, relative to Stokes's boundary layer thickness, $\bar{\delta}_s$, where the latter is defined by

$$\bar{\delta}_s=2\pi\sqrt{\frac{2\,\bar{\nu}}{\bar{\omega}}}, \quad (34)$$

and $\bar{\nu}$, the kinematic viscosity, is related to the dynamic viscosity, $\bar{\eta}$, through $\bar{\nu}=\bar{\eta}/\bar{\rho}_0$. The phase-speed values

TABLE I. Thermo-viscous parameter values for water and air, taken from Dunn *et al.* (2015), noting that $\bar{\beta} = 1/\bar{T}_0$ for an ideal gas.

| Parameter | Unit | Symbol | Water (10 °C) | Air (27 °C) |
|---|---|---|---|---|
| Speed of sound | $\mathrm{m\,s^{-1}}$ | $\bar{c}_0$ | 1490 | 343 |
| Density | $\mathrm{kg\,m^{-3}}$ | $\bar{\rho}_0$ | 1000 | 1.19 |
| Dynamic shear viscosity | $\mathrm{kg\,m^{-1}\,s^{-1}}$ | $\bar{\eta}$ | $1.002 \times 10^{-3}$ | $1.846 \times 10^{-5}$ |
| Dynamic bulk viscosity | $\mathrm{kg\,m^{-1}\,s^{-1}}$ | $\bar{\eta}_B$ | $3.006 \times 10^{-3}$ | $1.108 \times 10^{-5}$ |
| Thermal conductivity | $\mathrm{W\,m^{-1}\,K^{-1}}$ | $\bar{\mathcal{K}}$ | 0.597 | $2.624 \times 10^{-2}$ |
| Specific heat at constant pressure | $\mathrm{J\,kg^{-1}\,K^{-1}}$ | $\bar{c}_p$ | 4192 | 1005 |
| Ambient temperature | K | $\bar{T}_0$ | 283.16 | 300 |
| Coefficient of thermal expansion | $\mathrm{K^{-1}}$ | $\bar{\beta}$ | $8.822 \times 10^{-5}$ | 1/300 |

obtained for an air-filled channel are compared with the experimental data of Ward *et al.* (2015), noting that these data are parameterized against $\bar{\delta}_\nu/\bar{W}$, rather than $\bar{\delta}_s/\bar{W}$, where

$$\bar{\delta}_\nu = \sqrt{\frac{\bar{\nu}}{\bar{\omega}}} \approx 0.11\bar{\delta}_s. \tag{35}$$

In Sec. IV B, we examine the fluid-particle-velocity profile across the channel for various channel widths in order to determine the extent to which the channel-wall boundary-layer influences the motion of the fluid and hence the propagation of acoustic waves.

### A. Phase speed and attenuation

Given the root, $k$, for any one of the dispersion Eqs. (23), (25), and (27), the *complex* non-dimensionalized phase-speed, $v$, along the channel is given by

$$v = \frac{\bar{v}}{\bar{c}_0} = \frac{\omega}{k}. \tag{36}$$

Roots for the dispersion equations were calculated using the MATLAB [version 9.2.0.556344 (R2017a)] command *fsolve*, which finds the local zero of a user-specified function close to a given starting point.

Before presenting the results thereby obtained, we first note that in air and water both $\omega\zeta$ and $\omega\mathcal{C}$ are very much less than unity at frequencies up to the order of 1 GHz. Under these circumstances, and provided $\omega \ll 1$, the following approximate expressions for the (dimensionless) complex phase-speed can be obtained from Eqs. (23) and (25):

$$v_{insul} \approx \sqrt{1 - \tanh\left(\frac{1-i}{\sqrt{2}\,\delta_\nu}\right)\Big/\left(\frac{1-i}{\sqrt{2}\,\delta_\nu}\right)} \tag{37}$$

and

$$v_{cond} \approx \sqrt{\frac{1 - \tanh\left(\frac{1-i}{\sqrt{2}\,\delta_\nu}\right)\Big/\left(\frac{1-i}{\sqrt{2}\,\delta_\nu}\right)}{1 + \frac{\mathcal{A}-1}{\sqrt{\mathrm{Pr}}}\tanh\left(\frac{1-i}{\sqrt{2}\,\delta_\theta}\right)\Big/\left(\frac{1-i}{\sqrt{2}\,\delta_\nu}\right)}}, \tag{38}$$

where $\delta_\nu = \bar{\delta}_\nu/\bar{L}$ is Ward's (Ward *et al.*, 2015) viscous boundary layer parameter, non-dimensionalized on the half-width $\bar{L}$ of the duct; $\delta_\theta = \bar{\delta}_\theta/\bar{L}$ is an equivalent thermal boundary layer parameter with $\bar{\delta}_\theta$ defined as

$$\bar{\delta}_\theta = \sqrt{\frac{\bar{\mathcal{K}}}{\bar{\rho}_0\bar{\omega}\bar{c}_p}}; \tag{39}$$

and Pr is the Prandtl number, which is given by

$$\mathrm{Pr} = \frac{\bar{\eta}\bar{c}_p}{\bar{\mathcal{K}}} = \left(\frac{\bar{\delta}_\nu}{\bar{\delta}_\theta}\right)^2. \tag{40}$$

The expression for $v_{insul}$ is independent of all thermal parameters and varies only with the dimensionless parameter $\bar{L}/\bar{\delta}_\nu$. However, $v_{cond}$ is additionally dependent upon Pr and the dimensionless parameter $\mathcal{A} - 1 = (\bar{\beta}^2\bar{T}_0\bar{c}_0^2)/\bar{c}_p$, noting that Eq. (38) recovers Stinson's solution for an ideal gas (Stinson, 1991) if $\mathcal{A}$ is replaced by the ratio of specific heats at constant pressure and volume.

If the fundamental thermo-viscous parameters are frequency independent, as assumed here, we see that in the cases of thermally insulating and perfectly conducting channel-wall boundary conditions, the functional frequency dependence of their associated complex phase-speeds is contained entirely within the expressions for the boundary layer parameters $\bar{\delta}_\nu$ and $\bar{\delta}_\theta$. Indeed, given the definition in Eq. (40) of Pr, it is sufficient to specify just one of the boundary layer parameters and the Prandtl number, which is frequency independent.

Although not illustrated herein, we find that for the range of channel-widths under consideration, Eqs. (37) and (38) are in almost exact agreement with values obtained using the full dispersion equations at all frequencies up to at least 1 MHz in air and 50 MHz in water. Furthermore, their validity is not confined to air and water. Indeed, these expressions are valid for any Newtonian fluid, provided the conditions specified in their derivation are satisfied, namely, $\omega\zeta \ll 1$, $\omega\mathcal{C} \ll 1$, and $\omega \ll 1$.

Returning to the solutions of the exact dispersion equations, we note from Eqs. (37) and (38) that as $\bar{L}, \bar{W} \to \infty$, both $v_{insul}$ and $v_{cond}$ tend to unity, which is equivalent to $k \to \omega$. Thus, an appropriate method for finding their roots, using *fsolve*, is to begin with a wide channel (we chose $\bar{W} = 100\bar{\delta}_s$), and to start the root search from $k = \omega$. We then gradually reduce $\bar{W}$ down to the desired value, using the root found for the previous (larger) value of $\bar{W}$ as a new starting point for *fsolve*.

By way of example, Fig. 2 shows the resulting *real* phase-speed and attenuation along an air-filled channel as a function of $\bar{\delta}_s/\bar{W}$. Here, real phase-speed is defined as $\Re(v)$, and the attenuation in dB/wavelength is $40\pi(k_i/k_r)\log_{10}(e)$, where $k_r = \Re(k)$ and $k_i = \Im(k)$. The curves for viscous only and thermally insulating channel-wall boundary conditions are identical, indicating that for a thermally insulating boundary condition, the lowest order symmetric duct mode is decoupled from thermal fluctuations as expected. However, a different behavior is observed for the conducting curve shown in Fig. 2, again as expected. We observe that the results of Ward *et al.* (2015), indicted by the black crosses of Fig. 2, lie in-between the two extreme thermal boundary conditions of conducting and insulating channel walls. Although not presented here, we find that the behavior in air, illustrated in Fig. 2, is valid at all frequencies up to the order of 1 MHz.

Figure 3 demonstrates the behavior of a water-filled channel, which is found to be valid at all frequencies below a maximum value approaching 50 MHz. The behavior of water is very similar to that of air, except that for water, thermal effects are seen to be negligible for both the thermally conducting (isothermal) and insulating channel-wall boundary conditions, primarily because of water's low coefficient of thermal expansion (as discussed previously). For water this leads to the parameter $\mathcal{A}$ being very close to unity, $\mathcal{A} \approx 1.001$ in water, whilst in air $\mathcal{A} \approx 1.39$. In addition, Pr in water is about ten times greater than in air. Taken together, these two factors lead to the second term in the denominator of Eq. (38) being negligible for water, thereby recovering Eq. (37).

In summary, we see that in water, thermal effects have a negligible impact upon acoustic propagation along narrow channels, and this is also true in air if the channel wall is

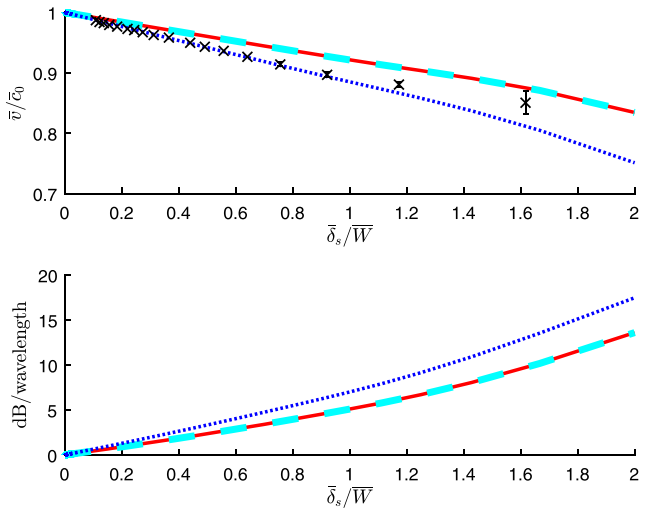


FIG. 2. (Color online) Phase speed and attenuation along an air-filled channel. The upper plot shows the phase speed relative to $\bar{c}_0$. The lower plot shows the attenuation along the channel. Different line styles indicate channel-wall boundary conditions corresponding to Viscous only (red, solid); Thermally insulating (cyan, dashed); Isothermal/conducting (blue, dotted). The black crosses indicate the *single slit* measured data extracted from Fig. 4 of Ward *et al.* (2015), and reproduced here by kind permission of Professor Alastair Hibbins.

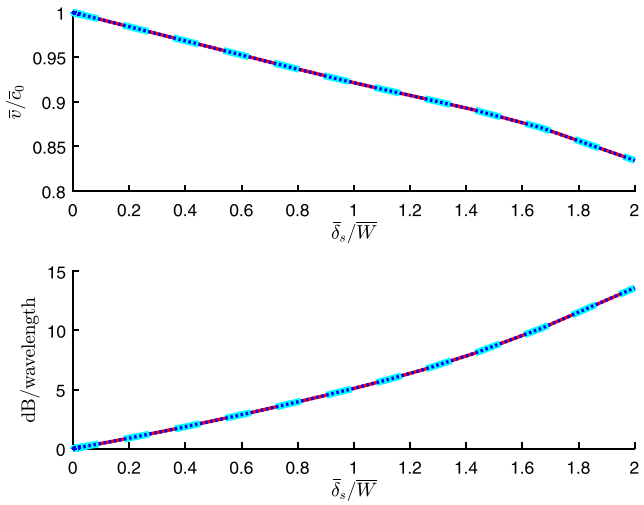


FIG. 3. (Color online) Phase speed and attenuation along a water-filled channel. The upper plot shows the phase speed relative to $\bar{c}_0$. The lower plot shows the attenuation along the channel. Line styles are as indicated in Fig. 2.

thermally insulating, which is perhaps not surprising as this boundary condition is close to the adiabatic thermal condition expected in freely propagating acoustic waves. However, in air, thermal effects are significant when the channel wall is conducting. For the thermally insulating channel wall boundary condition, the behavior of air and water with respect to their dimensionless phase speed and attenuation along the channel in dB/wavelength is essentially identical when parameterized against the dimensionless parameter $\bar{\delta}_s/\bar{W}$. Note, however, that the attenuation along a fixed distance, say 1 m, is much less in water than in air due to the higher dimensional phase speed of water, leading to a wavelength in water that is about five times greater than in air. As an example in this case of rigid boundaries where the channel width is of the order of the boundary layer thickness, the attenuation in air at 10 kHz can be over 200 dB m$^{-1}$, whereas in water it is less than 37 dB m$^{-1}$.

### B. Fluid particle velocity profiles

Similar behavior to that discussed above is observed for the fluid particle velocity profiles across the channel. Below, we plot the $x$- and $y$-components of fluid particle velocity, normalized so that $u_x(y=0) = 1$. For fluids such as air and water, which are characterized by low viscous and diffusion coefficients, we find that for both the insulating and isothermal channel-wall boundary conditions, $u_x(y)/u_x(0)$ depends only upon the non-dimensionalized viscous boundary layer parameter $\delta_\nu = \bar{\delta}_\nu/\bar{L}$; *there is no dependence upon the thermal properties of the fluid*. For air, this is illustrated in the upper plot of Fig. 4 for a channel-width of $10\bar{\delta}_s$. Both the magnitude and the phase (the latter is not shown) of $u_x(y)/u_x(0)$ have the same values for all three channel wall boundary conditions. The same behavior (not shown) is observed in water.

For the $y$-component of fluid-particle velocity, we find that in the case of a thermally insulating channel-wall, the scaled parameter $u_y(y)/(\eta\, u_x(0))$ depends upon only $\delta_\nu$. However, when the channel wall is perfectly conducting,

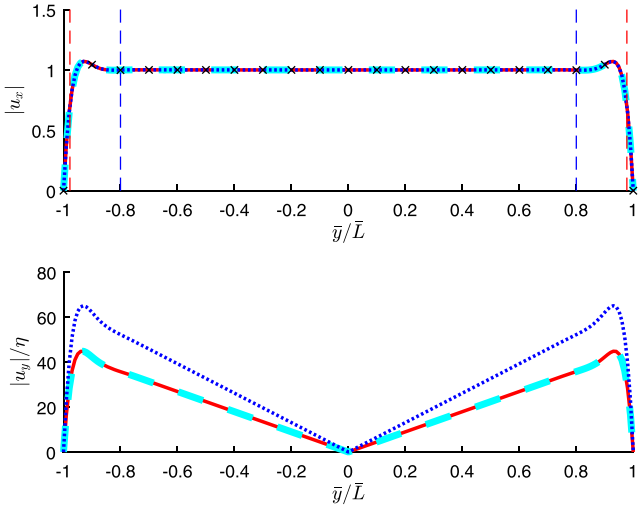


FIG. 4. (Color online) Magnitude of the fluid particle velocity across an air-filled channel of width of 10 $\bar{\delta}_s$. The upper plot shows the $x$-component of the fluid particle velocity, and the lower plot shows the $y$-component; $\boldsymbol{u}$ is normalized, independently for each boundary condition, such that $u_x(y=0)=1$. Line styles are as indicated in Fig. 2. On the upper plot: the black crosses indicate Stokes solution for a fluid half-space; the blue-dashed vertical lines indicate the position of Stokes's boundary layer thickness, $\bar{\delta}_s/\bar{L}$, relative to the channel walls at $y=\pm 1$; the red-dashed vertical lines indicate the location of $\bar{\delta}_\nu/\bar{L}$.

$u_y(y)/(\eta\, u_x(0))$ depends, in general, also upon the additional parameters $\delta_\theta = \bar{\delta}_\theta/\bar{L}$ and $\mathcal{A}-1=\beta^2/c_p$, or alternatively its behavior may be characterized in terms of $\delta_\nu$, the Prandtl number Pr, and $\beta^2/c_p$. For air, this behavior is illustrated in the lower plot of Fig. 4 for a channel-width of $10\bar{\delta}_s$. We see that whilst the viscous only and thermally insulating velocity profiles are identical, the profile for a conducting wall is different, demonstrating the influence of thermal effects in this case. Although not shown here, in water, the three thermal boundary conditions have identical velocity profiles as a result of water's low coefficient of expansion.

In the absence of boundary layer effects, the $y$-component of fluid particle velocity would be zero everywhere, and the $x$-component would be constant across the channel; that is $u_x$ would be independent of $y$. The red and blue, vertical, dashed lines marked on the upper plot of Fig. 4 indicate, respectively, the positions of the non-dimensionalized boundary layer thickness parameters, $\bar{\delta}_\nu/\bar{L}$ and $\bar{\delta}_s/\bar{L}$, relative to the channel walls on $y=\pm 1$. The black crosses show Stokes's solution for an oscillating pressure gradient within a fluid-filled half-space lying above a rigid surface, under the assumption that the boundary layers on the two walls of the channel are well separated and hence non-interacting (Batchelor, 2000). For this relatively wide channel, the fluid-particle-velocity profile for $u_x$ is very similar to that of Stokes's half-space solution, and we observe that $\bar{\delta}_s$ is a significantly better indicator than $\bar{\delta}_\nu$, of the extent to which the channel-wall boundary layers disturb the motion of the fluid. $\bar{\delta}_\nu$ underestimates the true extent of the boundary layer but as we have seen above it is a very useful parameter with which to characterize the fluid's behavior when it is influenced by boundary layer effects.

Figure 5 shows the velocity profile for a much narrower channel, $\bar{W}=\bar{\delta}_s/2$, in which the boundary layers on the two walls are strongly interacting. Stokes's solution for a fluid half-space is no longer relevant; rather the velocity profile resembles that of Poiseuille flow, as indicated by the red crosses. Using $\bar{\delta}_\nu/\bar{L}$ as boundary layer thickness can be seen in Fig. 5 to be severely underestimating this length.

The large difference in the magnitude of the $y$-component of fluid particle velocity, which is observed in Figs. 4 and 5, arises mainly because the expression for $u_y(y)/(\eta\, u_x(0))$ contains a scaling factor of $1/\delta_\nu$.

## V. FLUID-STRUCTURE INTERACTION EFFECTS

Until now, all boundaries have been considered rigid, which is a sensible approximation in the air-filled channel but not necessarily so in the case of a water-filled channel. In order to investigate the effect of elastic boundaries, and in particular their impact upon phase-speed and attenuation in this case, let us consider a water-filled channel in an undamped elastic medium of infinite extent; the only damping mechanism considered is the viscosity of the fluid. The presence of semi-infinite elastic walls requires the consideration of body waves, both compressional and shear, propagating within the elastic material. Generally, this necessitates the mathematical formulation of a physical problem with some specified forcing, the solution of which will be expressed in terms of integrals around branch-cuts that are then associated with outgoing and incoming body waves and additionally, a sum of the natural modes of propagation in the waveguide. However, such an analysis is beyond the scope of the present study; we are primarily concerned with demonstrating the impact of an elastic boundary on the natural modes of propagation within the water-filled channel, and comparing this behavior to the idealized case of a rigid boundary. In order to proceed here then we must

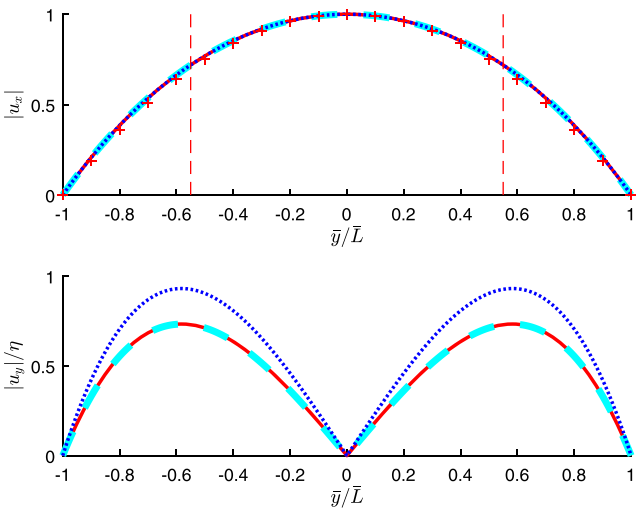


FIG. 5. (Color online) Magnitude of the fluid particle velocity across an air-filled channel of width of $\bar{\delta}_s/2$. The upper plot shows the $x$-component of fluid-particle-velocity, and the lower plot shows the $y$-component; $\boldsymbol{u}$ is normalized, independently for each boundary condition, such that $u_x(y=0)=1$. Line styles are as indicated in Fig. 2. On the upper plot: the red crosses indicate the velocity profile for Poiseuille flow across a narrow channel, the red-dashed vertical lines indicate the location of $\bar{\delta}_\nu/\bar{L}$.

merely ensure that the choice of branch cuts is consistent with the requirements of causality. This is discussed further below.

We shall neglect all thermal effects in this analysis since as shown earlier these are negligible in the case of acoustic propagation in water (due to the low value of the thermal expansion coefficient). Recalling that as $\beta \to 0$, $s \to p$, the (time-harmonic) fluid velocity here is therefore written compactly in terms of the condensation and vorticity, i.e.,

$$\tilde{\mathbf{u}} = \frac{-i}{\omega}\left((1 - i\omega\zeta)\nabla\tilde{s} + \eta\nabla \times \tilde{\Omega}\right), \tag{41}$$

where $\tilde{s}$ is governed by

$$\left(\nabla^2 + \frac{\omega^2}{1 - i\omega\zeta}\right)\tilde{s} = 0. \tag{42}$$

The components of the *total* (time-harmonic) fluid stress tensor are

$$\tilde{\Sigma}_{ij} = \tilde{\sigma}_{ij} - \tilde{p}\delta_{ij} = \eta\left(\frac{\partial\tilde{u}_i}{\partial x_j} + \frac{\partial\tilde{u}_j}{\partial x_i}\right) - \delta_{ij}(1 - i\omega\eta')\tilde{s}. \tag{43}$$

Next, referring back to Fig. 1, instead of imposing the rigid no-slip conditions [Eq. (19)] on the boundary, we now suppose that the medium in $|y| \geq 1$ is a linear isotropic elastic medium of infinite extent. Using a consistent non-dimensionalization scheme to that defined for the fluid with time-harmonic dependence $e^{-i\omega t}$, Navier's equations of linear elasticity may be written as

$$(\lambda + 2\mu)\nabla\tilde{\phi} - \mu\nabla \times \tilde{\boldsymbol{\psi}} + \omega^2\rho_s\tilde{\boldsymbol{w}} = 0, \tag{44}$$

where $\lambda$ is the Lamé modulus and $\mu$ the shear modulus, both being non-dimensionalized on $\bar{\rho}_0\bar{c}_0^2$. Furthermore, $\rho_s = \bar{\rho}_s/\bar{\rho}_0$ denotes the non-dimensionalized solid density and $\boldsymbol{w} = (w_x, w_y, 0) = \bar{\boldsymbol{w}}/\bar{L}$ is the non-dimensionalized elastic displacement, with a tilde denoting its time-harmonic counterpart. Furthermore, the following potentials have been introduced, $\tilde{\phi} = \nabla \cdot \tilde{\boldsymbol{w}}$, and $\tilde{\boldsymbol{\psi}} = \nabla \times \tilde{\boldsymbol{w}}$. As with the fluid vorticity, the rotation vector $\tilde{\boldsymbol{\psi}}$ points in the $z$-direction and may be written $\tilde{\boldsymbol{\psi}} = \hat{\boldsymbol{k}}\tilde{\psi}$. The scalar potentials $\tilde{\phi}$ and $\tilde{\psi}$ satisfy the Helmholtz equations

$$(\nabla^2 + \kappa_p^2)\tilde{\phi} = 0, \tag{45}$$

$$(\nabla^2 + \kappa_s^2)\tilde{\psi} = 0, \tag{46}$$

where $\kappa_p$ and $\kappa_s$ are the non-dimensionalized compressional and shear wavenumbers

$$\kappa_p = \omega\sqrt{\frac{\rho_s}{\lambda + 2\mu}} = \bar{\omega}\bar{L}\sqrt{\frac{\bar{\rho}_s}{\bar{\lambda} + 2\bar{\mu}}},$$
$$\kappa_s = \omega\sqrt{\frac{\rho_s}{\mu}} = \bar{\omega}\bar{L}\sqrt{\frac{\bar{\rho}_s}{\bar{\mu}}}. \tag{47}$$

The elastic displacement is written simply using Eq. (44) in the form

$$\tilde{\boldsymbol{w}} = -\frac{1}{\omega^2\rho_s}\left[(\lambda + 2\mu)\nabla\tilde{\phi} - \mu\nabla \times \tilde{\boldsymbol{\psi}}\right], \tag{48}$$

which is the analogous form, in terms of potentials, to the fluid velocity expression in Eq. (41). Finally, the (time-harmonic) elastic stress tensor is given by

$$\tilde{\sigma}_{ij} = \delta_{ij}\lambda\tilde{\phi} + \mu\left(\frac{\partial\tilde{w}_i}{\partial x_j} + \frac{\partial\tilde{w}_j}{\partial x_i}\right). \tag{49}$$

As with the case of a rigid-walled channel, we seek solutions in $k$-space, which again we denote by the $\hat{}$ symbol. For the fluid-structure interaction problem, it is convenient to relate the $x$- and $k$-space potentials of the elastic solid as follows:

$$\tilde{\phi}(x, y, w) = \frac{\rho_s}{\lambda + 2\mu}\hat{\phi}(k, y, w)e^{ikx},$$
$$\tilde{\psi}(x, y, w) = \frac{\rho_s}{\mu}\hat{\psi}(k, y, w)e^{ikx}, \tag{50}$$

with $\hat{\phi}$ and $\hat{\psi}$ satisfying

$$\left(\frac{\partial^2}{\partial y^2} - \gamma_p^2\right)\hat{\phi} = 0, \quad \left(\frac{\partial^2}{\partial y^2} - \gamma_s^2\right)\hat{\psi} = 0, \tag{51}$$

where

$$\gamma_p = (k^2 - \kappa_p^2)^{1/2}, \quad \gamma_s = (k^2 - \kappa_s^2)^{1/2}. \tag{52}$$

The choice of cuts for $\gamma_p$ and $\gamma_s$ are discussed shortly. For the fluid, we write

$$\tilde{s}(x, y, w) = \frac{1}{1 - i\omega\zeta}\hat{s}(k, y, w)e^{ikx},$$
$$\tilde{\Omega}(x, y, w) = \frac{1}{\eta}\hat{\Omega}(k, y, w)e^{ikx}, \tag{53}$$

with $\hat{s}$ and $\hat{\Omega}$ satisfying

$$\left(\frac{\partial^2}{\partial y^2} - \gamma_2^2\right)\hat{s} = 0, \quad \left(\frac{\partial^2}{\partial y^2} - \alpha^2\right)\hat{\Omega} = 0, \tag{54}$$

where $\gamma_2 = (k^2 - \omega^2/(1 - i\omega\zeta))^{1/2}$ and we recall that $\alpha = (k^2 - i\omega/\eta)^{1/2}$.

### A. The boundary value problem

Boundary conditions require continuity of displacement/velocity at the fluid-solid interface and continuity of the traction components across the channel wall. In $k$-space, these conditions require, for the velocity

$$\frac{\partial\hat{\boldsymbol{w}}}{\partial t}(k, y = \pm 1) = -i\omega\hat{\boldsymbol{w}}(k, y = \pm 1) = \hat{\boldsymbol{u}}(k, y = \pm 1); \tag{55}$$

and for the traction

$$\hat{\sigma}_{yy}(k,y=\pm1)=\hat{\Sigma}_{yy}(k,y=\pm1), \tag{56}$$

$$\hat{\sigma}_{xy}(k,y=\pm1)=\hat{\Sigma}_{xy}(k,y=\pm1), \tag{57}$$

noting that $\tilde{\boldsymbol{w}}(x,y,\omega)=\hat{\boldsymbol{w}}(k,y,\omega)e^{ikx}$, $\tilde{\boldsymbol{u}}(x,y,\omega)=\hat{\boldsymbol{u}}(k,y,\omega)e^{ikx}$ and similarly for the stress components.

By inserting Eqs. (50) and (53) into Eqs. (41), (43), (48), and (49), as appropriate, and imposing the boundary conditions from Eqs. (55)–(57), we obtain the following constraints upon our solutions at $y=\pm1$:

$$\boldsymbol{\nabla}\hat{s}+\boldsymbol{\nabla}\times\hat{\boldsymbol{\Omega}}=-\left[\boldsymbol{\nabla}\hat{\phi}-\boldsymbol{\nabla}\times\hat{\boldsymbol{\psi}}\right], \tag{58}$$

$$\left(\frac{\omega^2}{\mu}+2ik^2\mathcal{P}\right)\hat{s}+2k\mathcal{P}\frac{\partial\hat{\Omega}}{\partial y}=\left(2k^2-\kappa_s^2\right)\hat{\phi}+2ik\frac{\partial\hat{\psi}}{\partial y}, \tag{59}$$

$$2k\mathcal{P}\frac{\partial\hat{s}}{\partial y}-\left(\frac{\omega^2}{\mu}+2ik^2\mathcal{P}\right)\hat{\Omega}=-2ik\frac{\partial\hat{\phi}}{\partial y}+\left(2k^2-\kappa_s^2\right)\hat{\psi}, \tag{60}$$

where

$$\mathcal{P}=\left(\frac{\omega\eta}{\mu}\right)=\left(\frac{\bar{\omega}\bar{\eta}}{\bar{\mu}}\right). \tag{61}$$

Note that $\omega^2/\mu(=\kappa_s^2/\rho_s=\bar{\rho}_0\bar{\omega}^2\bar{L}^2/\bar{\mu})$ and $\mathcal{P}$ are measures of the fluid loading acting on the elastic wall, i.e., they are measures of the fluid's inertial and viscous forces relative to the elastic stresses at the channel-wall. Clearly they are important non-dimensional parameters that will influence significantly the characteristics of our solution, although we note below that in the air and water cases, as well as a wide range of other scenarios $\mathcal{P}\ll1$ and can be set to zero in order to simplify the dispersion relation. Other important non-dimensional parameters (most of which have been defined previously) include

$$\mu=\frac{\bar{\mu}}{\bar{\rho}_0\bar{c}_0^2},\quad \eta=\frac{\bar{\eta}}{\bar{\rho}_0\bar{c}_0\bar{L}},\quad \rho_s=\frac{\bar{\rho}_s}{\bar{\rho}_0},\quad \epsilon=\frac{\bar{\eta}'}{\bar{\eta}},\quad \delta_\nu=\sqrt{\frac{\eta}{\omega}}. \tag{62}$$

With these definitions, the other non-dimensional parameters that arise can be written as

$$\kappa_s=\omega\sqrt{\frac{\rho_s}{\mu}},\quad \kappa_p=\kappa_s\sqrt{\frac{1-2\upsilon}{2(1-\upsilon)}},\quad \omega\zeta=(2+\epsilon)\mu\mathcal{P}, \tag{63}$$

where $\upsilon$ denotes Poisson's ratio.

### B. Dispersion relations for symmetric modes in a fluid-filled channel within an infinite elastic solid

As for the rigid-walled channel, only modes where $s$ is symmetric in $y$ are considered here. In this problem (that is independent of thermal effects), the $k$-space vorticity and condensation then take the form

$$\hat{\Omega}=E\sinh(\alpha y),\quad \hat{s}=F\cosh(\gamma_2 y). \tag{64}$$

For the solid, appropriate symmetric solutions to Eqs. (51) and (52) are similarly given by

$$\hat{\phi}(k,y\geq1)=Xe^{-\gamma_p(y-1)},\quad \hat{\phi}(k,y\leq-1)=Xe^{\gamma_p(y+1)}, \tag{65}$$

$$\hat{\psi}(k,y\geq1)=Ye^{-\gamma_s(y-1)},\quad \hat{\psi}(k,y\leq-1)=-Ye^{\gamma_s(y+1)}, \tag{66}$$

in which the square root functions of Eq. (52) are chosen such that $\gamma_p\to k$ and $\gamma_s\to k$ as $k\to\infty$, with the branch cuts from $\kappa_p$ and $\kappa_s$ taken in the upper-half plane and those from $-\kappa_p$ and $-\kappa_s$ taken in the lower-half plane. To be definitive in the calculations below, the branch cuts are chosen to run parallel to the imaginary axis from their respective branch points.

The dispersion equation in $k$ for the natural modes of propagation is obtained by substituting the solution forms from Eqs. (64)–(66) into the boundary conditions from Eqs. (58)–(60), evaluated on $y=\pm1$. Requiring the determinant of the resulting set of simultaneous equations, in the unknown coefficients $E$, $F$, $X$, and $Y$, to be zero then leads to the following dispersion equation:

$$\begin{aligned}\mathcal{D}_{ve}=\frac{1}{\mathcal{D}_1\mathcal{D}_2}\Bigg\{&\mathcal{D}_{vr}\left\{\mathcal{D}_1+4ik^2\mathcal{P}\left[\mathcal{D}_2(2+i\mathcal{P})-\kappa_s^2\right]\right\}\\&+\frac{\kappa_s^2}{\rho_s}\Big\{2k^2\left[2\mathcal{D}_2(1+i\mathcal{P})-\kappa_s^2\right]\\&\times\tanh\alpha-\kappa_s^2\left[\alpha\gamma_p+\gamma_s\gamma_2\tanh\gamma_2\tanh\alpha\right]\Big\}\\&+\frac{\kappa_s^4}{\rho_s^2}\mathcal{D}_2\tanh\alpha\Bigg\}=0,\end{aligned} \tag{67}$$

where $\mathcal{D}_1=(2k^2-\kappa_s^2)^2-4k^2\gamma_s\gamma_p=0$ is Rayleigh's dispersion equation for natural modes on the surface of a stress-free elastic half-space, and $\mathcal{D}_2=k^2-\gamma_s\gamma_p$ is the dispersion equation for the natural modes on the surface of a clamped elastic half-space. Furthermore, $\mathcal{D}_{vr}$ is the dispersion equation [Eq. (27)] for the natural modes of propagation along a rigid-walled channel filled with a viscous fluid in which thermal effects are negligible. We note that in the limit of $\mu,\rho_s\to\infty$ with $\mu/\rho_s=$constant, Eq. (67) reduces to $\mathcal{D}_{vr}=0$.

### C. Fluid structure interaction implementation for air and water filled channels in steel

Let us now consider the implementation of the above in the specific case of a fluid-filled channel in steel with density $\bar{\rho}_s=7871\,\mathrm{kg\ m^{-3}}$, and compressional and shear wave-speed $\bar{v}_p=6000\ \mathrm{m\ s^{-1}}$ and $\bar{v}_s=3000\ \mathrm{m\ s^{-1}}$, respectively. These parameter values imply a shear modulus $\bar{\mu}=70.839$ GPa and a Lamé modulus $\bar{\lambda}=141.68$ GPa.

For air- and water-filled channels, $\mathcal{P}\ll1$ and may be set to zero in Eq. (67). Furthermore, as discussed in Sec. IV A, at frequencies and channel-widths of interest $\omega\zeta\ll1$, $\omega\ll1$, and we expect $k=O(\omega)$. Thus, $\alpha\approx\sqrt{-i\omega/\eta}=(1-i)/\sqrt{2}\delta_\nu$, which is independent of $k$, and $\gamma_2\approx\sqrt{k^2-\omega^2}$, where $|\gamma_2|\ll1$. Under these conditions, we find that the non-dimensional phase speed, $v=\omega/k$, satisfies the following approximate dispersion equation:

$$\mathcal{D}_{ve} \approx \frac{1}{\hat{\mathcal{D}}_1\hat{\mathcal{D}}_2}\left\{\hat{\mathcal{D}}_1\left[\frac{\tanh\alpha}{\alpha}-(1-v^2)\right]\right.$$
$$+\frac{1}{\rho_s}\frac{v^2}{v_s^2}\left\{2\left[2\hat{\mathcal{D}}_2-\frac{v^2}{v_s^2}\right]\frac{\tanh\alpha}{\alpha}\right.$$
$$\left.\left.-\frac{v^2}{v_s^2}\left[\frac{v}{\omega}\hat{\gamma}_p+\frac{\omega}{v}\hat{\gamma}_s(1-v^2)\frac{\tanh\alpha}{\alpha}\right]\right\}\right.$$
$$\left.+\frac{1}{\rho_s^2}\frac{v^4}{v_s^4}\hat{\mathcal{D}}_2\frac{\tanh\alpha}{\alpha}\right\}=0, \tag{68}$$

where $\hat{\gamma}_p=\sqrt{1-v^2/v_p^2}$, $\hat{\gamma}_s=\sqrt{1-v^2/v_s^2}$, $\hat{\mathcal{D}}_1=(2-v^2/v_s^2)^2-4\hat{\gamma}_s\hat{\gamma}_p$, $\hat{\mathcal{D}}_2=1-\hat{\gamma}_s\hat{\gamma}_p$, with $v_p=\bar{v}_p/\bar{c}_0$ and $v_s=\bar{v}_s/\bar{c}_0$ being the non-dimensional compressional and shear wave-speeds; all of these parameters are independent of frequency.

It is clear from the above expression that the dependence of phase speed upon frequency is somewhat more complicated for an elastic-walled channel than it is for the case of a rigid-walled channel, expressions for which are provided in Eqs. (37) and (38).

### 1. Phase speed and attenuation

All the results presented in this section were obtained from the full dispersion equation [Eq. (67)]. Figure 6 shows results for phase speed and attenuation as a function of $\bar{\delta}_s/\bar{W}$ along an air-filled channel in steel at 10 kHz, compared with those for a rigid-walled channel, noting that thermal effects have been neglected. Figure 7 reveals the behavior of a water-filled channel. Also illustrated in the latter are the phase speed and attenuation along a steel-walled channel neglecting viscosity. The latter data were obtained from the roots of the dispersion equation for an elastic-walled channel, filled with an inviscid fluid; these are derived from the boundary conditions applicable to this case, namely,

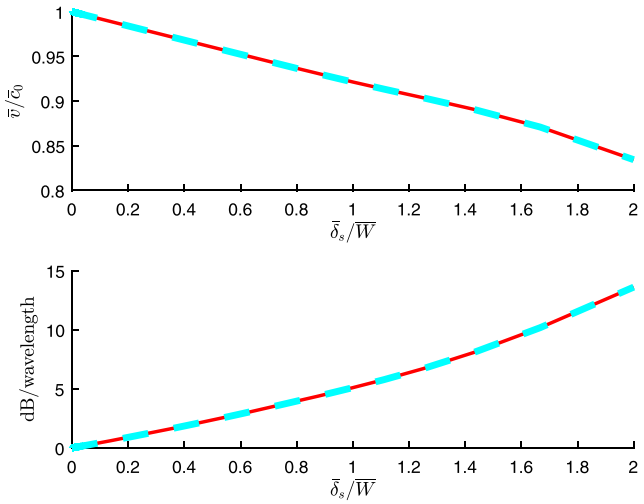


FIG. 6. (Color online) Phase speed and attenuation along an air-filled channel at 10 kHz. The upper plot shows the phase speed relative to $\bar{c}_0$. The lower plot shows the attenuation along the channel (dB/wavelength). In both plots, the solid red curve indicates a rigid-walled channel, and the dashed cyan curve is associated with a steel-walled channel. Thermal effects are neglected.

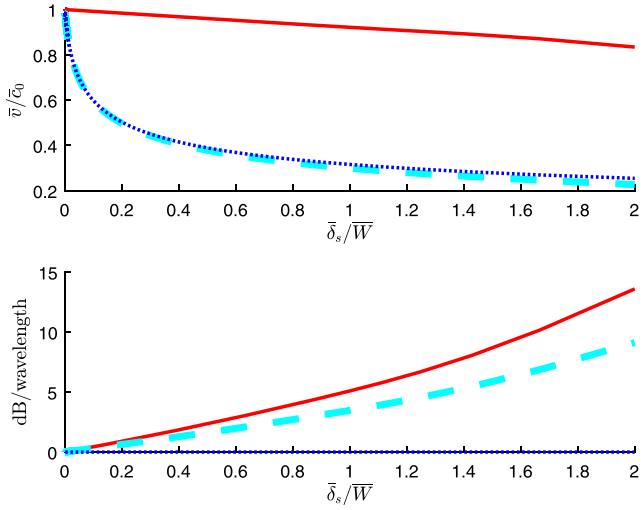


FIG. 7. (Color online) Phase speed and attenuation along a water-filled channel at 10 kHz. The upper plot shows the phase speed relative to $\bar{c}_0$. The lower plot shows the attenuation along the channel (dB/wavelength). In both plots, the solid red curve indicates results for a water-filled rigid-walled channel; the dashed cyan curve is associated with a water-filled steel-walled channel. The dotted blue curve is associated with propagation in a steel-walled water-filled channel where fluid viscosity is neglected. In all three cases, thermal effects are neglected.

$$\hat{\sigma}_{yy}(k,y=\pm1)=\hat{\Sigma}_{yy}(k,y=\pm1), \tag{69}$$
$$\hat{\sigma}_{xy}(k,y=\pm1)=0, \tag{70}$$
$$-i\omega\hat{w}_y(k,y=\pm1)=\hat{u}_y(k,y=\pm1), \tag{71}$$

in which viscosity is excluded by setting $E=\eta=\eta_B=0$. The dispersion equation, $\mathcal{D}_{ie}(\omega,k)=0$, is then readily shown to be

$$\mathcal{D}_{ie}(\omega,k)=\rho_s\gamma_2\tanh(\gamma_2)\left[(2k^2-\kappa_s^2)^2-4k^2\gamma_s\gamma_p\right]$$
$$+\kappa_s^4\gamma_p=0, \tag{72}$$

noting that if $\tanh(\gamma_2)$ were set to unity, Eq. (72) recovers the dispersion equation for Scholte waves, i.e., the dispersion equation for surface waves at the interface between elastic and fluid half spaces (Rauch, 1980).

It is clear from Fig. 6 that for air, the natural-mode behavior of the steel-walled channel is essentially indistinguishable from that of a rigid-walled channel when thermal effects are neglected, whereas in the case of a water-filled channel, these behaviors are dramatically different as seen in Fig. 7. This is due to the strong interaction between water and the steel wall, which has the effect of slowing down the phase speed of the natural mode and reducing its attenuation along the channel in terms of dB/wavelength. The damping mechanism for the mode is still that of dissipation within the viscous boundary layer on the steel wall, as opposed to radiation loss through the wall into the elastic material. This is apparent from the inviscid curves of Fig. 7, which show that fluid structure interaction is the main cause of the dramatic reduction in phase speed, but alone this mechanism gives no damping.

Although the attenuation in terms of dB/wavelength is substantially smaller in water for the steel-walled channel

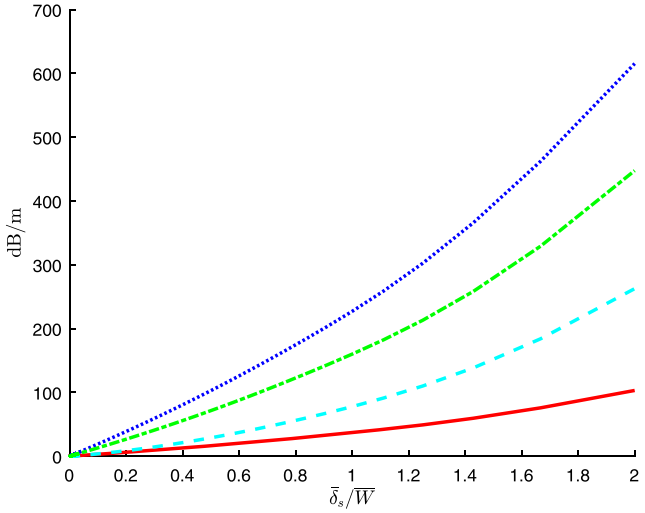


FIG. 8. (Color online) Attenuation along air and water-filled channels at 10 kHz (dB m$^{-1}$). Line styles indicate attenuation associated with propagation in a water-filled rigid-walled channel (solid red); a water-filled steel-walled channel (dashed cyan); an air-filled rigid-walled channel with isothermal boundary conditions (dotted blue); an air-filled rigid-walled channel with insulating boundary conditions (dash-dotted green).

than the rigid-walled case, the attenuation measured along a fixed length of say 1 m is actually greatly increased due to the large reduction in phase speed, which gives rise to a much smaller wavelength. This is illustrated in Fig. 8, which compares the attenuation at 10 kHz in dB m$^{-1}$ along water-filled rigid and elastic walled channels. For comparison, the attenuation along an air-filled channel is also shown. We see that taken together, fluid-structure interaction and viscosity lead to a large increase in attenuation for the water-filled channel.

For completeness, Fig. 9 shows the behavior of a water-filled steel-walled channel at 100 kHz. Unlike the rigid-walled results discussed earlier, we see by comparison with Fig. 7

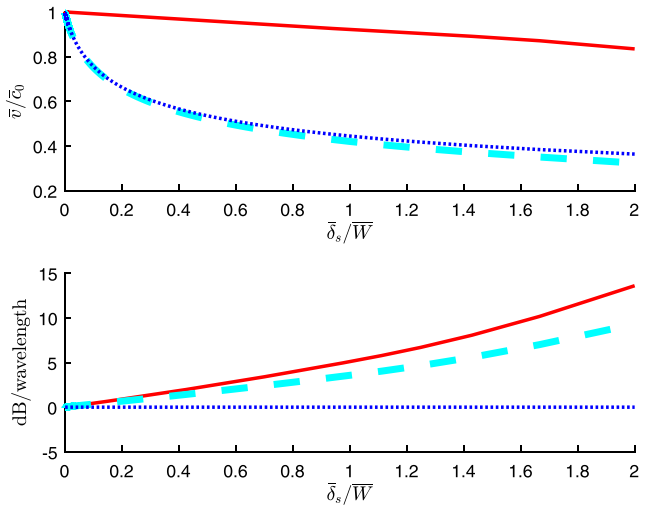


FIG. 9. (Color online) Phase speed and attenuation along a water-filled channel at 100 kHz. The upper plot shows the phase speed relative to $\bar{c}_0$. The lower plot shows the attenuation along the channel (dB/wavelength). In both plots, the solid red curve indicates results for a water-filled rigid-walled channel; the dashed cyan curve is associated with a water-filled steel-walled channel. The dotted blue curve is associated with propagation in a steel-walled water-filled channel, where fluid viscosity is neglected. In all three cases, thermal effects are neglected.

that the steel walled channel shows an additional frequency dependence beyond that associated with the thickness of the viscous boundary layer. This characteristic is illustrated further in Fig. 10, which illustrates the variation in phase speed and attenuation against non-dimensional frequency at a fixed value of $\bar{\delta}_s/\bar{W} = 1$. Whilst the attenuation is fairly constant across the range of values shown for $\omega$, the variation in phase speed is considerable unlike the case of a rigid channel wall for which both parameters would be constant.

### 2. Particle velocity profiles

Figures 11 and 12 compare fluid particle velocity profiles across a fluid-filled channel of width $10\bar{\delta}_s$ for rigid and steel walls, neglecting thermal effects. Figure 11, for air, shows no discernable difference in the behavior of the two wall types. The same is also true of the $x$-component of fluid particle velocity when the channel is filled with water. This is evident from the upper plot of Fig. 12. However, the lower plot of Fig. 12 shows that, for a water-filled channel, replacing the rigid wall with steel leads to a substantial change in the behavior of the $y$-component of fluid particle velocity. Indeed, for a steel-walled channel, $|u_y|$ is so much greater than that found for a rigid-walled channel that the plot of $|u_y|$ for the latter is only just observable at the bottom of the figure. Note that $|u_y| \not\to 0$ on the steel-walls. We observe that whilst in an air-filled channel, the steel wall may be regarded as rigid, this is not so when the channel is filled with water.

Similar behavior is seen for a much narrower channel as illustrated in Fig. 13 for a water-filled channel of width $\bar{\delta}_s/2$. Although not shown, for an air-filled channel, there is again no discernable difference between steel and rigid-walled channels.

Figure 14 shows the evolution of elastic-velocity with distance $\bar{y}_s$ from the channel wall for the case of a water-filled channel of width $\bar{\delta}_s/2$, noting that the elastic-velocity at the channel wall ($\bar{y}_s = 0$) matches that within the fluid of

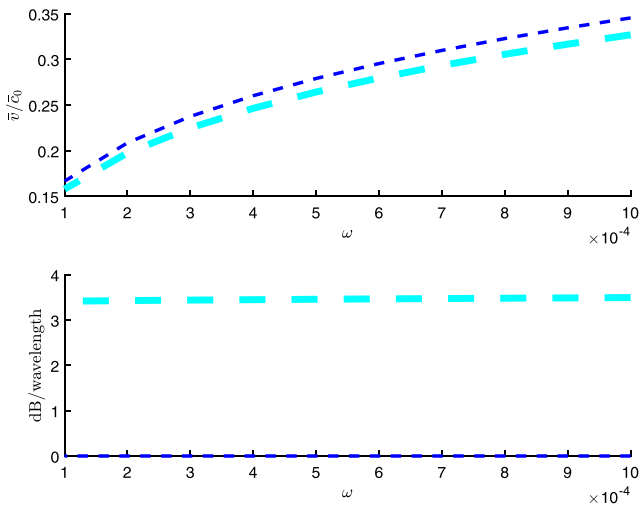


FIG. 10. (Color online) Phase speed and attenuation along a water filled channel of fixed width $\bar{\delta}_s/\bar{W} = 1$ as a function of the non-dimensional frequency $\omega$. The long-dashed cyan curves are associated with a water-filled channel including viscosity. The short-dashed blue curves are associated with a water-filled channel neglecting viscosity. The exterior elastic medium is steel. Thermal effects are neglected.

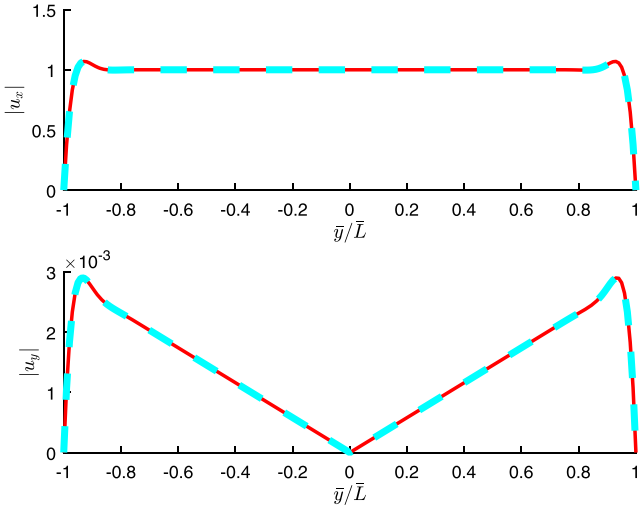


FIG. 11. (Color online) Magnitude of fluid particle velocity across an air-filled channel at 10 kHz for a channel width of $10\bar{\delta}_s$. The upper plot shows the $x$-component of fluid-particle-velocity, and the lower plot shows the $y$-component. $\boldsymbol{u}$ is normalized, independently for each boundary condition, such that $u_x(y=0)=1$. The solid-red curves indicate results associated with a rigid-walled channel, and the dashed-cyan curves are for a steel-walled channel. Thermal effects are neglected.

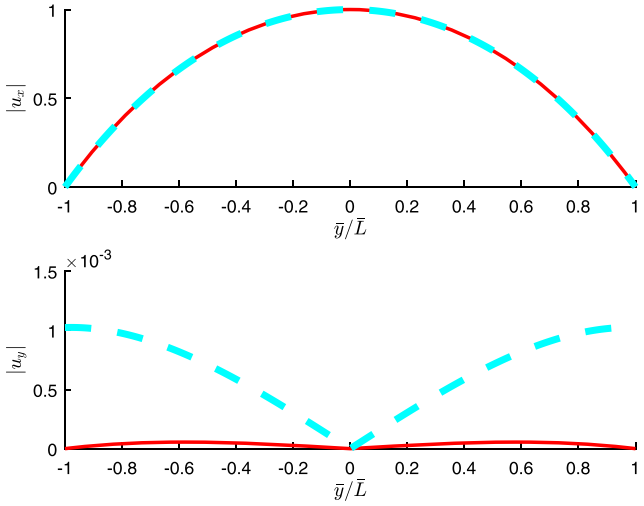


FIG. 13. (Color online) Magnitude of fluid particle velocity across a water-filled channel at 10 kHz for a channel width of $\bar{\delta}_s/2$. The upper plot shows the $x$-component of fluid-particle-velocity, and the lower plot shows the $y$-component. $\boldsymbol{u}$ is normalized, independently for each boundary condition, such that $u_x(y=0)=1$. The solid-red curves indicate a rigid-walled channel, and the dashed-cyan curves are for a steel-walled channel. Thermal effects are neglected.

Fig. 13 at $\bar{y}/\bar{L}=1$. It is clear that the elastic-velocity decays rapidly with increasing distance from the wall and hence the elastic waves associated with this mode do not carry energy away from the channel as surmised in Sec. V C 1.

It is perhaps worth considering in a little detail the nature of the propagating wave in a water-filled elastic-walled channel. For a semi-infinite elastic body, it is well known since the work of Lord Rayleigh that waves confined to its free surface can propagate without attenuation at a speed slightly less than that of shear body waves. If an inviscid fluid occupies the space above the elastic body, then the Rayleigh wave becomes *leaky* because its speed is greater than the wave speed in the fluid (i.e., it is supersonic). That is, energy is shed into acoustic waves above the solid, and hence the wave becomes attenuating. However, there is another wave at fluid/solid boundaries, called the Scholte wave, which is subsonic in both media and propagates without loss along the interface, decaying exponentially away from the boundary into both fluid and solid domains. It is found (Zhu *et al.*, 2004) that Scholte waves are not easily excited, as most of the energy is confined to the fluid region; the higher the acoustic impedance of the fluid, the stronger the Scholte wave becomes for a given forcing. Hence, for an air-steel interface, one expects to see near the surface that the Rayleigh waves dominate; they will leak energy slowly

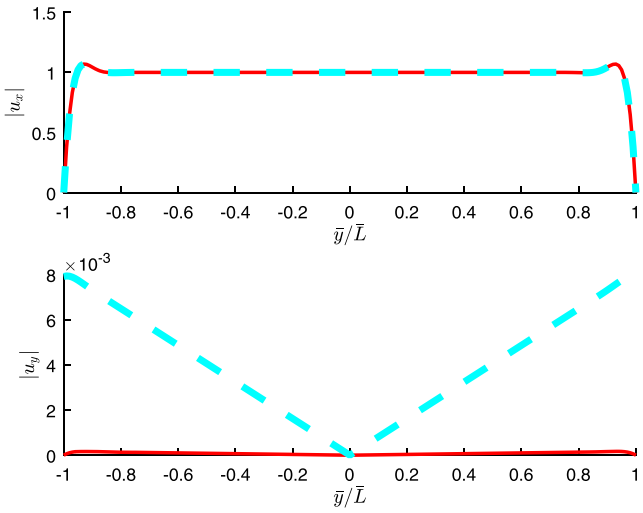


FIG. 12. (Color online) Magnitude of fluid particle velocity across a water-filled channel at 10 kHz for a channel width of $10\bar{\delta}_s$. The upper plot shows the $x$-component of fluid-particle-velocity, and the lower plot shows the $y$-component. $\boldsymbol{u}$ is normalized, independently for each boundary condition, such that $u_x(y=0)=1$. The solid-red curves indicate results associated with a rigid-walled channel, and the dashed-cyan curves are for a steel-walled channel. Thermal effects are neglected.

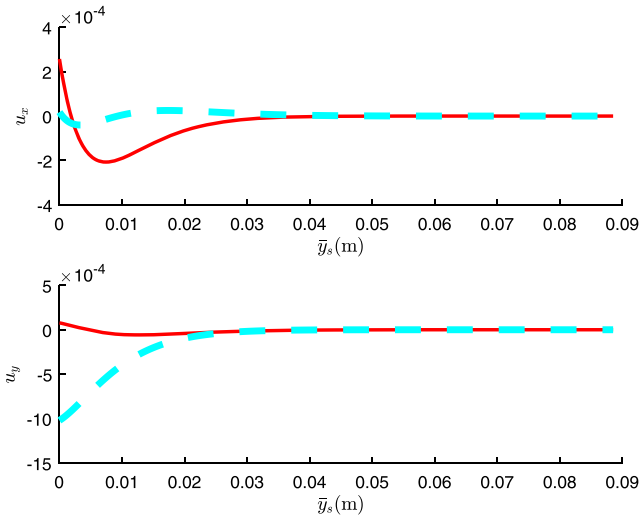


FIG. 14. (Color online) Steel wall velocity external to a water-filled channel at 10 kHz and $\bar{W}=\bar{\delta}_s/2$. The upper plot shows the $x$-component of particle-velocity, and the lower plot shows the $y$-component. In these plots, $\bar{y}_s$ denotes the dimensional distance from the channel wall within the solid. The velocity $\boldsymbol{u}$ is normalized such that $u_x=1$ at the center of the fluid-filled channel. The solid-red curves indicate the real part of velocity, and the dashed-cyan curves show the imaginary part. Thermal effects are neglected.

and the Scholte waves will be negligible. For water and steel, the Rayleigh waves will attenuate strongly due to radiation loss and Scholte waves will be more strongly excited.

The situation can be expected to be somewhat similar for water- or air-filled channels in steel; however, the leaky Rayleigh waves in both cases cannot radiate acoustic energy due to confinement and so will persist. However, the channel must be wide enough to allow the shed acoustic waves to propagate, or conversely, if the channel is too narrow, the coupled duct-Rayleigh wave mode will be cut-off. A numerical examination of the dispersion equation for the water-filled steel-walled channel indicates that at 10 kHz, the coupled duct-Rayleigh wave mode is cut-off for channel widths less than about $35\bar{\delta}_s$; we can then expect to find only a Scholte-type propagating wave mode in the water-filled steel-walled channel. This is consistent with results presented in Figs. 13 and 14 where most of the motion (and hence energy) is confined to the fluid region. Note that the presence of viscosity in the fluid means that the mode is attenuating along the channel, but otherwise it has little effect on the phase speed of the mode, as already seen.

## VI. CONCLUSIONS

A general framework has been presented with which one can study the influence of thermal and viscous effects on acoustic propagation in narrow channels or ducts filled with an arbitrary Newtonian fluid. Of specific interest here was to put the experimental results of Ward *et al.* (2015) on a formal theoretical footing and better understand their conclusions regarding the influence of the boundary layer on the attenuation of acoustic waves in channels. Furthermore, of great importance as regards applications was to extend this analysis to the consideration of thermo-visco acoustic propagation in water. The theoretical analysis presented indicates that it is *Stokes's* boundary layer thickness that gives a proper indication of the extent to which acoustic propagation along narrow channels is influenced by thermal and viscous boundary effects. The parameter $\bar{\delta}_\nu$ considered in the work of Ward *et al.* (2015) is an underestimate of the extent of the influence of the boundary layer and this therefore explains the effect that was noted in the analysis of the experimental results presented there. In the context of propagation *in-air*, it has been demonstrated here that thermal effects can be significant in a channel with thermally conducting walls, but they are negligible if the wall is thermally insulating. As should be expected, the results presented in Ward *et al.* (2015) sit between these two idealized cases. Turning to the context of acoustic propagation in the channel when it is water filled, it has been shown here that any associated thermal effects are always negligible thanks to the extremely low coefficient of thermal expansion of water.

For *rigid-walled* channels, filled with low viscosity fluids such as air and water, we find that the behavior of the lowest order symmetric duct-mode is captured by simple analytic expressions, one for each of the two channel-wall thermal boundary conditions that were considered. These expressions, valid up to at least 1 MHz in air and 50 MHz in water, demonstrate explicitly that for the thermally insulating boundary condition, the complex phase speed along the channel, $v = \bar{v}/\bar{c}_0$, is independent of thermal effects. Indeed, it depends only upon the channel's width relative to the viscous boundary layer parameter, $\bar{\delta}_\nu$; that is, $v$ depends only upon the dimensionless parameter $\bar{L}/\bar{\delta}_\nu$, with the latter containing all of the frequency dependence of $v$. For the thermally conducting boundary condition, we find that in addition to $\bar{L}/\bar{\delta}_\nu$, $v$ depends upon the Prandtl number, Pr, and the dimensionless parameter, $\mathcal{A} - 1 = \beta^2/c_p = (\bar{\beta}^2\bar{T}_0\bar{c}_0^2)/\bar{c}_p$; if $\sqrt{1/\mathrm{Pr}}\,(\beta^2/c_p)$ is small, as is the case for water, thermal effects are negligible.

An important aspect that *must* be taken into account for water-filled channels is the effect of the fluid-structure interaction associated with the channel wall. Although for the *in-air* context all boundaries can be considered as perfectly rigid, it is well known that the *in-water* situation cannot be treated with such a simplification. Attenuation of acoustic energy from the channel is thereby achieved via both viscous and radiative mechanisms (i.e., energy flux into the surrounding elastic medium). Only modal solutions in the channel have been considered here, therefore the partition of this attenuated energy into viscous and radiated parts was not discussed; there is a need to investigate this when considering *forced* problems, and this shall be the focus of future work. The latter shall also examine the cut-on of possible coupled duct-Rayleigh wave modes, and the partition of energy between this and the present Scholte-type channel mode.

For the present study of the lowest order symmetric duct mode, we find that for a water-filled channel in steel, the interaction between water and the steel-wall dramatically reduces the phase speed of the mode, even when the water is treated as inviscid. For example, in a channel whose width is on the order of $\bar{\delta}_s$, the phase speed reduces by approximately 70% at a frequency of 10 kHz. The introduction of viscosity has little further impact upon phase speed, but when the reduction in phase-speed arising from fluid-structure interaction is combined with viscous losses due to boundary layer effects, we find that the mode's attenuation, in $\mathrm{dB\,m^{-1}}$, is much greater than it would be for a rigid-walled channel. For example, at 10 kHz and a channel width of order $\bar{\delta}_s$, the attenuation increases from about $37\ \mathrm{dB\,m^{-1}}$ in a rigid-walled channel to over $77\ \mathrm{dB\,m^{-1}}$ in a steel-walled channel.

We close by commenting that although the main focus of this study has been to investigate the differences between thermo-viscous acoustic propagation in air and water-filled channels, the general theoretical framework presented here for arbitrary Newtonian fluids and elastic walls permits future study of more general configurations. Further studies on higher order modes can also be conducted although the study here of the leading order symmetric mode already indicates key, important differences between the air-filled and water-filled scenarios.

## ACKNOWLEDGMENTS

This work was carried out under the Thales UK SMART Hub 2 agreement. W.J.P. acknowledges the EPSRC for funding his research fellowship (EP/L018039/1). I.D.A. undertook part of this work whilst in receipt of a Royal Society Wolfson Research Merit Award, and part was supported by the Isaac Newton Institute under EPSRC Grant No. EP/R014604/1. E.G.-N. acknowledges the EPSRC and Thales UK for funding via a KTN Industrial CASE PhD Studentship. The authors are grateful to Ward *et al.* for permission to reproduce their data (Ward *et al.*, 2015).

## APPENDIX: NOTATION

Table II summarizes the notation employed.

TABLE II. Table summarizing notation employed, noting that quantities with an over-bar are dimensional and those without are non-dimensional.

| | |
|---|---|
| $\bar{L}$ | Channel half-width |
| $\bar{\mathcal{L}}$ | Problem specific length scale (set to $\bar{L}$ for the channel problem) |
| $\bar{T}_0, \bar{T}$, $\theta = (\bar{T} - \bar{T}_0)/\bar{T}_0$ | Ambient, total and fractional fluctuation of the fluids temperature |
| $\bar{\rho}_0$, $\bar{\rho}, s = (\bar{\rho} - \bar{\rho}_0)/\bar{\rho}_0$ | Ambient, total and fractional fluctuation (condensation) of the fluid's density |
| $\bar{p}_0, \bar{p}$, $p = (\bar{p} - \bar{p}_0)/(\bar{\rho}_0 \bar{c}_0^2)$ | Ambient, total and non-dimensional acoustic pressure of the fluid |
| $\bar{c}_0$ | Adiabatic sound speed of the fluid |
| $\bar{\omega}, \omega = \bar{\omega}\bar{\mathcal{L}}/\bar{c}_0$ | Radian frequency and non-dimensional counterpart |
| $\bar{c}_p, c_p = \bar{T}_0 \bar{c}_p/\bar{c}_0^2$ | Specific heat at constant pressure of the fluid and non-dimensional counterpart |
| $\bar{\beta}$, $\beta = \bar{\beta}\bar{T}_0$ | Coefficient of thermal expansion of the fluid and non-dimensional counterpart |
| $\mathcal{A} = 1 + \beta^2/c_p$, | Non-dimensional parameter associated with $\beta$ and $c_p$ |
| $\bar{\eta} = \bar{\rho}_0 \bar{c}_0 \bar{\mathcal{L}} \eta$, $\bar{\eta}' = \bar{\rho}_0 \bar{c}_0 \bar{\mathcal{L}} \eta'$ | First (shear) and second coefficients of fluid viscosity |
| $\bar{\eta}_B = \bar{\eta}' + 2/3\bar{\eta}$ $= \bar{\rho}_0 \bar{c}_0 \bar{\mathcal{L}} \eta_B$ | Bulk fluid viscosity |
| $\zeta = 2\eta + \eta'$ $= \eta_B + (4/3)\eta$ | Non-dimensional viscosity parameter |
| $\bar{\nu} = \bar{\eta}/\bar{\rho}_0$ | Kinematic viscosity of the fluid |
| $\bar{\delta}_\nu = \sqrt{\bar{\nu}/\bar{\omega}}$, | Viscous boundary layer parameter |
| $\bar{\delta}_s = 2\pi\sqrt{2}\,\bar{\delta}_\nu$ | Stokes' boundary layer parameter |
| $\bar{h}_0, \bar{h}$, $h = \bar{T}_0(\bar{h} - \bar{h}_0)/\bar{c}_0^2$ | Ambient, total and non-dimensional fluctuation of the fluid's entropy |
| $\bar{\mathcal{K}}, \mathcal{K} = \bar{T}_0 \bar{\mathcal{K}}/(\bar{\rho}_0 \bar{c}_0^3 \bar{\mathcal{L}})$ | Coefficient of thermal conductivity of the fluid and non-dimensional counterpart |
| $\mathcal{C} = \mathcal{K}/c_p$ | Non-dimensional thermal diffusion coefficient of the fluid |
| $\lambda = \bar{\lambda}/(\bar{\rho}_0 \bar{c}_0^2)$, $\mu = \bar{\mu}/(\bar{\rho}_0 \bar{c}_0^2)$ | Lamé's elastic and shear modulus |
| $\rho_s = \bar{\rho}_s/\bar{\rho}_0$ | Solid density |
| $\bar{v}_p, v_p = \bar{v}_p/\bar{c}_0$ | Compressional wave-speed of the solid and non-dimensional counterpart |
| $\bar{v}_s, v_s = \bar{v}_s/\bar{c}_0$ | Shear wave-speed of the solid and non-dimensional counterpart |
| $\kappa_1, \kappa_2$ | Coupled thermo-compressional wavenumbers of the fluid |
| $\gamma_j = (k^2 - \kappa_j^2)^{1/2}$, j = 1,2 | Arises in argument of thermo-compression solution, given $e^{ikx}$ dependence |
| $\alpha = (k^2 - i\omega/\eta)^{1/2}$ | Arises in argument of vorticity solution, given $e^{ikx}$ dependence |
| $\kappa_p = \omega/v_p$, $\kappa_s = \omega/v_s$ | Non-dimensional compressional and shear elastic wavenumbers |
| $\gamma_p = (k^2 - \kappa_p^2)^{1/2}$ | Arises in argument of compressional elastic solution, given $e^{ikx}$ dependence |
| $\gamma_s = (k^2 - \kappa_s^2)^{1/2}$ | Arises in argument of shear elastic solution, given $e^{ikx}$ dependence |
| $\Omega$ | $z$ component of vorticity $\boldsymbol{\Omega} = \nabla \times \mathbf{u} = \Omega\hat{\mathbf{k}}$ |
| $\phi = \nabla \cdot \boldsymbol{w}$ | Compressional elastic potential (dilation) |
| $\psi$ | $z$ component of shear elastic potential, $\boldsymbol{\psi} = \nabla \times \boldsymbol{w} = \psi\hat{\mathbf{k}}$ |
| $\bar{\boldsymbol{\sigma}} = \bar{\rho}_0 \bar{c}_0^2 \boldsymbol{\sigma}$ | Viscous stress tensor |
| $\bar{\boldsymbol{u}} = \bar{c}_0 \boldsymbol{u}$ | Fluid particle velocity |
| $v = \bar{v}/\bar{c}_0 = \omega/k$ | Phase speed along channel |
| $\bar{\boldsymbol{w}} = \bar{L}\boldsymbol{w}$ | Elastic displacement |
| $\bar{W} = 2\bar{L}$ | Channel width |


Allard, J., and Atalla, N. (**2009**). *Propagation of Sound in Porous Media: Modelling Sound Absorbing Materials* (Wiley, New York).

Baik, K., Jiang, J., and Leighton, T. G. (**2010**). "Acoustic attenuation, phase and group velocities in liquid-filled pipes: Theory, experiment, and examples of water and mercury," J. Acoust. Soc. Am. **128**(5), 2610–2624.

Batchelor, G. K. (**2000**). *An Introduction to Fluid Dynamics* (Cambridge University Press, Cambridge, UK).

Beltman, W. (**1999a**). "Viscothermal wave propagation including acousto-elastic interaction, Part I: Theory," J. Sound Vib. **227**(3), 555–586.

Beltman, W. (**1999b**). "Viscothermal wave propagation including acousto-elastic interaction, Part II: Applications," J. Sound Vib. **227**(3), 587–609.

Bruneau, M., Herzog, P., Kergomard, J., and Polack, J. (**1989**). "General formulation of the dispersion equation in bounded visco-thermal fluid, and application to some simple geometries," Wave Motion **11**(5), 441–451.

Christensen, J., Martin-Moreno, L., and Garcia-Vidal, F. J. (**2008**). "Theory of resonant acoustic transmission through subwavelength apertures," Phys. Rev. Lett. **101**(1), 014301.

Del Grosso, V. (**1971**). "Analysis of multimode acoustic propagation in liquid cylinders with realistic boundary conditions–application to sound speed and absorption measurements," Acta Acust. united Acust. **24**(6), 299–311.

Dokumaci, E. (**2014**). "On the effect of viscosity and thermal conductivity on sound propagation in ducts: A re-visit to the classical theory with extensions for higher order modes and presence of mean flow," J. Sound Vib. **333**(21), 5583–5599.

Dunn, F., Hartmann, W., Campbell, D., and Fletcher, N. (**2015**). *Springer Handbook of Acoustics* (Springer, New York).

Elvira-Segura, L. (**2000**). "Acoustic wave dispersion in a cylindrical elastic tube filled with a viscous liquid," Ultrasonics **37**(8), 537–547.

Estrada, H., Candelas, P., Uris, A., Belmar, F., De Abajo, F. G., and Meseguer, F. (**2008**). "Extraordinary sound screening in perforated plates," Phys. Rev. Lett. **101**(8), 084302.

Feynman, R. P., Leighton, R. B., and Sands, M. (**1965**). *The Feynman Lectures on Physics, Vol. II, Quantum Mechanics 1-1* (California Institute of Technology, Pasadena, CA).

Gomperts, M. C., and Kihlman, T. (**1967**). "The sound transmission loss of circular and slit-shaped apertures in walls," Acta Acust. united Acust. **18**(3), 144–150.

Gompeters, M. C. (**1964**). "The 'sound insulation' of circular and slit-shaped apertures," Acta Acust. united Acust. **14**(1), 1–16.

Helmholtz, H. (**1863**). "On the influence of friction in the air on sound motion," Verhandl. Naturhist. Med. Ver. Heidelberg **3**, 16–20.

Jiménez, N., Cox, T. J., Romero-García, V., and Groby, J.-P. (**2017**). "Metadiffusers: Deep-subwavelength sound diffusers," Sci. Rep. **7**(1), 5389.

Jiménez, N., Huang, W., Romero-García, V., Pagneux, V., and Groby, J.-P. (**2016**). "Ultra-thin metamaterial for perfect and quasi-omnidirectional sound absorption," Appl. Phys. Lett. **109**(12), 121902.

Kirchhoff, G. (**1868**). "Ueber den einfluss der wärmeleitung in einem gase auf die schallbewegung" ("On the effect of heat conduction on the propagation of sound waves"), Ann. Phys. **210**(6), 177–193.

Kundt, A. (**1868**). "Untersuchungen über die schallgeschwindigkeit der luft in röhren" ("Studies on the sound speed of air in pipes"), Ann. Phys. **211**(11), 337–372.

Leppington, F. G., and Levine, H. (**1973**). "Reflexion and transmission at a plane screen with periodically arranged circular or elliptical apertures," J. Fluid Mech. **61**(1), 109–127.

Liangh, P., and Scarton, H. (**2002**). "Coincidence of thermoelastic and thermoviscous acoustic waves in fluid-filled elastic tubes," J. Sound Vib. **250**(3), 541–565.

Oldham, D., and Zhao, X. (**1993**). "Measurement of the sound transmission loss of circular and slit-shaped apertures in rigid walls of finite thickness by intensimetry," J. Sound Vib. **161**(1), 119–135.

Pierce, A. D. (**1978**). "Aeroacoustic fluid dynamic equations and their acoustic energy conservation corollary with $O_2$ and $N_2$ vibrational relaxation effects included," J. Sound Vib. **58**(2), 189–200.

Putra, A., and Thompson, D. J. (**2010**). "Sound radiation from perforated plates," J. Sound Vib. **329**(20), 4227–4250.

Rauch, D. (**1980**). "Seismic interface waves in coastal waters: A review," Technical Report No. SR-42, Saclant ASW Research Centre, La Spezia, Italy.
Rayleigh, J. W. S. B. (**1896**). *The Theory of Sound, Vol. 2* (Macmillan, London).
Stinson, M. (**1991**). "The propagation of plane sound waves in narrow and wide circular tubes, and generalization to uniform tubes of arbitrary cross-sectional shape," J. Acoust. Soc. Am. **89**(2), 550–558.
Stinson, M., and Champoux, Y. (**1992**). "Propagation of sound and the assignment of shape factors in model porous materials having simple pore geometries," J. Acoust. Soc. Am. **91**(2), 685–695.
Tijdeman, H. (**1975**). "On the propagation of sound waves in cylindrical tubes," J. Sound Vib. **39**(1), 1–33.
Ward, G., Lovelock, R., Murray, A., Hibbins, A., Sambles, J., and Smith, J. (**2015**). "Boundary-layer effects on acoustic transmission through narrow slit cavities," Phys. Rev. Lett. **115**(4), 044302.
Weston, D. (**1953**). "The theory of the propagation of plane sound waves in tubes," Proc. Phys. Soc. B **66**(8), 695–709.
Wilson, G. P., and Soroka, W. W. (**1965**). "Approximation to the diffraction of sound by a circular aperture in a rigid wall of finite thickness," J. Acoust. Soc. Am. **37**(2), 286–297.
Zhu, J., Popovics, J. S., and Schubert, F. (**2004**). "Leaky Rayleigh and Scholte waves at the fluid-solid interface subjected to transient point loading," J. Acoust. Soc. Am. **116**(4), 2101–2110.
Zwikker, C., and Kosten, C. (**1949**). *Sound Absorbing Materials* (Elsevier, Amsterdam, the Netherlands).

## 2.3 Additional comments

Here we provide some further observations that were not discussed in the paper above. In order to avoid confusion, where possible the notation employed follows that of the paper.

### 2.3.1 Acoustic admittance approximation for channels

Here we simply include some extra plots comparing some solutions obtained in the first part of the above paper involving rigid boundaries. In particular, we want to illustrate how the acoustic admittance approximation discussed in Section 1.3.2 can be applied to the waveguide problem and directly compared to the results obtained above, anticipating good approximations in the wide channel regions but less so in the narrow channel regime. The approximate solution is discussed in detail in Bruneau [2006] so we will simply provide a short justification.

In a similar way to the half-space problem which reduces to (1.127), (1.128) in the purely acoustic case, for the slit in consideration here we must also solve the Helmholtz equation (1.127) and instead apply (1.121) on $y = \pm 1$ which gives (recalling that $k = \omega$)

$$\left(\nabla^2 + \omega^2\right)\tilde{p} = 0, \tag{2.1a}$$

$$\left(\frac{\partial}{\partial y} + \mathrm{i}\omega\mathcal{B}\right)\tilde{p} = 0 \quad \text{on} \quad y = -1, \tag{2.1b}$$

$$\left(\frac{\partial}{\partial y} - \mathrm{i}\omega\mathcal{B}\right)\tilde{p} = 0 \quad \text{on} \quad y = 1, \tag{2.1c}$$

noting that the admittance $\mathcal{B} = 1/\mathcal{Z}$ generalised to an arbitrary incident profile mentioned earlier can be written as [Bruneau et al., 1987]

$$\mathcal{B} = \mathrm{e}^{\frac{-\mathrm{i}\pi}{4}}\sqrt{\omega}\left((\mathcal{A}-1)\sqrt{\mathcal{C}} + \left(1 - \frac{k_\perp^2}{k^2}\right)\sqrt{\eta}\right), \tag{2.2}$$

where in this case $k_\perp$ represents the y-component of the acoustic wavenumber, which we shall find next. We seek separable solutions of the form[1] $\tilde{p} = Y(y)\mathrm{e}^{\mathrm{i}\ell x}$ (where $\ell \in \mathbb{C}$)

[1] Note that $\ell$ has got the role of $k$ in the paper above, and the extra notation must be included since 'pure' acoustic propagation is not considered in the article. Instead $k = k_0 = \omega$ here is the freespace acoustic wavenumber which is clear from (2.1a).

to arrive at the following eigenvalue problem

$$Y''(y) - (\ell^2 - \omega^2)Y(y) = 0, \tag{2.3a}$$

$$Y'(y=-1) - \mathrm{i}\omega\mathcal{B}Y(y=-1) = 0, \tag{2.3b}$$

$$Y'(y=+1) + \mathrm{i}\omega\mathcal{B}Y(y=+1) = 0, \tag{2.3c}$$

whose general solution can be written, on defining $\chi^2 = -(\ell^2 - \omega^2)$, as

$$Y(y) = A\cos(\chi y) + B\sin(\chi y), \tag{2.4}$$

for constants $A, B$. Direct substitution of (2.4) onto (2.1b), (2.1c) leads to the system

$$\begin{pmatrix} 0 & -\mathrm{i}\omega\mathcal{B}\tan(\chi) + \chi \\ \chi\tan(\chi) + \mathrm{i}\omega\mathcal{B} & 0 \end{pmatrix} \begin{pmatrix} A \\ B \end{pmatrix} = \begin{pmatrix} 0 \\ 0 \end{pmatrix}. \tag{2.5}$$

Non-trivial solutions to this BVP arise when the determinant of the matrix above vanishes, which occurs whether

$$-\mathrm{i}\omega\mathcal{B}\tan(\chi) + \chi = 0, \qquad \text{or} \qquad \chi\tan(\chi) + \mathrm{i}\omega\mathcal{B} = 0, \tag{2.6}$$

which are the dispersion relations of the anti-symmetric and symmetric modes respectively and whose solutions encapsulate all the corresponding modes of propagation of this set-up. Numerical solutions to these dispersion equations for general parameters are given in Morse and Ingard [1986]. In this case nevertheless it is easy to see from (2.2) given prior discussion and the fact that $|k_\perp/k| \leq 1$ that $|\mathcal{B}| \ll 1$ for frequencies of interest, which allows for convenient asymptotic expansions. Namely for symmetric modes (introducing a subscript "$n$" to distinguish between modes)

$$\chi_n = n\pi - \frac{\mathrm{i}\omega\mathcal{B}}{n\pi} \quad \text{for } n > 0, \quad \text{and} \tag{2.7a}$$

$$\chi_0 = \sqrt{-\mathrm{i}\omega\mathcal{B}} \qquad \text{for } n = 0, \tag{2.7b}$$

see e.g. Bruneau et al. [1987]. We can therefore write,

$$\begin{aligned} \ell_n^2 &= \omega^2 - n^2\pi^2 + (2 - \delta_{n0})\mathrm{i}\omega\mathcal{B} + O(\mathcal{B}^2), \\ \implies \ell_n &\approx \omega\sqrt{1 - \frac{n^2\pi^2}{\omega^2}} + \frac{(2-\delta_{n0})\mathrm{i}\mathcal{B}}{2\sqrt{1 - \frac{n^2\pi^2}{\omega^2}}}, \end{aligned} \tag{2.8}$$

where $\delta_{n0} = 1$ for $n = 0$ and is zero otherwise. From the leading order term in (2.7a), we obtain that $k_\perp^2 \approx (n\pi)^2$ so that the expression for the admittance (2.2) becomes mode dependent, namely

$$\mathcal{B}_n \approx \mathrm{e}^{\frac{-\mathrm{i}\pi}{4}}\sqrt{\omega}\left((\mathcal{A}-1)\sqrt{\mathcal{C}} + \left(1 - \left(\frac{n\pi}{\omega}\right)^2\right)\sqrt{\eta}\right). \tag{2.9}$$

Description of higher order modes is given in Bruneau et al. [1987], but we are only interested in the fundamental plane wave mode, since the cut-off frequency in an equivalent inviscid fluid-filled channel requires[2] $\omega \leq n\pi$, and the main frequencies and channel widths of interest are such that $\omega < 1$, so setting $n = 0$ in (2.9) and (2.8) gives

$$\ell_0 \approx \omega + \frac{1+\mathrm{i}}{2}\sqrt{\frac{\omega}{2}}\left((\mathcal{A}-1)\sqrt{\mathcal{C}} + \sqrt{\eta}\right), \tag{2.10}$$

and hence, the associated pressure field due to this mode is

$$\widetilde{p} = \cos\left(\sqrt{-\mathrm{i}\omega\mathcal{B}_0}y\right)\mathrm{e}^{\mathrm{i}\ell_0 x} = \frac{1}{2}\left(\mathrm{e}^{\mathrm{i}\sqrt{-\mathrm{i}\omega\mathcal{B}_0}y + \mathrm{i}\ell_0 x} + \mathrm{e}^{-\mathrm{i}\sqrt{-\mathrm{i}\omega\mathcal{B}_0}y + \mathrm{i}\ell_0 x}\right), \tag{2.11}$$

which shows the very slight $y$ dependence. As given in the paper above, with (2.10) the phase speed along the direction of the channel is generally obtained by $v = \mathrm{Re}\{\omega/\ell\}$ and we measure the attenuation in dB/wavelength given by $40\pi\log_{10}(\mathrm{e})\,\mathrm{Im}(\ell)\,/\,\mathrm{Re}(\ell)$.

In Figure 2.1 we give comparisons of phase speed and attenuation for air between the approximate solution just obtained via the admittance BC approach (2.10), the low frequency approximation obtained in (38) of Section 2.2 as well as the numerical solutions to the full (isothermal) dispersion relation (25) of the same article. As discussed in the paper, the low frequency (LF) approximation for air is highly accurate up until frequencies of up to 1 MHz above which the phase speed and especially the attenuation starts deviating, as can be seen from the right of Figure 2.1. As we expected, the acoustic admittance BC is excellent for wide channels, but remains remarkably accurate for channel widths of the order of the boundary layer, particularly the phase speed (real part). Both the simplicity and accuracy of this approach in this regime make it a convenient modelling tool to incorporate losses. For example, Molerón et al. [2016] used this model for the characterization of visco-thermal losses in different types of various in-air acoustic metamaterials with complex geometries and good agreement with experiments was found. For much narrower channels, the

[2] As can be seen by setting $\mathcal{B} = 0$ in (2.8).

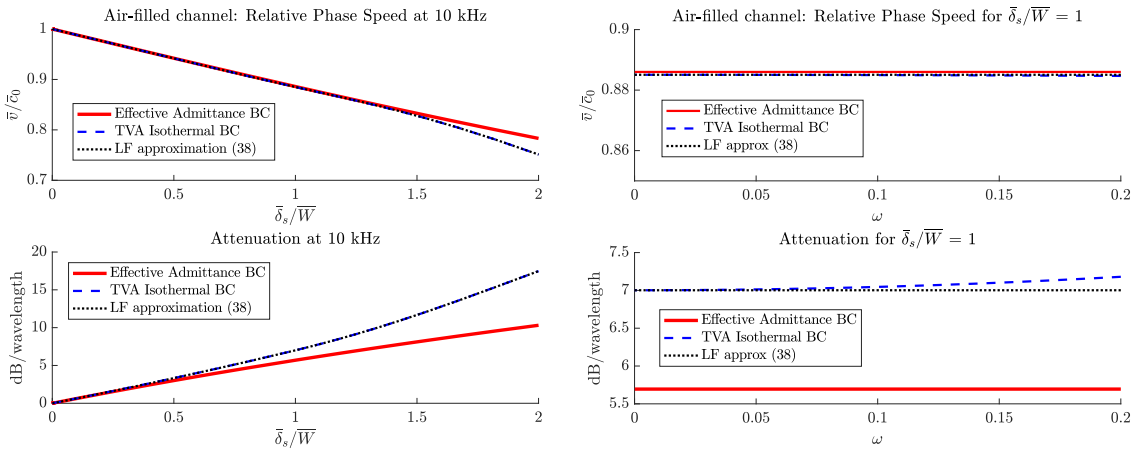


Figure 2.1: Comparisons between phase speed and attenuation of the fundamental mode in a rigid (infinitely extending) air-filled channel as a function of (non-dimensional) channel width (left) and frequency (right).

situation becomes more difficult to asses without further work because even the full TVA solution seems to diverge from the experiments by Ward et al. [2015] illustrated in Fig 2 of Section 2.2. Furthermore, the experimental data from Ward et al. [2015] in this regime is also not reliable as can be seen explicitly from the large error bars in FIG 4 of that work.

### 2.3.2 FSI effects for softer solid media

As we have been discussing (and is written explicitly in the above conclusions) when doing *in-air* acoustics (most) solid boundaries may be considered perfectly rigid, in contrast to the *in-water* case, which is explicitly illustrated in FIGs 6, 7 of Section 2.2. This can be illustrated by the difference in density ratio with the parameters used above giving $\rho_s \approx 6614$ for air–steel whereas for water–steel we obtain $\rho_s = 7.871$. We thought it would be interesting to analyse the dependence of the behaviour obtained on the particular properties of steel, which is very 'acoustically hard' even for water, manifested by its shear wave speed ($\bar{v}_s = 3000$ m/s) being more than twice that of the speed of sound in water ($\bar{c}_0 = 1490$ m/s). We therefore consider a contrasting material consisting of a softer synthetic resin (PVC) analysed in Favretto-Anrès [1996] which we consider to be elastic with parameters $\bar{v}_p = 2268$ m/s, $\bar{v}_s = 1100$ m/s and $\bar{\rho}_s = 1360$ kg/m$^3$, noting that the shear wave speed of the solid is now *subsonic*.

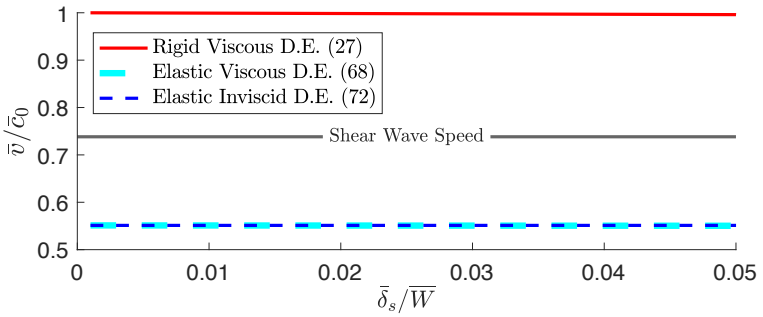


Figure 2.2: Phase speed along wide, water-filled PVC channels at 10 kHz for various dispersion equations discussed above. There is a significant reduction in phase speed which was not observed with steel.

The results obtained for air are the same as those for steel in FIG 6 (of Section 2.2), as expected since $\rho_s = 1142.9$. However for water, we now have $\rho_s = 1.36$ and the results (particularly the phase speed) are significantly different to those obtained for water–steel and illustrated above in FIGs 7–14 (of Section 2.2). This is illustrated explicitly in Figure 2.2, where we observe that unlike in all previous cases, the solution does not get close to $\bar{c}_0$. In order to understand this, as it was done for the rigid case where we saw that $\bar{v} \to \bar{c}_0$, we must take the limit $\bar{L} \to \infty$ in the relevant dispersion equations, namely (68), (72) of Section 2.2. Since viscosity does not play an important role for wide channels (which is clear from Figure 2.2), we choose to do it for (72) given its simplicity, to obtain

$$\rho_s \sqrt{k^2 - \omega^2} \left[ (2k^2 - \kappa_s^2)^2 - 4k^2 \gamma_s \gamma_p \right] + \kappa_s^4 \gamma_p = 0, \tag{2.12}$$

which is the Scholte dispersion equation for surface waves at the interface between ideal fluid–elastic half–spaces. Intuitively, we can see how the larger $\rho_s$ becomes (with the other quantities fixed), the closer $k = \omega$ becomes a solution to (2.12), which is normally the case for air. It turned out that the same occurs for water–steel, but as we have illustrated with Figure 2.2 this is certainly not the case when $\rho_s \to 1$. Therefore, in terms of extending the framework presented above for *any* elastic solid, it is the roots of (2.12) which must dictate the initial point of our iterative solver, noting that we believe it is useful to address the mode consideration as the 'coupled duct–Scholte mode'.

The analysis of this chapter has been focused around boundary losses within the fluid at small length-scales, but the solids considered in the FSI section were modelled

as perfectly elastic following Section 1.4.1 which is particularly relevant for hard solids like steel. However, from a physical perspective as suggested in Section 1.4.2 we notice that *soft* solid media can be particularly attenuating in many circumstances [Chen, 2000]. It is therefore of interest to be able to include such effects in order to asses the overall differences with the results presented above. This will be considered further in Chapter 4, but before this we will focus on the development of a theory for (coupled) linear TVE.

# Chapter 3

# A framework for linear TVE

## 3.1 Introduction

This chapter is devoted to the development of a framework for linear thermo-viscoelasticity (TVE), as suggested in Section 1.4.3. Starting from the conservation equations of continuum mechanics, the first half of the paper in Section 3.2 is centred around the theoretical considerations and assumptions that are necessary in order to ultimately obtain the relevant governing equations. Emphasis is put on the distinction between time 'locality' and 'non-locality' and how the latter is generally necessary in order to characterize both creep and stress relaxation (see Figures 1.10, 1.11). We show how the resulting equations can be decomposed in the frequency domain in order to yield three Helmholtz type equations for the two thermo-compressional wave potentials and the shear wave potential, as in TVA. We then provide asymptotic approximations that highly simplify the thermo-compressional wavenumbers, and show how TVA as well as other more classical theories such as those presented in Section 1.4.2 can be recovered from this general TVE formulation. In particular, we show how it becomes possible to study thermo-viscous losses in fluids and solids simultaneously as depicted in Figures 1.12, 1.13. The framework is then applied to a canonical scattering problem consisting of plane wave forcing on two semi-infinite TVE half-spaces. The physical results are mainly concerned with reflection and transmission on fluid-solid interfaces, and results for air, water, steel and rubber are provided. For the latter, we show how stress relaxation effects can be important.

This paper was first written by E García Neefjes, based on some preliminary notes on local TVE initiated by WJ Parnell and AL Gower for a separate multiple-scattering project in collaboration with VJ Pinfield. The initial numerical implementation was done by E García Neefjes under the supervision of AL Gower. Most of the code involved in this piece of work is available at AL Gower (GitHub). The physical results and parameter space studies were discussed extensively with D Nigro. Specific feedback and general discussions with the remaining co-authors helped improve the paper to the current standard. This work is intended to be submitted for publication shortly.

## 3.2 Article

# A unified framework for linear thermo-visco-elastic wave propagation including the effects of stress-relaxation.

Erik García Neefjes[1], David Nigro[2], Artur L. Gower[3],
Raphaël C. Assier[1], Valerie J. Pinfield[4], William J. Parnell[1]

[1]Department of Mathematics, University of Manchester, Oxford Rd, Manchester, M13 9PL, UK

[2]Thales UK, 350 Longwater Avenue Green Park, Reading RG2 6GF, UK

[3] Department of Mechanical Engineering, University of Sheffield, Sheffield, S10 2TN, UK

[4] Department of Chemical Engineering, Loughborough University, Loughborough, LE11 3TU, UK

March 9, 2022

**Abstract**

Lossless wave propagation models for diverse continua, including fluids and solids, have severe limitations in problems of practical interest. Even in linear problems, the additional complexities that arise due to the incorporation of attenuating mechanisms are such that in practice, they are often approximated or models are fitted to experimental data at fixed frequencies or in narrow frequency ranges. Although often sufficient for good agreement with experiments on given materials or in certain frequency ranges, the validity of the approximations (frequently introduced in a rather ad-hoc manner) are rarely discussed extensively and the wider applicability of such models is therefore not clear. With this as motivation, here we present a unified framework for the study of wave propagation in linear thermo-visco-elastic (TVE) media. This framework establishes that although the various limits taken from full TVE to more simple theories that neglect specific effects are often useful, coupling these theories at boundaries can be non-trivial. Furthermore it also established that developing an accurate description of material behaviour in the time domain requires a careful evaluation of the frequency dependence of material properties and how this is accommodated in models. This is especially the case for polymeric materials.

Our starting point is the general theory of TVE. We then illustrate how common simpler theories are derived via limits of that theory. In the general unified linear model, the incorporation of creep and stress relaxation permits models for wave propagation in realistic time-dependent scenarios via transform to the frequency domain. We discuss polymeric and soft materials in particular, where such effects are often stronger and coupling between media can also arise more easily given that the distinction between fluid and elastic behaviour is not always particularly clear. The general framework is applied to the canonical problem of scattering from an interface between two TVE halfspaces in perfect contact. To illustrate dominant effects and the efficacy of the various approximations, we provide results for cases involving air, water, steel and rubber. We illustrate the conversion of energy into different modes, taking into account all aspects of transfer.

The incorporation of general frequency-dependent behaviour in the unified model means that the theory can be used as a convenient starting point for more complex problems involving time dependence. It can also be employed as the basis for the resonant behaviour of more complex media such as metamaterials, where modelling the attenuation mechanisms accurately is critical

in order to understand their realistic response over a broad range of frequencies. Finally the framework is also a good foundation for materials discovery problems, where there is great potential for new effects to be discovered.

# 1 Introduction

Even under small deformations, complex continua exhibit a variety of constitutive effects over a broad range of frequencies, associated with their atomistic, molecular or mesoscopic properties. In the field of continuum mechanics it has become common place to label a material either as *fluid* or *solid* and even when viscoelastic, for reasons of model simplification, there is a tendency to specify a medium as a viscoelastic *fluid* or viscoelastic *solid*. This matter is however made more complex when considering wave propagation in the medium over a wide range of frequencies and temperatures. Polymers are an exemplary example; they are fluid-like at low frequencies and solid-like at high frequencies and they take on similar properties as a (reciprocal) function of temperature [1, 2]. The shear modulus of a polymeric material can vary by several orders of magnitude after transitioning through the glass-transition frequency/temperature [3, 4].

Whilst the concept of assigning specific material behaviour is understandable in order to limit the number of parameters that have to be measured experimentally, it has led to unintended consequences and in some cases to additional complexities. For example, even in the simple case when two *homogeneous* continua couple at an interface one may consider one medium as an *acoustic* medium, with the other as *elastodynamic* [5]. Whilst seemingly a straightforward modelling problem, this is not always the case when there is strong coupling and the potential for loss, or when there are more complicated effects close to interfaces, which can be neglected in free space but cannot be in domains close to boundaries. In the context of thermo-visco-acoustics, effective boundary conditions have been devised to simplify the problem [6] but when strong coupling occurs, this same approach cannot be employed. What follows are then rather ad-hoc approaches and often questionnable approximations, particularly with regard to modelling in the time domain.

In more complex, inhomogeneous media or *metamaterials*, the frequency dependence can often be very strong due to inherent resonances associated with microstructure [7, 8]. These resonances are often tuned to be strong at low frequencies, given that this is often the regime in which traditional materials cannot yield dispersive effects. However the frequency dependence is tuned by resonator size and geometry, and the material properties of the matrix medium.

Understanding the wave propagation characteristics of metamaterials is frequently achieved by employing asymptotic theories, which rely on specific scalings of the material property contrast [9], [10]. If this dependence changes with frequency then the entire theory underpinning these materials could be described as unstable. And the kinds of materials involved in high contrast resonance *are* precisely materials that would possess strong frequency dependence.

One may argue that experiments at fixed frequencies can be fitted to a theory with certain fixed parameters, whether one considers a metamaterial or a simple, homogeneous medium. This is certainly the case and this approach has been employed very successfully in the past [11, 12]. However one may reasonably ask what happens when we change frequency, or design a resonator in the same matrix material to act at a different frequency, or even more reasonably what happens in the time domain? In all of these cases, of crucial importance is the ability to model the material's behaviour properly in the frequency domain. It appears uncomfortable from both a practical and scientific perspective to fit different parameters to the behaviour over a broad range of frequencies. It is certainly more beneficial to bring forth a theoretical framework that can accommodate such dependence. Kelvin-Voigt viscoelasticity has been used with some success, but this theory does not accommodate stress relaxation, which is critically important in polymers, when they undergo their

glass transition, considered in either frequency or temperature space. Although for most materials this transition seems to occur in the lower frequency regime, one of the crucial aspects is that it affects both the real and imaginary part of the particular modulus [13] whereas Kelvin-Voigt models only capture the latter.

In the present article, we return to the fundamentals of linear continuum mechanics and present a general, unified framework with which to model a variety of TVE materials of interest, with the specific interest in modelling how they couple at interfaces. We discuss Kelvin-Voigt visco-elasticity and the standard linear models that extend this to incorporate stress relaxation. The same governing equations are used in any domain, without any need to identify the medium as a fluid, solid, viscoelastic, or otherwise. Needless to say parameters are required, but this means that a priori, all that is required is the identification of values that identify the medium as linear TVE, thus allowing one to model a vast range of important materials.

Over time the scientific community has developed a range of terms for specific media, e.g. *visco-acoustic*, *viscoelastic*, *thermoelastic* etc. where certain physical effects are neglected. These are certainly useful and helpful because in many cases the neglected effects are not important. Here we also provide the asymptotic framework with which one can switch between these theories. In many cases it is straightforward and we simply set specific constants to zero, meaning that a lack of coupling arises. However in some cases one must be careful in the manner by which the theory is simplified, as we discuss.

In Section 2 we begin with the conservation equations of homogeneous TVE materials, and describe local (in time) thermo-visco-elasticity before moving onto the more general non-local models that incorporate stress relaxation. These models are defined in the frequency domain and we consider Prony series that permit frequency dependence of material properties [14]. In Section 3 we go on to describe useful and appropriate asymptotic limits of the theory of thermo-visco-elasticity. Section 4 covers the application of the various theories to the canonical problem of wave reflection from an interface between two continua, with the effects of coupling being illustrated and in particular the effects of relaxation on the frequency-dependent transmission and reflection. We close in Section 5 with conclusions.

The equations governing linear TVE wave propagation can be summarised as the following.

Solve three Helmholtz equations

$$\Delta\vartheta + k_\vartheta^2\vartheta = 0, \qquad \Delta\varphi + k_\varphi^2\varphi = 0, \qquad \Delta\boldsymbol{\Phi} + k_\Phi^2\boldsymbol{\Phi} = 0 \tag{1.1}$$

where

$$k_\theta^2 = \mathrm{i}\tilde{c}_v(\mathrm{i}\omega)\frac{\rho_0\omega}{\mathscr{K}}, \quad k_\phi^2 = \frac{\rho_0\omega^2}{\tilde{\lambda}(\mathrm{i}\omega)+2\tilde{\mu}(\mathrm{i}\omega)}, \quad k_\Phi^2 = \frac{\rho_0\omega^2}{\tilde{\mu}(\mathrm{i}\omega)}, \tag{1.2a}$$

$$L_\phi = \frac{\mathrm{i}\omega\tilde{\mathcal{R}}_3(\mathrm{i}\omega)}{\mathscr{K}}, \quad L_\theta = -\frac{T_0\tilde{\mathcal{R}}_3(\mathrm{i}\omega)}{\tilde{\lambda}(\mathrm{i}\omega)+2\tilde{\mu}(\mathrm{i}\omega)}. \tag{1.2b}$$

with notation defined in Table 1 and where the dependence of the material properties on the frequency $\omega$ is discussed throughout this paper, noting the non-local (in time) discussion required to accommodate stress relaxation.

The frequency dependence of material properties, as discussed above, is particularly critical as we shall discuss in much greater detail later in this paper. The framework set up here motivates a need for improved measurements of the frequency dependence of material properties over a broad

regime. Indeed, the literature is scant on information with regard to the frequency dependence of even the most simple properties such as shear modulus and frequently assumptions are made with little justification, e.g. the apparent lack of frequency dependence of the bulk modulus or Poisson's ratio [15].

| **Notation** | |
|---|---|
| Time derivative | $\dot{\circ} = \partial \circ / \partial t$ |
| Gradient operator | $\nabla \circ = \partial \circ / \partial x_i$ |
| Laplacian operator | $\Delta \circ = \nabla \cdot \nabla \circ$ |
| Tensor contraction | $\boldsymbol{A} : \boldsymbol{B} = A_{ij} B_{ij}$ |
| Matrix trace | $\mathrm{tr}(\circ)$ |
| Matrix transpose | $\circ^T$ |
| Fourier component | $\hat{\circ} = \circ \mathrm{e}^{-\mathrm{i}\omega t}$ |
| Complex conjugate | $\circ^*$ |
| Heaviside function | $H$ |
| Three-dimensional Identity tensor | $\boldsymbol{I}$ |
| Average over wave period | $\langle \circ \rangle = \frac{\omega}{2\pi} \int_t^{t+2\pi/\omega} (\circ)\, \mathrm{d}s$ |

| **Thermo-Visco-Elastic Parameters** | | |
|---|---|---|
| **Parameters** | **Unit(s)** | **Symbols and Definitions** |
| Continuum's displacement vector | m | $\mathbf{u}$ |
| Infinitesimal strain tensor | – | $\boldsymbol{\varepsilon} = (\nabla \mathbf{u} + (\nabla \mathbf{u})^T)/2$ |
| Off-diagonal entries of the strain tensor | – | $\boldsymbol{e} = \boldsymbol{\varepsilon} - \mathrm{tr}(\boldsymbol{\varepsilon})\boldsymbol{I}/3$ |
| Cauchy stress tensor per unit mass | $\mathrm{N/m^2}$ | $\boldsymbol{\sigma}$ |
| Off-diagonal entries of the stress tensor | – | $\boldsymbol{s} = \boldsymbol{\sigma} - \mathrm{tr}(\boldsymbol{\sigma})\boldsymbol{I}/3$ |
| Linear and angular frequency | Hz, rad /s | $f$, $\omega$ $\quad \omega = 2\pi f$ |
| Classical (isothermal) Lamé coefficients | $\mathrm{N/m^2}$ | $\mu, \lambda > 0$ |
| Elastic bulk modulus (isothermal) | $\mathrm{N/m^2}$ | $K = \lambda + 2\mu/3$ |
| Bulk and shear viscosity | $\mathrm{N\cdot\, s/m^2}$ | $\eta_K, \eta_\mu > 0, \quad \eta_\lambda = \eta_K - 2\eta_\mu/3$ |
| Viscosity parameter | $\mathrm{N\cdot\, s/m^2}$ | $\zeta = 2\eta_\mu + \eta_\lambda$ |
| Local in time complex Lamé quantities | $\mathrm{N/m^2}$ | $\hat{\lambda} = \lambda - \mathrm{i}\omega\eta_\lambda, \quad \hat{\mu} = \mu - \mathrm{i}\omega\eta_\mu$ |
| Local in time complex bulk modulus | $\mathrm{N/m^2}$ | $\hat{K} = K - \mathrm{i}\omega\eta_K$ |
| Thermal conductivity | W/m·K | $\mathscr{K}$ |
| Internal energy density per unit mass | N·m/kg | $\mathcal{E}$ |
| Total and ambient temperature | K | $T, T_0$ |
| Non-dimensional temperature variation | – | $\theta = (T - T_0)/T_0$ |
| Total and ambient mass density | $\mathrm{kg/m^3}$ | $\rho, \rho_0$ |
| Total and ambient entropy per unit mass | N·m/(kg·K) | $h, h_0$ |
| Specific heat at constant pressure/volume | J/(kg·K) | $c_p, c_v \quad \rho_0(c_p - c_v) = \alpha^2 K T_0$ |
| Ratio of specific heats | – | $\gamma = c_p/c_v$ |
| Adiabatic/isothermal acoustic speed of sound | m/s | $c_\mathrm{A}, c_\mathrm{Iso} \quad c_\mathrm{A} = \sqrt{\gamma} c_\mathrm{Iso}$ |
| Coefficient of thermal expansion | 1/K | $\alpha$ |
| Volumetric heat supply per unit mass | N·m/(kg·s) | $B$ |
| Body force per unit mass | N/kg | $\mathbf{G}$ |
| Fourier-Stokes heat flux vector | N/(m·s) | $\mathbf{q}$ |
| Total and ambient Helmholtz free energy per unit mass | N·m/kg | $\Psi, \Psi_0$ |
| Thermal parameter | $1/\ \mathrm{m^2}$ | $L_\phi$ |
| Thermo-visco-elastic coupling quantity | – | $L_\theta$ |
| Thermo-compressional wave-potentials/wavenumbers | $\mathrm{m^2}$, 1/ m | $\varphi, \vartheta \quad k_\varphi, k_\vartheta$ |
| Pressure/Shear wave-potentials/wavenumbers | $\mathrm{m^2}$, 1/ m | $\phi, \boldsymbol{\Phi} \quad k_\phi, k_\Phi$ |
| Temperature contributions | $1/\ \mathrm{m^2}$ | $\mathscr{T}_\varphi, \mathscr{T}_\vartheta$ |
| Mechanical relaxation functions | $\mathrm{N/m^2}$ | $\mathcal{R}_1, \mathcal{R}_2$ |
| Thermo-mechanical relaxation function | $\mathrm{N/(m^2\cdot\, K)}$ | $\mathcal{R}_3$ |
| Specific heat relaxation function | $\mathrm{J/(m^3{\cdot}K^2)}$ | $\mathcal{R}_4$ |
| Energy flux vector per unit volume | N/(m · s) | $\mathbf{J}$ |
| Total TVE energy per unit volume | $\mathrm{N/m^2}$ | $\mathcal{U}$ |
| Energy dissipation per unit time/volume | $\mathrm{N/(m^2\cdot\, s)}$ | $\mathcal{D}$ |

Table 1: Thermo-viscous parameters and other quantities that appear in the general TVE model. By the "ambient" value of a quantity, we refer to its value prior to deformation, i.e. in the undeformed configuration which we assume to be still.

# 2 Modelling linear TVE media

## 2.1 Governing equations

Our starting point is the classical set of conservation laws of linear continuum mechanics: conservation of mass, momentum and energy, together with the Clausius-Duhem inequality [16]

$$\dot{\rho} + \rho \nabla \cdot \dot{\mathbf{u}} = 0, \tag{2.1a}$$

$$\rho \ddot{\mathbf{u}} = \nabla \cdot \boldsymbol{\sigma} + \rho \mathbf{G}, \tag{2.1b}$$

$$\rho \dot{\mathcal{E}} + \nabla \cdot \mathbf{q} = \boldsymbol{\sigma} : \dot{\boldsymbol{\varepsilon}} + \rho B, \tag{2.1c}$$

$$\rho T \dot{h} + \nabla \cdot \mathbf{q} \geq \rho B + \frac{\mathbf{q} \cdot \nabla \mathbf{T}}{T}, \tag{2.1d}$$

where notation is summarised in Table 1, and the symmetry of the Cauchy stress tensor $\boldsymbol{\sigma} = \boldsymbol{\sigma}^T$ arises due to conservation of angular momentum.

## 2.2 Local (in time) TVE

We assume that all constitutive models considered are local in space. We begin with the simplest (local) dependence on time, where we introduce the Helmholtz free energy per unit mass [17]

$$\Psi(t) \equiv \Psi(\boldsymbol{\varepsilon}(t), T(t)) = \mathcal{E}(t) - T(t)h(t). \tag{2.2}$$

Using this in (2.1c), (2.1d) yields

$$\left(\boldsymbol{\sigma} - \rho \frac{\partial \Psi}{\partial \boldsymbol{\varepsilon}}\right) \dot{\boldsymbol{\varepsilon}} - \left(\frac{\partial \Psi}{\partial T} + h\right) \rho \dot{T} - \frac{\mathbf{q} \cdot \nabla T}{T} \geq 0. \tag{2.3}$$

We then adopt the approach of *Coleman-Noll* ([18]) and *Liu* ([19]) to yield further information; since (2.3) must hold for arbitrary deformations, the imposition of specific deformations permits conclusions to be deduced on functional form. A purely isothermal process ($\dot{T} = 0, \nabla T = \mathbf{0}$) and a process that involves no deformation but a change in uniform temperature, respectively, yields

$$\boldsymbol{\sigma}^{\mathrm{TE}} = \rho \frac{\partial \Psi}{\partial \boldsymbol{\varepsilon}}, \quad \text{and} \quad h = -\frac{\partial \Psi}{\partial T}, \tag{2.4}$$

where the superscript "TE" refers to *thermo-elastic*. The conditions (2.4) are *sufficient* but not *necessary* to satisfy (2.3): one can include an additional visco-elastic (VE) contribution to the Cauchy stress, e.g. for isotropic media

$$\boldsymbol{\sigma} = \boldsymbol{\sigma}^{\mathrm{TE}} + \boldsymbol{\sigma}^{\mathrm{VE}} = \rho \frac{\partial \Psi}{\partial \boldsymbol{\varepsilon}} + 2\eta_\mu \dot{\boldsymbol{\varepsilon}} + \left(\eta_K - \frac{2}{3}\eta_\mu\right) \mathrm{tr}(\dot{\boldsymbol{\varepsilon}}) \boldsymbol{I}, \tag{2.5}$$

where the shear and bulk viscosities[1] satisfy $\eta_\mu > 0, \eta_\lambda = \eta_K - 2\eta_\mu/3 > 0$ and hence (2.5) also satisfies (2.3).

The introduction of $\boldsymbol{\sigma}^{\mathrm{VE}}$ distinguishes the current local-in-time TVE models from the commonly employed classical TE models. However, the absence of stress rate terms in (2.5) is a strong restriction, since it fails to predict stress relaxation effects, which are important in many common materials

[1] These terms are defined in several ways throughout the literature, our choice of $\eta_K$ as the bulk viscosity matches the convention of the elastic bulk modulus.

such as polymers [20]. Incorporating stress rates results in models that we refer to as *non-local in time*, and this is the focus of Section 2.3. We first describe the thermal constitutive models and then the associated equations that describe local-in-time TVE wave propagation.

We adopt Fourier's law of heat conduction,

$$\mathbf{q} = -\mathscr{K}\nabla T, \tag{2.6}$$

where $\mathscr{K} > 0$ is the thermal conductivity of the material, whose positivity ensures that the last term in (2.3) is never negative. The form (2.6) is the simplest admissible choice, resulting in a parabolic diffusion equation (2.8) for which the thermal wave-speed is infinite. Thermal waves with finite velocity (e.g. Maxwell-Cattaneo heat waves) are obtained with a thermal relaxation time which arises when taking into account the rate of heat flux vector in (2.6) [21], [22].

At this stage it only remains to determine the thermodynamically consistent form of $\Psi$. As shown in Appendix A, for a (local) linear theory of TVE we obtain

$$\boldsymbol{\sigma} = 2\mu\boldsymbol{\varepsilon} + 2\eta_\mu\dot{\boldsymbol{\varepsilon}} + (\lambda\,\mathrm{tr}(\boldsymbol{\varepsilon}) + \eta_\lambda\,\mathrm{tr}(\dot{\boldsymbol{\varepsilon}}) - \alpha K T_0\theta)\boldsymbol{I}, \tag{2.7a}$$

$$h = h_0 + c_v\theta + \frac{\alpha K}{\rho_0}\,\mathrm{tr}(\boldsymbol{\varepsilon}), \tag{2.7b}$$

where $\theta = (T - T_0)/T_0$ is the non-dimensional temperature difference, and $K = \lambda + 2\mu/3$ denotes the (isothermal) elastic bulk modulus. Substituting (2.2), (2.5) and (2.7b) into (2.1c) yields the energy equation

$$\mathscr{K}\Delta\theta - \rho_0 c_v\dot{\theta} = \alpha K\,\mathrm{tr}(\dot{\boldsymbol{\varepsilon}}), \tag{2.8}$$

where we have assumed no external heat supply such that $B = 0$. Note that viscous effects are not explicit in (2.8) since they are quadratic in $\dot{\boldsymbol{\varepsilon}}$, and hence at this order the energy is analogous to that of linear thermo-elasticity [17]. Finally for convenience we write

$$\rho_0(\gamma - 1) = \frac{\alpha^2 K T_0}{c_v}, \tag{2.9}$$

where $\gamma = c_p/c_v$ denotes the ratio of specific heats. Equation (2.9) is a classical conserved quantity in thermo-elasticity (see Appendix A). It is useful in practice since for solids $c_v$ is difficult to measure as opposed to $c_p$. As we see shortly it plays an important role when considering the thermo-visco-acoustic (TVA) limit.

### 2.2.1 Frequency domain decomposition for the local-in-time equations

Assume time-harmonic propagation of the form $\mathbf{u}(\mathbf{x},t) = \mathrm{Re}\,\{\hat{\mathbf{u}}(\mathbf{x})\mathrm{e}^{-\mathrm{i}\omega t}\}$, $\theta(\mathbf{x},t) = \mathrm{Re}\,\{\hat{\theta}(\mathbf{x})\mathrm{e}^{-\mathrm{i}\omega t}\}$ and define the complex valued Lamé parameters

$$\hat{\lambda} = \lambda - \mathrm{i}\omega\eta_\lambda \quad \text{and} \quad \hat{\mu} = \mu - \mathrm{i}\omega\eta_\mu, \tag{2.10}$$

so that upon defining $\boldsymbol{\sigma}(\mathbf{x},t) = \mathrm{Re}\,\{\hat{\boldsymbol{\sigma}}(\mathbf{x})\mathrm{e}^{-\mathrm{i}\omega t}\}$, we can write

$$\hat{\boldsymbol{\sigma}} = \left(\hat{\lambda}\nabla\cdot\hat{\mathbf{u}} - \alpha K T_0\hat{\theta}\right)\boldsymbol{I} + \hat{\mu}\left(\nabla\hat{\mathbf{u}} + (\nabla\hat{\mathbf{u}})^T\right). \tag{2.11}$$

Substituting (2.11) in the conservation of momentum equation (2.1b) yields

$$(\hat{\lambda} + 2\hat{\mu})\nabla(\nabla\cdot\hat{\mathbf{u}}) - \hat{\mu}\nabla\times\nabla\times\hat{\mathbf{u}} + \rho_0\omega^2\hat{\mathbf{u}} = \alpha K T_0\nabla\hat{\theta}, \tag{2.12}$$

which corresponds to Navier-Lamé with thermo-mechanical coupling as in classical linear TE.

Introducing the classical Helmholtz potentials $\phi, \mathbf{\Phi}$ in the form

$$\hat{\mathbf{u}} = \nabla\phi + \nabla \times \mathbf{\Phi}, \qquad \nabla \cdot \mathbf{\Phi} = 0 \tag{2.13}$$

and making use of Helmholtz' theorem [23], allows us to deduce that the potentials satisfy

$$\Delta\phi + k_\phi^2\phi + L_\theta\hat{\theta} = 0, \tag{2.14a}$$
$$\Delta\mathbf{\Phi} + k_\Phi^2\mathbf{\Phi} = \mathbf{0}, \tag{2.14b}$$
$$\Delta\hat{\theta} + k_\theta^2\hat{\theta} + L_\phi\Delta\phi = 0, \tag{2.14c}$$

where

$$k_\theta^2 = \mathrm{i}c_v\frac{\rho_0\omega}{\mathscr{K}}, \quad k_\phi^2 = \frac{\rho_0\omega^2}{\hat{\lambda}+2\hat{\mu}}, \quad k_\Phi^2 = \frac{\rho_0\omega^2}{\hat{\mu}}, \tag{2.15}$$

and where we have defined $L_\phi$ (with dimension $\mathrm{m}^{-2}$), and the non-dimensional thermo-mechanical coupling parameter $L_\theta$ as

$$L_\phi = \frac{\mathrm{i}\alpha K\omega}{\mathscr{K}}, \quad \text{and} \quad L_\theta = -\frac{\alpha T_0 K}{\hat{\lambda}+2\hat{\mu}}. \tag{2.16}$$

In the limit $\alpha T_0 \to 0$ the system (2.14) uncouples immediately. Moreover, it is the size of $|L_\theta|$ that determines the importance of thermo-elastic coupling. In order to obtain a less restrictive theory, it is often argued for many materials in common scenarios that $|L_\phi| \times (\text{"characteristic length"})^2 \ll 1$ so that the energy equation (2.14c) becomes uncoupled. The corresponding solution can then be fed into (2.14a) to obtain a forced Helmholtz equation with a known source term. This approximation is sometimes referred to as the *theory of thermal stresses* in order to distinguish it from fully coupled thermo-elasticity [24].

To decouple the system completely substitute (2.14a) into (2.14c) to obtain

$$\mathcal{L}_O\{\phi\} = 0, \qquad \text{where} \qquad \mathcal{L}_O = (\Delta + (a-b))(\Delta + (a+b)) \tag{2.17}$$

where

$$a = \frac{1}{2}\left(k_\theta^2 + k_\phi^2 - L_\theta L_\phi\right), \quad \text{and} \quad b = \sqrt{a^2 - k_\phi^2 k_\theta^2}. \tag{2.18}$$

The solution to (2.17) is thus equivalent to solving the pair of Helmholtz equations

$$\Delta\vartheta + k_\vartheta^2\vartheta = 0, \tag{2.19a}$$
$$\Delta\varphi + k_\varphi^2\varphi = 0, \tag{2.19b}$$

with

$$k_\vartheta^2 = a + b, \quad k_\varphi^2 = a - b. \tag{2.20}$$

Employing (2.14a), the two newly introduced potentials $\varphi, \vartheta$ are related to $\phi$ and $\hat{\theta}$ via the matrix form[2]

$$\begin{pmatrix}\phi\\ \hat{\theta}\end{pmatrix} = \begin{pmatrix}1 & 1\\ \mathscr{T}_\varphi & \mathscr{T}_\vartheta\end{pmatrix}\begin{pmatrix}\varphi\\ \vartheta\end{pmatrix}, \tag{2.21}$$

[2]Due to the uniqueness of the solution to the linear PDE (2.17) being up to a constant, we may also write $\phi = C_1\vartheta + C_2\varphi$, whence $\hat{\theta}L_\theta = C_1(a-b-k_\phi^2)\varphi + C_2(a+b-k_\phi^2)\vartheta$, for constants $C_1, C_2$ but here we choose $C_1 = C_2 = 1$ to match the conventional approach.

where

$$\mathscr{T}_\varphi = \frac{1}{L_\theta}(k_\varphi^2 - k_\phi^2), \quad \mathscr{T}_\vartheta = \frac{1}{L_\theta}(k_\vartheta^2 - k_\phi^2). \tag{2.22}$$

As is well known therefore, the equations of motion for linear local-in-time TVE are thus governed by the three Helmholtz equations (2.14b), (2.19a) and (2.19b) from which we can recover the temperature and displacement fields through (2.13), and (2.21). These wave potentials consist of two thermo-compressional potentials $\varphi, \vartheta$ and a shear potential $\boldsymbol{\Phi}$, the latter being indepedent of thermal effects. They can be directly correlated to those of [25] as well as [26] (by taking the limit of zero volume fraction of voids). Asymptotic approximations to (2.20), (2.22) and their validity will be discussed in Section 2.4 but now we move on to incorporating the influence of stress relaxation.

## 2.3 Non-local (in time) TVE: the influence of stress relaxation

The local-in-time TVE constitutive model (2.7a) has no dependence on *history*, or equivalently as it turns out, no information with regard to stress rates. Whilst the model as presented permits the modelling of *creep*, it means that *stress relaxation* cannot be modelled. From a physical viewpoint, this limits its applicability, especially for the diverse range of polymeric materials in which relaxation, or equivalently, strongly frequency-dependent material properties, is common. In order to accommodate this effect *and* creep, we must take into consideration the kinematical and thermal *time histories*, so that the Helmholtz free energy per unit mass now takes the form

$$\Psi \equiv \Psi(\boldsymbol{\varepsilon}(\tau)|_{\tau=-\infty}^{t}, T(\tau)|_{\tau=-\infty}^{t}). \tag{2.23}$$

This makes the question of whether the Clausius-Duhem inequality (2.1d) is solved less trivial, even for linear theories [27], [28]. Instead, for a linear isotropic medium, (2.7) become [27]

$$\boldsymbol{s} = \int_{-\infty}^{t} \mathcal{R}_1(t-\mathcal{T})\dot{\boldsymbol{e}}(\mathcal{T})\,\mathrm{d}\mathcal{T}, \tag{2.24a}$$

$$\mathrm{tr}\,(\boldsymbol{\sigma}) = \int_{-\infty}^{t} \mathcal{R}_2(t-\mathcal{T})\,\mathrm{tr}(\dot{\boldsymbol{\varepsilon}}(\mathcal{T}))\,\mathrm{d}\mathcal{T} - 3T_0\int_{-\infty}^{t} \mathcal{R}_3(t-\mathcal{T})\dot{\theta}(\mathcal{T})\,\mathrm{d}\mathcal{T}, \tag{2.24b}$$

$$\rho_0 h = \rho_0 h_0 + T_0\int_{-\infty}^{t} \mathcal{R}_4(t-\mathcal{T})\dot{\theta}(\mathcal{T})\,\mathrm{d}\mathcal{T} + \int_{-\infty}^{t} \mathcal{R}_3(t-\mathcal{T})\,\mathrm{tr}(\dot{\boldsymbol{\varepsilon}}(\mathcal{T}))\,\mathrm{d}\mathcal{T}, \tag{2.24c}$$

and the energy equation (2.8) is replaced by

$$\mathscr{K}\Delta\theta = \frac{\partial}{\partial t}\left(T_0\int_{-\infty}^{t} \mathcal{R}_4(t-\mathcal{T})\dot{\theta}(\mathcal{T})\,\mathrm{d}\mathcal{T} + \int_{-\infty}^{t} \mathcal{R}_3(t-\mathcal{T})\,\mathrm{tr}(\dot{\boldsymbol{\varepsilon}}(\mathcal{T}))\,\mathrm{d}\mathcal{T}\right), \tag{2.25}$$

where $\boldsymbol{s}$ and $\boldsymbol{e}$ are defined as

$$\boldsymbol{s} = \boldsymbol{\sigma} - \frac{1}{3}\,\mathrm{tr}(\boldsymbol{\sigma})\boldsymbol{I}, \tag{2.26a}$$

$$\boldsymbol{e} = \boldsymbol{\varepsilon} - \frac{1}{3}\,\mathrm{tr}(\boldsymbol{\varepsilon})\boldsymbol{I}, \tag{2.26b}$$

and the kernels $\mathcal{R}_1, \mathcal{R}_2, \mathcal{R}_3, \mathcal{R}_4$ are relaxation functions[3] containing the time varying thermo-mechanical properties of the medium. Note that despite including thermal history in the present theory, general thermodynamic consistency again requires Fourier's law (2.6) to hold with a constant thermal conductivity $\mathscr{K}$, so that (2.25) remains parabolic.

[3] Here these functions are scalar valued since we are only considering isotropic deformations.

Restrictions on $\mathcal{R}_i$ include causality, giving $\mathcal{R}_i(\tau) = 0$ for $\tau < 0$ (where $i$ =1−4) and choosing a form such that all integrals in (2.24), (2.25) are convergent. Finally, the choice must satisfy the *dissipation inequality*:

$$\Lambda \geq 0, \tag{2.27}$$

where $\Lambda$ is detailed in Appendix C. Despite being frequently neglected, the requirement (2.27) is also present in the analogue isothermal VE theory. For a particular choice of $\mathcal{R}_i$, it can in principle be checked whether (2.27) is satisfied (see Appendix C). We note that the thermodynamics of certain widely used theories are often unclear, as in the case of Fung's Quasilinear Viscoelasticity (QLV) theory [29]. Unless otherwise stated, in the subsequent work we assume that we meet the necessary requirements for equations (2.24)-(2.25) to apply.

In general it is non-trivial to determine the time-dependent form of the relaxation functions for a given material. They are assumed to depend only on the background temperature (assumed constant) $T_0$ as any more general temperature dependence must involve non-linearities, which are outside the scope of this paper. An exception is given by "thermo-rheologically simple" materials [30], where the dependence of the material properties on temperature has a particularly appealing structure that allows for description with a linear theory. The dependence of these properties on temperature can be associated with a shift of the behaviour at a base constant temperature which is commonly known as the *"time-temperature superposition"*. The particular shift function can in general be found experimentally but a very common empirical shift function is that of the Williams–Landel–Ferry [20].

Having established a sufficiently general constitutive framework with which to model materials with time-dependent material properties we now discuss how this can be described in the frequency domain.

### 2.3.1 Frequency domain decomposition for the non-local equations

Assume now that the fields are time-harmonic, of the form

$$\{\mathbf{u}, \theta, \boldsymbol{\sigma}, \boldsymbol{s}, \boldsymbol{\varepsilon}, \boldsymbol{e}\}(\mathbf{x}, t) = \mathrm{Re}\left\{\{\hat{\mathbf{u}}, \hat{\theta}, \hat{\boldsymbol{\sigma}}, \hat{\boldsymbol{s}}, \hat{\boldsymbol{\varepsilon}}, \hat{\boldsymbol{e}}\}(\mathbf{x})\mathrm{e}^{-\mathrm{i}\omega t}\right\}. \tag{2.28}$$

and for convenience we decompose all relaxation functions as

$$\mathcal{R}_i(t) = \mathcal{R}_i{}' + \mathscr{R}_i(t), \qquad \text{s.t.} \qquad \mathscr{R}(t) \to 0 \quad \text{as} \quad t \to \infty, \tag{2.29}$$

for $i = 1, 2, 3, 4$. We can then substitute (2.28) with (2.29) into (2.24) to obtain

$$\hat{\boldsymbol{s}} = 2\tilde{\mu}(\mathrm{i}\omega)\hat{\boldsymbol{e}}, \tag{2.30a}$$

$$\mathrm{tr}(\hat{\boldsymbol{\sigma}}) = 3(\tilde{K}(\mathrm{i}\omega)\,\mathrm{tr}(\hat{\boldsymbol{\varepsilon}}) - T_0\tilde{\mathcal{R}}_3(\mathrm{i}\omega)\hat{\theta}), \tag{2.30b}$$

on defining

$$\tilde{\mu}(\mathrm{i}\omega) = \frac{1}{2}\left(\mathcal{R}_1' - \mathrm{i}\omega\int_0^\infty \mathscr{R}_1(\mathcal{V})\mathrm{e}^{\mathrm{i}\omega\mathcal{V}}\,\mathrm{d}\mathcal{V}\right), \tag{2.31a}$$

$$\tilde{K}(\mathrm{i}\omega) = \frac{1}{3}\left(\mathcal{R}_2' - \mathrm{i}\omega\int_0^\infty \mathscr{R}_2(\mathcal{V})\mathrm{e}^{\mathrm{i}\omega\mathcal{V}}\,\mathrm{d}\mathcal{V}\right), \tag{2.31b}$$

$$\tilde{\mathcal{R}}_3(\mathrm{i}\omega) = \quad \mathcal{R}_3' - \mathrm{i}\omega\int_0^\infty \mathscr{R}_3(\mathcal{V})\mathrm{e}^{\mathrm{i}\omega\mathcal{V}}\,\mathrm{d}\mathcal{V}, \tag{2.31c}$$

which respectively correspond to the complex shear modulus, the three-dimensional complex bulk modulus, and the complex modulus associated with the coefficient of thermo-mechanical coupling. From (2.31a), (2.31b) it follows that we can define the generalized first Lamé modulus, Poisson's ratio and Young's modulus, respectively as [15]

$$\tilde{\lambda}(\mathrm{i}\omega) = \tilde{K}(\mathrm{i}\omega) - \frac{2}{3}\tilde{\mu}(\mathrm{i}\omega), \qquad \tilde{\nu}(\mathrm{i}\omega) = \frac{3\tilde{K}(\mathrm{i}\omega) - 2\tilde{\mu}(\mathrm{i}\omega)}{6\tilde{K}(\mathrm{i}\omega) + 2\tilde{\mu}(\mathrm{i}\omega)}, \qquad \tilde{E}(\mathrm{i}\omega) = \frac{9\tilde{K}(\mathrm{i}\omega)\tilde{\mu}(\mathrm{i}\omega)}{3\tilde{K}(\mathrm{i}\omega) + \tilde{\mu}(\mathrm{i}\omega)}. \tag{2.32}$$

Finally, using (2.31c) the energy balance equation (2.25) becomes

$$\mathscr{K}\Delta\hat{\theta} + \mathrm{i}\omega\left(T_0\tilde{\mathcal{R}}_4(\mathrm{i}\omega)\hat{\theta} + \tilde{\mathcal{R}}_3(\mathrm{i}\omega)\,\mathrm{tr}(\hat{\boldsymbol{\varepsilon}})\right) = 0, \tag{2.33}$$

where we defined the complex modulus

$$\tilde{\mathcal{R}}_4(\mathrm{i}\omega) = \mathcal{R}_4' - \mathrm{i}\omega\int_0^\infty \mathscr{R}_4(\mathcal{V})\mathrm{e}^{\mathrm{i}\omega\mathcal{V}}\,\mathrm{d}\mathcal{V}. \tag{2.34}$$

In fact, by direct comparison with the energy equation commonly used in linear thermo-elasticity (e.g. (1.12.22) in [17]) we observe that this quantity can be interpreted as a specific heat at constant strain/volume per unit volume, which in the setting of TVE with temperature history allows for frequency dependency, i.e.

$$\tilde{\mathcal{R}}_4(\mathrm{i}\omega) = \frac{\rho_0}{T_0}\tilde{c}_v(\mathrm{i}\omega). \tag{2.35}$$

Hence, the associated Cauchy stress in the frequency domain becomes

$$\hat{\boldsymbol{\sigma}}^{\mathrm{TVE}} = 2\tilde{\mu}(\mathrm{i}\omega)\hat{\boldsymbol{e}} + (\tilde{K}(\mathrm{i}\omega)\,\mathrm{tr}(\hat{\boldsymbol{\varepsilon}}) - T_0\tilde{\mathcal{R}}_3(\mathrm{i}\omega)\hat{\theta})\boldsymbol{I} \tag{2.36}$$

$$= 2\tilde{\mu}(\mathrm{i}\omega)\hat{\boldsymbol{\varepsilon}} + (\tilde{\lambda}(\mathrm{i}\omega)\,\mathrm{tr}(\hat{\boldsymbol{\varepsilon}}) - T_0\tilde{\mathcal{R}}_3(\mathrm{i}\omega)\hat{\theta})\boldsymbol{I}. \tag{2.37}$$

The associated energy and momentum equations reduce to

$$\mathscr{K}\Delta\hat{\theta} + \mathrm{i}\omega\rho_0\tilde{c}_v(\mathrm{i}\omega)\hat{\theta} + \mathrm{i}\omega\tilde{\mathcal{R}}_3(\mathrm{i}\omega)\nabla\cdot\hat{\mathbf{u}} = 0, \tag{2.38a}$$

$$(\tilde{\lambda}(\mathrm{i}\omega) + 2\tilde{\mu}(\mathrm{i}\omega))\nabla\left(\nabla\cdot\hat{\mathbf{u}}\right) - \tilde{\mu}(\mathrm{i}\omega)\nabla\times\nabla\times\hat{\mathbf{u}} - T_0\tilde{\mathcal{R}}_3(\mathrm{i}\omega)\nabla\hat{\theta} + \rho_0\omega^2\hat{\mathbf{u}} = \mathbf{0}. \tag{2.38b}$$

Conveniently, equations (2.36)-(2.38b) have the same structure as (2.10)-(2.12), (2.14), for a fixed frequency $\omega$. Now however, rich frequency dependent behaviour can be accommodated by the incorporation of the relaxation functions.

The equivalent form however means that the decomposition of Section 2.2.1 remains valid so that the fields remain solutions of the decoupled Helmholtz equations (2.14b), (2.19a) and (2.19b), as in the local case, with the only change (but a critical one) being that now the relevant quantities appearing in the wavenumbers have a more general frequency dependence:

$$k_\theta^2 = \mathrm{i}\tilde{c}_v(\mathrm{i}\omega)\frac{\rho_0\omega}{\mathscr{K}}, \quad k_\phi^2 = \frac{\rho_0\omega^2}{\tilde{\lambda}(\mathrm{i}\omega) + 2\tilde{\mu}(\mathrm{i}\omega)}, \quad k_\Phi^2 = \frac{\rho_0\omega^2}{\tilde{\mu}(\mathrm{i}\omega)}, \tag{2.39a}$$

$$L_\phi = \frac{\mathrm{i}\omega\tilde{\mathcal{R}}_3(\mathrm{i}\omega)}{\mathscr{K}}, \quad L_\theta = -\frac{T_0\tilde{\mathcal{R}}_3(\mathrm{i}\omega)}{\tilde{\lambda}(\mathrm{i}\omega) + 2\tilde{\mu}(\mathrm{i}\omega)}. \tag{2.39b}$$

As in the local case, the displacement and temperatures are given respectively by appropriate combinations of the potentials:

$$\hat{\mathbf{u}}^{\mathrm{TVE}} = \nabla(\vartheta + \varphi) + \nabla\times\boldsymbol{\Phi}, \tag{2.40a}$$

$$\hat{\theta}^{\mathrm{TVE}} = \frac{1}{L_\theta}(a - b - k_\phi^2)\varphi + \frac{1}{L_\theta}(a + b - k_\phi^2)\vartheta. \tag{2.40b}$$

Note, in particular, that the more general frequency dependence of the TVE coupling parameter $L_\theta$ shows that certain materials may exhibit significant thermal coupling only for certain frequency ranges.

### 2.3.2 Form of relaxation functions

Stress relaxation tests aim to investigate the viscoelastic properties of a given sample of material via specific loading modes, e.g. shear, uniaxial or bi-axial compression, etc. A general expression for relaxation functions is the so-called *Prony series* [14], which takes the form

$$\mathcal{R}(t) = \left( \mathcal{R}_\infty + \sum_{n=1}^{N} \mathcal{R}_n e^{-t/t_r} \right) H(t) \tag{2.41}$$

where $H(\circ)$ denotes the Heaviside function and $t_n$ are characteristic relaxation times of the medium in question. $R_\infty$ is the associated *long-term modulus*, resulting from the limit $t \to \infty$, whilst $\mathcal{R}_0 = \mathcal{R}_\infty + \sum_{n=1}^{N} \mathcal{R}_n$ is the *instantaneous* modulus. In practice modes of deformation or propagation are chosen that can isolate the dependence of relaxation functions so that they can be measured experimentally [31]. A common scenario for the purposes of modelling is to assume a single relaxation time:

$$\mathcal{R}(t) = \left( \mathcal{R}_\infty + (\mathcal{R}_0 - \mathcal{R}_\infty) \mathrm{e}^{-t/t_r} \right) H(t), \tag{2.42}$$

where in practice the relaxation time is obtained by fitting the model to the relaxation test data [14]. Following (2.31), (2.34), in the frequency domain (2.42) becomes

$$\mathcal{R}(\mathrm{i}\omega) = \mathcal{R}_\infty - (\mathcal{R}_0 - \mathcal{R}_\infty) \frac{\mathrm{i}\omega t_r}{1 - \mathrm{i}\omega t_r}, \tag{2.43}$$

and it is apparent from (2.43) that, in the low frequency (long time, or *rubbery*) and high frequency (short time, or *glassy*) limits, $\mathcal{R}_\infty$ and $\mathcal{R}_0$ are respectively obtained (see Figure 1). When separating (2.43) into real and imaginary parts, the "loss tangent" may be defined which is frequently used in order to characterize viscoelastic losses under steady state oscillatory conditions and associated experimental data [32]. In practice, the ratio $\mathcal{R}_0/\mathcal{R}_\infty$ can be very large, up to several orders of magnitude, see e.g. [4] for the shear modulus of an unfilled crosslinked rubber material.

Temperature can play a very important role in the behaviour of the moduli [1], [3]. Linear TVE theory allows only for dependence of the mechanical properties on the background temperature $T_0$ as is the case in an isothermal theory. Stress relaxation tests as described above are associated with specific modes of deformation and, therefore, the corresponding data obtained provides, e.g. the time-dependent Young's modulus (e.g. $\mathcal{R}(t)$ in (2.42)) under uniaxial compression or tension. On the other hand, several other experimental methods are used to approximate the shear modulus, e.g. [3]. As a result, one would expect that for an isotropic medium these 2 independent constants are sufficient to describe the continuum in consideration. It turns out that this is often not the case due to the required accuracy of the experiments, and tests involving primarily volumetric effects are necessary (see [15]). This is particularly evidenced for nearly incompressible elastic materials, and a method to determine $\tilde{K}(\mathrm{i}\omega)$ was presented in [33], where it is assumed that bulk loss is a constant fraction of the loss in shear. This assumption led to good agreement with the observed experimental results, for polyethylene (PE) and Plexiglass (PMMA) the bulk loss ($\mathrm{Im}\{\tilde{K}\}/\,\mathrm{Re}\{\tilde{K}\}$) represents 20% of the shear loss, whereas in polystyrene the bulk loss was calculated to be around 0.1%. Nevertheless, to this day, data for bulk losses in general materials remains difficult to find, as discussed in [34].

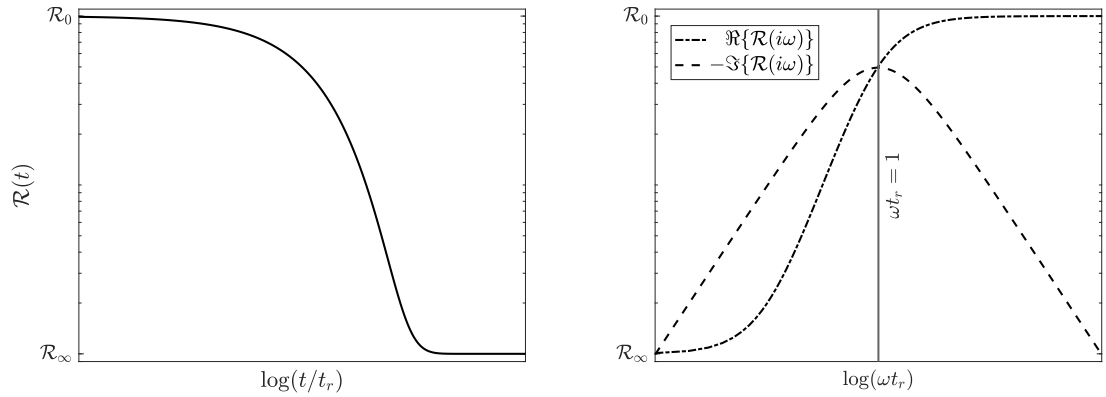


Figure 1: An example of prototype, single relaxation time, scalar relaxation function time-domain behaviour (left) given by (2.42), and its frequency domain counterpart (right) from (2.43).

The frequency dependence of the specific heat and thermo-mechanical coupling term in (2.31c) and (2.34) are reported even less, and these quantities are usually considered static, although relaxation type phenomena of the specific heat has been observed, e.g. [35]. This discussion for VE behaviour together with the thermal properties illustrates the intricacies involved in the correct determination of many of the quantities appearing in a TVE model. As a result, in studies seeking more qualitative results over a wider range of materials, common simplifications are made. In [36] it is argued that in most instances VE effects are mainly related to the isochoric part of the deformation and therefore if we write the Cauchy stress (2.36) in terms of the isochoric and deviatoric parts we have (noting (2.26a))

$$\hat{\boldsymbol{\sigma}} = 2\tilde{\mu}(\mathrm{i}\omega)\hat{\boldsymbol{e}} + (K\,\mathrm{tr}(\boldsymbol{\varepsilon}) - T_0\tilde{\mathcal{R}}_3(\mathrm{i}\omega)\hat{\theta})\boldsymbol{I} \tag{2.44}$$

where $K$ becomes a real valued constant from which the value of $\tilde{\lambda}(\mathrm{i}\omega)$ follows through (2.32). In [2] it is instead assumed that the Young's modulus takes the form (2.43), whilst the Poisson's ratio is kept constant. In turn this implies that the shear modulus also takes the form (2.43). The magnitude of the variation in the specific heat is such that it will be assumed constant.

### 2.3.3 Relaxation function interpretation of local TVE

The local TVE model discussed in Section 2.2 can be thought of as a special case from that of Section 2.3 where the kinematical and thermal time histories represented by $\mathcal{R}_1, \mathcal{R}_2, \mathcal{R}_3, \mathcal{R}_4$ in (2.24) are described by Heaviside and delta functions. In the frequency domain, this simply results in the choice

$$\tilde{\lambda}(\mathrm{i}\omega) = \lambda - \mathrm{i}\omega\eta_\lambda, \quad \tilde{\mu}(\mathrm{i}\omega) = \mu - \mathrm{i}\omega\eta_\mu, \quad \tilde{c}_v(\mathrm{i}\omega) = c_v, \quad \tilde{\mathcal{R}}_3(\mathrm{i}\omega) = \alpha K, \tag{2.45}$$

in (2.36)-(2.38b) to arrive at the local TVE theory. In the time domain, the instantaneous local viscous effects are represented by delta functions such that e.g. for the shear modulus

$$\mathcal{R}_1(t) = 2(\mu H(t) + \eta_\mu \delta(t)), \tag{2.46}$$

as can be checked from (2.31a), and similarly for the bulk modulus. The time domain representation for the shear modulus (2.46) shows how relaxation effects as discussed in Section 2.3.2 are clearly

not captured with local TVE. In the frequency domain the real part remains constant whereas the imaginary part becomes unbounded as the frequency increases. For this reason Local TVE is in general not suitable in studies beyond single frequency analyses. Given that in general we are interested in wave propagation in materials over rather general frequencies this is significantly restrictive.

Next we consider asymptotic limits under which thermo-compressional coupling can be significantly simplified in the context of the general TVE theory, before moving onto specific physical limits in the next Section.

## 2.4 Asymptotic approximations for thermo-compressional coupling

We simplify the decoupled thermo-compressional wavenumbers $a \pm b$ in (2.20), and the temperature field (2.40b). Asymptotic analysis illustrates that $k_\varphi$ is a quasi-acoustic wavenumber, whilst $k_\vartheta$ is a quasi-thermal wavenumber. Similar expressions for 1D TVE waves are given in [28], Section 6.3.

We start by assuming that the (viscous) pressure wavenumber is much smaller than the bulk thermal wavenumber, and thus introduce the following small parameter:

$$\delta = \frac{k_\phi^2}{k_\theta^2} = \frac{-\mathrm{i}\omega\mathscr{K}}{c_v(\mathrm{i}\omega)(\tilde{\lambda}(\mathrm{i}\omega) + 2\tilde{\mu}(\mathrm{i}\omega))} \ll 1 \tag{2.47}$$

and we assume that

$$|\delta| \ll \left| \frac{L_\phi L_\theta}{k_\theta^2} \right|. \tag{2.48}$$

These assumptions[4] hold true over vast ranges of frequencies and materials of interest, including solids, liquids and gases. The inequality in (2.48) is equivalent to $\omega\mathscr{K} \ll c_v K(\gamma - 1)$ which for a given a material can be a useful upper bound on the admissible frequency of the forthcoming expansions. Based on the discussion in Section 2.3.2, we will neglect thermal histories and thus write

$$\tilde{c}_v(\mathrm{i}\omega) = c_v, \quad \tilde{\mathcal{R}}_3(\mathrm{i}\omega) = \alpha K. \tag{2.49}$$

Expanding in $\delta$ then,

$$b = \pm\frac{1}{2}\left[k_\theta^2 - L_\theta L_\phi - \frac{k_\theta^4 + k_\theta^2 L_\theta L_\phi}{k_\theta^2 - L_\theta L_\phi}\delta - \frac{2k_\theta^6 L_\theta L_\phi}{(k_\theta^2 - L_\theta L_\phi)^3}\delta^2 + O(\delta^3)\right],$$

where the sign chosen depends on the complex argument of the term within the square-root, and the chosen branch cut. Depending on this choice we will have either $a \pm b = k_\varphi^2$ and $a \mp b = k_\vartheta^2$, with $k_\varphi^2$ and $k_\vartheta^2$ shown below:

$$k_\varphi^2 = \frac{k_\theta^4}{k_\theta^2 - L_\theta L_\phi}\delta + \frac{k_\theta^6 L_\theta L_\phi}{(k_\theta^2 - L_\theta L_\phi)^3}\delta^2 + O(\delta^3), \tag{2.50a}$$

$$k_\vartheta^2 = k_\theta^2 - L_\theta L_\phi - \frac{k_\theta^2 L_\theta L_\phi}{k_\theta^2 - L_\theta L_\phi}\delta + O(\delta^2). \tag{2.50b}$$

[4] Alternatively, this can be achieved by simply assuming $|a^2| \ll |k_\varphi^2 k_\vartheta^2|$ which also holds true in most cases but this approach is avoided since its physical interpretation is not as straightforward.

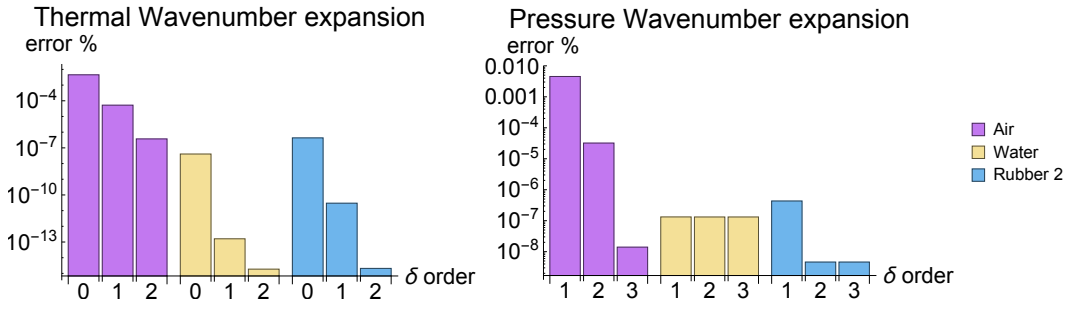


Figure 2: Maximum relative errors for the asymptotic expansions (2.50) for a frequency range of 10kHz to 10MHz and material parameters from Table 4. For Rubber 2, the shear modulus is described by the single Prony term relaxation function (2.43) where the frequencies cover both the rubber and glassy phase.

Similarly, we can now expand the temperature contributions $(a \pm b - k_\phi^2)/L_\theta$ given in (2.22). We find

$$\mathscr{T}_\varphi = \frac{1}{L_\theta}(k_\varphi^2 - k_\phi^2) = \frac{k_\theta^2 L_\phi}{k_\theta^2 - L_\theta L_\phi}\delta + \frac{k_\theta^6 L_\phi}{(k_\theta^2 - L_\theta L_\phi)^3}\delta^2 + O(\delta^3), \tag{2.51a}$$

$$\mathscr{T}_\vartheta = \frac{1}{L_\theta}(k_\vartheta^2 - k_\phi^2) = \frac{k_\theta^2 - L_\theta L_\phi}{L_\theta} - \frac{k_\theta^4}{k_\theta^2 - L_\theta L_\phi}\delta + O(\delta^2), \tag{2.51b}$$

so that $\mathscr{T}_\varphi$ ($\mathscr{T}_\vartheta$) is the temperature contribution corresponding to the mode with wavenumber $k_\varphi$ ($k_\vartheta$). An illustration of the accuracy of the expansions for the thermo-compressional wavenumbers for different materials is given in Figure 2. Similar results were obtained for the temperature contributions (2.51) but have not been included here.

# 3 Limits to theories that neglect specific physical effects

A plethora of approximate thermo-visco-elastic theories exist that neglect certain physical effects. Here we describe such theories in terms of parameter limits of the general TVE theory described above, noting that we have already described how local TVE is recovered from non-local TVE in Section 2.3.3 via the choice of specific relaxation functional forms. More generally, it is important to understand how significant the neglected terms are when the full TVE is compared with the simpler theories. The efficacy of the various limits is thus studied with regard to a canonical problems involved half-spaces in Section 4.

Figure 3 summarises the various limits taken from the TVE theory in the frequency domain, starting from the current general framework, where various effects can be switched off and on to yield various commonly used theories. Other relevant dissipative theories concerning thermal relaxation in solids and those involving molecular relaxation effects in the acoustics of gases are not included since these require further modelling considerations, (see e.g. Section 2.4 in [6]).

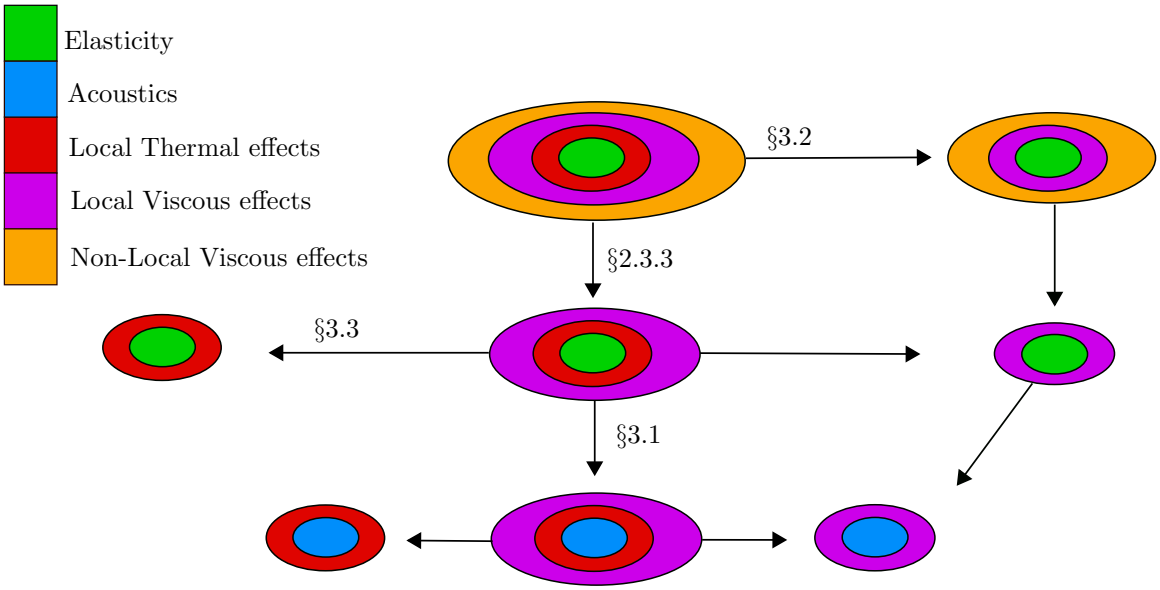


Figure 3: Representation of various elasto/acoustic dissipative theories, where the arrows indicate various limits that can be taken to arrive at other (more restrictive) theories.

## 3.1 Thermo-visco-acoustic (TVA) fluids

Starting with the local TVE theory described in Section 2.2 and taking the standard limit of zero shear modulus,

$$\mu \to 0, \tag{3.1}$$

leads to the widely used model for Thermo-visco-acoustics (local in time) [37], [6]. In this regime the thermodynamic identity (2.9) becomes

$$\gamma - 1 = \frac{\alpha^2 T_0 c_{\text{Iso}}^2}{c_v}, \qquad \text{where} \qquad c_{\text{Iso}}^2 = \frac{\lambda_{\text{Iso}}}{\rho_0}, \tag{3.2}$$

since in the limit $K_{\text{Iso}} \to \lambda_{\text{Iso}}$. The subscript "Iso" in the definition of the isothermal sound speed $c_{\text{Iso}}$ is chosen to emphasize that these quantities are defined at a state of constant temperature[5] (see e.g. (78) in [34]). Note that here the Lamé parameters are isothermal by definition ($\lambda \equiv \lambda_{\text{Iso}}$) since the Helmholtz free energy is expanded from a state of constant temperature $T_0$ and zero strain (see (A.1) in Appendix A). With (3.1) the thermo-mechanical coupling constant $L_\theta$ (2.16) can be approximated by

$$L_\theta \approx -\alpha T_0, \tag{3.3}$$

[5]This distinction is often ignored for liquids and solids since it is not as important (see e.g. Section 1.9.2 of [37]), but is paramount for gases.

since for frequencies of interest we have $\omega\eta_\lambda, \omega\eta_\mu \ll \lambda$. Furthermore, with (3.1) and (3.2) the quantities (2.15) and (2.16) become

$$k_\theta^2 = \frac{\mathrm{i}\rho_0\omega c_p}{\gamma\mathscr{K}}, \qquad k_\phi^2 \to \frac{\rho_0\omega^2}{\rho_0 c_{\mathrm{Iso}}^2 - \mathrm{i}\omega\zeta}, \qquad k_\Phi^2 \to \frac{\mathrm{i}\rho_0\omega}{\eta_\mu}, \tag{3.4a}$$

$$L_\phi \to \frac{\mathrm{i}\rho_0\omega\alpha c_{\mathrm{Iso}}^2}{\mathscr{K}}, \qquad L_\theta \to -\frac{\alpha\rho_0 c_{\mathrm{Iso}}^2 T_0}{\rho_0 c_{\mathrm{Iso}}^2 - \mathrm{i}\omega\zeta}, \tag{3.4b}$$

with $\zeta = \eta_\lambda + 2\eta_\mu$ and given that $c_v = c_p/\gamma$. With (3.4) and in the limit $\mu \to 0$, the linear operator (2.17) becomes

$$\mathcal{L}_O \to \mathcal{L}_{\mathrm{TVA}} = (\rho_0 c_{\mathrm{A}}^2 - \mathrm{i}\omega\zeta\gamma)\mathscr{K}\nabla^4 + \mathrm{i}\omega[\rho_0^2 c_{\mathrm{A}}^2 c_p - \mathrm{i}\omega\rho_0(c_p\zeta + \mathscr{K}\gamma)]\nabla^2 + \mathrm{i}\rho_0^2 c_p\omega^3, \tag{3.5}$$

where we have made use of (3.2) in terms of the *adiabatic* speed of sound $c_{\mathrm{A}}$ as is common in acoustics with the relation $c_{\mathrm{A}}^2 = \gamma c_{\mathrm{Iso}}^2$. The operator (3.5) is identical to that in (2.70) of [6] for TVA when the latter is written in the frequency domain and in the absence of any sources. This confirms that the local TVE theory recovers TVA but says nothing about the decomposition (in particular the connection between wave potentials) which, as we saw in (2.21), is unique up to a constant. For completeness we match the potentials to those by [5] in Appendix D.

## 3.2 Non-local Visco-elasticity (VE)

Starting with the general non-local TVE theory described above and taking the limit of zero thermo-mechanical coupling[6], that is

$$\tilde{\mathcal{R}}_3(\mathrm{i}\omega) \to 0, \tag{3.6}$$

in (2.36), (2.38), results in

$$\hat{\boldsymbol{\sigma}}^{\mathrm{VE}} = 2\tilde{\mu}(\mathrm{i}\omega)\hat{\boldsymbol{\varepsilon}} + \tilde{\lambda}(\mathrm{i}\omega)\,\mathrm{tr}(\hat{\boldsymbol{\varepsilon}})\boldsymbol{I}, \tag{3.7}$$

as well as

$$\left(\Delta + \frac{\mathrm{i}\omega\rho_0\tilde{c}_v(\mathrm{i}\omega)}{\mathscr{K}}\right)\hat{\theta}^{\mathrm{VE}} = 0, \tag{3.8a}$$

$$(\tilde{\lambda}(\mathrm{i}\omega) + 2\tilde{\mu}(\mathrm{i}\omega))\nabla(\nabla\cdot\hat{\mathbf{u}}) - \tilde{\mu}(\mathrm{i}\omega)\nabla\times\nabla\times\hat{\mathbf{u}} + \rho_0\omega^2\hat{\mathbf{u}} = \mathbf{0}. \tag{3.8b}$$

These are the governing equations for visco-elasticity, including stress relaxation. It is apparent in (3.8) that there is no longer coupling between kinematic and thermal effects, and hence the wave potentials directly give

$$\hat{\mathbf{u}}^{\mathrm{VE}} = \nabla\phi + \nabla\times\boldsymbol{\Phi}, \tag{3.9}$$

where

$$\left(\Delta + \frac{\rho_0\omega^2}{\tilde{\lambda}(\mathrm{i}\omega) + 2\tilde{\mu}(\mathrm{i}\omega)}\right)\phi = 0, \tag{3.10a}$$

$$\left(\Delta + \frac{\rho_0\omega^2}{\tilde{\mu}(\mathrm{i}\omega)}\right)\boldsymbol{\Phi} = \mathbf{0}, \tag{3.10b}$$

[6] In the local TVE case we simply take the limit of zero thermal expansion coefficient, that is $\alpha T_0 \to 0$.

recalling that the Lamé parameters in (3.10) are isothermal[7] Nevertheless, in practice it is important to understand the effect of this limit on the decomposition that leads to the corresponding TVE wave potentials. It is clear that the shear wave potential remains unchanged in the limit (since it is independent of thermal effects). The situation for the thermo-compressional fields is slightly more subtle. Direct substitution of (3.6) into (2.14b), (2.19a) and (2.19b) with (2.39) leads to

$$\varphi \to \mathcal{A}_1\phi, \quad \vartheta \to \mathcal{A}_2\theta^{\mathrm{VE}}, \quad \text{since} \quad a-b \to \frac{\rho_0\omega^2}{\tilde{\lambda}(\mathrm{i}\omega)+2\tilde{\mu}(\mathrm{i}\omega)} = k_\phi^2, \quad a+b \to \frac{\mathrm{i}\omega\rho_0\tilde{c}_v(\mathrm{i}\omega)}{\mathscr{K}} = k_\theta^2, \tag{3.11}$$

for some constants $\mathcal{A}_1, \mathcal{A}_2$ arising due to the uniqueness of the linear PDE solution being up to a constant. However, direct comparison between the curl free components of the TVE and VE displacements (2.40a), (3.9) implies $\mathcal{A}_1 = 1$ and $\vartheta \to 0$ which restricts the form of $\mathcal{A}_2$ but this is not sufficient to determine it explicitly. Therefore, in order to find this constant we consider the effect of the limit (3.6) on the TVE temperature (2.40b). We obtain $\mathscr{T}_\varphi \to 0$, which gives $\theta^{\mathrm{TVE}} \to (k_\theta^2 - k_\phi^2)\mathcal{A}_2\theta^{\mathrm{VE}}/L_\theta$ (after using the second equation of (3.11)) so that in order to recover the VE solution we must choose

$$\mathcal{A}_2 = \frac{L_\theta}{k_\theta^2 - k_\phi^2} = \frac{\mathrm{i}T_0\tilde{\mathcal{R}}_3(\mathrm{i}\omega)\mathscr{K}}{\rho_0\omega(c_v(\mathrm{i}\omega)(\tilde{\lambda}(\mathrm{i}\omega)+2\tilde{\mu}(\mathrm{i}\omega)) + \mathrm{i}\omega\mathscr{K}}, \tag{3.12}$$

from which it is clear that in the limit both $\theta^{\mathrm{TVE}} \to \theta^{\mathrm{VE}}$ and $\vartheta \to 0$ as required. Furthermore, (local) visco–acoustic Newtonian fluids (e.g. [39]) can also be described by (3.8)-(3.10) by further letting $\mu \to 0$ so that $\mu(\omega) = -\mathrm{i}\omega\eta_\mu$ which gives a convenient way to model viscous fluids such as water [40, 41].

## 3.3 Thermo-elasticity (TE)

The final simplified theory is the case when viscous dissipation is neglected, leading to the theory of linear thermo-elasticity. In the frequency domain this can be thought of as the local TVE model presented in Section 2.2 with real-valued Lamé parameters. Indeed let

$$\tilde{\lambda}(\mathrm{i}\omega) = \lambda, \quad \tilde{\mu}(\mathrm{i}\omega) = \mu, \quad \tilde{c}_v(\mathrm{i}\omega) = c_v, \quad \tilde{\mathcal{R}}_3(\mathrm{i}\omega) = \alpha K, \tag{3.13}$$

and substitute (3.13) in (2.36) and (2.38) so that we obtain the corresponding equations for time-harmonic thermo-elasticity [17]

$$\hat{\boldsymbol{\sigma}}^{\mathrm{TE}} = 2\mu\hat{\boldsymbol{\varepsilon}} + (\lambda\,\mathrm{tr}(\hat{\boldsymbol{\varepsilon}}) - \alpha K T_0\hat{\theta})\boldsymbol{I}, \tag{3.14a}$$

$$\mathscr{K}\Delta\hat{\theta} + \mathrm{i}\omega\rho_0 c_v\hat{\theta} + \mathrm{i}\omega\alpha K\nabla\cdot\hat{\mathbf{u}} = 0, \tag{3.14b}$$

$$(\lambda+2\mu)\nabla(\nabla\cdot\hat{\mathbf{u}}) - \mu\nabla\times\nabla\times\hat{\mathbf{u}} - \alpha K T_0\nabla\hat{\theta} + \rho_0\omega^2\hat{\mathbf{u}} = \mathbf{0}. \tag{3.14c}$$

The structure of (3.14b), (3.14c) allows for the same decomposition

$$\hat{\mathbf{u}}^{\mathrm{TE}} = \nabla(\vartheta+\varphi) + \nabla\times\boldsymbol{\Phi} \tag{3.15}$$

where the wave potentials must still satisfy (2.14b), (2.19a) and (2.19b) with simplified TVE parameters in (2.15), (2.16) becoming real valued and frequency independent, i.e.

$$k_\phi^2 = \frac{\rho_0\omega^2}{\lambda+2\mu}, \quad k_\Phi^2 = \frac{\rho_0\omega^2}{\mu}, \quad L_\theta = -\frac{T_0\alpha K}{\lambda+2\mu}, \tag{3.16}$$

whereas $k_\theta^2$, $L_\phi$ remain unchanged.

[7] For the particular relations with the corresponding adiabatic moduli, see e.g. [38].

# 4 Two TVE half spaces in perfect contact

As a means to put into practice the framework that we have presented above, we next consider a forced boundary value problem (BVP) consisting of two TVE half-spaces. In the absence of thermal effects (using the theory presented in Section 3.2) a detailed analysis for this problem is given in [42], who generalized the work pioneered by [43] to include attenuation in reflection/transmission problems for ultrasonics. More recent work has included the presence of voids [44] or thermal relaxation [45], but only for a single traction free half-space, presumably because their goal was to understand loss mechanisms for solids.

Here we are interested in interactions between different TVE media when in contact and in particular those that are deemed as "fluid" and "solid". With two half spaces we can illustrate the advantages of the general TVE model, the limits discussed in Section 3, as well as the importance of stress relaxation effects presented in Section 2.3 as opposed to the local TVE version in Section 2.2, which is a common "go to" theory when experiments are performed at specific frequencies.

## 4.1 Problem formulation

We consider a plane-strain problem consisting of two distinct TVE half spaces in perfect contact at an interface along $y = 0$, see Figure 4. All of the quantities have been non-dimensionalised following Appendix F.1, and relevant dimensional parameters are distinguished by an overbar.

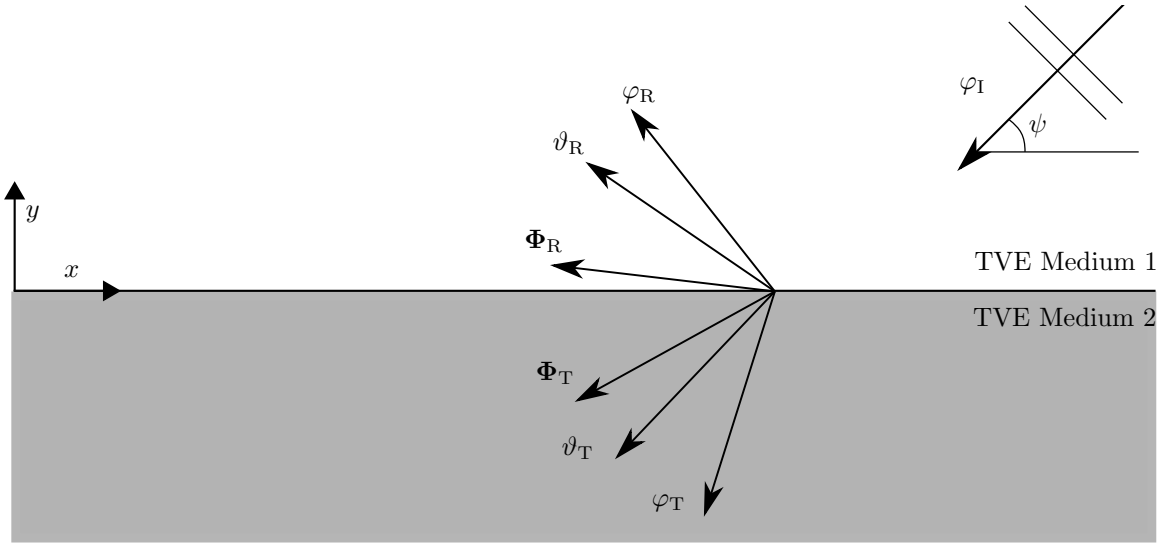


Figure 4: Schematic representation of the configuration of the problem of two welded semi-infinite TVE media. An incident P-dominated bulk mode impinging on the interface of the two distinct TVE domains gives rise to three reflected modes and three transmitted modes.

We choose the forcing to be a pressure-dominated plane wave

$$\varphi_{\mathrm{I}} = \mathrm{e}^{-\mathrm{i}k_{\varphi 1}(x\cos\psi + y\sin\psi)}, \qquad \psi \in (0, \pi), \tag{4.1}$$

where $\psi$ is the angle of incidence (measured anticlockwise from $y = 0$), and we assume $\operatorname{Re} k_{\varphi 1} \geq 0$ and $\operatorname{Im} k_{\varphi 1} \geq 0$.

This incoming energy will be converted into reflected/transmitted thermo-compressional and shear modes. Given the translational invariance of the problem in the $x$-direction, each potential will depend on $x$ through $\mathrm{e}^{-\mathrm{i}k_{\varphi_1} x\cos\psi}$, and therefore we write

$$\varphi_{\mathrm{R}} = R_\varphi \mathrm{e}^{\mathrm{i}k_{\varphi_1}\sin\psi y}\mathrm{e}^{-\mathrm{i}k_{\varphi_1}x\cos\psi}, \qquad \varphi_{\mathrm{T}} = T_\varphi \mathrm{e}^{-\mathrm{i}d_{\varphi_{\mathrm{T}}}y}\mathrm{e}^{-\mathrm{i}k_{\varphi_1}x\cos\psi}, \tag{4.2a}$$

$$\vartheta_{\mathrm{R}} = R_\vartheta \mathrm{e}^{\mathrm{i}d_{\vartheta_{\mathrm{R}}}y}\mathrm{e}^{-\mathrm{i}k_{\varphi_1}x\cos\psi}, \qquad \vartheta_{\mathrm{T}} = T_\vartheta \mathrm{e}^{-\mathrm{i}d_{\vartheta_{\mathrm{T}}}y}\mathrm{e}^{-\mathrm{i}k_{\varphi_1}x\cos\psi}, \tag{4.2b}$$

$$\boldsymbol{\Phi}_{\mathrm{R}} = \mathbf{e_z} R_\Phi \mathrm{e}^{\mathrm{i}d_{\Phi_{\mathrm{R}}}y}\mathrm{e}^{-\mathrm{i}k_{\varphi_1}x\cos\psi}, \qquad \boldsymbol{\Phi}_{\mathrm{T}} = \mathbf{e_z} T_\Phi \mathrm{e}^{-\mathrm{i}d_{\Phi_{\mathrm{T}}}y}\mathrm{e}^{-\mathrm{i}k_{\varphi_1}x\cos\psi}, \tag{4.2c}$$

where the potentials $\varphi_{\mathrm{R}}$, $\vartheta_{\mathrm{R}}$, and $\Phi_{\mathrm{R}}$ are defined in the upper half space $y \geq 0$, while the potentials $\varphi_{\mathrm{T}}$, $\vartheta_{\mathrm{T}}$, and $\Phi_{\mathrm{T}}$ are defined in the lower half space $y \leq 0$. We use subscripts R/T to denote reflected/transmitted respectively. In the above we introduced the notation

$$\begin{aligned} &d_{\varphi_{\mathrm{T}}} = \mathrm{i}\sqrt{-(k_{\varphi_2}^2 - k_{\varphi_1}^2\cos^2\psi)}, \quad d_{\vartheta_{\mathrm{R}}} = \mathrm{i}\sqrt{-(k_{\vartheta_1}^2 - k_{\varphi_1}^2\cos^2\psi)}, \quad d_{\vartheta_{\mathrm{T}}} = \mathrm{i}\sqrt{-(k_{\vartheta_2}^2 - k_{\varphi_1}^2\cos^2\psi)}, \\ &d_{\Phi_{\mathrm{R}}} = \mathrm{i}\sqrt{-(k_{\Phi_1}^2 - k_{\varphi_1}^2\cos^2\psi)}, \quad d_{\Phi_{\mathrm{T}}} = \mathrm{i}\sqrt{-(k_{\Phi_2}^2 - k_{\varphi_1}^2\cos^2\psi)}. \end{aligned} \tag{4.3}$$

With (4.3), when using the standard branch cut for the square root along the negative real line we have

$$\operatorname{Im} d_{\varphi_{\mathrm{T}}}, \operatorname{Im} d_{\vartheta_{\mathrm{R}}}, \operatorname{Im} d_{\vartheta_{\mathrm{T}}}, \operatorname{Im} d_{\Phi_{\mathrm{R}}}, \operatorname{Im} d_{\Phi_{\mathrm{T}}} \geq 0, \tag{4.4}$$

which guarantees that each of the potentials in (4.2) are bounded within their respective halfspaces.

To completely determine the potentials (4.2) we use the boundary conditions representing continuity of traction, displacement, temperature, and temperature flux, across $y = 0$, [8]

$$\hat{\boldsymbol{\sigma}}_1 \mathbf{e_y} = \hat{\boldsymbol{\sigma}}_2 \mathbf{e_y}, \quad \hat{\mathbf{u}}_1 = \hat{\mathbf{u}}_2 \tag{4.5a}$$

$$\hat{\theta}_1 = \hat{\theta}_2, \quad \mathscr{K}_1 \nabla\hat{\theta}_1 \cdot \mathbf{e_y} = \mathscr{K}_2 \nabla\hat{\theta}_2 \cdot \mathbf{e_y}, \tag{4.5b}$$

where $\hat{\boldsymbol{\sigma}}_1$ and $\hat{\boldsymbol{\sigma}}_2$ are the stress tensors in the upper (1) and lower (2) media respectively, while $\mathbf{u}_1$ and $\mathbf{u}_2$ are the displacements in media 1 and 2.

Substituting (4.2) into (4.5), using (2.36) and (2.40), leads to the following six equations

$$\begin{pmatrix} a_{11} & a_{12} & a_{13} & a_{14} & a_{15} & a_{16} \\ a_{21} & a_{22} & a_{23} & a_{24} & a_{25} & a_{26} \\ a_{31} & a_{32} & a_{33} & a_{34} & a_{35} & a_{36} \\ a_{41} & a_{42} & a_{43} & a_{44} & a_{45} & a_{46} \\ a_{51} & a_{52} & a_{53} & a_{54} & 0 & 0 \\ a_{61} & a_{62} & a_{63} & a_{64} & 0 & 0 \end{pmatrix} \begin{pmatrix} R_\varphi \\ T_\varphi \\ R_\vartheta \\ T_\vartheta \\ R_\Phi \\ T_\Phi \end{pmatrix} = \begin{pmatrix} a_{11} \\ -a_{21} \\ -a_{31} \\ a_{41} \\ -a_{51} \\ a_{61} \end{pmatrix}. \tag{4.6}$$

To calculate the entries $a_{ij}$ we provide a Mathematica notebook as supplementary material [46]. The above can be used to uniquely determine the six amplitudes $R_\varphi, T_\varphi, R_\vartheta, T_\vartheta, R_\Phi$, and $T_\Phi$.

## 4.2 The VE-VE limit

In the limit of no thermal coupling we let $\alpha_1$, $\alpha_2 \to 0$ (and hence $k_{\varphi_1} \to k_{\phi_1}$, $k_{\varphi_2} \to k_{\phi_2}$ and $\mathscr{T}_{\varphi_1}$, $\mathscr{T}_{\varphi_2} \to 0$) in (4.6) as discussed in Section 3.2. From this we conclude that $R_\vartheta, T_\vartheta \to 0$ and the scattering system reduces to

$$\begin{pmatrix} a_{11} & a_{12} & a_{15} & a_{16} \\ a_{21} & a_{22} & a_{25} & a_{26} \\ a_{31} & a_{32} & a_{35} & a_{36} \\ a_{41} & a_{42} & a_{45} & a_{46} \end{pmatrix} \begin{pmatrix} R_\varphi \\ T_\varphi \\ R_\Phi \\ T_\Phi \end{pmatrix} = \begin{pmatrix} a_{11} \\ -a_{21} \\ -a_{31} \\ a_{41} \end{pmatrix}, \tag{4.7}$$

[8] Where in component form we have $\hat{\boldsymbol{\sigma}}_1 \mathbf{e_y} = ((\hat{\boldsymbol{\sigma}}_1)_{xy}, (\hat{\boldsymbol{\sigma}}_1)_{yy}, (\hat{\boldsymbol{\sigma}}_1)_{zy})$.

where the limit of $\alpha_1, \alpha_2 \to 0$ should be taken for each of the $a_{ij}$. For normal incidence, $\psi = \pi/2$ we obtain the classical solutions

$$R_\varphi = \frac{-k_{\phi_1}(\tilde{\lambda}_1 + 2\tilde{\mu}_1) + k_{\phi_2}(\tilde{\lambda}_2 + 2\tilde{\mu}_2)}{k_{\phi_1}(\tilde{\lambda}_1 + 2\tilde{\mu}_1) + k_{\phi_2}(\tilde{\lambda}_2 + 2\tilde{\mu}_2)} = \frac{\bar{\rho}_2\bar{c}_{\phi_2} - \bar{\rho}_1\bar{c}_{\phi_1}}{\bar{\rho}_2\bar{c}_{\phi_2} + \bar{\rho}_1\bar{c}_{\phi_1}}, \tag{4.8a}$$

$$T_\varphi = \frac{2k_{\phi_1}^2(\tilde{\lambda}_1 + 2\tilde{\mu}_1)}{k_{\phi_2}[k_{\phi_1}(\tilde{\lambda}_1 + 2\tilde{\mu}_1) + k_{\phi_2}(\tilde{\lambda}_2 + 2\tilde{\mu}_2)]} = \frac{2\bar{\rho}_1\bar{c}_{\phi_2}}{\bar{\rho}_2\bar{c}_{\phi_2} + \bar{\rho}_1\bar{c}_{\phi_1}}, \tag{4.8b}$$

where we have introduced the free space compressional wave speed in each medium through the relation $\bar{c}_\phi = \bar{\omega}/\bar{k}_\phi$. The well-known equations (4.8) give a clear interpretation of the role of the mechanical impedance $\bar{\rho}\bar{c}_\phi$ when it comes to reflection/transmission, see e.g. §1.4. in [47] (for elasticity). We next discuss the more subtle aspect of the partition of energy at the interface.

## 4.3 Energy partitioning at the interface

Consider the energy flux through the boundary $y = 0$. The average energy flux vectors are defined in (E.2), and since for this problem we have two distinct media, we write[9]

$$\langle \mathbf{J} \rangle = \begin{cases} \langle \mathbf{J}_1 \rangle = \frac{1}{2}\,\mathrm{Re}\{\boldsymbol{\sigma}_1 \dot{\mathbf{u}}_1^* + \theta_1 \mathscr{K}_1 \nabla\theta_1^*\} & \text{for} \quad y \geq 0, \\ \langle \mathbf{J}_2 \rangle = \frac{1}{2}\,\mathrm{Re}\{\boldsymbol{\sigma}_2 \dot{\mathbf{u}}_2^* + \theta_2 \mathscr{K}_2 \nabla\theta_2^*\} & \text{for} \quad y < 0. \end{cases} \tag{4.9}$$

If the boundary conditions (4.5) have been correctly enforced, we expect to have

$$\langle \mathbf{J}_1 \rangle \cdot \mathbf{e_y} = \langle \mathbf{J}_2 \rangle \cdot \mathbf{e_y} \quad \text{at} \quad y = 0, \tag{4.10}$$

meaning that the normal component of the mean energy flux (or power per unit area averaged over a period) is *continuous* across the boundary $y = 0$. We show in Appendix E how (4.10) can be written in terms of *energy ratios* for reflected, transmitted and interacting modes as

$$E_{R_\varphi} + E_{R_\vartheta} + E_{R_\Phi} + E_{IR_{\mathrm{IR}}} + E_{IR_{\mathrm{RR}}} + E_{T_\varphi} + E_{T_\vartheta} + E_{T_\Phi} + E_{IT_{\mathrm{TT}}} = 1. \tag{4.11}$$

After solving for all the relevant wave potentials, the above can be used as a check to ensure both numerical accuracy and algebraic correctness. We have noted that the presence of 'crossed terms' (Appendix E.1) represented by interaction coefficients $E_{IR}, E_{IT}$ in (4.11) has been repeatedly ignored in the literature without justification e.g. [45], [44]. We find (not shown) that despite their contribution being small at lower frequencies, their importance in the energy balance equation becomes essential at higher frequencies, and it should therefore be emphasized under what conditions it is a valid approximation to ignore them. Further details can be found in [42] (in the absence of thermal coupling).

## 4.4 Numerical results and discussion

We now present some illustrations of numerical solutions of the general system (4.6) for specific pairs of TVE materials. All results were checked to accurately satisfy the energy flux balance (4.11). We thus demonstrate when thermal or viscous effects are important for these examples, and in particular we can illustrate the effect of stress relaxation. We do this by comparing solutions from the general TVE-TVE case in (4.6) with the solutions of VE-VE (4.7), which ignores thermal effects,

[9] Where the product between the Cauchy stress and velocity is written in component form as $\boldsymbol{\sigma}_1 \dot{\mathbf{u}}_1^* = (\boldsymbol{\sigma}_1)_{ij}(\dot{\mathbf{u}}_1)_j^*$ where we sum over $j$.

the TVA-rigid solutions (F.7), which consider no transmission, and other variations specified in Table 2.

We use typical values for air, water, steel and rubber as summarized in Table 4. The large parameter space involved allows for an incredibly wide range of materials to be considered. Here we only consider a small fraction of this space, but hope that this work enables further exploration in the future. In particular we stress that the general TVE framework allows general materials to be considered and no distinction to be required between fluids or solids, etc. which frequently hampers progress via the necessary use of distinct notation for each medium.

| Acronym | TVA–Local TVE | VA–Local VE | TVA–Rigid | A–Rigid | TVE–TVA | VE–VA | TVA–TVE |
|---|---|---|---|---|---|---|---|
| Equation | (4.6) with (4.12) | (4.7) with (4.12) | (F.6) with (F.7) | (F.6) with (F.11) | (4.6) with (4.13) | (4.7) with (4.13) | (4.6) with (4.15) |

Table 2: Specific equations corresponding to the various acronyms used in the results and discussion of Section 4.4.

### 4.4.1 TVA - Local TVE: Thermo-visco-elastic effects and fluid-strucure interaction

In this first instance we restrict the material parameters of medium 1 to those of air/water whereas for medium 2 we will concentrate on steel/rubber. Both air and water have many applications, while investigating steel and rubber means we are considering both soft and hard solids.

We first investigate the use of TVA in medium 1 (or local TVE with $\mu_1 = 0$) and local TVE in medium 2 such that the complex moduli appearing in (4.6) are given by

$$\tilde{\mu}_1(\mathrm{i}\omega) = -\mathrm{i}\omega\eta_{\mu 1}, \quad \tilde{\lambda}_1(\mathrm{i}\omega) = \lambda_1 - \mathrm{i}\omega\eta_{\lambda 1}, \quad \tilde{\mu}_2(\mathrm{i}\omega) = \mu_2 - \mathrm{i}\omega\eta_{\mu 2}, \quad \tilde{\lambda}_2(\mathrm{i}\omega) = \lambda_2 - \mathrm{i}\omega\eta_{\lambda 2}, \tag{4.12}$$

as discussed in Sections 2.3.3, 3.1. For some of these parameters, it is difficult to find numerical values in the literature, take for example $\eta_{\lambda 2}$ [34]. In these cases, we attempt to use reasonable values based on similar materials. The viscoelastic parameters for steel are taken from Table 6.2.2. in [42].

**Air-Solid interface.** Thermal effects are known to be important in air, as we can clearly see in Figure 5a, where various reflection coefficients are compared. This is evidenced by the value of thermo-mechanical coupling term for air (3.3) given by $|L_\theta| \approx 1$ due to air's high thermal expansion coefficient. The pressure dominated reflection coefficient $R_\varphi$ (responsible for most of the energy) is clearly different for a system which does not include thermal effects in air, such as VA-VE. This is especially true at higher frequencies, in agreement with [5] for narrow slits. Here thermal effects for air are less pronounced for lower frequencies, as shown in Figure 5b for $f = 10$ kHz. The reflected shear wave is no longer excited and $|R_\varphi|$'s minimum moves closer to the grazing angle of incidence $\psi = 0$. This behaviour is due to viscous and thermal boundary layer effects near the interface, and can be described through an analytical expression for the *specific admittance*, where the influence of frequency and angle of incidence become apparent, see e.g. Section 3.2.1 in [6]. Naturally, the solution to the A-Rigid configuration in the absence of any losses gives $R_\varphi = 1$ everywhere, independently of the incident frequency, see (F.11).

Note that neither thermal nor viscous effects are important in medium 2, as using the rigid boundary conditions, TVA-rigid, accurately recovers the reflection coefficient of TVA-TVE.

For all of these parameters we obtained almost identical results when swapping rubber for steel, noting that for air-steel the small discrepancy between TVA-rigid and TVA-TVE observed near

grazing in Figure 5b disappears. The overall excellent agreement is because in both cases there is little transmission into the solid. The same cannot be said of a water-solid interface as we now describe.

**Water-Solid interface.** As the mechanical impedance of water is closer to the impedance of most solids, more mechanical energy will be transmitted into the solid giving rise to FSI effects. This is apparent from Figures 5c, 5d where the TVA-rigid solutions no longer agree with the TVA-TVE system. On the other hand, in contrast to air, thermal effects are no longer particularly important, indicated by the fact that TVA-TVE and VA-VE solutions are almost the same. This is due to the smaller thermal coupling for water $|L_\theta| \approx 0.078$. We observe that the $|R_\varphi|$ behaviour for water-Rubber 2 is indistinguishable at low and high frequencies, resembling the purely elastic solutions ((4.7) with $\eta_{\mu 1}, \eta_{\mu 2}, \eta_{\lambda 1}, \eta_{\lambda 2} = 0$) which are independent of frequency. The same can be said for the transmitted modes. Nevertheless, we will observe shortly how this behaviour can change when stress relaxation is considered.

For water-steel the frequency dependence is nevertheless apparent. In the TVA-TVE solutions, boundary layer effects are visible near grazing incidence at higher frequencies (Figure 5c), in contrast to the lower frequency regime, where $|R_\varphi|$ remains very close to one as seen in Figure 5d. The TVA-Rigid solutions greatly overestimate these effects near $\psi = 0$ at both frequencies. As opposed to the in-air case, reflected boundary layer shear waves into the water were not found i.e. $|R_\Phi| \approx 0$ in each case and hence not included in the figures. The other notable frequency-dependent feature for water-steel is the emergence of a significant reduction in amplitude at high frequencies for a narrow range of angles of incidence around the interval $(\pi/4, 3\pi/8)$. This phenomenon was first observed experimentally in the 1960s for water-aluminum and it was noticed that it disagreed with predictions of elastic reflection–refraction theory. It has been discussed by several authors since including [43], [25], [42] where the latter reference provides a detailed explanation under a VA-VE model. Under the framework presented in this work, we have extended their model to include thermal losses in both media, although as we can observe these are not manifested in the solutions when compared to the isothermal solution. Finally, we note that the $|R_\varphi|$ behaviour for $\psi \in (3\pi/8, \pi/2)$ in Figures 5c and 5d is elastic and independent of frequency, and the two distinct features in this region are a consequence of the transmitted SV and P waves in the lower half-space being induced respectively (not shown).

### 4.4.2 Influence of stress relaxation

We now explore the effect of stress relaxation in the solid. Little discussion is found on stress relaxation times for metals in the literature since in most instances they are nearly undamped materials e.g. [13], so here we focus on results for rubbery media following the values in Table 4.

**Rubber-Air interface.** We first investigate a TVE-TVA interface, where the incident energy arises from the solid. Following the discussion in Section 2.3.2, we assume that the relaxation is purely in shear and is governed by a single-term Prony series, with the bulk modulus being a real valued constant such that

$$\tilde{\mu}_1(\mathrm{i}\omega) = \mu_{\infty 1} - (\mu_{01} - \mu_{\infty 1})\frac{\mathrm{i}\omega t_r}{1 - \mathrm{i}\omega t_r}, \qquad \tilde{\lambda}_1(\mathrm{i}\omega) = K_1 - \frac{2}{3}\tilde{\mu}_1(\mathrm{i}\omega), \tag{4.13}$$

$$\tilde{\mu}_2(\mathrm{i}\omega) = -\mathrm{i}\omega\eta_{\mu 2}, \qquad \tilde{\lambda}_2(\mathrm{i}\omega) = \lambda_2 - \mathrm{i}\omega\eta_{\lambda 2}. \tag{4.14}$$

As discussed in Section 2.3.2, the relevant non-dimensional parameter to investigate the different regions of the modulus is $\omega t_r$. For a given material, the relaxation time is fixed and it scales the

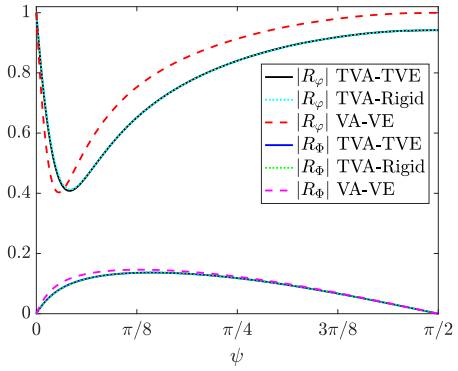


(a) Air-Rubber 2 $f = 10$ MHz.

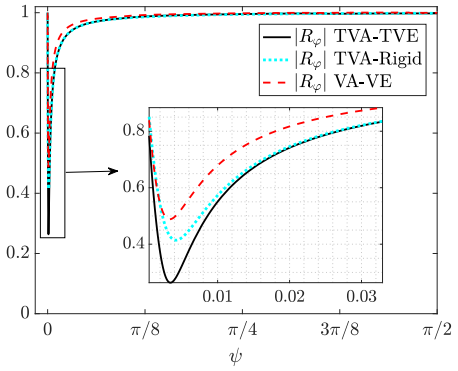


(b) Air-Rubber 2 $f = 10$ kHz

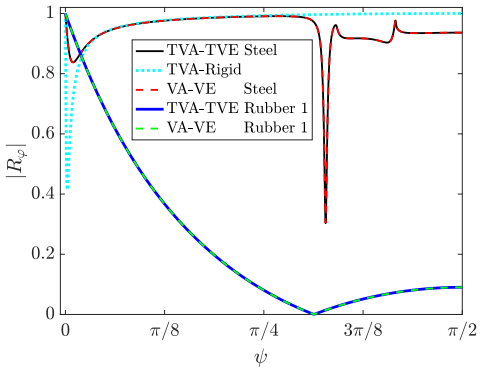


(c) Water-Rubber 1/Steel $f = 10$ MHz

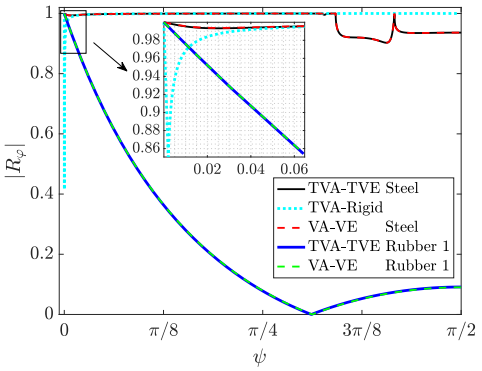


(d) Water-Rubber 1/Steel $f = 10$ kHz

Figure 5: Magnitude of the reflection coefficients as predicted by the different systems in Table 2 with the material constants used shown in Table 4. The results cover different fluid-solid interfaces for both higher ($f = 10$MHz) and lower ($f = 10$kHz) frequencies, and the $x$-axis shows the angle of incidence $\psi$.

resulting frequency behaviour. Here we choose three distinct values, namely $\omega t_r = 0.063, 1.005, 62.83$ corresponding to the rubbery, transition and glassy regions of the shear modulus, as shown explicitly in Table 3.

For Rubber 1 in Table 4, it was found that $R_\varphi \approx -1$, independently of $\psi, \omega t_r$. This is due to the fact that for Rubber 1 $K_1 \gg |\tilde{\mu}_1(\mathrm{i}\omega)|$ at all frequencies since this material is nearly incompressible, and hence the associated Poisson's ratio remains very close to $1/2$ in each case. Nevertheless, for Rubber 2 the situation is much different, as shown in Figure 6. In the rubbery region $\omega t_r = 0.063$, the incident angle dependence on reflection remains small but this changes in the transition region and especially in the glassy region. For $\omega t_r = 62.83$ we observe that the reflected SV wave gets excited with a global maximum near $\psi = \pi/4$ where the amplitude $R_\Phi$ becomes almost 50% of that of the incident wave. Despite the smaller ratio $\mu_{01}/\mu_{\infty 1}$ of Rubber 2 compared to Rubber 1, its higher magnitude implies that it becomes more compressible and the Poisson's ratio reduces (see Table 3) which in turn excites the reflected shear wave, e.g. for $\omega t_r = 1.005$, we have $|\tilde{\nu}(\mathrm{i}\omega)| = 0.425$. Since these solutions are mainly influenced by the Poisson's ratio, for a practical realization it is the frequency dependence $\tilde{\nu}(\mathrm{i}\omega)$ that should be studied more in depth, see e.g. [15] for an extensive review.

| Modulus / $\omega t_r$ | $\bar{\tilde{\mu}}$ Rubber 1/Rubber 2 | $\tilde{\nu}$ Rubber 1/Rubber 2 |
|---|---|---|
| 0.062 | $3.38 \times 10^5 - 6.07 \times 10^5\mathrm{i}/2.1 \times 10^7 - 1.7 \times 10^7\mathrm{i}$ | $0.4999 + 0.00018\mathrm{i}/0.489 + 0.008\mathrm{i}$ |
| 1.005 | $5.2 \times 10^6 - 4.85 \times 10^6\mathrm{i}/1.6 \times 10^8 - 1.4 \times 10^8\mathrm{i}$ | $0.498 + 0.00142\mathrm{i}/0.42 + 0.06\mathrm{i}$ |
| 62.83 | $9.99 \times 10^6 - 1.54 \times 10^5\mathrm{i}/2.99 \times 10^8 - 4.4 \times 10^6\mathrm{i}$ | $0.497 + 0.00004\mathrm{i}/0.36 + 0.0018\mathrm{i}$ |

Table 3: Shear modulus and Poisson's ratio values according to the SLSM, the values of $\omega t_r$ have been chosen to cover the rubbery, transition and glassy regions.

For both rubbers the thermo-mechanical coupling is small such that $L_\theta = O(10^{-2})$, and therefore equivalent results are obtained when using the VE-VE system (4.7). Again due to the mechanical impedance mismatch, transmission into the air is negligible. In fact, these results obtained for air in the lower medium had excellent agreement with the associated problem of a single TVE half-space with traction free and isothermal/adiabatic boundary conditions. Although not included in this report, these simpler solutions showcase explicitly the role of $\nu$ described above (see e.g. §5.6 in [47] in the absence of losses).

**Fluid-Rubber interface.** In the second example, we want to investigate whether stress relaxation effects in rubber can still alter the reflection/transmission pattern when the incident energy comes from the fluid, so we return to a fluid-solid TVA-TVE interface such that

$$\tilde{\mu}_1(\mathrm{i}\omega) = -\mathrm{i}\omega\eta_{\mu 1}, \quad \tilde{\lambda}_1(\mathrm{i}\omega) = \lambda_1 - \mathrm{i}\omega\eta_{\lambda 1}, \quad \tilde{\mu}_2(\mathrm{i}\omega) = \mu_{\infty 2} - (\mu_{02} - \mu_{\infty 2})\frac{\mathrm{i}\omega t_r}{1 - \mathrm{i}\omega t_r}, \quad \tilde{\lambda}_2(\mathrm{i}\omega) = K_2 - \frac{2}{3}\tilde{\mu}_2(\mathrm{i}\omega). \tag{4.15}$$

In the case of air-rubber (1 & 2), for each value of $\omega t_r$ the reflected modes behave as discussed with the local TVE model in Figures 5a, 5b and the transmission into the rubber is negligible. Although as we observed in Figure 5c, energy gets transmitted into the solid in a water-Rubber 1 interface, the frequency variation of the shear modulus according to the SLSM did not manifest in any results that deviated much from the Local TVE case. This occurs due to the high Poisson's ratio of Rubber 1, as discussed above for the rubber-air interface. For water-Rubber 2 however, significant differences in $|R_\varphi|, |T_\varphi|, |T_\Phi|$ do arise.

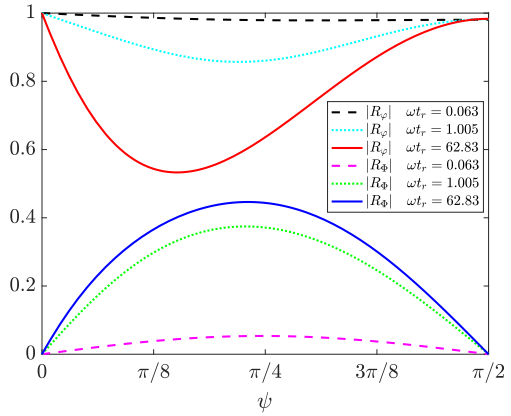


Figure 6: Reflection coefficients for a Rubber2-air interface in the rubbery, transition and glassy regions of the shear modulus according to the SLSM. The material constants used are shown in Table 4.

It is often of interest in application to avoid any acoustic reflection in the incident medium, which requires impedance matching with the neighbouring medium. Since for these materials thermal coupling was found to be unimportant, (4.8) can be used to tune Rubber 2 in order to impedance match it with the water for a particular value of frequency. As an illustration, following this principle we simply tune the density of Rubber 2 ($\bar{\rho}_2$ : 2300 $\rightarrow$ 1588 kg/m$^3$) in order to impedance match it with water in the glassy region represented by $\omega t_r = 62.83$, as shown in Figure 7. For the reflected/transmitted P waves, the differences between $\omega t_r$ increase monotonically as $\psi$ moves from grazing to normal incidence, where the maximum difference occurs. A 10% variation in the magnitude of the reflected amplitude was found between the glassy and rubbery regions. Similar values for this variation yield for the transmitted shear wave, where the maximum difference occurs near $\psi = \pi/4$.

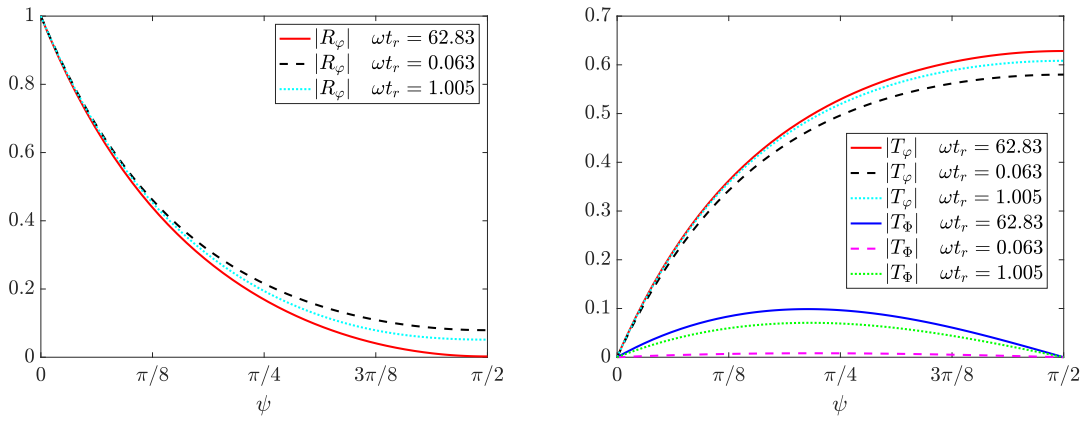


Figure 7: Reflection/Transmission of a water-Rubber 2 interface according to (4.6), where the density of material 2 has been adapted to impedance match with $\mu_0$ in the glassy region.

| **TVE Parameter Values** | | | | | | |
|---|---|---|---|---|---|---|
| Parameter | Unit | Symbol | Air | Water | Steel | Rubber 1/2 |
| **Elastic** | | | | | | |
| Background density | kg/m$^3$ | $\rho_0$ | 1.19 | 1000 | 7932 | 1522/2300 |
| Bulk modulus (isothermal) | Pa | $K$ | $100.72\times10^3$ | $2.2\times10^9$ | $1.57\times10^{11}$ | $1.7\times10^9/10^9$ |
| Shear modulus | Pa | $\mu_0$ | 0 | 0 | $7.83\times10^{10}$ | $10^7/\ 3\times10^8$ |
| Relaxed Shear modulus (for SLSM) | Pa | $\mu_\infty$ | - | - | - | $3\times10^5/2\times10^7$ |
| **Local Viscous** | | | | | | |
| Dynamic shear viscosity | Pa·s | $\eta_\mu$ | $1.8\times10^{-5}$ | $10^{-3}$ | 15 | $10^{-2}/\ 10^{-2}$ |
| Dynamic bulk viscosity | Pa·s | $\eta_K$ | $1.1\times10^{-5}$ | $3\times10^{-3}$ | $10^{-8}$ | $10^{-2}/\ 10^{-2}$ |
| **Thermal** | | | | | | |
| Thermal conductivity | W/m·K | $\mathcal{K}$ | 0.026 | 0.597 | 30 | 2 |
| Specific heat at constant pressure | J/kg·K | $c_p$ | 1005 | 4181.6 | 500 | 1300 |
| Ambient temperature | K | $T_0$ | 300 | 300 | 300 | 300 |
| Coefficient of thermal expansion | 1/K | $\alpha$ | 1/300 | $2.6\times10^{-4}$ | $1.7\times10^{-5}$ | $2.5\times10^{-4}$ |
| Ratio of specific heats | - | $\gamma$ | 1.39 | 1.01 | 1.0003 | 1.008 |

Table 4: Thermo-viscous parameter values for air, water, steel and rubber employed in the several plots of Section 4. Air is taken from [37] and Water from engineeringtoolbox. The VE values for Steel are taken from Table 6.2.2. in [42], which follow from experiments. The high value of $\eta_\mu$ arises from 'fitting' a KV model to the imaginary part of the shear modulus which comes from measurements at 10MHz. The values of rubber are based on the ranges provided in [48].

# 5 Conclusions

Understanding how to model and exploit loss mechanisms in complex materials is important in many applications and increasingly so in the areas of composite media and metamaterials science. Here we have presented a general unified framework, permitting the incorporation of both creep and relaxation via time non-locality, with which one can study linear wave propagation in thermo-visco-elastic media. We illustrated the framework with the configuration of two semi-infinite half-

spaces in perfect contact, with plane compressional-wave incidence on the interface that separates the media. We used this example to compare solutions when incorporating viscosity and thermal effects. For fluid-solid interfaces we noted the important role of the incident frequency and angle on the contribution to visco-thermal effects as well as visco-elastic attenuation within the solid. For the latter we emphasized the differences induced when the shear modulus includes stress relaxation, as opposed to the local-in-time counterpart where the real part of the modulus remains fixed.

There are many advantages to the unified framework presented here, but three are key. Firstly, it provides a mechanism to study canonical wave propagation problems when there is coupling between different media, and specifically between what are classically perceived as *fluid* and *solid*. As we have shown this distinction is often clear away from boundaries but is less clear close to such interfaces. A unified framework allows such modelling to be carried out once and for all, without the need to develop separate models for each, as is often done [49, 5]. To help illustrate the connection between the framework and other well-known models for dissipation, such as thermo-visco-acoustics in fluids, or visco-elasticity, we have demonstrated how to take the appropriate limits to recover these special cases from our framework.

The second key advantage is the potential use of the framework to understand fully time-dependent problems. It is common for wave propagation problems to be studied at single frequencies, which is sufficient in its own right, but if a viscoelastic model is employed, one must be confident that this model is capable of representing the behaviour across a broad range of frequencies, especially if one wishes to subsequently use this model in the time domain, given that a time domain signal will encompass a vast range of frequency content in general. It is often seen as standard practice to employ simple Kelvin-Voigt models to account for viscoelasticity, with "parameters that are frequency dependent" [12, 50]. Whilst this may be sufficient to model the material response at fixed frequencies, it is not sufficient to be employed in the time domain.

The third advantage of the unified framework that incorporates stress relaxation and creep is that one can then employ these models to understand and describe wave propagation in polymeric media. Such materials have the behaviour as illustrated throughout this paper, with a specific frequency at which maximum loss occurs, also related to a temperature, know as the glass-transition. This behaviour is particularly important to accommodate when polymers are employed in the metamaterial context since the design of metamaterials focuses on internal resonance and therefore one may wish to design this resonance with knowledge of this transition in mind, either to increase or decrease inherent attenuation in the material.

We anticipate that the presented framework can now be employed on various problems of interest. In particular it can be used to unify the approach to the problem described in [5] and this will therefore now be extended in Chapter 4 in order to study fluid-filled slits and fluid-loaded plates, when the "solid" in both cases is *soft* and therefore can couple strongly to the fluid.

# REFERENCES

[1] A.V. Tobolsky and J.R. McLoughlin. Elastoviscous properties of polyisobutylene. v. the transition region. *Journal of Polymer Science*, 8(5):543–553, 1952.

[2] N. Obaid, M.T. Kortschot, and M. Sain. Understanding the stress relaxation behavior of polymers reinforced with short elastic fibers. *Materials*, 10(5):472, 2017.

[3] Y.H. Jeong. Frequency-dependent shear modulus of glycerol near the glass transition. *Physical Review A*, 36(2):766, 1987.

[4] L. Kari, P. Eriksson, and B. Stenberg. Dynamic stiffness of natural rubber cylinders in the audible frequency range using wave guides. *Kautschuk Gummi Kunststoffe*, 54(3):106–106, 2001.

[5] P.A. Cotterill, D. Nigro, I.D. Abrahams, E. Garcia-Neefjes, and W.J. Parnell. Thermo-viscous damping of acoustic waves in narrow channels: A comparison of effects in air and water. *The Journal of the Acoustical Society of America*, 144(6):3421–3436, 2018.

[6] M. Bruneau. *Fundamentals of acoustics*. John Wiley & Sons, 2013.

[7] S.A. Cummer, J. Christensen, and A. Alù. Controlling sound with acoustic metamaterials. *Nature Reviews Materials*, 1(3):16001, 2016.

[8] N. Jiménez, V. Romero-García, V. Pagneux, and J-P. Groby. Rainbow-trapping absorbers: Broadband, perfect and asymmetric sound absorption by subwavelength panels for transmission problems. *Scientific reports*, 7(1):13595, 2017.

[9] K. Pham, A. Maurel, and J-J. Marigo. Two scale homogenization of a row of locally resonant inclusions-the case of anti-plane shear waves. *Journal of the Mechanics and Physics of Solids*, 106:80–94, 2017.

[10] M. Touboul, K. Pham, A. Maurel, J-J. Marigo, B. Lombard, and C. Bellis. Effective resonant model and simulations in the time-domain of wave scattering from a periodic row of highly-contrasted inclusions. *Journal of Elasticity*, 142(1):53–82, 2020.

[11] A.A. Fernández-Marín, N. Jiménez, J-P. Groby, J. Sánchez-Dehesa, and V. Romero-García. Aerogel-based metasurfaces for perfect acoustic energy absorption. *Applied Physics Letters*, 115(6):061901, 2019.

[12] N. Favretto-Anrès and G. Rabau. Excitation of the stoneley–scholte wave at the boundary between an ideal fluid and a viscoelastic solid. *Journal of sound and vibration*, 203(2):193–208, 1997.

[13] Y. Liao and V. Wells. Estimation of complex modulus using wave coefficients. *Journal of Sound and Vibration*, 295(1-2):165–193, 2006.

[14] T. Chen. Determining a Prony series for a viscoelastic material from time varying strain data, 21p. *NASA*, 2000.

[15] N.W. Tschoegl, W.G. Knauss, and I. Emri. Poisson's ratio in linear viscoelasticity–a critical review. *Mechanics of Time-Dependent Materials*, 6(1):3–51, 2002.

[16] J.E. Marsden and T.J.R. Hughes. *Mathematical foundations of elasticity*. Dover publications, 1994.

[17] B.A. Boley and J.H. Weiner. *Theory of thermal stresses*. Courier Corporation, 2012.

[18] B.D. Coleman and W. Noll. The thermodynamics of elastic materials with heat conduction and viscosity. *Archive for rational mechanics and analysis*, 13(1):167–178, 1963.

[19] I-S. Liu. Method of lagrange multipliers for exploitation of the entropy principle. *Archive for Rational Mechanics and Analysis*, 46(2):131–148, 1972.

[20] J.D. Ferry. *Viscoelastic properties of polymers*. John Wiley & Sons, 1980.

[21] C. Cattaneo. A form of heat conduction equation which eliminates the paradox of instantaneous propagation. *Comptes Rendus*, 247:431–433, 1958.

[22] H.W. Lord and Y. Shulman. A generalized dynamical theory of thermoelasticity. *Journal of the Mechanics and Physics of Solids*, 15(5):299–309, 1967.

[23] K.F. Graff. *Wave motion in elastic solids*. Courier Corporation, 2012.

[24] W. Nowacki. *Thermoelasticity*. Elsevier, 2013.

[25] M. Deschamps and C. Cheng. Liquid-thermoviscoelastic solids interface. *Ultrasonics*, 27(5):308–313, 1989.

[26] D. Ieşan. On a theory of thermoviscoelastic materials with voids. *Journal of Elasticity*, 104(1-2):369–384, 2011.

[27] R.M. Christensen and P.M. Naghdi. Linear non-isothermal viscoelastic solids. *Acta Mechanica*, 3(1):1–12, 1967.

[28] R.M. Christensen. *Theory of viscoelasticity: an introduction*. Elsevier, 2012.

[29] H. Berjamin, M. Destrade, and W.J. Parnell. On the thermodynamic consistency of quasi-linear viscoelastic models for soft solids. *Mechanics Research Communications*, 111:103648, 2021.

[30] S.C. Hunter. Tentative equations for the propagation of stress, strain and temperature fields in viscoelastic solids. *Journal of the Mechanics and Physics of Solids*, 9(1):39–51, 1961.

[31] V. Balbi, T. Shearer, and W.J. Parnell. A modified formulation of quasi-linear viscoelasticity for transversely isotropic materials under finite deformation. *Proceedings of the Royal Society A: Mathematical, Physical and Engineering Sciences*, 474(2217):20180231, 2018.

[32] W.G. Gottenberg and R.M. Christensen. An experiment for determination of the mechanical property in shear for a linear, isotropic viscoelastic solid. *International Journal of Engineering Science*, 2(1):45–57, 1964.

[33] J.M. Lifshitz and H. Kolsky. The propagation of spherically divergent stress pulses in linear viscoelastic solids. *Journal of the Mechanics and Physics of Solids*, 13(6):361–376, 1965.

[34] E.A. Ivanova. Derivation of theory of thermoviscoelasticity by means of two-component medium. *Acta mechanica*, 215(1):261–286, 2010.

[35] N.O. Birge and S.R. Nagel. Wide-frequency specific heat spectrometer. *Review of scientific instruments*, 58(8):1464–1470, 1987.

[36] M. Kaliske and H. Rothert. Formulation and implementation of three-dimensional viscoelasticity at small and finite strains. *Computational Mechanics*, 19(3):228–239, 1997.

[37] A.D. Pierce. *Acoustics: an introduction to its physical principles and applications*, volume 678. McGraw-Hill New York, 1981.

[38] V.A. Lubarda. On thermodynamic potentials in linear thermoelasticity. *International Journal of Solids and Structures*, 41(26):7377–7398, 2004.

[39] R.W. Scharstein and A.M.J. Davis. Acoustic scattering by a rigid elliptic cylinder in a slightly viscous medium. *The Journal of the Acoustical Society of America*, 121(6):3300–3310, 2007.

[40] J. Wu and Z. Zhu. An alternative approach for solving attenuated leaky rayleigh waves. *The Journal of the Acoustical Society of America*, 97(5):3191–3193, 1995.

[41] FB Cegla, P Cawley, and MJS Lowe. Material property measurement using the quasi-scholte mode—a waveguide sensor. *The Journal of the Acoustical Society of America*, 117(3):1098–1107, 2005.

[42] R.D. Borcherdt. *Viscoelastic waves in layered media*. Cambridge University Press, 2009.

[43] F.L. Becker, C.E. Fitch, and R.L. Richardson. Ultrasonic reflection and transmission factors for materials with attenuation. Technical report, Battelle-Northwest, Richland, Wash. Pacific Northwest Lab., 1970.

[44] S.K. Tomar, J. Bhagwan, and H. Steeb. Time harmonic waves in a thermo-viscoelastic material with voids. *Journal of Vibration and Control*, 20(8):1119–1136, 2014.

[45] N. Das, S. De, and N. Sarkar. Reflection of plane waves in generalized thermoelasticity of type iii with nonlocal effect. *Mathematical Methods in the Applied Sciences*, 43(3):1313–1336, 2020.

[46] Linear Thermo-Visco-Elasticity GitHub. https://github.com/arturgower/LinearThermoViscoElasticity.

[47] J. Achenbach. *Wave propagation in elastic solids*, volume 16. Elsevier, 2012.

[48] AZO Materials Silicone Rubber material parameters. https://www.azom.com/properties.aspx?ArticleID=920. Accessed: 2021-11-29.

[49] J.T Karlsen and H. Bruus. Forces acting on a small particle in an acoustical field in a thermo-viscous fluid. *Physical Review E*, 92(4):043010, 2015.

[50] N Favretto-Anrès. Theoretical study of the stoneley-scholte wave at the interface between an ideal fluid and a viscoelastic solid. *Acta Acustica united with Acustica*, 82(6):829–838, 1996.

[51] G. Caviglia and A. Morro. Harmonic waves in thermoviscoelastic solids. *International journal of engineering science*, 43(17-18):1323–1336, 2005.

# Appendices

## A Local isotropic TVE stress-strain relations

We first begin by assuming that the free energy $\Psi$ can be written as a function of the strain $\boldsymbol{\varepsilon}$ and temperature $T$. Then the form of the stress (2.5) suggests the strain energy can be written explicitly as a series expansion, at about $\boldsymbol{\varepsilon} = \mathbf{0}$ and $T = T_0$, up to second order in $\boldsymbol{\varepsilon}$, and $T$. This leads to

$$\rho_0 \Psi(\boldsymbol{\varepsilon}, T) = \rho_0 \Bigg( \Psi|_{\boldsymbol{\varepsilon}=\mathbf{0}, T=T_0} + \left.\frac{\partial \Psi}{\partial \boldsymbol{\varepsilon}}\right|_{\mathbf{0},T_0} : \boldsymbol{\varepsilon} + \left.\frac{\partial \Psi}{\partial T}\right|_{\mathbf{0},T_0} (T - T_0) + \frac{1}{2!} \boldsymbol{\varepsilon} : \left.\frac{\partial^2 \Psi}{\partial \boldsymbol{\varepsilon} \partial \boldsymbol{\varepsilon}}\right|_{\mathbf{0},T_0} : \boldsymbol{\varepsilon} + \left.\frac{\partial^2 \Psi}{\partial T^2}\right|_{\mathbf{0},T_0} \frac{(T - T_0)^2}{2!} + 2 \frac{(T - T_0)}{2!} \left.\frac{\partial^2 \Psi}{\partial \boldsymbol{\varepsilon} \partial T}\right|_{\mathbf{0},T_0} : \boldsymbol{\varepsilon} \Bigg), \tag{A.1}$$

where we have assumed that $\boldsymbol{\varepsilon}, (T - T_0)/T_0 \ll 1$ and both are of the same order.

If we further assume isotropy, we can reach

$$\rho_0 \left.\frac{\partial \Psi}{\partial \boldsymbol{\varepsilon}}\right|_{\mathbf{0},T_0} : \boldsymbol{\varepsilon} = a_0 \operatorname{tr} \boldsymbol{\varepsilon}, \quad \left.\frac{\partial^2 \Psi}{\partial T^2}\right|_{\mathbf{0},T_0} = -\frac{c_v}{T_0}, \tag{A.2a}$$

$$\rho_0 \boldsymbol{\varepsilon} : \left.\frac{\partial^2 \Psi}{\partial \boldsymbol{\varepsilon} \partial \boldsymbol{\varepsilon}}\right|_{\mathbf{0},T_0} : \boldsymbol{\varepsilon} = \lambda (\operatorname{tr} \boldsymbol{\varepsilon})^2 + 2\mu \operatorname{tr}(\boldsymbol{\varepsilon}^2), \tag{A.2b}$$

$$\rho_0 \left.\frac{\partial^2 \Psi}{\partial \boldsymbol{\varepsilon} \partial T}\right|_{\mathbf{0},T_0} : \boldsymbol{\varepsilon} = -\alpha K \operatorname{tr} \boldsymbol{\varepsilon}, \tag{A.2c}$$

where $K = \left(\lambda + \frac{2\mu}{3}\right)$, and the material constants $\mu, \lambda, c_v, \alpha, a_0$ have conveniently been chosen to fit standard conventions. Using (2.4), and (A.2) we may rewrite (A.1) as

$$\begin{aligned} \rho_0 \Psi(\boldsymbol{\varepsilon}, T) = \rho_0 (\mathcal{E}_0 - T_0 h_0 - h_0 (T - T_0) - \frac{c_v}{2T_0} (T - T_0)^2) + a_0 \operatorname{tr} \boldsymbol{\varepsilon} \\ + \frac{1}{2} \left(\lambda (\operatorname{tr} \boldsymbol{\varepsilon})^2 + 2\mu \operatorname{tr}(\boldsymbol{\varepsilon}^2)\right) - \alpha K (T - T_0) \operatorname{tr}(\boldsymbol{\varepsilon}). \end{aligned} \tag{A.3}$$

From the above, (2.4), and (2.5) it follows that the Cauchy stress tensor and entropy are of the form

$$\boldsymbol{\sigma} = a_0 \boldsymbol{I} + \lambda \operatorname{tr}(\boldsymbol{\varepsilon}) \boldsymbol{I} + 2\mu \boldsymbol{\varepsilon} - \alpha K (T - T_0) \boldsymbol{I} + 2\eta_\mu \dot{\boldsymbol{\varepsilon}} + \left(\eta_K - \frac{2\eta_\mu}{3}\right) \boldsymbol{I} \operatorname{tr}(\dot{\boldsymbol{\varepsilon}}), \tag{A.4a}$$

$$h = h_0 + \frac{c_v}{T_0} (T - T_0) + \frac{\alpha K}{\rho_0} \operatorname{tr} \boldsymbol{\varepsilon}. \tag{A.4b}$$

We can let $a_0 = 0$ since we are not considering any form of pre-stress.

By comparing with (2.7), we can now identify: $\lambda$ and $\mu$ as the (isothermal) Lamé coefficients, $c_v = T_0 (\partial h / \partial T)_{\boldsymbol{\varepsilon}=\mathbf{0}}$ as the specific heat at constant deformation (see e.g. Article 1.12 in [17]), and $\alpha$ as the coefficient of volumetric thermal expansion[10] $\alpha = (\partial \operatorname{tr}(\boldsymbol{\varepsilon}) / \partial T)_{\boldsymbol{\varepsilon}=\mathbf{0}}$.

Equivalent theories for TVE can be derived similarly, in particular if (2.2) is replaced with the Gibbs energy, the specific entropy can be written in terms of stress as (see e.g. [38] equation (34))

$$h = h_0 + \frac{\alpha}{3\rho_0} \operatorname{tr} \boldsymbol{\sigma} + c_p \theta, \tag{A.5}$$

where similarly $c_p = T_0 (\partial h / \partial T)_{\boldsymbol{\sigma}=\mathbf{0}}$ is defined as the specific heat at constant deformation of the solid in consideration.

When $\operatorname{tr}(\dot{\boldsymbol{\varepsilon}})$ can be neglected in (A.4a), then we can write (A.4b) in terms of stress to obtain

$$h = h_0 + c_v \theta + \frac{\alpha}{3\rho_0} \left(\operatorname{tr} \boldsymbol{\sigma} + 3\alpha K (T - T_0)\right), \tag{A.6}$$

which can be directly equated with (A.5) in order to obtain the identity (2.9).

[10] Note that for an isotropic material, this term is three times the coefficient of linear thermal expansion, which is also commonly found in the thermodynamic literature.

## B The local energy-conservation-dissipation corollary

As we have seen above, the Cauchy stress, and the conservation of momentum and energy equations under our local TVE framework can be written as

$$\rho_0 \frac{\partial \dot{\mathbf{u}}}{\partial t} = \nabla \cdot \boldsymbol{\sigma}, \tag{B.1a}$$

$$\boldsymbol{\sigma} = 2\mu\boldsymbol{\varepsilon} + 2\eta_\mu \dot{\boldsymbol{\varepsilon}} + (\lambda \operatorname{tr}(\boldsymbol{\varepsilon}) + \eta_\lambda \operatorname{tr}(\dot{\boldsymbol{\varepsilon}}) - \alpha K T_0 \theta)\boldsymbol{I}, \tag{B.1b}$$

$$\mathscr{K} \Delta\theta - \rho_0 c_v \dot{\theta} = \alpha K \operatorname{tr}(\dot{\boldsymbol{\varepsilon}}), \tag{B.1c}$$

We will use these equations to illustrate the mechanisms of energy dissipation. The first step is to take the inner product of both sides of (B.1a) with $\nabla\dot{\boldsymbol{u}}$ to reach

$$\nabla \cdot (\boldsymbol{\sigma}\dot{\mathbf{u}}) = \frac{1}{2}\frac{\mathrm{d}}{\mathrm{d}t}(\rho_0 |\dot{\mathbf{u}}|^2) + \boldsymbol{\sigma} : \nabla\dot{\mathbf{u}}, \tag{B.2}$$

where we define the contraction $\boldsymbol{A} : \boldsymbol{B} = A_{ij}B_{ij}$.
For convenience, let us write the (isotropic) TVE Cauchy stress tensor (B.1b) as

$$\boldsymbol{\sigma}^{\mathrm{TVE}} = \boldsymbol{\sigma}^{\mathrm{VE}} + \boldsymbol{\sigma}^{\mathrm{TH}}, \tag{B.3}$$

where

$$\boldsymbol{\sigma}^{\mathrm{VE}} = 2\mu\boldsymbol{\varepsilon} + 2\eta_\mu\dot{\boldsymbol{\varepsilon}} + (\lambda \operatorname{tr}\boldsymbol{\varepsilon} + \eta_\lambda \operatorname{tr}\dot{\boldsymbol{\varepsilon}})\boldsymbol{I}, \qquad \boldsymbol{\sigma}^{\mathrm{TH}} = -\alpha K T_0 \theta \boldsymbol{I}. \tag{B.4}$$

Using (B.3) and (B.4) in (B.2) leads to

$$\nabla \cdot (\boldsymbol{\sigma}^{\mathrm{TVE}}\dot{\mathbf{u}}) = \frac{1}{2}\frac{\mathrm{d}}{\mathrm{d}t}(\rho_0 |\dot{\mathbf{u}}|^2) - \alpha K T_0 \theta \operatorname{tr}(\dot{\boldsymbol{\varepsilon}}) + \boldsymbol{\sigma}^{\mathrm{VE}} : \nabla\dot{\mathbf{u}}\,. \tag{B.5}$$

Next we multiply both sides of the energy equation (B.1c) by $T_0\theta$ to obtain

$$T_0 \left( \mathscr{K} \nabla \cdot (\theta \nabla\theta) - \mathscr{K} \nabla\theta \cdot \nabla\theta - \frac{\rho_0 c_v}{2}\dot{\theta}^2 \right) = \alpha K T_0 \theta \operatorname{tr}(\dot{\boldsymbol{\varepsilon}}) \tag{B.6}$$

Then we can substitute the left hand-side of (B.6) into (B.5) to reach

$$\nabla \cdot (\boldsymbol{\sigma}^{\mathrm{TVE}}\dot{\mathbf{u}} + T_0\theta\mathscr{K}\nabla\theta) = \frac{1}{2}\frac{\mathrm{d}}{\mathrm{d}t}\left(\rho_0|\dot{\mathbf{u}}|^2 + \rho_0 T_0 c_v \theta^2\right) + T_0\mathscr{K}|\nabla\theta|^2 + \boldsymbol{\sigma}^{\mathrm{VE}} : \nabla\dot{\mathbf{u}}. \tag{B.7}$$

Finally we use (B.4) to rewrite

$$\boldsymbol{\sigma}^{\mathrm{VE}} : \nabla\dot{\mathbf{u}} = \frac{\mathrm{d}}{\mathrm{d}t}\left(\mu|\boldsymbol{\varepsilon}|^2 + \frac{\lambda}{2}(\operatorname{tr}\boldsymbol{\varepsilon})^2\right) + 2\eta_\mu|\dot{\boldsymbol{\varepsilon}}|^2 + \eta_\lambda\left(\operatorname{tr}\dot{\boldsymbol{\varepsilon}}\right)^2, \tag{B.8}$$

and hence (B.7) becomes

$$\nabla \cdot \mathbf{J} + \frac{1}{2}\dot{\mathcal{U}} = -\mathcal{D}, \tag{B.9}$$

where

$$\mathbf{J} = -(\boldsymbol{\sigma}^{\mathrm{TVE}}\dot{\mathbf{u}} + T_0\theta\mathscr{K}\nabla\theta), \quad \mathcal{D} = T_0\mathscr{K}|\nabla\theta|^2 + 2\eta_\mu|\dot{\boldsymbol{\varepsilon}}|^2 + \eta_\lambda\left(\operatorname{tr}\dot{\boldsymbol{\varepsilon}}\right)^2 \tag{B.10a}$$

$$\mathcal{U} = \rho_0|\dot{\mathbf{u}}|^2 + \rho_0 T_0 c_v \theta^2 + 2\mu|\boldsymbol{\varepsilon}|^2 + \lambda(\operatorname{tr}\boldsymbol{\varepsilon})^2, \tag{B.10b}$$

are the energy flux vector, energy dissipation and total TVE energy respectively. Note that $\mathcal{D} \geq 0$, so that a non-zero temperature gradient and strain rate always dissipates energy. Similar results are given for VE in [42, p. 20] and for TE in [51].

# C The dissipation inequality for non-local TVE

As we have seen in Section 2.3, the expressions for the stress-strain relationships as well as entropy and Fourier's heat law of conduction are determined such that they are consistent with the overall conservation of energy equation and the Clausius- Duhem inequality. Despite this, we must still ensure that the resulting dissipation inequality is always satisfied which restricts our choice of relaxation functions. We must have

$$\Lambda \geq 0, \tag{C.1}$$

where in the isotropic case $\Lambda$ is given by

$$\begin{aligned}\Lambda = &-\frac{1}{2}\int_{-\infty}^{t}\int_{-\infty}^{t}\frac{\partial}{\partial t}\mathcal{R}_1(t-\mathcal{T},t-\mathcal{U})\frac{\partial \boldsymbol{\varepsilon}(\mathcal{T})}{\partial \mathcal{T}}\frac{\partial \boldsymbol{\varepsilon}(\mathcal{U})}{\partial \mathcal{U}}\,\mathrm{d}\mathcal{T}\,\mathrm{d}\mathcal{U}\\ &-\frac{1}{6}\int_{-\infty}^{t}\int_{-\infty}^{t}\frac{\partial}{\partial t}\mathcal{R}_2(t-\mathcal{T},t-\mathcal{U})\frac{\partial\,\mathrm{tr}(\boldsymbol{\varepsilon}(\mathcal{T}))}{\partial \mathcal{T}}\frac{\partial\,\mathrm{tr}(\boldsymbol{\varepsilon}(\mathcal{U}))}{\partial \mathcal{U}}\,\mathrm{d}\mathcal{T}\,\mathrm{d}\mathcal{U}\\ &+T_0\int_{-\infty}^{t}\int_{-\infty}^{t}\frac{\partial}{\partial t}\mathcal{R}_3(t-\mathcal{T},t-\mathcal{U})\frac{\partial\,\mathrm{tr}(\boldsymbol{\varepsilon}(\mathcal{T}))}{\partial \mathcal{T}}\frac{\partial \theta(\mathcal{U})}{\partial \mathcal{U}}\,\mathrm{d}\mathcal{T}\,\mathrm{d}\mathcal{U}\\ &+\frac{T_0^2}{2}\int_{-\infty}^{t}\int_{-\infty}^{t}\frac{\partial}{\partial t}\mathcal{R}_4(t-\mathcal{T},t-\mathcal{U})\frac{\partial \theta(\mathcal{T})}{\partial \mathcal{T}}\frac{\partial \theta(\mathcal{U})}{\partial \mathcal{U}}\,\mathrm{d}\mathcal{T}\,\mathrm{d}\mathcal{U}.\end{aligned} \tag{C.2}$$

We note that in (C.2) the relaxation functions appear with 2 arguments, as opposed to the governing equations (2.24), (2.25). The relation is given by $\mathcal{R}_i(t-\mathcal{T},0)=\mathcal{R}_i(t-\mathcal{T})$. This is a result of Leibnitz's rule for the time derivative of the free energy in the derivation. Moreover, in order to verify (C.1) from relaxation functions appearing in (2.24), (2.25) we must therefore have $\mathcal{R}_i(\mathcal{T},\mathcal{U})=\mathcal{R}_i(\mathcal{T}+\mathcal{U})$.

# D TVA wave potentials

In Section 3.1 we showed how how the classical TVA theory for fluids is recovered from the local TVE model by taking the limit of zero shear modulus [5]. For completeness, we show here how the TVE potentials are linked to those used in [5]. We commence by summarizing the (frequency domain) dimensional decomposition of the TVA theory used under the current TVE notation (note that the TVA theory is written in terms of velocity, whereas here we write it in terms of displacement) (see equations (13)-(14) of [5])

$$\left(\nabla^2+\frac{\rho_0\omega}{\eta_\mu}\right)\boldsymbol{\Omega}=\mathbf{0},\quad \nabla\times(-\mathrm{i}\omega\mathbf{u})=\boldsymbol{\Omega}, \tag{D.1a}$$

$$\left(\nabla^2+\kappa_1^2\right)\Theta_1=0,\quad \kappa_1^2=\mathrm{i}\omega\frac{\rho_0^2c_\mathrm{A}^2c_p-\mathrm{i}\omega\rho_0(c_p\zeta+\gamma\mathscr{K})+\mathcal{S}}{2(\rho_0c_\mathrm{A}^2-\mathrm{i}\omega\zeta\gamma)\mathscr{K}}, \tag{D.1b}$$

$$\left(\nabla^2+\kappa_2^2\right)\Theta_2=0,\quad \kappa_2^2=\mathrm{i}\omega\frac{\rho_0^2c_\mathrm{A}^2c_p-\mathrm{i}\omega\rho_0(c_p\zeta+\gamma\mathscr{K})-\mathcal{S}}{2(\rho_0c_\mathrm{A}^2-\mathrm{i}\omega\zeta\gamma)\mathscr{K}}, \tag{D.1c}$$

$$\mathcal{S}=\sqrt{[\rho_0^2c_\mathrm{A}^2c_p-\mathrm{i}\omega\rho_0(c_p\zeta-\gamma\mathscr{K})]^2-4\mathrm{i}\omega\rho_0^3c_\mathrm{A}^2c_p\mathscr{K}(\gamma-1)}, \tag{D.1d}$$

from which the temperature and displacement can be obtained respectively by

$$T_0\theta^{\mathrm{TVA}}=\Theta_1+\Theta_2, \tag{D.2a}$$

$$\rho_0\omega^2\mathbf{u}^{\mathrm{TVA}}=\frac{c_p}{2\alpha T_0c_\mathrm{A}^2}\overline{\nabla}\left\{M(\omega)\Theta_1+N(\omega)\Theta_2\right\}+\eta_\mu\overline{\nabla}\times\boldsymbol{\Omega}, \tag{D.2b}$$

where

$$M(\omega) = \rho_0 c_{\mathrm{A}}^2 - \mathrm{i}\omega\left(\zeta - \frac{\gamma\mathscr{K}}{c_p}\right) - \frac{\mathcal{S}}{\rho_0 c_p}, \qquad N(\omega) = \rho_0 c_{\mathrm{A}}^2 - \mathrm{i}\omega\left(\zeta - \frac{\gamma\mathscr{K}}{c_p}\right) + \frac{\mathcal{S}}{\rho_0 c_p}. \tag{D.3}$$

The divergence free component potential of the Helmholtz decomposition for TVE (2.13), satisfying (2.14b), where in the limit the corresponding wavenumber is given by the last of (3.4a) can be substituted in the curl of (D.2b) to give (note that in order to be able to this we require that $\mathbf{u}^{\mathrm{TVE}} \to \mathbf{u}^{\mathrm{TVA}}$ as $\mu \to 0$)

$$\boldsymbol{\Phi} \to \frac{\eta_\mu}{\rho_0\omega^2}\boldsymbol{\Omega}, \qquad \text{as} \qquad \mu \to 0. \tag{D.4}$$

From (3.5)

$$a - b \to \kappa_2^2, \quad a + b \to \kappa_1^2 \qquad \text{as } \mu \to 0. \tag{D.5}$$

It therefore only remains to find the scaling between the TVE thermo-compressional fields $\{\varphi, \vartheta\}$ and those of TVA $\{\Theta_1, \Theta_2\}$. If we take the divergence of (D.2b) with (2.13), (2.21) we can then use the respectives PDEs (2.19) with their limiting values (D.5) to arrive at

$$\vartheta \to \frac{c_p M(\omega)}{2\rho_0\omega^2 T_0 c_{\mathrm{A}}^2 \alpha}\Theta_1, \qquad \varphi \to \frac{c_p N(\omega)}{2\rho_0\omega^2 T_0 c_{\mathrm{A}}^2 \alpha}\Theta_2 \qquad \text{as } \mu \to 0. \tag{D.6}$$

Alternatively, (D.6) can also be obtained by considering the $\mu \to 0$ limit on $\theta^{\mathrm{TVE}}$ from the second of (2.21) and equating it to (D.2a).

# E Energy ratios for TVE scattering

It is useful to represent the intensity of a given time-harmonic wave as an average of $\mathbf{J}$ (B.10a) over the wave period $(2\pi/\omega)$ which can be written as

$$\langle \mathbf{J} \rangle = \frac{\omega}{2\pi}\int_t^{t+2\pi/\omega} \mathbf{J}\, \mathrm{d}s. \tag{E.1}$$

Given the corollary in Appendix B, it follows that

$$\langle \mathbf{J} \rangle = -\frac{1}{2}\,\mathrm{Re}\{\boldsymbol{\sigma}\dot{\mathbf{u}}^* + \theta\mathscr{K}\nabla\theta^*\}, \tag{E.2}$$

denotes the average energy flux (per unit area) due to both the mechanical power and the heat flux, see [51]. In particular, note that this is an extension to the widely used definition presented in [47] (page 34) for isothermal elasticity. Nevertheless, we have noted that several works doing coupled thermo-elasticity do not seem to take into account the thermal flux term e.g. (61) in [44], (60) in [45]. To arrive at (E.2) we have used the result that for two general time harmonic signals $F = F_0\mathrm{e}^{-\mathrm{i}(\omega t+\gamma_1)}$ $f = f_0\mathrm{e}^{-\mathrm{i}(\omega t+\gamma_2)}$, ($\gamma_1$, $\gamma_2$ represent arbitrary phase shifts) we have

$$\langle \mathrm{Re}\{F\} \times \mathrm{Re}\{f\} \rangle = \frac{1}{2}\,\mathrm{Re}\{F f^*\}, \tag{E.3}$$

where asterisk $^*$ denotes complex conjugate. As we have seen, the displacement, Cauchy stress and temperature are linear combinations of $\{\varphi, \vartheta, \Phi\}$ and we can therefore decompose $\langle \mathbf{J} \rangle$ accordingly.

## E.1 Interface between 2 TVE media: Continuity of normal mean energy flux

The continuity boundary conditions at the interface between the two TVE media imply (4.10). The TVE-TVE set-up (4.2) implies that in medium 1 we have an incident P dominated wave as well as reflected P, SV and T waves, so we write

$$\langle \mathbf{J^1} \rangle = \langle \mathbf{J^1}_{\mathrm{NI}} \rangle + \langle \mathbf{J^1}_{\mathrm{IRR}} \rangle + \langle \mathbf{J^1}_{\mathrm{IRI}} \rangle, \tag{E.4}$$

where $\langle \mathbf{J^1}_{\mathrm{NI}} \rangle$, $\langle \mathbf{J^1}_{\mathrm{IRR}} \rangle$, $\langle \mathbf{J^1}_{\mathrm{IRI}} \rangle$ denote the contribution to the power due to "Non-Interacting", "Interacting Reflected" and "Interacting between Reflected and Incident" modes respectively. These are specifically given by

$$\langle \mathbf{J^1}_{\mathrm{NI}} \rangle = \langle \mathbf{J}_{\varphi_{\mathrm{I}}} \rangle + \langle \mathbf{J}_{\varphi_{\mathrm{R}}} \rangle + \langle \mathbf{J}_{\vartheta_{\mathrm{R}}} \rangle + \langle \mathbf{J}_{\Phi_{\mathrm{R}}} \rangle, \tag{E.5a}$$

$$\langle \mathbf{J^1}_{\mathrm{IRR}} \rangle = \langle \mathbf{J}_{\varphi_{\mathrm{R}}\vartheta_{\mathrm{R}}} \rangle + \langle \mathbf{J}_{\vartheta_{\mathrm{R}}\varphi_{\mathrm{R}}} \rangle + \langle \mathbf{J}_{\varphi_{\mathrm{R}}\Phi_{\mathrm{R}}} \rangle + \langle \mathbf{J}_{\Phi_{\mathrm{R}}\varphi_{\mathrm{R}}} \rangle + \langle \mathbf{J}_{\vartheta_{\mathrm{R}}\Phi_{\mathrm{R}}} \rangle + \langle \mathbf{J}_{\Phi_{\mathrm{R}}\vartheta_{\mathrm{R}}} \rangle, \tag{E.5b}$$

$$\langle \mathbf{J^1}_{\mathrm{IRI}} \rangle = \langle \mathbf{J}_{\varphi_{\mathrm{I}}\varphi_{\mathrm{R}}} \rangle + \langle \mathbf{J}_{\varphi_{\mathrm{R}}\varphi_{\mathrm{I}}} \rangle + \langle \mathbf{J}_{\varphi_{\mathrm{I}}\vartheta_{\mathrm{R}}} \rangle + \langle \mathbf{J}_{\vartheta_{\mathrm{R}}\varphi_{\mathrm{I}}} \rangle + \langle \mathbf{J}_{\varphi_{\mathrm{I}}\Phi_{\mathrm{R}}} \rangle + \langle \mathbf{J}_{\Phi_{\mathrm{R}}\varphi_{\mathrm{I}}} \rangle, \tag{E.5c}$$

where the subscripts indicate the mode(s) contributing to (E.2). For NI terms e.g. $\langle \mathbf{J}_{\varphi I} \rangle$ in (E.5a) we must compute the stress, velocity, temperature and temperature gradient due to the incident P wave $\varphi_{\mathrm{I}}$. In the case of interacting terms we have e.g.

$$\langle \mathbf{J}_{\varphi_{\mathrm{R}}\vartheta_{\mathrm{R}}} \rangle = -\frac{1}{2} \mathrm{Re}\{\boldsymbol{\sigma}_{\varphi_{\mathrm{R}}} \dot{\mathbf{u}}^*_{\vartheta_{\mathrm{R}}} + \theta_{\varphi_{\mathrm{R}}} \mathscr{K} \nabla \theta^*_{\vartheta_{\mathrm{R}}}\}, \tag{E.6}$$

so that we need the stress and temperature due to $\varphi_{\mathrm{R}}$, and the velocity and temperature gradient due to $\vartheta_{\mathrm{R}}$. Note that the order of the subscripts is important since it indicates whether the mode is contributing towards the stress or velocity (and temperature or temperature gradient) in each case. Recall that the temperature is independent of the shear wave motion, that is $\theta_\Phi = 0$.

The situation in the lower half-space is simpler, since there is no incident and as a result there is no interaction between the transmitted and incident mode i.e. $\langle \mathbf{J^2}_{\mathrm{ITI}} \rangle = 0$, so that

$$\langle \mathbf{J^2} \rangle = \langle \mathbf{J^2}_{\mathrm{NI}} \rangle + \langle \mathbf{J^2}_{\mathrm{ITT}} \rangle. \tag{E.7}$$

The "Non-Interacting" and "Interacting Transmitted" terms are given by

$$\langle \mathbf{J^2}_{\mathrm{NI}} \rangle = \langle \mathbf{J}_{\varphi_{\mathrm{T}}} \rangle + \langle \mathbf{J}_{\vartheta_{\mathrm{T}}} \rangle + \langle \mathbf{J}_{\Phi_{\mathrm{T}}} \rangle, \tag{E.8a}$$

$$\langle \mathbf{J^2}_{\mathrm{ITT}} \rangle = \langle \mathbf{J}_{\varphi_{\mathrm{T}}\vartheta_{\mathrm{T}}} \rangle + \langle \mathbf{J}_{\vartheta_{\mathrm{T}}\varphi_{\mathrm{T}}} \rangle + \langle \mathbf{J}_{\varphi_{\mathrm{T}}\Phi_{\mathrm{T}}} \rangle + \langle \mathbf{J}_{\Phi_{\mathrm{T}}\varphi_{\mathrm{T}}} \rangle + \langle \mathbf{J}_{\vartheta_{\mathrm{T}}\Phi_{\mathrm{T}}} \rangle + \langle \mathbf{J}_{\Phi_{\mathrm{T}}\vartheta_{\mathrm{T}}} \rangle. \tag{E.8b}$$

We can now substitute (E.5a), (E.8a) into (4.10) to obtain

$$(\langle \mathbf{J}_{\varphi_{\mathrm{I}}} \rangle + \langle \mathbf{J}_{\varphi_{\mathrm{R}}} \rangle + \langle \mathbf{J}_{\vartheta_{\mathrm{R}}} \rangle + \langle \mathbf{J}_{\Phi_{\mathrm{R}}} \rangle + \langle \mathbf{J^1}_{\mathrm{IRR}} \rangle + \langle \mathbf{J^1}_{\mathrm{IRI}} \rangle) \cdot \mathbf{e_y} = (\langle \mathbf{J^2}_{\mathrm{NI}} \rangle + \langle \mathbf{J^2}_{\mathrm{ITT}} \rangle) \cdot \mathbf{e_y}, \tag{E.9}$$

which by defining the energy ratios for the reflected modes $E_R$ and interaction-reflected coefficients $E_{IR}$

$$E_{R_\varphi} = -\frac{\langle \mathbf{J}_{\varphi_{\mathrm{R}}} \rangle \cdot \mathbf{e_y}}{\langle \mathbf{J}_{\varphi_{\mathrm{I}}} \rangle \cdot \mathbf{e_y}}, \quad E_{R_\vartheta} = -\frac{\langle \mathbf{J}_{\vartheta_{\mathrm{R}}} \rangle \cdot \mathbf{e_y}}{\langle \mathbf{J}_{\varphi_{\mathrm{I}}} \rangle \cdot \mathbf{e_y}}, \quad E_{R_\Phi} = -\frac{\langle \mathbf{J}_{\Phi_{\mathrm{R}}} \rangle \cdot \mathbf{e_y}}{\langle \mathbf{J}_{\varphi_{\mathrm{I}}} \rangle \cdot \mathbf{e_y}}, \tag{E.10a}$$

$$E_{IR_{\mathrm{RR}}} = -\frac{\langle \mathbf{J}_{\mathrm{IRR}} \rangle \cdot \mathbf{e_y}}{\langle \mathbf{J}_{\varphi_{\mathrm{I}}} \rangle \cdot \mathbf{e_y}}, \quad E_{IR_{\mathrm{IR}}} = -\frac{\langle \mathbf{J}_{\mathrm{IRI}} \rangle \cdot \mathbf{e_y}}{\langle \mathbf{J}_{\varphi_{\mathrm{I}}} \rangle \cdot \mathbf{e_y}}, \tag{E.10b}$$

as well as the *transmission* coefficients $E_T$ and interaction-transmitted coefficients $E_{IT}$

$$E_{T_\varphi} = \frac{\langle \mathbf{J}_{\varphi_\mathrm{R}} \rangle \cdot \mathbf{e_y}}{\langle \mathbf{J}_{\varphi_\mathrm{I}} \rangle \cdot \mathbf{e_y}}, \quad E_{T_\vartheta} = \frac{\langle \mathbf{J}_{\vartheta_\mathrm{R}} \rangle \cdot \mathbf{e_y}}{\langle \mathbf{J}_{\varphi_\mathrm{I}} \rangle \cdot \mathbf{e_y}}, \quad E_{T_\Phi} = \frac{\langle \mathbf{J}_{\Phi_\mathrm{R}} \rangle \cdot \mathbf{e_y}}{\langle \mathbf{J}_{\varphi_\mathrm{I}} \rangle \cdot \mathbf{e_y}}, \tag{E.11a}$$

$$E_{IT_{\mathrm{TT}}} = \frac{\langle \mathbf{J}_{\mathrm{ITT}} \rangle \cdot \mathbf{e_y}}{\langle \mathbf{J}_{\varphi_\mathrm{I}} \rangle \cdot \mathbf{e_y}}. \tag{E.11b}$$

With (E.10), (E.11) we can finally rewrite (E.9) as

$$E_{R_\varphi} + E_{R_\vartheta} + E_{R_\Phi} + E_{IR_{\mathrm{IR}}} + E_{IR_{\mathrm{RR}}} + E_{T_\varphi} + E_{T_\vartheta} + E_{T_\Phi} + E_{IT_{\mathrm{TT}}} = 1, \tag{E.12}$$

which gives a total of 25 different terms. In the absence of thermal coupling, the number of terms reduces to 13 and (E.12) reduces to (5.4.58) in [42]. See Section 5.4.6. of the same reference for further useful details including analytical expressions for some of the coefficients in (E.10), (E.11).

# F Section 4 further details

## F.1 Non-dimensionalisation

For the numerical implementation it is convenient to re-write the dimensional equations with non-dimensional quantities. We choose to non-dimensionalise with respect to the thermo-elastic quantities from (the top) medium 1. In particular, we choose $c_1$ to denote the (adiabatic) longitudinal speed of sound of the upper material in the lossless case, i.e. $c_1^2 = (\lambda_1 + 2\mu_1)/\rho_1$. In order to distinguish between dimensional/non-dimensional quantities here, we write all dimensional quantities with an overbar.

$$\nabla = \bar{\ell}\bar{\nabla}, \quad \omega = \frac{\bar{\ell}}{\bar{c}_1}\bar{\omega}, \quad \{\mathbf{u}_1, \mathbf{x}\} = \frac{1}{\bar{\ell}}\{\bar{\mathbf{u}}_1, \bar{\mathbf{x}}\}, \quad \{\phi_1, \varphi_1, \vartheta_1, \Phi_1\} = \frac{1}{\bar{\ell}^2}\{\bar{\phi}_1, \bar{\varphi}_1, \bar{\vartheta}_1, \bar{\Phi}_1\},$$

$$\mathscr{K}_1 = \frac{\bar{T}_1 \bar{\mathscr{K}}_1}{\bar{\rho}_1 \bar{c}_1^3 \bar{\ell}}, \quad c_{v1} = \frac{\bar{T}_1}{\bar{c}_1^2}\bar{c}_{v1}, \quad \alpha_1 = \bar{\alpha}_1 \bar{T}_1, \quad \{\eta_{\lambda 1}, \eta_{\mu 1}\} = \frac{1}{\bar{\rho}_1 \bar{c}_1 \bar{\ell}}\{\bar{\eta}_{\lambda 1}, \bar{\eta}_{\mu 1}\},$$

$$\{\tilde{\lambda}_1, \tilde{\mu}_1, \tilde{K}_1, \boldsymbol{\sigma}_1\} = \frac{1}{\bar{\rho}_1 \bar{c}_1^2}\{\bar{\tilde{\lambda}}_1, \bar{\tilde{\mu}}_1, \bar{\tilde{K}}_1, \bar{\boldsymbol{\sigma}}_1\}, \quad \{k_{\theta 1}^2, k_{\phi_1}^2, k_{\Phi_1}^2, L_{\phi 1}\} = \bar{\ell}^2\{\bar{k}_{\theta 1}^2, \bar{k}_{\phi 1}^2, \bar{k}_{\Phi 1}^2, \bar{L}_{\phi 1}\},$$

$$k_{\theta 1}^2 = \frac{\mathrm{i}\omega c_{v1}}{\mathscr{K}_1}, \quad k_{\phi_1}^2 = \frac{\omega^2}{\tilde{\lambda}_1 + 2\tilde{\mu}_1}, \quad k_{\Phi_1}^2 = \frac{\omega^2}{\tilde{\mu}_1}, \quad L_{\phi 1} = \frac{\mathrm{i}\alpha_1 \omega K_1}{\mathscr{K}_1}, \quad L_{\theta 1} = -\frac{\alpha_1 K_1}{\tilde{\lambda}_1 + 2\tilde{\mu}_1}.$$

And similarly, in material 2 we use the same scalings as in material 1, hence we obtain

$$\mathbf{u}_2 = \frac{1}{\bar{\ell}}\bar{\mathbf{u}}_2, \quad \{\phi_2, \varphi_2, \vartheta_2, \Phi_2\} = \frac{1}{\bar{\ell}^2}\{\bar{\phi}_2, \bar{\varphi}_2, \bar{\vartheta}_2, \bar{\Phi}_2\}$$

$$\mathscr{K}_2 = \frac{\bar{T}_1 \bar{\mathscr{K}}_2}{\bar{\rho}_1 \bar{c}_1^3 \bar{\ell}}, \quad c_{v2} = \frac{\bar{T}_1}{\bar{c}_1^2}\bar{c}_{v2}, \quad \alpha_2 = \bar{\alpha}_2 \bar{T}_1, \quad \{\eta_{\lambda 2}, \eta_{\mu 2}\} = \frac{1}{\bar{\rho}_1 \bar{c}_1 \bar{\ell}}\{\bar{\eta}_{\lambda 2}, \bar{\eta}_{\mu 2}\}$$

$$\{\tilde{\lambda}_2, \tilde{\mu}_2, \tilde{K}_2, \boldsymbol{\sigma}_2\} = \frac{1}{\bar{\rho}_1 \bar{c}_1^2}\{\bar{\tilde{\lambda}}_2, \bar{\tilde{\mu}}_2, \bar{\tilde{K}}_2, \bar{\boldsymbol{\sigma}}_2\}, \quad \{k_{\theta 2}^2, k_{\phi_2}^2, k_{\Phi_2}^2, L_{\phi 2}\} = \bar{\ell}^2\{\bar{k}_{\theta 2}^2, \bar{k}_{\phi 2}^2, \bar{k}_{\Phi 2}^2, \bar{L}_{\phi 2}\},$$

$$k_{\theta 2}^2 = \mathrm{i}\frac{\omega c_{v2}}{\mathscr{K}_2}\left(\frac{\bar{\rho}_2}{\bar{\rho}_1}\right), \quad k_{\phi_2}^2 = \frac{\omega^2}{\tilde{\lambda}_2 + 2\tilde{\mu}_2}\left(\frac{\bar{\rho}_2}{\bar{\rho}_1}\right), \quad k_{\Phi_2}^2 = \frac{\omega^2}{\tilde{\mu}_2}\left(\frac{\bar{\rho}_2}{\bar{\rho}_1}\right), \quad L_{\phi 2} = \frac{\mathrm{i}\alpha_2 \omega K_2}{\mathscr{K}_2}, \quad L_{\theta 2} = -\frac{\alpha_2 K_2}{\tilde{\lambda}_2 + 2\tilde{\mu}_2}\left(\frac{\bar{T}_2}{\bar{T}_1}\right),$$

where we have $\bar{T}_2/\bar{T}_1 = 1$ due to continuity of temperature across the boundary.

## F.2 TVE-TVE scattering system

Open access to this Mathematica file is given in [46].

## F.3 VE-VE scattering system

In Section 3.2 we learned how to recover the theory of isothermal visco-elasticity (VE) from that of TVE. For completeness purposes, we next formulate the scattering problem in Section 4 for such media. This problem is well discussed in the VE literature, see e.g. [42] Section 5.3. Equations (4.1)-(4.5) are replaced by

$$\phi_{\mathrm{I}} = \mathrm{e}^{-\mathrm{i}k_{\phi_1}(x\cos\psi + y\sin\psi)}, \qquad \psi \in [0,\pi], \tag{F.1}$$

$$\phi_{\mathrm{R}} = R_\phi \mathrm{e}^{\mathrm{i}k_{\phi_1}\sin\psi y}\mathrm{e}^{-\mathrm{i}k_{\phi_1}x\cos\psi}, \qquad \phi_{\mathrm{T}} = T_\phi \mathrm{e}^{-\mathrm{i}d_{\Phi_{\mathrm{T}}}y}\mathrm{e}^{-\mathrm{i}k_{\phi_1}x\cos\psi}, \tag{F.2a}$$

$$\boldsymbol{\Phi}_{\mathrm{R}} = \mathbf{e_z} R_\Phi \mathrm{e}^{\mathrm{i}d_{\Phi_{\mathrm{R}}}y}\mathrm{e}^{-\mathrm{i}k_{\phi_1}x\cos\psi}, \qquad \boldsymbol{\Phi}_{\mathrm{T}} = \mathbf{e_z} T_\Phi \mathrm{e}^{-\mathrm{i}d_{\Phi_{\mathrm{T}}}y}\mathrm{e}^{-\mathrm{i}k_{\phi_1}x\cos\psi}, \tag{F.2b}$$

where $\operatorname{Im} d_{\Phi_{\mathrm{T}}}, \operatorname{Im} d_{\Phi_{\mathrm{R}}}, \operatorname{Im} d_{\Phi_{\mathrm{T}}} \geq 0$ is ensured with

$$d_{\Phi_{\mathrm{T}}} = \mathrm{i}\sqrt{-(k_{\Phi_2}^2 - k_{\Phi_1}^2\cos^2\psi)}, \quad d_{\Phi_{\mathrm{R}}} = \mathrm{i}\sqrt{-(k_{\Phi_1}^2 - k_{\Phi_1}^2\cos^2\psi)}, \quad d_{\Phi_{\mathrm{T}}} = \mathrm{i}\sqrt{-(k_{\Phi_2}^2 - k_{\Phi_1}^2\cos^2\psi)}. \tag{F.3}$$

The BCs reduce to

$$\hat{\boldsymbol{\sigma}}_1^{\mathrm{VE}}\mathbf{e_y} = \hat{\boldsymbol{\sigma}}_2^{\mathrm{VE}}\mathbf{e_y}, \quad \hat{\mathbf{u}}_1^{\mathrm{VE}} = \hat{\mathbf{u}}_2^{\mathrm{VE}}, \tag{F.4a}$$

which have to hold on $y = 0$. The application of (F.4a) will determine the unique four constants $\{R_\phi, T_\phi, R_\Phi, T_\Phi\}$, see equation (5.3.21) [42] for details.

## F.4 TVA-Rigid scattering problem

In Section 3.1 we discussed how local TVE yields the classical TVA theory for fluids in the limit of vanishing shear modulus, so we let $\mu \to 0$. For a thermo-viscous fluid in contact with a rigid interface at $y = 0$, we impose no-slip and for the temperature field an isothermal boundary condition, that is

$$-\mathrm{i}\omega\mathbf{u} = 0 \quad \text{and} \quad \theta = 0, \tag{F.5a}$$

on $y = 0$, noting that we have dropped the subscript since here we are only considering motion on $y \geq 0$. Following (4.2) our fields are given by

$$\varphi = \mathrm{e}^{-\mathrm{i}k_\varphi x\cos\psi}\left(\mathrm{e}^{-\mathrm{i}k_\varphi y\sin\psi} + R_\varphi \mathrm{e}^{\mathrm{i}k_\varphi y\sin\psi}\right) \tag{F.6a}$$

$$\vartheta = R_\vartheta \mathrm{e}^{-\mathrm{i}k_\varphi x\cos\psi + \mathrm{i}d_\vartheta y}, \tag{F.6b}$$

$$\Phi = R_\Phi \mathrm{e}^{-\mathrm{i}k_\varphi x\cos\psi + \mathrm{i}d_\Phi y}, \tag{F.6c}$$

with $d_\vartheta = \mathrm{i}\sqrt{-(k_\vartheta^2 - k_\varphi^2\cos^2\psi)}$, $d_\Phi = \mathrm{i}\sqrt{-(k_\Phi^2 - k_\varphi^2\cos^2\psi)}$ which ensures $\operatorname{Im} d_\vartheta, \operatorname{Im} d_\Phi \geq 0$. Substitution of (F.6) into the governing equations (2.14b), (2.19) and using (2.13), (2.14a) for the boundary conditions (F.5), we obtain exact expressions

$$\begin{pmatrix} R_\varphi \\ R_\vartheta \\ R_\Phi \end{pmatrix} = \begin{pmatrix} \frac{-\cos^2\psi + \mathcal{B}(\mathcal{F}+\mathcal{G})}{\cos^2\psi - \mathcal{B}(\mathcal{F}-\mathcal{G})} \\ \frac{-2\sin\psi\mathcal{F}}{\cos^2\psi - \mathcal{B}(\mathcal{F}-\mathcal{G})}\frac{k_\varphi}{d_\vartheta} \\ \frac{\sin 2\psi}{\cos^2\psi - \mathcal{B}(\mathcal{F}-\mathcal{G})} \end{pmatrix}, \tag{F.7}$$

where

$$\mathcal{B} = \sqrt{\frac{k_\Phi^2}{k_\varphi^2} - \cos^2\psi}, \quad \mathcal{F} = \frac{d_\vartheta \mathscr{T}_\varphi}{k_\varphi(\mathscr{T}_\vartheta - \mathscr{T}_\varphi)}, \quad \mathcal{G} = \frac{\mathscr{T}_\vartheta \sin\psi}{\mathscr{T}_\vartheta - \mathscr{T}_\varphi}. \tag{F.8}$$

Following (E.12) with the current potentials (F.6), it is clear that the energy balance in this case reduces to

$$E_{R_\varphi} + E_{R_\vartheta} + E_{R_\Phi} + E_{IR_{\mathrm{IR}}} + E_{IR_{\mathrm{RR}}} = 1, \tag{F.9}$$

which are defined in (E.10) and we must use the current potentials (F.6).

The visco-acoustic VA solution can be directly obtained from (F.7), (F.8) by letting $\mathscr{T}_\varphi \to 0$ which results in $\mathcal{F} \to 0$ and $\mathcal{G} \to \sin\psi$ so that (F.7) becomes

$$\begin{pmatrix} R_\varphi \\ R_\vartheta \\ R_\Phi \end{pmatrix} \to \begin{pmatrix} \frac{-\cos^2\psi + \mathcal{B}\sin\psi}{\cos^2\psi + \mathcal{B}\sin\psi} \\ 0 \\ \frac{\sin 2\psi}{\cos^2\psi + \mathcal{B}\sin\psi} \end{pmatrix}, \tag{F.10}$$

Finally, for the purely acoustic solution in the absence of any losses, we must further let $\eta_\mu \to 0$, which results in $\mathcal{B} \to \infty$, obtaining only the trivial solution

$$\begin{pmatrix} R_\varphi \\ R_\vartheta \\ R_\Phi \end{pmatrix} \to \begin{pmatrix} 1 \\ 0 \\ 0 \end{pmatrix}. \tag{F.11}$$

## 3.3 Additional comments

### 3.3.1 Recovering the TVA–rigid slit dispersion equations

As we have discussed above, one of the advantages of the TVE framework is the fact that the TVA theory for fluids simply arises as a special case when considering the vanishing shear modulus limit (to the local theory). As an additional illustration, here we show how the dispersion equations (23), (25) from Section 2.2 for (symmetric) natural modes along a rigid channel filled with a TVA fluid are recovered under the TVE framework presented in the preceding section. Additionally, we will use the resulting equations in order to test the asymptotic expansions derived in Section 3.2.

Suppose we consider a time-harmonic, plane-strain, local TVE medium occupying an infinitely extending semi-infinite channel parametrized by $-\infty < x < \infty$ and $|y| \leq 1$ such that $\boldsymbol{\Phi} = \Phi \mathbf{e_z}$ with *clamped* boundaries, so that

$$\hat{\mathbf{u}} = 0 \quad \text{on} \quad y = \pm 1, \tag{3.1}$$

and we will consider both isothermal and adiabatic thermal boundary conditions, so that as we have seen

$$\hat{\theta} = 0 \qquad \text{or} \qquad \frac{\partial \hat{\theta}}{\partial y} = 0 \quad \text{on} \quad y = \pm 1. \tag{3.2}$$

We seek solutions with horizontal particle displacement $\hat{u}_x$ being symmetric around $y = 0$, such that the TVE potentials obeying (2.14b), (2.19) in Section 3.2 take the form

$$\begin{cases} \varphi = A \cosh(\gamma_\varphi y) \mathrm{e}^{\mathrm{i}kx} & \gamma_\varphi = \sqrt{k^2 - k_\varphi^2}, \\ \vartheta = B \cosh(\gamma_\vartheta y) \mathrm{e}^{\mathrm{i}kx} & \gamma_\vartheta = \sqrt{k^2 - k_\vartheta^2}, \\ \Phi = C \sinh(\gamma_\Phi y) \mathrm{e}^{\mathrm{i}kx} & \gamma_\Phi = \sqrt{k^2 - k_\Phi^2}, \end{cases} \tag{3.3}$$

and direct substitution of (3.3) into (3.1) and (the first of) (3.2) gives (recalling that $\hat{\mathbf{u}} = \nabla(\varphi + \vartheta) + \nabla \times \boldsymbol{\Phi}$ and $\hat{\theta} = \mathscr{T}_\varphi \varphi + \mathscr{T}_\vartheta \vartheta$) the simultaneous equations

$$\begin{pmatrix} \mathrm{i}k \cosh(\gamma_\varphi) & \mathrm{i}k \cosh(\gamma_\vartheta) & \gamma_\Phi \cosh(\gamma_\Phi) \\ \gamma_\varphi \sinh(\gamma_\varphi) & \gamma_\vartheta \sinh(\gamma_\vartheta) & -\mathrm{i}k \sinh(\gamma_\Phi) \\ \cosh(\gamma_\varphi) \mathscr{T}_\varphi & \cosh(\gamma_\vartheta) \mathscr{T}_\vartheta & 0 \end{pmatrix} \cdot \begin{pmatrix} A \\ B \\ C \end{pmatrix} = \begin{pmatrix} 0 \\ 0 \\ 0 \end{pmatrix}, \tag{3.4}$$

whose non-trivial solutions are obtained by letting the determinant of the matrix vanish, which after rearranging reduces to

$$\gamma_\Phi \left\{ \mathscr{T}_\vartheta \gamma_\varphi \tanh\left(\gamma_\varphi\right) - \mathscr{T}_\varphi \gamma_\vartheta \tanh\left(\gamma_\vartheta\right) \right\} - k^2 \tanh\left(\gamma_\Phi\right)\left(\mathscr{T}_\vartheta - \mathscr{T}_\varphi\right) = 0. \tag{3.5}$$

In the adiabatic case, only the bottom equation of (3.4) is replaced by $\gamma_\varphi \sinh(\gamma_\varphi)\mathscr{T}_\varphi A + \gamma_\vartheta \sinh(\gamma_\vartheta)\mathscr{T}_\vartheta B = 0$ which results in the dispersion relation

$$k^2 \tanh\left(\gamma_\Phi\right)\left\{\gamma_\varphi \tanh\left(\gamma_\varphi\right)\mathscr{T}_\varphi - \gamma_\vartheta \tanh\left(\gamma_\vartheta\right)\mathscr{T}_\vartheta\right\} + \gamma_\vartheta\gamma_\varphi\gamma_\Phi \tanh\left(\gamma_\vartheta\right)\tanh\left(\gamma_\varphi\right)\left(\mathscr{T}_\vartheta - \mathscr{T}_\varphi\right) = 0. \tag{3.6}$$

Furthermore, in the absence of coupling with thermal effect so that $\alpha \to 0$ which implies $\mathscr{T}_\varphi \to 0$, both (3.5), (3.6) reduce to

$$k^2 \tanh\left(\gamma_\Phi\right) - \gamma_\phi\gamma_\Phi \tanh\left(\gamma_\phi\right) = 0, \tag{3.7}$$

which can also be seen by simply setting $B = 0$ in (3.4). We now note that (3.5), (3.6) and (3.7) have got the identical functional form to (25), (23) and (27) in Section 2.2. Furthermore, it is straightforward to check by expanding $\mathscr{T}_\varphi, \mathscr{T}_\vartheta$ using (2.15), (2.16) and (2.22) in Section 3.2 that, as $\mu \to 0$ the equations become identical.

Finally, we use (3.5), (3.6) in order to test the asymptotic expansions (2.50), (2.51) in Section 3.2 to simplify the thermo–compressional coupling of the wavenumbers $k_\varphi, k_\vartheta$ and temperature contributions $\mathscr{T}_\varphi, \mathscr{T}_\vartheta$. Figure 3.1 illustrates the associated results at 10 kHz when the TVE medium is air, following the values in Table A.1. From the absolute error plots, it is clear that the consideration of higher order terms of $\delta$ results in more accurate answers, as expected from the results for air in Figure 2 in Section 3.2. We do not provide the approximate equations to (3.5), (3.6) at each order here since despite simpler, the resulting equations give no particular useful insights. Nevertheless, if we further assume low frequencies such that $\omega = O(\delta)$ then at this order with $\mu = 0$, we found that (3.5), (3.6) can be written in the form of (38), (37) in Section 2.2 which as discussed there are of great use in order to understand the importance of viscous and thermal effects on these modes.

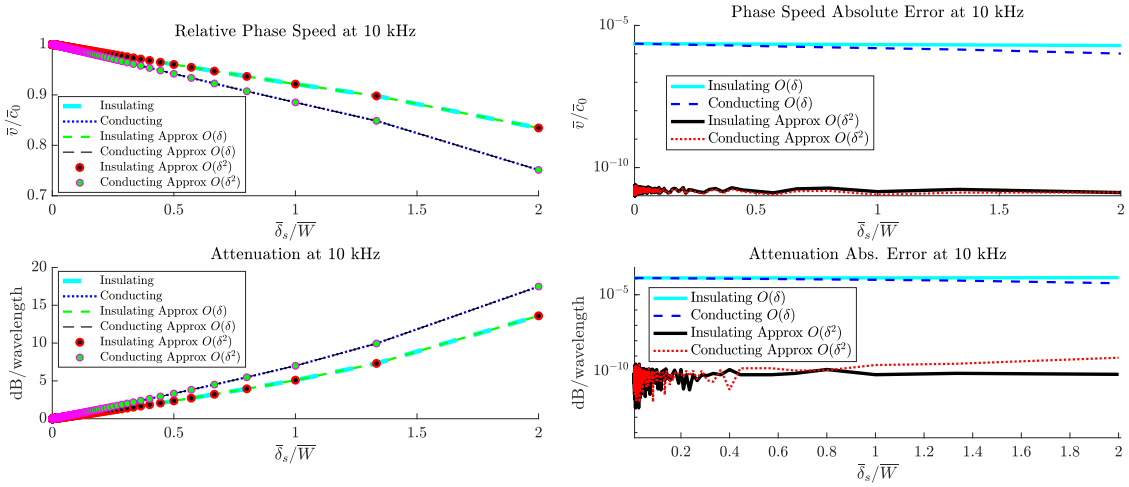


Figure 3.1: Full solutions and asymptotic approximations to (3.5), (3.6) according to the expansions (2.50), (2.51) in Section 3.2 at 10 kHz. The TVE medium chosen is air following values in Table A.1, which implies that $\mu = 0$ and (3.5), (3.6) reduce to (23), (25) in Section 3.2. The physical results are equivalent to those in FIG 2 of Section 2.2.

# Chapter 4

# FSI, stress relaxation and boundary layer effects in slits and plates

## 4.1 Introduction

This chapter consists of an application of the framework developed in Chapter 3 to some canonical problems involving FSI and the role of losses in the form of boundary layers in the fluid-solid interfaces together with intrinsic material loss due to viscoelastic effects. In particular, we will continue the analysis from Section 2.2 following the comments in Section 2.3.2 and show how this problem is in fact related to the problem of wave propagation in fluid-loaded plates.

The initial idea of this paper was developed between E García Neefjes and D Nigro. RC Assier helped with initial suggestions regarding the transition of roots in the complex plane. The paper was fully written by E García Neefjes, who also developed the numerical implementation and obtained the final results after useful discussions with the remaining co-authors. This work is intended to be submitted for publication simultaneously with that of Section 3.2. This piece of work is presented here as an extended paper, which we note might be a bit lengthy for certain journals so the final structure of the paper is yet to be fully discussed. We hope to obtain experimental results in order to further validate some of the discoveries presented in this paper.

## 4.2 Article

# Stress relaxation and boundary layer effects in fluid-filled visco-elastic slits and fluid-loaded visco-elastic plates

Erik García Neefjes[1], David Nigro[2], Raphaël C. Assier[1], William J. Parnell[1]

[1]Department of Mathematics, University of Manchester, Oxford Rd, Manchester, M13 9PL, UK

[2]Thales United Kingdom, 350 Longwater Avenue Green Park, Reading RG2 6GF, UK

February 21, 2022

**Abstract**

In this paper, we theoretically analyse wave propagation in two canonical problems of interest: fluid-filled visco-elastic slits and fluid-loaded visco-elastic plates. We show that these two configurations can be studied under the same pair of dispersion equations with the aid of the framework developed in [1] (the paper in Chapter 3). These two problems are further interrelated, since in the short wavelength limit (relative to the slit/plate width) the respective modes are governed by the same dispersion equation, commonly known as the Scholte–Stoneley equation. It is the Scholte-type modes which are mainly analyzed in this paper. Despite the theory being valid for any Newtonian fluid, the results are applied to water. Both 'hard' and 'soft' solids are compared, with emphasis put on the importance of viscoelastic effects, particularly when *stress relaxation* is considered. Two main recent works are discussed extensively, namely [2] (the paper in Chapter 2) for the slits and [3] for the loaded plates, both of which do not incorporate viscoelastic mechanisms. We show how the consideration of viscoelasticity can extend the results discussed therein, and explain the circumstances under which they arise.

## 1 Introduction

In a previous study [2], acoustic propagation in water-filled steel slits was analysed in detail. The paper was focused around the importance of boundary layer attenuation in the fluid region as the slits become narrow, partly motivated by some experimental data in [4] for air. It was found that although the presence of fluid viscosity is necessary in order to describe the attenuation of the mode along the slit, in order to capture the large reduction in phase speed as the width decreases, it is key to capture the fluid-structure interaction (FSI) effects, as is well known in underwater acoustics. On the other hand, for air–filled slits FSI may be ignored in most instances, even for considerably soft media such as rubbers [1], but instead thermal dissipative effects should be taken into account [5, 6] as opposed to water under standard circumstances [7].

One of the main objectives of this paper is to extend the analysis in [2] by considering *soft* solid slits and in particular by taking into account viscoelastic losses. Following the discussion above, in order to exploit these mechanisms for fluid-filled slits, it is required to have FSI and therefore only results for water are discussed (although the theory is applicable to any Newtonian fluid). The fluid-solid half–space which has been widely studied under many circumstances [8, 9, 10, 11], is considered first since it constitutes the geometrical limit as the channel width increases (relative to

the wavelength of the transverse wave in the in the fluid). This configuration gives rise to two well known main families of interface wave solutions corresponding to *Leaky–Rayleigh* (LR) and *Stoneley–Scholte* (Sc) modes. Unlike the LR [12], the Sc mode propagates for any fluid-solid interface and in particular is the only propagating mode for water–soft interfaces [11] which we will consider. The Sc phase speed is reduced significantly for 'soft' fluid-solid interfaces [3] as opposed to 'hard' fluid-solid interfaces where the Sc phase speed is approximately equal to the speed of sound in the fluid. The influence of viscoelasticity on this mode for water–soft media (synthetic resins) is studied theoretically and experimentally in a series of papers [10, 13, 14] with the objective of using Sc waves to characterise the properties of the ocean's sedimentary bottom.

In the current work, we bring special attention to the importance of viscoelastic *stress relaxation* in the phase-speed and attenuation of the Sc mode (and body waves) and the corresponding regimes where these effects become important. Under the standard linear solid model (SLSM) used here, the key dimensionless parameter in the frequency domain is the *Deborah number* $\omega t_r$ where $\omega$ is the angular frequency and $t_r$ the single relaxation time of the material in consideration [1]. Although the relaxation times of soft materials can vary over several orders of magnitude (e.g. [15]), the frequencies involved in the majority of reported studies are such that $\omega t_r \gg 1$ which we presume is the reason for the lack of stress relaxation analyses in the form presented in this paper. Despite this, we believe the regime considered here remains of high interest since these effects are clearly visible in experiments [16] and the importance of stress relaxation is often reported in the literature [3, 17].

Another important part of this paper is devoted to the study of (viscous) fluid-loaded viscoelastic plates. Despite perhaps seemingly unrelated to the fluid–filled slits, the dispersion equations (DEs) are in fact identical in both problems thanks to the generality of the media considered [1]. Early work on fluid-loaded plates [18, 19] identified that the presence of the liquid causes the standard plate Lamb wave solutions to become *leaky* (as for Rayleigh modes in the half–space) and another two solutions arise which are not present in the absence of the fluid. These solutions are in fact Scholte-like interface waves which become coupled in the plate region as the thicknesses decreases, and in order to distinguish them from their half–space counterpart we define them as 'coupled plate–Scholte' modes [3]. Many works have been focused around the consequences of attenuation due to fluid viscosity [20, 21, 22, 23] on the modes of fluid-loaded plates. Nevertheless, the majority of these studies have been based around 'hard' interfaces, presumably since this is the regime most common in sensing and non-destructive applications. Very recently, the authors in [3] considered water-loaded acrylic plates which is a 'soft' interface, and illustrated the significant differences that arise in the phase speed of the coupled plate–Sc with respect to standard metal interfaces. In particular, they justified and experimentally demonstrated the dispersive behaviour of the symmetric coupled plate–Scholte mode which had previously only been characterized for soft films at very high frequencies [24]. Although not provided in their analysis, it is remarked in the experimental verification of [3] the importance of viscoelastic properties of soft media, and in particular the importance of stress relaxation under particular frequency ranges. In this paper, we contribute to this study by taking into account these dissipative mechanisms in order to assess their influence (and that of boundary layers) in both the symmetric and anti–symmetric coupled plate–Scholte modes for a very wide range of plate thicknesses (and frequencies).

In Section 2, we briefly introduce the visco-elastic (VE) formulation that we will employ throughout this work which allows us to simultaneously consider (visco)elastic solid and visco-acoustic fluid media as explained in [1]. We discuss two classical models to capture the frequency dependence of the elastic moduli, namely the Kelvin-Voigt model (KVM) and the SLSM. These two models will be compared repeatedly in this work. In Section 3 we analyse the single interface configuration

consisting of two half–space VE media in perfect contact. By seeking interface solutions to this set-up we derive the *Stoneley* DE, from which the *Scholte* and *Rayleigh* DEs can be obtained by considering the inviscid fluid and zero density limits respectively. The Stoneley and Scholte DEs give rise to Sc and LR waves which we discuss in detail. Since our fluid of interest is water, we study 'hard' and 'soft' interfaces (definitions are provided) by considering material parameters associated to steel and PVC. For the soft case, we analyse in detail the additional behaviour that arises when the SLSM is employed.

In Section 4 we consider the double interface configuration, with the finite width medium constituting the slit/plate. We show how generalised DEs for symmetric/anti–symmetric modes valid for both configurations can be obtained. These equations recover more common forms found in the literature when certain effects are neglected such as the fluid's viscosity, which is illustrated. In the short wavelength-limit the general DEs reduce to the half–space Stoneley DE considered in Section 3, which is used as the initial value of the recursive root finding technique. For the slits, we show how the softness of the solid, together with viscoelastic damping gives rise to rather different results to those presented for water-filled steel slits in [2]. For plates, both the symmetric/anti–symmetric coupled plate-Scholte modes are considered, and we observe the dispersive behaviour for the symmetric mode for soft plates reported recently in [3]. We extend the theoretical analysis in [3] by including the effect of boundary layer attenuation (which is minimal) as well as viscoelastic damping in the solid which we show can be very important, especially near the *glass transition* of the moduli. The presence of a global maximum of the attenuation as a function of plate thickness for the symmetric mode is highlighted. We finish with conclusions in Section 5.

## 2 Governing equations for linear, isotropic VE continua

We assume that the media under consideration are linear, isotropic and further we make the approximation that all deformations are *isothermal*, so that thermo–mechanical coupling need not be taken into account. Consequently, the energy balance equation is automatically satisfied, so that the focus is to solve the linearised equation of motion, namely

$$\nabla \cdot \hat{\boldsymbol{\sigma}} = \rho_0 \frac{\partial^2 \hat{\mathbf{u}}}{\partial t^2}, \tag{2.1}$$

where $\rho_0$ denotes the constant mass density, $\hat{\mathbf{u}} = \{\hat{u}_x, \hat{u}_y, \hat{u}_z\}$ the continuum's displacement vector, $\nabla$ is the vectorial gradient operator and $\hat{\boldsymbol{\sigma}}$ is the Cauchy stress tensor which must capture all the required properties of the media we want to consider. Hereditary integrals give a general way to express the VE constitutive behaviour of the medium (e.g. [25], Chapter 1)

$$\hat{\boldsymbol{\sigma}} = \int_{-\infty}^{t} 2\hat{\mu}(t-\mathcal{T}) \frac{\partial \hat{\boldsymbol{e}}(\mathcal{T})}{\partial \mathcal{T}} \, \mathrm{d}\mathcal{T} + \left( \int_{-\infty}^{t} \hat{K}(t-\mathcal{T}) \, \mathrm{tr} \left( \frac{\partial \hat{\boldsymbol{\varepsilon}}(\mathcal{T})}{\partial \mathcal{T}} \right) \mathrm{d}\mathcal{T} \right) \boldsymbol{I}, \tag{2.2}$$

where $\hat{\boldsymbol{\varepsilon}} = (\nabla \hat{\mathbf{u}} + (\nabla \hat{\mathbf{u}})^T)/2$ is the linearised strain tensor, $\mathrm{tr}\,(\cdot)$ the trace operator, $\boldsymbol{I}$ the identity tensor and $\hat{\boldsymbol{e}} = \hat{\boldsymbol{\varepsilon}} - \mathrm{tr}\,(\hat{\boldsymbol{\varepsilon}})\boldsymbol{I}/3$ represents the off–diagonal terms of the strain tensor. Further, $\hat{\mu}(t), \hat{K}(t)$ are time–dependent (visco) elastic moduli, which must be identically zero for $t < 0$ to obey causality and are such that the integrals in (2.2) are convergent. In this paper we will be considering time-harmonic disturbances, so that all the fields satisfy

$$\{\hat{\mathbf{u}}, \hat{\boldsymbol{\sigma}}, \hat{\boldsymbol{\varepsilon}}, \hat{\boldsymbol{e}}\}(\mathbf{x}, t) = \mathrm{Re}\,\{\{\mathbf{u}, \boldsymbol{\sigma}, \boldsymbol{\varepsilon}, \boldsymbol{e}\}(\mathbf{x}) \mathrm{e}^{-\mathrm{i}\omega t}\}, \tag{2.3}$$

which when substituted in (2.2), (2.1) and factoring out the common term give respectively

$$\boldsymbol{\sigma} = 2\mu(\omega)\boldsymbol{e} + K(\omega)\,\mathrm{tr}(\boldsymbol{\varepsilon})\boldsymbol{I}, \tag{2.4a}$$

$$(K(\omega)+\frac{4}{3}\mu(\omega))\nabla\left(\nabla\cdot\mathbf{u}\right) - \mu(\omega)\nabla\times\nabla\times\mathbf{u} + \rho_0\omega^2\mathbf{u} = \mathbf{0}, \tag{2.4b}$$

where $\mu(\omega), K(\omega)$ are scaled Fourier transforms of the original moduli [1]. On adopting the Helmholtz decomposition

$$\mathbf{u} = \nabla\phi + \nabla\times\boldsymbol{\Phi}, \tag{2.5}$$

with $\nabla\cdot\boldsymbol{\Phi} = 0$, the compressional and shear wave potentials $\phi, \Phi$ must respectively satisfy

$$\left(\Delta + k_\phi^2\right)\phi = 0, \qquad k_\phi^2(\omega) = \frac{\rho_0\omega^2}{K(\omega)+\frac{4}{3}\mu(\omega)}, \tag{2.6a}$$

$$\left(\Delta + k_\Phi^2\right)\boldsymbol{\Phi} = \mathbf{0}, \qquad k_\Phi^2(\omega) = \frac{\rho_0\omega^2}{\mu(\omega)}, \tag{2.6b}$$

recalling that the material parameters appearing in the compressional/shear wavenumbers $k_\phi, k_\Phi$ in (2.6) are isothermal, which is particularly important to consider for viscous gases such as air (since the isothermal bulk modulus can differ significantly from the corresponding more common adiabatic modulus) [1]. Given the shear and bulk moduli present in (2.6), we can define the generalized first Lamé coefficient, Poisson's ratio and Young's modulus respectively as [26]

$$\lambda(\omega) = K(\omega) - \frac{2}{3}\mu(\omega), \qquad \nu(\omega) = \frac{3K(\omega)-2\mu(\omega)}{6K(\omega)+2\mu(\omega)}, \qquad E(\omega) = \frac{9K(\omega)\mu(\omega)}{3K(\omega)+\mu(\omega)}. \tag{2.7}$$

There exist plenty of models to capture the frequency dependence of these moduli which are appropriate in particular circumstances (e.g. [27]), but in this work we focus on the Kelvin–Voigt Model (KVM) (which we also refer to as local VE) and the Standard Linear Solid Model (SLSM), which are discussed extensively in [1] starting from their time domain behaviour. For a given modulus $\mathcal{M}(\omega)$ we have

$$\text{(KVM)} \quad \mathcal{M}(\omega) = \mathcal{M}_0 - \mathrm{i}\omega\eta_{\mathcal{M}}, \tag{2.8a}$$

$$\text{(SLSM)} \quad \mathcal{M}(\omega) = \mathcal{M}_\infty - (\mathcal{M}_0-\mathcal{M}_\infty)\frac{\mathrm{i}\omega t_r}{1-\mathrm{i}\omega t_r} = \frac{\mathcal{M}_\infty + \mathcal{M}_0(\omega t_r)^2}{1+(\omega t_r)^2} - \mathrm{i}\frac{(\mathcal{M}_0-\mathcal{M}_\infty)\omega t_r}{1+(\omega t_r)^2}. \tag{2.8b}$$

In the KVM, the real part ($\mathcal{M}_0$) is fixed and the (attenuative) imaginary part known as the *loss modulus* is characterized by $\omega\eta_{\mathcal{M}}$ where $\eta_{\mathcal{M}}$ is a constant viscosity coefficient. In the SLSM, $\mathcal{M}_\infty, \mathcal{M}_0$ correspond to the long-term and instantaneous moduli and $t_r$ represents the (single) relaxation time of the material. The Deborah number $\omega t_r$ in (2.8b), relates the characteristic time of the problem $(1/\omega)$ with the relaxation time of the material in consideration. The moduli further satisfy $\mathcal{M}_\infty \leq \mathcal{M}_0$, with the equality implying the medium is perfectly elastic. We note that for $\omega t_r \gg 1$, $\mathcal{M} \to \mathcal{M}_0$ and conversely for $\omega t_r \ll 1$, $\mathcal{M} \to \mathcal{M}_\infty$ and therefore higher frequencies correspond to the *glassy* (stiffer) phase of the materials and lower frequencies to a *rubbery* (softer) phase. The loss modulus has a global maximum at $\omega t_r = 1$ which defines the *glass transition region*, and therefore it is in the vicinity of this region where the majority of intrinsic VE losses are manifested.

Visco–acoustic (Newtonian) fluids can also be described by (2.4)-(2.6) with $\mu(\omega) = -\mathrm{i}\omega\eta_\mu$, where $\eta_\mu > 0$ is the kinematic viscosity [1, 21, 23], so that the square of the shear wavenumber becomes purely imaginary, i.e. $k_\Phi^2 = \mathrm{i}/\delta_\nu^2$ where $\delta_\nu = \sqrt{\eta_\mu/\rho_0\omega}$ is a boundary layer parameter related to the common Stokes' boundary layer thickness by $\delta_s = 2\pi\sqrt{2}\delta_\nu$.

# 3 Single interface: Two VE half–spaces in perfect contact

We first seek interface waves associated with the configuration of VE–VE half–spaces separated by an interface at $y = 0$, as seen on the left of Figure 1. From the resulting DEs we can determine the Leaky Rayleigh and Scholte-Stoneley modes and analyse some of their key properties. As we will observe in the next section, the understanding of the half–space will facilitate the study of the double interface configuration (right of Figure 1).

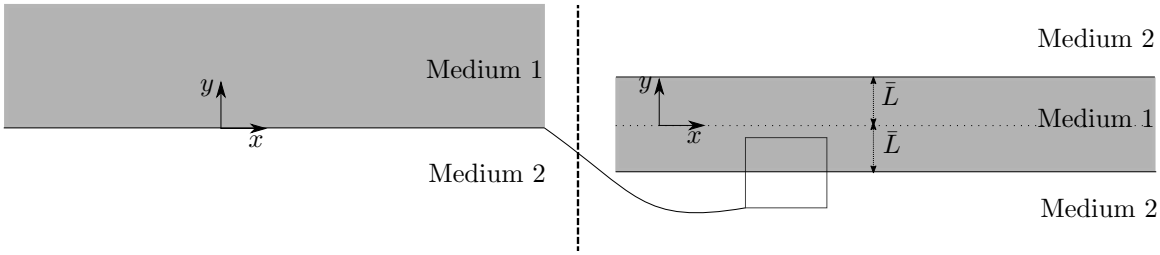


Figure 1: Schematic representations of the 2D geometric configurations considered in this paper, noting that all media are infinitely extending in the $x$-direction. Left: Two semi-infinite VE continua as considered in Section 3 (single interface). Right: A VE medium of width $\bar{W} = 2\bar{L}$ bounded by two semi-infinite VE media as considered in Section 4 (double interface).

## 3.1 The Stoneley, Rayleigh and Scholte Dispersion Equations

In Section 2 all the relevant equations were given in dimensional form. It will be convenient in the subsequent analysis to have a notational distinction between dimensional/non–dimensional quantities and therefore from here onwards we will introduce an over–bar $\bar{\cdot}$ to all dimensional quantities. We seek potential solutions to the governing equations (2.4) that decay away from the boundary in each half–space, since interface waves can be represented as a linear combination of these four waves:

$$\bar{\phi}_1 = \bar{P}_1 \mathrm{e}^{-\bar{\gamma}_{\phi_1}\bar{y}+\mathrm{i}\bar{k}\bar{x}}, \qquad \bar{\phi}_2 = \bar{P}_2 \mathrm{e}^{\bar{\gamma}_{\phi_2}\bar{y}+\mathrm{i}\bar{k}\bar{x}}, \tag{3.1a}$$

$$\bar{\Phi}_1 = \bar{S}_1 \mathrm{e}^{-\bar{\gamma}_{\Phi_1}\bar{y}+\mathrm{i}\bar{k}\bar{x}}, \qquad \bar{\Phi}_2 = \bar{S}_2 \mathrm{e}^{\bar{\gamma}_{\Phi_2}\bar{y}+\mathrm{i}\bar{k}\bar{x}}, \tag{3.1b}$$

where

$$\bar{\gamma}_{\phi_1} = (\bar{k}^2 - \bar{k}_{\phi_1}^2)^{1/2}, \quad \bar{\gamma}_{\phi_2} = (\bar{k}^2 - \bar{k}_{\phi_2}^2)^{1/2}, \quad \bar{\gamma}_{\Phi_1} = (\bar{k}^2 - \bar{k}_{\Phi_1}^2)^{1/2}, \quad \bar{\gamma}_{\Phi_2} = (\bar{k}^2 - \bar{k}_{\Phi_2}^2)^{1/2}, \tag{3.2}$$

for some complex amplitudes $\bar{P}_1, \bar{P}_2, \bar{S}_1, \bar{S}_2$. We must ensure that the choice of the various branch cuts of the square root functions in (3.2) is consistent with causality, which is further discussed below. At the interface between the two media, the solutions must satisfy continuity of traction and displacement boundary conditions (BCs), that is on $\bar{y} = 0$,

$$\bar{\sigma}_{yy}^1 = \bar{\sigma}_{yy}^2, \quad \bar{\sigma}_{xy}^1 = \bar{\sigma}_{xy}^2, \quad \bar{\mathbf{u}}_1 = \bar{\mathbf{u}}_2. \tag{3.3}$$

Substitution of (3.1) into (3.3) then leads to the VE Stoneley DE, that is

$$\begin{aligned}\bar{\mathcal{D}}_{\mathrm{St}} = \bar{c}^4[(\bar{\rho}_1 - \bar{\rho}_2)^2 - (\bar{\rho}_2 A_1 + \bar{\rho}_1 A_2)(\bar{\rho}_2 B_1 + \bar{\rho}_1 B_2)] \\ + 2\bar{c}^2\bar{\mathcal{Q}}(-\bar{\rho}_2 A_1 B_1 + \bar{\rho}_1 A_2 B_2 - \bar{\rho}_1 + \bar{\rho}_2) + \bar{\mathcal{Q}}^2(A_1 B_1 - 1)(A_2 B_2 - 1) = 0,\end{aligned} \tag{3.4}$$

which for a purely elastic-elastic interface takes the form as in Stoneley's original paper [28], (as expected prior to the specification of the frequency dependence of the elastic moduli due to the correspondence principle for elasticity see e.g. [27]) with

$$\bar{c} = \frac{\bar{\omega}}{\bar{k}}, \qquad \{A_1, A_2, B_1, B_2\} = \frac{1}{\bar{k}}\{\bar{\gamma}_{\phi_1}, \bar{\gamma}_{\phi_2}, \bar{\gamma}_{\Phi_1}, \bar{\gamma}_{\Phi_2}\} \qquad \bar{\mathcal{Q}} = 2(\bar{\rho}_1\bar{c}_{\Phi_1}^2 - \bar{\rho}_2\bar{c}_{\Phi_2}^2), \tag{3.5}$$

where $\bar{c}_\Phi = \bar{\omega}/\bar{k}_\Phi$ in each medium. If we let the density of the upper medium vanish, i.e. $\bar{\rho}_1 \to 0$ in (3.4), after some manipulation using (3.5) we obtain the Rayleigh DE, namely

$$\bar{\mathcal{D}}_{\mathrm{Ra}} = (2\bar{k}^2 - \bar{k}_{\Phi_2}^2)^2 - 4\bar{k}^2\bar{\gamma}_{\phi_2}\bar{\gamma}_{\Phi_2} = 0, \tag{3.6}$$

which governs the ubiquitous *Rayleigh waves*, originally described in [29] for elastic media. Alternatively, in the inviscid fluid limit $\bar{\mu}_1(\omega) \to 0$, it follows that $\bar{k}_{\Phi_1}^2 \to \infty$ and hence $\bar{\gamma}_{\Phi_1}, B_1 \to \infty$ whereas $\bar{\mathcal{Q}} \to -2\bar{\rho}_2\bar{c}_{\Phi_2}^2$ so that (3.4) becomes

$$\bar{\mathcal{D}}_{\mathrm{Sc}} = \bar{\mathcal{D}}_{\mathrm{Ra}} + \frac{\bar{\gamma}_{\phi_2}\bar{k}_{\Phi_2}^4}{\bar{\gamma}_{\phi_1}\rho_s} = 0, \quad \text{with} \quad \rho_s = \frac{\bar{\rho}_2}{\bar{\rho}_1}, \tag{3.7}$$

which is the common Scholte DE (also referred to as Scholte–Stoneley DE [3]). As we will discuss shortly, in general (3.7) and (3.4) admit two families of interface wave solutions, namely *Leaky Rayleigh* and *Scholte* waves. Direct observation of (3.7) illustrates the role of the density ratio $\rho_s$, when $\rho_s \gg 1$ i.e. for "hard" interfaces, the fluid-loading term will have negligible influence and therefore the behaviour of $\bar{\mathcal{D}}_{\mathrm{Sc}}$ can be seen as a small perturbation to $\bar{\mathcal{D}}_{\mathrm{Ra}}$. Nevertheless, for softer interfaces such that $\rho_s \approx 1$ significantly different behaviour of the spectrum can be expected.

Naturally, due to the symmetry of the configuration, (3.6) and (3.7) can also be recovered by taking the limits $\bar{\rho}_2 \to 0$, $\bar{\mu}_2(\omega) \to 0$ respectively (and interchanging the subscripts '1' and '2' in the subsequent equations). Despite the interest of this work being on losses in fluid–solid configurations, this symmetry property makes the use of the general VE–VE configuration convenient, which will become apparent in Section 4 where we will be able to consider two physically different problems under the same set of DEs.

The roots of (3.4), (3.6), (3.7) and the various DEs studied in Section 4 are calculated using the MATLAB [version 9.8.0.1380330 (R2020a)] command *fsolve*, which finds the local zero of a function close to a given starting point specified by the user. This initial value will differ depending on the mode under consideration, as we will specify below.

Throughout the paper, the several square root functions (3.2) are chosen such that, as $|\bar{k}| \to \infty$ $\bar{\gamma}_{\phi_1}, \bar{\gamma}_{\phi_2}, \bar{\gamma}_{\Phi_1}, \bar{\gamma}_{\Phi_2} \to \bar{k}$, with the branch cuts from $\bar{k}_{\phi_1}, \bar{k}_{\phi_2}, \bar{k}_{\Phi_1}, \bar{k}_{\Phi_2}$ taken in the upper half–plane and those from $-\bar{k}_{\phi_1}, -\bar{k}_{\phi_2}, -\bar{k}_{\Phi_1}, -\bar{k}_{\Phi_2}$ taken in the lower half–plane. The branch cuts are chosen to run with fixed real parts (i.e. parallel to the imaginary axis) from the respective branch points. We note that in order to analyse *all* roots of these equations, in principle it is necessary to consider all possible combinations of Riemann sheets giving e.g. $2^4$ for (3.4), $2^3$ for (3.7) and $2^2$ for (3.6), see e.g. [12, 30, 31]. In this work, we are concerned with the influence of VE effects on the well established roots of these equations, so we simply need to make sure the obtained solutions are causal and do not jump Riemann sheets. On top of this, we ensure they behave as expected in the absence of any form dissipation.

In what follows, the roots of the DEs will be plotted in terms of non-dimensional phase speed and attenuation, which are given by

$$\text{Phase Speed } = \frac{\bar{v}}{\bar{c}_\square} = \frac{\text{Re}\{\bar{c}\}}{\bar{c}_\square} = \frac{\bar{\omega}}{\text{Re}\{\bar{k}\}\bar{c}_\square}, \tag{3.8a}$$

$$\text{Attenuation (dB/wavelength)} = 40\pi \frac{\text{Im}\{\bar{k}\}}{\text{Re}\{\bar{k}\}} \log_{10}(\text{e}), \tag{3.8b}$$

where $\bar{c}_\square$ represents a particular sound velocity which we assume constant. In particular $\bar{c}_0$ denotes the speed of sound of water, and $\bar{c}_s$ is the lossless shear wave speed of sound in a certain solid material (from Table 1 water gives $\bar{c}_0 = 1490$ m/s, steel $\bar{c}_s = 3000$ m/s, and PVC $\bar{c}_s = 1100$ m/s).

## 3.2 Material parameters: hard/soft solids

We have seen above that different limits of the density ratio $\rho_s$ can give some insights on the importance of certain terms in the various DEs above. Generally, knowing whether a given fluid-solid pair is hard/soft is intuitive although in some instances this can lead to ambiguity, as recently noticed in [3], which is focused on the Scholte mode solution to (3.7). Indeed, a common definition is whether the material parameters are such that $\text{Re}\{\bar{k}_\phi\} < \text{Re}\{\bar{k}_\Phi\} \leq \text{Re}\{\bar{k}_\text{F}\}$ or $\text{Re}\{\bar{k}_\phi\} \leq \text{Re}\{\bar{k}_\text{F}\} < \text{Re}\{\bar{k}_\Phi\}$ which correspond to hard or soft respectively, as in e.g. [11]. Note that since we are fixing materials 1/2 to be fluid/solid respectively (for definition purposes) we have written $\bar{k}_\text{F} \equiv \bar{k}_{\phi_1}$ for the visco-*acoustic* wavenumber, and $\bar{k}_\phi \equiv \bar{k}_{\phi_2}$, $\bar{k}_\Phi \equiv \bar{k}_{\Phi_2}$ corresponding to the standard pressure and shear VE wavenumbers. Nevertheless, in some instances the definition implied by the inequalities can be inaccurate e.g. it is shown in [3] by considering the transition between $\text{Re}\{\bar{k}_\Phi\}$, and $\text{Re}\{\bar{k}_\text{F}\}$ that the Scholte mode's phase speed remains constant (which should not be the case when transitioning between a 'hard' and 'soft' solid). For this reason, in their work a hard interface is defined as one where the Scholte velocity is approximately equal to the speed of sound in the fluid, and conversely a soft interface is one where the Scholte velocity is notably less than the speed of sound in the fluid. This definition is more physically precise in their context, whereas the former indicated by the inequalities above is motivated by the complex plane spectrum. In [9] the same idea is discussed in terms of acoustic impedance of the fluid/solid pair.

| **VE Parameter Values (Kelvin–Voigt Model)** | | | | | |
|---|---|---|---|---|---|
| Parameter | Unit | Symbol | Water | Steel | PVC |
| Background density | kg/m$^3$ | $\rho_0$ | 1000 | 7871 | 1360 |
| Shear modulus | GPa | $\mu_0$ | – | 70.84 | 1.65 |
| Young's modulus | GPa | $E_0$ | – | 188.904 | 4.431 |
| Bulk modulus (isothermal) | GPa | $K_0$ | 2.22 | 188.9 | 4.8 |
| Dynamic shear viscosity | Pa·s | $\eta_\mu$ | $10^{-3}$ | $2\times10^{-5}$ | $10^{-1}$ |
| Dynamic bulk viscosity | Pa·s | $\eta_K$ | $3\times10^{-3}$ | $10^{-8}$ | $10^{-2}$ |

Table 1: Parameter values used for water, steel and PVC employed here, taken from [32], [2] and [10] respectively, assumed to be independent of frequency. The PVC values are only applicable for local VE (KVM); the values for the stress relaxation discussion are given in Sections 3.3.3, 4.3.3 and 4.4.3.

Our primary physical interest here is in water–solid interfaces, so that in most of what follows medium 1 in (3.1) is fixed by the parameters of water, which are given in Table 1. For a given fluid, the behaviour of the interface modes can be greatly influenced by the (visco-)elastic properties of

the solid, which we explore below. As is done in several works (e.g. [11]) in order to illustrate this, we will concentrate on two solids of opposing nature, namely steel and PVC whose values are also shown in Table 1. As we will showcase below, when compared to water these values correspond to hard/soft materials respectively (for both definitions presented above). Furthermore, in order to aid our study of the effect for the hard–soft transition on the relevant modes, we will make use of a linear continuous transition in all Material 2 parameters (listed in Table 1) through a function $\mathbf{f} : [0, 1] \to \mathbb{R}^n$ s.t.

$$\mathbf{f}(\tau) = [\mathbf{Steel}](1 - \tau) + [\mathbf{PVC}](\tau) \qquad 0 \leq \tau \leq 1. \tag{3.9}$$

With regards to the frequency dependence of the VE moduli in the solid, we commence by considering the KVM in Sections 3.3.1, 3.3.2 following (2.8a) for both the shear and bulk moduli, characterized by the viscosity coefficients $\eta_\mu, \eta_K$ respectively. Consequently, the SLSM from (2.8a) is employed in Section 3.3.3, with further details provided there.

## 3.3 Modes at the interface of 2 semi-infinite half–spaces

Having defined the relevant equations to our physical set–up and material parameters in consideration, we now focus our attention to the solutions of the Stoneley DE (3.4), that can give rise to Leaky–Rayleigh and Stoneley–Scholte modes, which are considered individually next.

### 3.3.1 The Leaky–Rayleigh (LR) Mode

We denote the LR mode solutions to (3.4), (3.7) by $\bar{k}_{\mathrm{LR}} = \bar{\omega}/\bar{c}_{\mathrm{LR}}$. It is well established that the LR wave propagates slightly slower than the associated solid's shear body wave, marginally faster than the ordinary Rayleigh wave and attenuates in the direction of propagation due to part of the energy being shed into acoustic waves (radiated) into the fluid [9]. In most instances, this leakage is a consequence of the LR being *supersonic* ($\mathrm{Re}\{\bar{k}_{\mathrm{LR}}\} < \mathrm{Re}\{\bar{k}_{\mathrm{F}}\}$). In fact, this was believed to be necessary for its existence (see e.g. [11]) prior to the work of [12], who showed the existence of subsonic leakage (although in a very small region) by careful analysis of the complex plane spectrum. Nevertheless, in most circumstances the LR cannot propagate and the inequality ($\mathrm{Re}\{\bar{k}_{\Phi}\} < \mathrm{Re}\{\bar{k}_{\mathrm{LR}}\} \leq \mathrm{Re}\{\bar{k}_{\mathrm{F}}\}$) usually holds. In realistic conditions, the LR mode is also subject to extra attenuating mechanism, namely that of visco-thermal boundary layer effects in the fluid, as well as the VE damping within the solid. In [21] it was explicitly found that viscous effects dominate over heat conduction effects (especially for water) based on the original work [7], who first concluded that the effect of viscosity can be neglected for fluids with Reynolds number larger than 2500. We will showcase the differences by comparing solutions to the general Stoneley DE (3.4) with the inviscid fluid equivalent solution (3.7). Nevertheless, the inclusion of fluid viscosity becomes paramount in narrow regions, as we discuss in Section 4.3.

Given the parameters in Table 1 and the discussion above, we note that for a water-PVC interface ($\tau = 1$ in (3.9)) the LR cannot be supported, since the shear wave is highly subsonic ($\mathrm{Re}\{\bar{k}_{\mathrm{F}}\} < \mathrm{Re}\{\bar{k}_{\Phi}\}$), whereas for water-Steel ($\tau = 0$ in (3.9)) the mode will exist. Starting from $\tau = 0$, as we transition through increasing $\tau$ we observe the LR root becomes increasingly attenuative (per unit metre), until it reaches the subsonic region. A detailed analysis of the transition from the existence of the LR in the complex plane was provided in [12] via an isotropic gold-silver alloy with variable content in contact with water.

In order to numerically obtain the LR root using *fsolve*, as initial guess we simply choose a real value that is slightly slower than the solid's shear wave speed. Indeed, we obtain that the LR mode solution to (3.4) for Steel at 10 kHz gives $\bar{k}_{\mathrm{LR}} = 22.41 + 0.24\mathrm{i}\ \mathrm{m}^{-1}$, whereas for $M_{\tau=0.9}$ (the artificial

material corresponding to $\tau = 0.9$ in (3.9)), $\bar{k}_{\mathrm{LR}} = 31.51 + 2.266\mathrm{i}\ \mathrm{m}^{-1}$, whose associated (normalized) horizontal particle displacements $\mathrm{Re}\{u_x\}$ are given in Figure 2 a),b),d), all of which have been normalized such that $u_x(y = x = 0) = 1$. We observe that the motion (and hence energy) of the LR is radiated as a pressure wave in the fluid propagating in the direction of the Rayleigh angle $\theta_{\mathrm{Ra}} = \arctan\{\mathrm{Re}(\mathrm{i}\bar{\gamma}_{\phi_1})/\,\mathrm{Re}(\bar{k}_{\mathrm{LR}})\}$ which is measured anti-clockwise from $x = 0$ (see Fig 2a)). For instance, water–steel gives $\theta_{\mathrm{Ra}} = 57.88°$, whereas for water–$M_{\tau=0.9} = 41.83°$. From the expanded Fig 2b) we observe the boundary layer region in the fluid, which we remark is very thin (at 10 kHz we have approximately $\bar{\delta}_\nu \approx 4\ \mu$m). As with the traditional Rayleigh mode, the motion within the solid half-space is very localized near the boundary. The dissipation for increasing $x$ parallel to $y = 0$ is very apparent for $M_{\tau=0.9}$, where the motion in the solid in Fig 2d) cannot be appreciated due to the higher magnitude of the mode along the positive $y$ direction (fluid region), as indicated by the colour bar.

When performing the same calculations as above but with the Scholte DE (3.7) (i.e. considering the inviscid fluit limit) we obtain very accurate answers for the phase speed and attenuation for both materials, despite the boundary layer effects observed for $u_x$ naturally not being captured since in this case we are allowing the fluid to slip in the horizontal direction. On the other hand, the (VE) pure Rayleigh DE (3.6) in the absence of fluid predicts the phase velocity fairly accurately but fails to predict the attenuation[1], as shown in Fig 2c), from which we can conclude that energy radiation is indeed the predominant effect contributing to the attenuation of this mode, with boundary layers and the solid's VE damping playing a much smaller role, which would be inconsequential in most practical scenarios. Furthermore, in Fig 2c) we can also observe the small dispersion of the LR mode for $M_{\tau=0.9}$ which we also found to be the case for steel, and tested it up to MHz frequencies.

### 3.3.2 The Scholte–Stoneley (Sc) Mode

We denote the Sc mode solutions to (3.4), (3.7) by $\bar{k}_{\mathrm{Sc}} = \bar{\omega}/\bar{c}_{\mathrm{Sc}}$. The Stoneley-Scholte mode is an acoustic surface wave whose velocity is *subsonic* and slower than the bulk waves of the solid (i.e. $\mathrm{Re}\{\bar{k}_\phi\}, \mathrm{Re}\{\bar{k}_\Phi\}, \mathrm{Re}\{\bar{k}_{\mathrm{F}}\} \leq \mathrm{Re}\{\bar{k}_{\mathrm{Sc}}\}$) and, when neglecting the viscoelastic effects of both liquid and solid, it travels unattenuated along the interface and decays exponentially away from it. Unlike the LR case above, it is present for all fluid-solid interfaces, although its behaviour is highly influenced by the material properties in question, as pointed out in [3]. Following Section 3.2, for a fixed fluid (in our case water), *soft* solids yield deeper penetration depths of the Sc mode and are therefore more convenient for applications [11]. With regards to losses in the fluid region, Stoneley-Scholte modes can be attenuated through two mechanisms, namely through leakage (viscous boundary layer) of shear/vortical waves from the interface into the fluid, and through the longitudinal bulk waves in the viscous fluid. Nevertheless, for the latter to be noticeable the frequencies must be very high, and in general for both mechanisms to become important the viscosity of these fluids must be fairly high (e.g. in the experiments of [23] glycerol and honey are used). Indeed, [33], [8] concluded that for low viscosity fluids (including water), the effects on the Sc mode are such that it can generally be ignored. The VE effects within softer solids were studied theoretically and experimentally by Favretto-Anrès [10], [13] who found weak dispersion in the lower frequency range for synthetic resins in contact with water.

In this case, for the starting point for our DE solver, we choose a real valued $\bar{k}$ whose real part is greater than $\max(\mathrm{Re}\{\bar{k}_{\mathrm{F}}\}, \mathrm{Re}\{\bar{k}_\Phi\})$. We obtain that the Sc solution to (3.4) for Steel at 10

[1] Particularly for $M_{\tau=0.9}$, which is in accordance with the observation noted just below (3.7) regarding the role of the density ratio $\rho_s$.

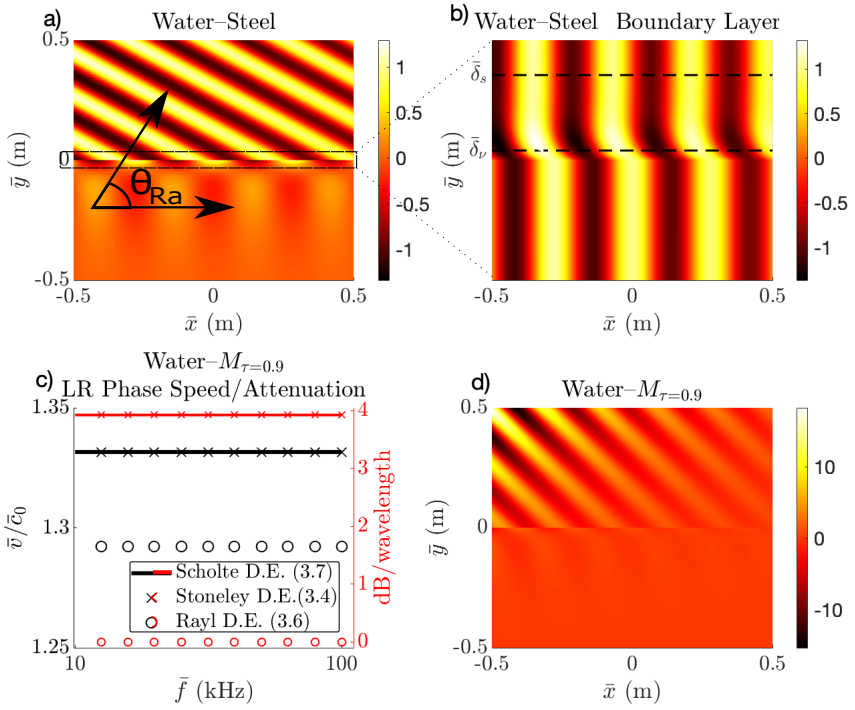


Figure 2: Heatmaps a), b), d) illustrate the dimensionless horizontal particle displacement $\mathrm{Re}\{u_x\}$ of the Leaky-Rayleigh mode from (3.4) at 10 kHz for water–steel (a), (b) and water–$M_{\tau=0.9}$ (d). (b) corresponds to the same calculation as (a) but near the boundary (as indicated by the small dotted lines) and all three plots have been normalized such that $u_x(y = x = 0) = 1$. In c) we give comparisons (in phase speed/attenuation) between the LR solutions obtained by different DEs for water–$M_{\tau=0.9}$, noting the two different $y$ scales represented by black/red.

kHz gives $\bar{k}_{\mathrm{Sc}} = 42.163 + 1.3 \times 10^{-4}\mathrm{i}$ m$^{-1}$ (noting that $\bar{k}_{\mathrm{F}} = 42.149 + 2.5 \times 10^{-6}\mathrm{i}$ m$^{-1}$), for PVC $\bar{k}_{\mathrm{Sc}} = 70.86 + 0.0012\mathrm{i}$ m$^{-1}$ whereas for $M_{\tau=0.9}$ we obtained $\bar{k}_{\mathrm{Sc}} = 43.82 + 0.001\mathrm{i}$ m$^{-1}$. The difference in the real parts of these roots is remarkable, showing that this PVC is also soft according to the definition in [3], as discussed in Section 3.2. Illustrations of these roots are given in Figure 3. Unlike the case with the LR above, we can now observe the 'trapped' nature of the mode (especially in Fig 3a)) propagating parallel to the $y = 0$ interface. We nevertheless observe the aforementioned large differences in penetration depths between steel and PVC. With steel Fig 3d), the decay length in the water is long and the overall behaviour near the boundary resembles that of a longitudinal wave in the fluid at grazing incidence, whereas for PVC we observe much more motion distributed into the solid, and much shorter decay lengths in the fluid as seen in Fig 3a). Given the roots this can also be easily seen analytically by simply assessing the real part of the various square root functions (3.2) appearing in (3.1). Similar qualitative results in terms of energies are explicitly given in [10] and [3]. From Fig 3b) we can observe how the smaller acoustic impedance mismatch between water and PVC also results in a weaker boundary layer effect compared to that for water-steel (as shown for the LR in Fig 2b)).

As for the LR case, from Fig 3c) we again observe that the Scholte DE gives very accurate approximations (with respect to the more general Stoneley DE (3.4)) to both the phase speed and attenuation of the Sc mode. Note, however the much smaller attenuation observed for this mode since (unlike for the LR) in an ideal fluid–solid interface there is no dissipative mechanism and the root becomes purely real. In Fig 3c) we do not see dispersion in the phase speed of the Sc mode for water–PVC, and we find (not shown) that the same occurs for steel and $M_{\tau=0.9}$ up to MHz frequencies. Furthermore, so far we have only been considering local VE such that e.g. $\mathrm{Im}\{\bar{\mu}(\bar{\omega})\} = -\mathrm{i}\bar{\omega}\bar{\eta}_{\mu}$ (in both the fluid and solid, for a constant $\bar{\eta}_{\mu}$) and therefore the larger $\bar{\omega}\bar{\eta}_{\mu}$, the higher values of dissipation, with the real part remaining constant. For the fluid this is an accurate model since in this work we are focused on water [34], but this is not generally the case for softer solid media, particularly due to the importance of stress relaxation effects [1]. These are the main topic of discussion in the next section.

### 3.3.3 Additional frequency dependence: Influence of stress relaxation

As aforementioned, VE effects on the Sc mode for water–synthetic resins were analysed in [10], [13]. Despite the model used corresponding to a Kelvin–Voigt type model (for fixed frequency), they made acoustical measurements to obtain attenuation coefficients that can be related to viscosity via non-linear functions of frequency. In particular this means that in their case e.g. $\bar{\eta}_{\mu} \equiv \bar{\eta}_{\mu}(\bar{\omega})$ (similarly with the bulk viscosity) which becomes a function that must be calculated at each individual frequency and is therefore not constant as in (2.8a). Furthermore, in their experiments they found the body wave speeds to be almost constant in the range 100 kHz–5 MHz, but they extended this range to cover lower frequencies in their study, so that the sound speeds (and hence the real part of the elastic moduli) are assumed constant in a wide range of frequencies ranging from 20 kHz–1 MHz. Despite these strong assumptions, they obtained accurate predictions of the Sc mode in a number of different scenarios that were confirmed experimentally. In particular, they found low frequency ($10 - 60$ kHz) dispersion in the water–PVC interface which were not captured with the KVM with the parameters from Table 1, see Fig 3c).

In what follows, from a theoretical standpoint we want to include the frequency dependence of the bulk speeds of sound and draw particular attention to the effect of stress relaxation, which is generally most noticeable at lower frequencies [16]. Coincidentally, the importance of these effects were recently pointed out in [3], who noticed their appearance by experimentally extracting values

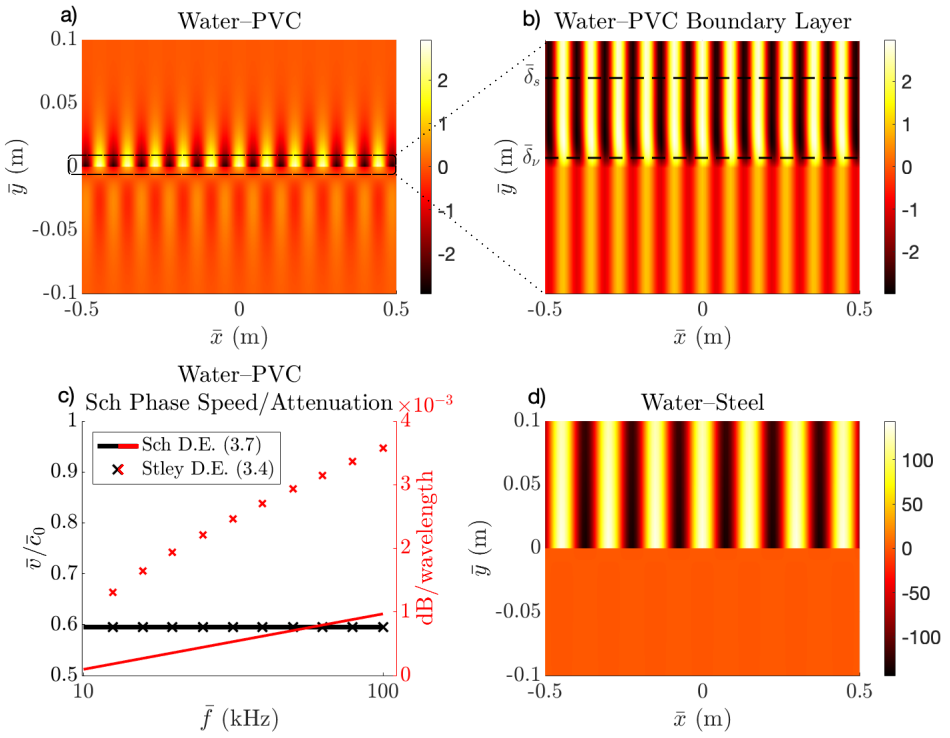


Figure 3: Heatmaps a), b), d) illustrate the dimensionless horizontal particle displacement $\mathrm{Re}\{u_x\}$ of the Scholte-Stoneley mode from (3.4) at 10 kHz for water–PVC (a), (b) and water–Steel (d). (b) corresponds to the same calculation as (a) but near the boundary (as indicated by the small dotted lines) and all three plots have been normalised such that $u_x(y = x = 0) = 1$. In c) we compare the phase speed and attenuation predicted by the (exact) Stoneley DE (3.4) and the Scholte approximation (3.7) for the water–PVC case, noting the two different $y$ scales represented by black/red.

of the Young's modulus for acrylic using *coupled Scholte modes* (which we discuss in Section 4.4). Although an analysis of stress relaxation effects is not considered in [3], it is shown that for a given fluid, the Sc mode is almost independent of the solid's Poisson ratio. More generally, weak frequency dependence of Poisson ratio in VE materials is often found in experiments [35]. We will therefore proceed by keeping $\nu_2$ constant and letting the frequency dependence of the Young's modulus $\bar{E}_2(\omega)$ obey the SLSM (2.8b), that is, Material 2 satisfies

$$\nu_2(\omega) = \nu_2, \qquad \bar{E}_2(\omega) = \bar{E}_\infty - (\bar{E}_0 - \bar{E}_\infty)\frac{\mathrm{i}\omega t_r}{1 - \mathrm{i}\omega t_r}, \tag{3.10}$$

noting that this assumption implies that the solid's shear modulus $\bar{\mu}_2(\omega)$ also satisfies the SLSM with the same relaxation time, and moduli $\bar{\mu}_0, \bar{\mu}_\infty$ (see e.g. [36]). Prony series have shown to be very useful to model the relaxation behaviour of a wide number of VE materials [37]. With (3.10) we are employing the simplest case of Prony series by accommodating a single relaxation time $\bar{t}_r$, which in practice is obtained by fitting the model to data from relaxation tests. Nevertheless, as discussed in [1], it is important to stress that for all real materials, a careful broadband experimental characterization will showcase frequency dependence in all material properties and ought to be taken into account for material-specific studies. Since we do not have easily accessible experimental data, here we will proceed with this assumption and analyze the behaviour resulting from different values of the relevant parameters. We want to observe how the phase speed/attenuation of the modes of propagation can vary according to these parameters and relate the results to those obtained above with local VE.

In Figure 4, we illustrate these effects by plotting the phase speed/attenuation for a particular example with parameters for Material 2

$$\text{a)}\quad \bar{E}_0/\bar{E}_\infty = 1.12, \quad \nu_2 = 0.346 \qquad \text{b)}\quad \nu_2 = 0.346, \quad \omega t_r \in [0.01, 50] \qquad \text{with 10 kHz}, \tag{3.11}$$

together with those for water (Material 1) in Table 1, where we have based the parameters around the PVC sample from Table 1 and assumed that they correspond to the rubbery phase of the material, such that $\bar{E}_\infty = 4.43$ GPa. In Fig 4a) we observe the phase speed and attenuation as a function of the relaxation time covering the range $\omega t_r \in [0.01, 50]$. We note an expected increase in velocity as the material transitions from rubbery to glassy, as well as a notable global maximum in attenuation close to $\omega t_r = 1$ (although not exactly due to the square root of the elastic moduli appearing in the wavenumbers). In order to obtain the value of this maximum with the KVM used above at 10 kHz, the shear viscosity coefficient of PVC in Table 1 would become as large as $\bar{\eta}_{\mu_2} = 1500$ Pa·s, illustrating the large differences between the SLSM and KV formulations. In Fig 4b) we provide the maximum phase speed difference (which given our parameters from (3.11) is given by max $\Delta\bar{v} = \bar{v}_{\omega t_r = 50} - \bar{v}_{\omega t_r = 0.01}$) as well as the maximum value of attenuation for different ratios $\bar{E}_0/\bar{E}_\infty$. As expected, as this ratio increases the effects observed in Fig 4a) become largely enhanced, noting the larger difference in the attenuation maximum between the body waves and the Sc solution.

These preliminary results illustrate the importance of the Deborah number and equivalently the frequency of operation and approximate relaxation time of the material in question which can cover several orders of magnitude e.g. for polyurethane (PU) it can vary between $10 - 10^3$ (sec) [38], and therefore these effects would only be noticeable at extremely low frequencies. At higher frequencies (due to the small dispersion of the Sc mode in this regime, e.g. Fig 3c), [13]) for fixed material parameters, the behaviour resembles the situation in Fig 4a) with the $x$ axis scaled accordingly.

So far we have only discussed these effects for the Sc mode (and body waves) since, as we saw above the PVC material from Table 1 could not support LR modes when in contact with water.

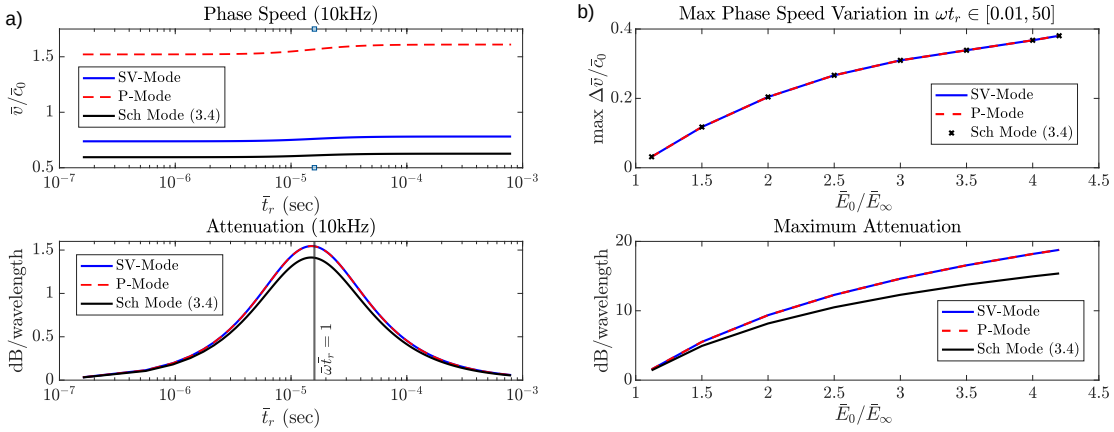


Figure 4: a) Relative phase speed/attenuation of the body and Sc modes following the SLSM at varying relaxation times. b) Maximum phase speed difference and maximum attenuation of the body and Sc modes following the SLSM for increasing values of the ratio $\bar{E}_0/\bar{E}_\infty$. Parameters are specified in (3.11). Note that the maximum attenuation in a) does not occur exactly at $\omega t_r = 1$, since the wavenumber is proportional to the square root of the moduli satisfying the SLSM.

Since this value is now being used as the rubbery phase of the Young's modulus, for a sufficiently large glassy phase ($\bar{E}_0$) the LR should also become a solution. We illustrate this in Figure 5 with $\bar{E}_0/\bar{E}_\infty = 4.06$, where we give a wider range of relaxation times in the glassy phase of the material, namely $\omega t_r \in [50, 5000]$. The increase in phase speed is therefore almost unnoticeable, nevertheless we can clearly see the decrease in attenuation for the various modes at higher relaxation times. As we saw in Fig 2c) for $M_{\tau=0.9}$, the LR mode has a much higher attenuation due to energy radiation, so a separate scale is given in Fig 5 (on the right, in cyan) to represent its decrease. From a practical perspective, this also shows that stress relaxation effects can be noticed far away from glass transition, especially the larger the ratio $\bar{E}_0/\bar{E}_\infty$ becomes.

It is worth remarking that the dispersive behaviour illustrated in Figures 4, 5 and discussed above requires a viscoelastic model that captures stress relaxation such as the SLSM employed here, as opposed to e.g. the standard KVM discussed earlier. Naturally, by using measurements to develop a frequency dissipation coefficient $\bar{\eta}_\mu(\bar{\omega})$ as employed in [13] (rather than the constant $\bar{\eta}_\mu$ in the standard KVM), the attenuative properties can be accurately predicted, however it cannot capture the changes in phase speed observed in the top figures of Fig 4a),b). Therefore, if the frequencies are sufficiently high this becomes a good approximation as seen from the top of Figure 5, but care must be taken in the lower frequency range, as discussed in e.g. [3] and [16].

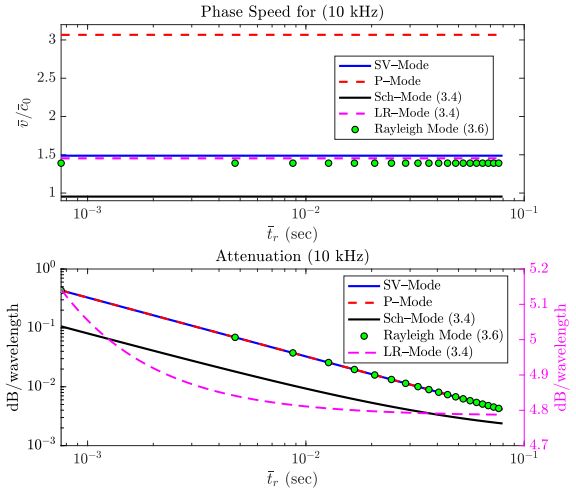


Figure 5: Relative phase speed/attenuation of various modes for the ratio $\bar{E}_0/\bar{E}_\infty = 4.06$ covering the larger range $\omega t_r \in [50, 5000]$ representing the stiffer phase of the material. The magenta $y$ axis in the lower plot corresponds to the magenta curve only (i.e. the LR Mode from DE (3.4)).

# 4 Double interface: VE waveguides/plates bounded by semi-infinite VE continua

Having analysed the acoustic surface mode solutions to the initial single interface configuration consisting of two semi-infinite half–spaces in 2D, we next consider an additional parallel interface separated from the first interface by a distance of $\bar{W} = 2\bar{L}$, as shown in the right of Figure 1. Our framework will conveniently allow us to study the dissipative mechanisms in two physically different problems under the same set of dispersion equations, namely fluid-filled channels within VE solids and fluid-loaded VE plates; analysed in Sections 4.3, 4.4 respectively. The relevant DEs are discussed shortly, but it will be convenient to first non–dimensionalise the problem.

## 4.1 Non-dimensionalisation

Unlike in the case of a single interface, in the current geometry there is a clear length scale dictated by the finite dimension of Material 1. It is therefore convenient to non–dimensionalise the relevant equations via

$$\Delta = \bar{L}^2\bar{\Delta} \quad \omega = \frac{\bar{L}\bar{\omega}}{\bar{c}_\square}, \quad \{\mathbf{u}_m, \mathbf{x}\} = \frac{1}{\bar{L}}\{\bar{\mathbf{u}}_m, \bar{\mathbf{x}}\}, \quad \{\boldsymbol{\sigma}_m, \lambda_m, \mu_m, E_m, \mathcal{Q}\} = \frac{1}{\bar{\rho}_1\bar{c}_\square^2}\{\bar{\boldsymbol{\sigma}}_m, \bar{\lambda}_m, \bar{\mu}_m, \bar{E}_m, \bar{\mathcal{Q}}\},$$

$$\rho_s = \frac{\bar{\rho}_2}{\bar{\rho}_1}, \quad \{k, k_{\phi_m}, k_{\Phi_m}, \gamma_{\phi_m}, \gamma_{\Phi_m}\} = \bar{L}\{\bar{k}, \bar{k}_{\phi_m}, \bar{k}_{\Phi_m}, \bar{\gamma}_{\Phi_m}, \bar{\gamma}_{\phi_m}\}, \quad \{c, c_{\phi_m}, c_{\Phi_m}\} = \frac{1}{\bar{c}_\square}\{\bar{c}, \bar{c}_{\phi_m}, \bar{c}_{\Phi_m}\},$$

$$t_r = \bar{c}_\square\bar{t}_r/\bar{L}, \quad \{\phi_m, \Phi_m\} = \frac{1}{\bar{L}^2}\{\bar{\phi}_m, \bar{\Phi}_m\}, \quad \{\eta_{\mu_m}, \eta_{K_m}\} = \frac{1}{\bar{\rho}_1\bar{c}_\square\bar{L}}\{\bar{\eta}_{\mu_m}, \bar{\eta}_{K_m}\},$$

where $m = 1, 2$. The (constant) sound speed ($\bar{c}_\square$) will be chosen accordingly in Sections 4.3, 4.4.

## 4.2 The generalised dispersion equations

We set up the 2D coordinate system such that the $x$ direction is aligned with the interfaces and $y = 0$ lies in the middle of Medium 1, and we therefore must ensure that the continuity of traction and displacement boundary conditions (3.3) are satisfied at $y = \pm 1$. By exploiting the symmetry of the configuration about $y = 0$, the general 8x8 system arising from the continuity BCs on each interface can be split into two independent 4x4 systems (see e.g. [18]). Indeed, *symmetric modes* require $u_x^1$, $\phi_1$ to be even functions of $y$ whereas $u_y^1$, $\Phi_1$ must be odd functions of $y$, therefore the potentials in (2.5) are given by

$$\phi_1 = \mathrm{P1_S}\cosh\left(\gamma_{\phi_1} y\right)\mathrm{e}^{\mathrm{i}kx}, \qquad \phi_2(x,y) = \begin{cases} \mathrm{P2_S}\mathrm{e}^{\gamma_{\phi_2}(y+1)+\mathrm{i}kx}, & y \le -1 \\ \mathrm{P2_S}\mathrm{e}^{-\gamma_{\phi_2}(y-1)+\mathrm{i}kx}, & y \ge 1 \end{cases}, \tag{4.1a}$$

$$\Phi_1 = \mathrm{S1_S}\sinh\left(\gamma_{\Phi_1} y\right)\mathrm{e}^{\mathrm{i}kx}, \qquad \Phi_2(x,y) = \begin{cases} \mathrm{S2_S}\mathrm{e}^{\gamma_{\Phi_2}(y+1)+\mathrm{i}kx}, & y \le -1 \\ \mathrm{S2_S}\mathrm{e}^{-\gamma_{\Phi_2}(y-1)+\mathrm{i}kx}, & y \ge 1 \end{cases}, \tag{4.1b}$$

for some complex valued amplitudes $\mathrm{P1_S}, \mathrm{P2_S}, \mathrm{S1_S}, \mathrm{S2_S}$. Given (4.1), it can be shown that symmetric modes are given by solutions to

$$\begin{aligned} &c^4\left((1-\rho_s)^2\tanh\left(\gamma_{\Phi_1}\right) - A_1\rho_s\tanh\left(\gamma_{\phi_1}\right)\left(B_2\tanh\left(\gamma_{\Phi_1}\right) + B_1\rho_s\right) - A_2B_2\tanh\left(\gamma_{\Phi_1}\right) - A_2B_1\rho_s\right) \\ &+ 2c^2\mathcal{Q}\left(-\rho_s A_1B_1\tanh\left(\gamma_{\phi_1}\right) + \left(A_2B_2 - 1 + \rho_s\right)\tanh\left(\gamma_{\Phi_1}\right)\right) \\ &+ \mathcal{Q}^2\left(A_1B_1\tanh\left(\gamma_{\phi_1}\right) - \tanh\left(\gamma_{\Phi_1}\right)\right)\left(A_2B_2 - 1\right) = 0, \end{aligned} \tag{4.2}$$

which was derived in Mathematica, recalling that the quantities $A_1, A_2, B_1, B_2, \mathcal{Q}$ are defined in (3.5) (and noting the non-dimensionalisation above). Conversely, *anti–symmetric modes* require $u_x^1$, $\phi_1$ to be odd functions of $y$ and $u_y^1$, $\Phi_1$ to be even, such that

$$\phi_1 = \mathrm{P1_A}\sinh\left(\gamma_{\phi_1} y\right)\mathrm{e}^{\mathrm{i}kx}, \qquad \phi_2(x,y) = \begin{cases} -\mathrm{P2_A}\mathrm{e}^{\gamma_{\phi_2}(y+1)+\mathrm{i}kx}, & y \le -1 \\ \mathrm{P2_A}\mathrm{e}^{-\gamma_{\phi_2}(y-1)+\mathrm{i}kx}, & y \ge 1 \end{cases}, \tag{4.3a}$$

$$\Phi_1 = \mathrm{S1_A}\cosh\left(\gamma_{\Phi_1} y\right)\mathrm{e}^{\mathrm{i}kx}, \qquad \Phi_2(x,y) = \begin{cases} \mathrm{S2_A}\mathrm{e}^{\gamma_{\Phi_2}(y+1)+\mathrm{i}kx}, & y \le -1 \\ \mathrm{S2_A}\mathrm{e}^{-\gamma_{\Phi_2}(y-1)+\mathrm{i}kx}, & y \ge 1 \end{cases}, \tag{4.3b}$$

for complex valued amplitudes $\mathrm{P1_A}, \mathrm{P2_A}, \mathrm{S1_A}, \mathrm{S2_A}$. Similarly, given (4.3) it can be shown that anti–symmetric modes are given by solutions to

$$\begin{aligned} &c^4\left((1-\rho_s)^2\tanh\left(\gamma_{\phi_1}\right) - B_1\rho_s\tanh\left(\gamma_{\Phi_1}\right)\left(A_2\tanh\left(\gamma_{\phi_1}\right) + A_1\rho_s\right) - A_2B_2\tanh\left(\gamma_{\phi_1}\right) - A_1B_2\rho_s\right) \\ &+ 2c^2\mathcal{Q}\left(-\rho_s A_1B_1\tanh\left(\gamma_{\Phi_1}\right) + \left(A_2B_2 - 1 + \rho_s\right)\tanh\left(\gamma_{\phi_1}\right)\right) \\ &+ \mathcal{Q}^2\left(A_1B_1\tanh\left(\gamma_{\Phi_1}\right) - \tanh\left(\gamma_{\phi_1}\right)\right)\left(A_2B_2 - 1\right) = 0, \end{aligned} \tag{4.4}$$

and it is straightforward to check that in the short–wavelength limit $\gamma_{\phi_1}, \gamma_{\Phi_1} \gg 1$ both (4.2), (4.4) recover the Stoneley DE (3.4) (since in this limit there is no distinction between symmetric and anti–symmetric motion). This natural geometric consequence will allow us to use the knowledge of the two semi–infinite half–space configuration discussed in Section 3 in order to obtain the initial behaviour within the slit/plate. Having obtained the general dispersion equations for natural modes of interest (4.2), (4.4), we will next focus on the analysis of the two distinct limits of physical interest here.

## 4.3 Fluid–filled channels within semi–infinite VE solids

As aforementioned, the effects of visco-thermal boundary layers and FSI in narrow water/air–filled slits were examined in [2]. In the FSI analysis, the discussion was focused on steel, which given the discussion above constitutes a hard solid when in contact with water (for air, in all cases FSI effects were negligible). In this section, we explore the differences arising when soft VE media are instead considered.

Following [2], the analysis below is focused only on the lowest order symmetric mode, so that here we will only be considering the roots of (4.2). The rationale employed in [2] was that this was sensible since for an inviscid fluid with rigid BCs it is the only propagating mode at our region of interest; namely thin channel widths/low frequencies. Of course, FSI effects arising from the consideration of solid VE media in contact with water are such that the rigid BC does not apply, and the current situation is far from this idealized scenario, especially for soft media. Nevertheless, the main objective of this section is to extend the results presented in [2] by including the effects of VE losses within the (infinite) solid bounding the fluid, together with the previously considered boundary layer effects.

As we will see shortly, the mode in consideration is in fact strongly related to the Sc mode from Section 3.3.2, which becomes coupled in the slit region as the thickness decreases (with respect to the transverse wavelength). For this reason we are essentially studying the 'coupled duct–Scholte mode' including viscosity. On the other hand, unlike for the half–space, geometrical confinement implies that LR waves cannot radiate energy away from the interfaces and hence propagate plane-wave like with little attenuation along the channel. Therefore, as opposed to the coupled duct–Scholte mode, they are only expected to propagate in sufficiently wide channels.

Given the non–dimesionalisation in Section 4.1, in this Section we let $\bar{c}_\square \equiv \bar{c}_0 = 1490$ m/s i.e. we choose the adiabatic speed of sound in water at 10 degrees Celsius and $\bar{\rho}_1 = 1000$ kg/m$^3$ (following Table 1). With regards to the choice of VE frequency dependence, we will follow a similar structure to Section 3 for the single interface: first we assume the KVM for the solid according to Table 1, and then we consider the SLSM in Section 4.3.3.

### 4.3.1 Phase speed and attenuation

In order to find the roots of (4.2) using *fsolve*, we make use of an iterative numerical scheme, whose starting point is dictated by the solutions to the Stoneley DE (3.4), corresponding to the wide channel limit, as noted just below (4.4). We subsequently gradually reduce the channel widths up to the values of interest, by using the root found for the prior larger value of $\bar{W}$ as a new starting point for *fsolve*. In Figure 6 we observe the phase speed/attenuation as a function of channel width in terms of $\bar{\delta}_s/\bar{W}$ at 10 kHz for a) water–steel and b) water–PVC. We directly observe the difference in phase speed between the hard/soft solids at wide channel widths. In particular, the mode in water–PVC is highly subsonic, as we observed in Fig 3c) for the half–space Sc mode. More generally, it is clear that FSI effects in both materials dramatically reduce the phase speed along the channel as opposed to the rigid case. For further comparisons we give additional curves that neglect particular physical effects. In particular, for the inviscid fluid we assume medium 1 is s.t. $\mu_1(\omega) \to 0$, implying that $k_{\Phi_1}^2 \to \infty$ and hence $\gamma_{\Phi_1}, B_1 \to \infty$ whereas $\mathcal{Q} \to -2\rho_s c_{\Phi_2}^2$ and (4.2) simplifies to

$$\tanh(\gamma_{\phi_1})\left[(2k^2 - k_{\Phi_2}^2)^2 - 4k^2\gamma_{\phi_2}\gamma_{\Phi_2}\right] + \frac{\gamma_{\phi_2}k_{\Phi_2}^4}{\gamma_{\phi_1}\rho_s} = 0, \tag{4.5}$$

noting the similarity with the limit taken to lead from the Stoneley DE (3.4) to the Scholte DE (3.7) in the half–space configuration. Equation (4.5) is identical to equation (72) in [2] except here in

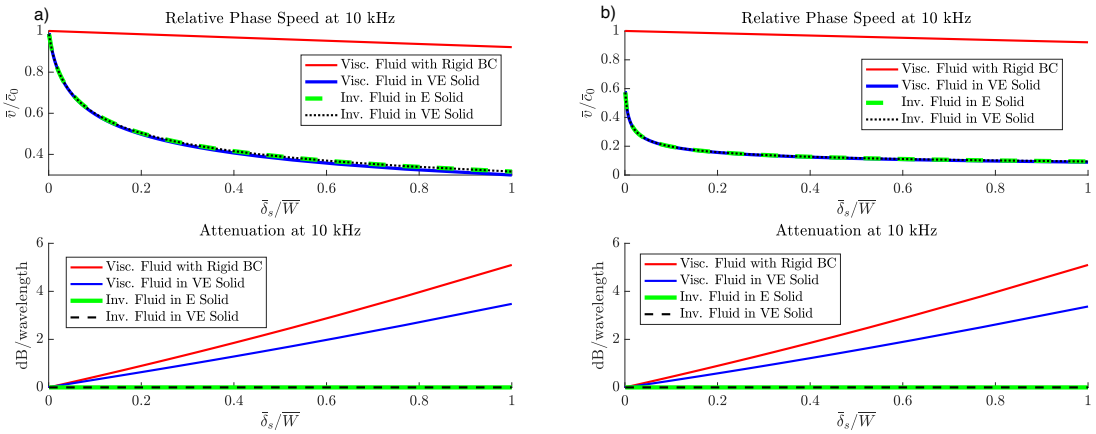


Figure 6: Phase Speed/Attenuation at 10 kHz for water–filled channels of decreasing width within: a) Steel, and b) PVC, according to the KVM with material properties in Table 1. In particular, we note the large difference in the initial value of the phase speed between a) and b) which is dictated by the Stoneley DE (3.4).

the parameters for medium 2 we are including frequency dependence (except for the green curves in Figures 6, 7 where we further let $\eta_{\mu_2}, \eta_{K_2} \equiv 0$ in the solid.). Nevertheless, these VE effects in either solid are not directly observable from Fig 6, and the attenuation is indeed due to the boundary layers in water. Note that this is expected for steel at these frequencies due to its negligible viscosity, but less so for PVC (Table 1). When performing similar calculations at higher frequencies, we find that the phase speed values for most (fixed) channel widths become larger, whilst the attenuation remains fairly constant. This is shown explicitly for water–PVC in Figure 7a) for the particular case when $\bar{\delta}_s/\bar{W} = 0.5$, noting that a similar frequency dependence is obtained for steel in [2]. Dispersion in attenuation can nevertheless be seen when a higher coefficient of viscosity is employed, as illustrated in Figure 7b) where we used $\bar{\eta}_{\mu_2} = 10$ Pa·s, although it has no effect on the relative phase speed. Finally, following our initial discussion above, we can only observe the coupled LR–duct mode for water–steel at 10 kHz up to $\bar{\delta}_s/\bar{W} \approx 0.03$; for thinner channels it becomes cut-off (not shown).

### 4.3.2 Displacement fields

The particle motion of the mode under consideration for a water–steel interface was studied in detail in [2]. Here we simply want to illustrate whether any significant changes occur when steel is replaced by a softer medium. In Figure 8 we give direct comparisons between steel/PVC of the horizontal displacement $\mathrm{Re}\{u_x\}$ for a wide channel, represented by $\bar{W} = 70\bar{\delta}_s$. The behaviour in the fluid region, Fig 8a),b) is rather similar between the two interfaces, noting that the boundary layer region is well approximated by Stokes's boundary layer $\bar{\delta}_s/\bar{L}$. Nevertheless, in Fig 8a) we also observe a slight decay from the boundary region towards the centre of the channel for PVC which is not observed in steel. We observe (not shown) that this feature becomes increasingly noticeable at wider channel widths. This is nevertheless expected, since as the channel width becomes larger, the solution begins to resemble that of the half–space Sc mode localized in each boundary, and as we observed above the decay length in the fluid is much longer for hard solids (Fig 3d)) than it is for softer media (Fig 3a)). On the other hand, in the solid region Fig 8c), we see a large difference between the motion in PVC and steel, with the displacement of the former being more than an

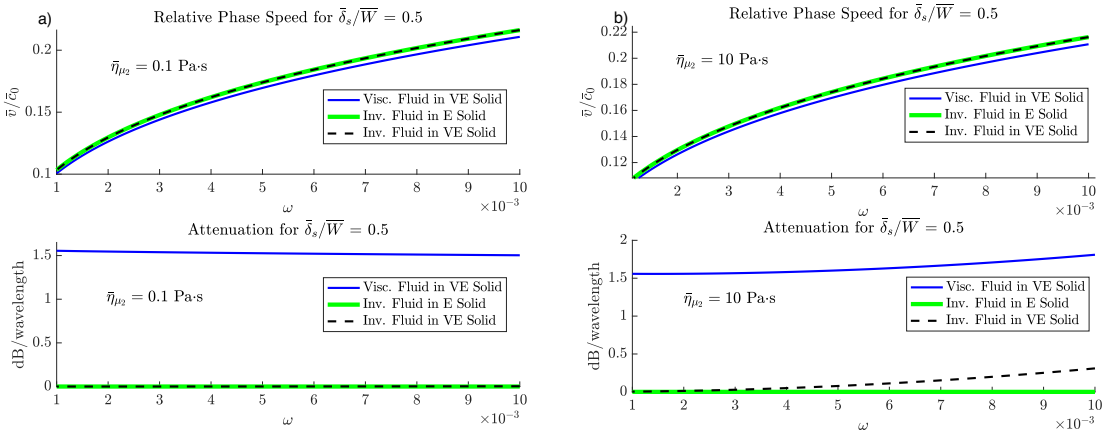


Figure 7: Relative phase speed/attenuation at fixed channel width $\bar{\delta}_s/\bar{W} = 0.5$ for increasing frequency in a water–filled PVC channel following the KVM for: a) Shear PVC viscosity coefficient $\eta_{\mu_2}$ from Table 1, b) Larger shear PVC viscosity coefficient. In a) we observe dispersion in phase speed, but not in attenuation, whereas in b) we observe an additional VE frequency dependence in attenuation.

order of magnitude larger than the latter at the interface $y = \pm 1$. Nevertheless, this motion still decays rapidly within the solid which is expected since we observed in Figure 6b) that there was no damping due to radiation loss in the form of elastic waves through the interfaces into the solid. At narrower channel widths (not shown) the motion at the interface with the solid region becomes increasingly reduced, although the difference between hard/solid can still be appreciated.

### 4.3.3 Additional frequency dependence: Influence of stress relaxation

As was done for the half–space, we now want to see whether the inclusion of stress relaxation effects via the SLSM in the "host" solid medium can alter the phase speed/attenuation of the Sc–duct mode in consideration. We observed in Figure 7 how when employing the KVM with sufficiently high viscosity coefficient, the attenuation increases (unboundedly) with $\omega$, but this has no effect on the corresponding relative phase speed. We will follow the assumptions from Section 3.3.3 and assume a constant Poisson's ratio and let the Young's modulus (of Medium 2) obey the SLSM as in (3.10), noting that under the current non-dimensionalization the relaxation time is given by $t_r = \bar{c}_0 \bar{t}_r / \bar{L}$.

For the illustrations, again we assume that the rubbery phase of the PVC material corresponds to the value given in Table 1, so that $\bar{E}_\infty = 4.43$ GPa. In Figure 9 we give the phase speed/attenuation at various frequencies and channel widths as a function of relaxation time $t_r$, chosen in each case so that the range $\omega t_r \in [0.01, 50]$ is covered, and therefore the glass transition of the material is showcased. The qualitative behaviour is therefore very similar within Figures 9a)–d), where we note the increasing phase speeds as the material becomes glassier, and the global maximum attenuation near $\omega t_r = 1$, as we saw in Figure 4a) for the half–space. Nevertheless, in this case there are significant changes in the relevant values when the main parameters vary, following what we saw in Figures 6, 7. That is, with higher frequencies (smaller channel widths) we observe overall higher values in phase speed, and the effect of the fluid's viscosity becomes particularly relevant at narrower channel widths. Furthermore, as we observed for the half–space in Figure 4b), the larger the ratio

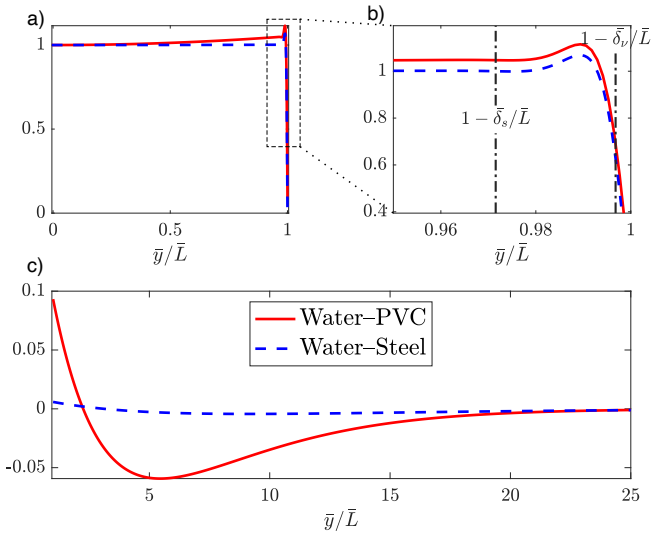


Figure 8: Real part of the horizontal displacement fields $\mathrm{Re}\{u_x(x=0,y)\}$ for the lowest order symmetric mode propagating in a viscous water–filled channel at 10 kHz within steel/PVC, for a channel width of $\bar{W}=70\bar{\delta}_s$. a) represents the fluid region $0\leq\bar{y}\leq\bar{L}$, b) the fluid behaviour near the boundary, and c) the solid region $\bar{L}\leq\bar{y}\leq 25\bar{L}$. In each case the plots have been normalized such that $u_x(y=x=0)=1$.

$\bar{E}_0/\bar{E}_\infty$ gets, the larger the maximum phase speed variation and maximum attenuation becomes.

In Figure 10 we give similar plots to those in Figs 6, 7 for various fixed relaxation times. In Figure 10a) the chosen $t_r$ are such that $\omega t_r=0.1,1,50$ at the initial value of frequency, so that at this (initial) frequency we are covering the rubbery/glassy phases and glass transition. As a result, we observe how as frequency increases the attenuation of the initially rubbery phase ($t_r=100$) undergoes glass transition, whereas naturally in the two other cases ($t_r=1000,50000$) an increase of frequency results in a reduction of attenuation (per wavelength). From Figure 10b) we observe how the initial phase speed is higher in the glassy phase, and particularly how with $\omega t_r$ fixed, VE relaxation effects together with boundary layers can lead to a significant increase in attenuation (compared to e.g. Fig 6b)). Note that the small decrease in attenuation observed for wide channels in Fig 10b) occurs since we are plotting attenuation per wavelength (following (3.8b)) and is therefore caused due to the sharp decrease in phase speed observed in this region. Moreover, it is physically useful to also have an idea of this quantity along a fixed distance. In Figure 11 we plot attenuation per unit metre (given by $20\,\mathrm{Im}(\bar{k})\log_{10}(\mathrm{e})$) as a function of channel width, and give differences between the viscous/inviscid fluid cases from (4.2), (4.5) respectively at different values of the Deborah number. In particular, we observe how for narrower slits, the large reduction in phase speed observed above results in shorter wavelengths and consequently higher attenuation per unit metre.

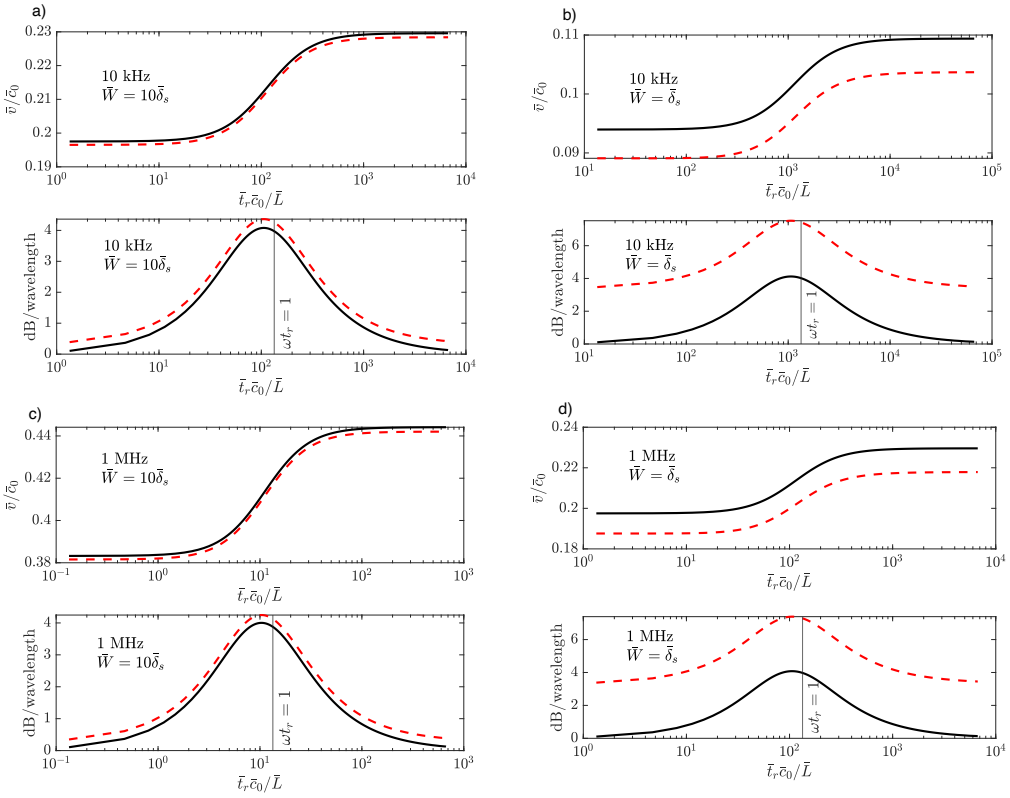


Figure 9: Relative phase speed/attenuation in a water–filled PVC slit obeying the SLSM, as a function of non-dimensional relaxation time $t_r$ for various channel widths and frequencies. The red–dashed curve represents viscous water given by (4.2), whereas the black curve is for inviscid water and is therefore a solution to (4.5). In all cases we have $\bar{E}_0/\bar{E}_\infty = 1.58$, and the relaxation times chosen cover the range $\omega t_r \in [0.01, 50]$.

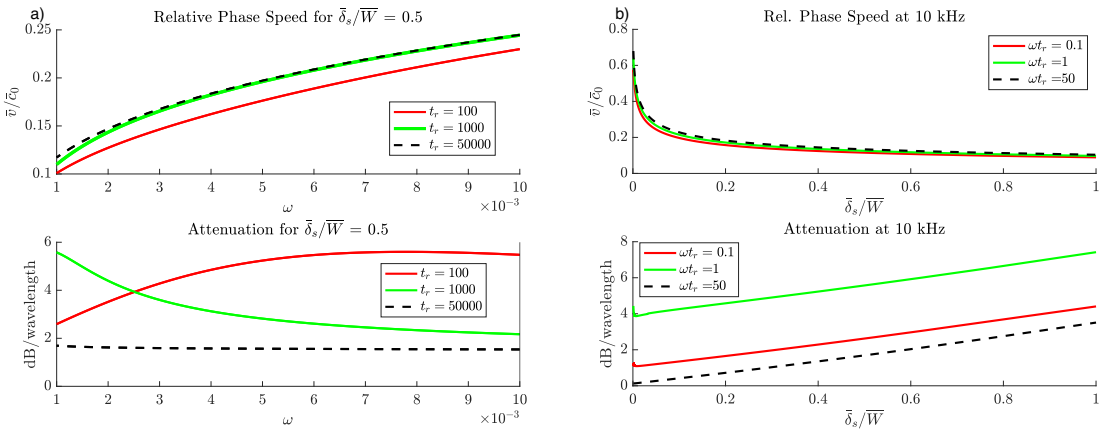


Figure 10: Relative phase speed/attenuation in a (viscous) water–filled PVC slit obeying the SLSM, with $\bar{E}_0/\bar{E}_\infty = 1.58$: a) as a function of frequency for a fixed channel width of $\bar{\delta}_s/\overline{W} = 0.5$, b) as a function of channel width with dimensional frequency 10 kHz. In each case the relaxation times have been chosen to represent the differences between the glassy/rubbery phases of the solid medium, noting the differences in attenuation in a) for the smaller relaxation times as the frequency increases.

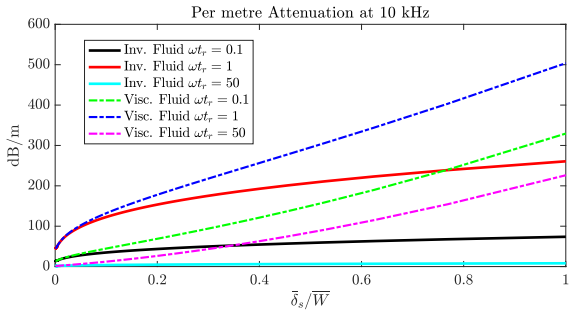


Figure 11: Attenuation per unit metre in a water–filled PVC slit obeying the SLSM, with $\bar{E}_0/\bar{E}_\infty = 1.58$. In each case the relaxation times have been chosen to represent the differences between the glassy/rubbery phases of the solid medium. Viscous (Visc.) fluid solutions are obtained from (4.2), whereas the inviscid (Inv.) fluid solutions are from (4.5).

## 4.4 Limit B): VE plates loaded with viscous fluids

We now want to explore the reciprocal situation to that above. Medium 1 in the right of Figure 1 corresponds to a solid and Medium 2 becomes a fluid (water), so that we have fluid-loaded plates. Much like for the half–space, in certain scenarios (hard interfaces) the fluid loading simply acts as a small perturbation to the traditional Lamb DEs for natural modes on a plate in vacuum (i.e. stress–free). In these cases the consideration of fluid loading causes the (pure) Lamb mode solutions to become leaky as some of their energy gets shed via radiation of acoustic waves in the fluid, and therefore the resulting modes are commonly addressed as 'Leaky–Lamb' modes in the literature, which have been widely studied including the effect of boundary layer losses e.g. [20, 22, 39].

However, the presence of Material 2 (here a fluid) gives rise to an additional set of solutions of a similar nature to the half–space Scholte–Stoneley addressed in Section 3.3.2. Naturally, the difference here is that for thin plates (compared to wavelength) these Sc type surface modes become interacting within the plate region and form two coupled interface modes, which are therefore the symmetric/anti–symmetric 'coupled plate–Scholte' modes, which we will refer to as 'coupled–Scholte' for brevity following [3]. For hard fluid–plate interfaces, the symmetric mode is often ignored since it is non–dispersive and lies on top of the sound line, and therefore the term 'quasi–Scholte' mode is often found in the literature to refer only to the anti–symmetric (e.g. [23]). The situation is nevertheless very different for soft interfaces, and in particular the symmetric coupled Sc can become highly dispersive, deviating from the Sc and fluid velocities, as recently confirmed experimentally in [3].

Following the same structure that we have employed in the preceding sections, here we want to emphasise the extra physical insights that our framework provides for the behaviour of coupled Sc modes. That is, the effects of the viscous boundary layers on either side of the plate as well as the VE of the plate itself, particularly when stress relaxation is considered.

Given the non–dimensionalisation in Section 4.1, in this limit we let $\bar{c}_\square \equiv \bar{c}_s$ i.e. we choose the lossless shear speed of sound in each solid material as appropriate (for steel $\bar{c}_s = 3000$ m/s, and for PVC $\bar{c}_s = 1100$ m/s) and similarly for the mass density (for steel $\bar{\rho}_1 = 7871$ kg/m$^3$, and for PVC $\bar{\rho}_1 = 1360$ kg/m$^3$). With regards to the choice of VE frequency dependence, we will follow a similar structure to what was done in the preceding sections: first we assume the KVM for the solid according to Table 1, and then we consider the SLSM in Section 4.4.3.

### 4.4.1 Phase speed and attenuation

By the equivalence of the DEs in consideration, in order to find the roots of (4.2), (4.4) using *fsolve*, we can make use of the same iterative procedure used for the slit, as explained in Section 4.3.1 so that the initial value in the thick plate limit relies on the roots of (3.4). As we have been doing thus far, in order to study the influence of the fluid viscosity, it is convenient to consider the inviscid limit such that $\mu_2(\omega) \to 0$, from which it follows that $k_{\Phi_2}^2 \to \infty$ and hence $\gamma_{\Phi_2}, B_2 \to \infty$ whereas $\mathcal{Q} \to 2c_{\Phi_1}^2$ so that (4.2), (4.4) become

$$\left[\left(2k^2 - k_{\Phi_1}^2\right)^2 \coth\left(\gamma_{\phi_1}\right) - 4k^2\gamma_{\phi_1}\gamma_{\Phi_1}\coth\left(\gamma_{\Phi_1}\right)\right] + \rho_s \frac{\gamma_{\phi_1} k_{\Phi_1}^4}{\gamma_{\phi_2}} = 0, \tag{4.6a}$$

$$\left[\left(2k^2 - k_{\Phi_1}^2\right)^2 \tanh\left(\gamma_{\phi_1}\right) - 4k^2\gamma_{\phi_1}\gamma_{\Phi_1}\tanh\left(\gamma_{\Phi_1}\right)\right] + \rho_s \frac{\gamma_{\phi_1} k_{\Phi_1}^4}{\gamma_{\phi_2}} = 0. \tag{4.6b}$$

for symmetric and anti–symmetric modes respectively, which we will both be considering in this section. From (4.6), we observe explicitly that the terms in square brackets correspond to the

classical Lamb DEs for modes on a free plate (in the absence of any loading $\rho_s = 0$), where the VE effects are captured through the frequency varying material parameters. The role of the density ratio $\rho_s$ is analogous to (3.7) for the half–space. For $\rho_s \ll 1$ we can see why (4.6) can be treated as a small perturbation to the stress–free Lamb DEs [40], nevertheless as the fluid density approaches that of the solid $\rho_s \to 1$, the similarities between the spectra can disappear completely [39].

In Figure 12 we give the relative phase speed/attenuation as a function of the plate thickness in terms of $\bar{\delta}_s/\bar{W}$ at 10 kHz for water–steel (a), and water–PVC (b). In both cases we observe how in the thin plate limit (low frequency) the anti–symmetric mode tends to zero, whereas the symmetric mode tends to the fluid's sound speed. Conversely in the thick plate limit (high frequency) the two curves converge to the Stoneley–Scholte value. These observations are in agreement with the analysis in [18] and the dispersion curves in [3]. In terms of attenuation, we first notice the significantly smaller magnitude compared to those in the slit e.g. Figure 6, which is expected, since here the boundary layers are located on either side exterior to the plate, and are therefore never interacting (which is the regime with major viscous losses as observed in the preceding section). It is also apparent from the low attenuation values that VE effects with the values given in Table 1 have a negligible impact. Given this, we nevertheless observe how the viscous boundary layer increases the attenuation of the anti–symmetric mode as the plate becomes very thin in both cases. Interestingly, this effect does not occur for the symmetric mode but instead we can observe a local maximum for water–PVC Figure 12b) around $\bar{\delta}_s/\bar{W} \approx 10^{-3}$ which occurs close to (but not exactly) the inflection point observed in the mode's phase speed, but is not observed for steel since the symmetric mode remains constant Figure 12a). In order to further analyse the dispersion of these modes, in Figure 13 we give an equivalent plot but instead at 100 kHz (so that the non-dimensional frequency $\omega$ is increased by an order of magnitude) and superimpose some of the relevant results from Figure 12. We observe how this results in the separation of the phase speeds (between the symmetric and anti–symmetric modes) at thinner plate thicknesses and correspondingly so does the maximum attenuation of the viscous symmetric mode for PVC in Fig 13b) which also increases slightly in magnitude. In general we observe that the inviscid fluid solutions obtained from (4.6) have an excellent agreement in phase speed with the full viscous solutions, but naturally cannot predict the attenuation due to the boundary layers.

### 4.4.2 Displacement fields

The energy density associated with the coupled Sc mode for hard/soft plates of various thicknesses was analysed respectively in [23, 3], so here we will focus on the mode's displacement fields. In Figure 14 we show heatmaps of (the real part of) the horizontal/vertical particle displacements fields for the symmetric coupled Sc mode in a PVC plate (Table 1) loaded with water at 10 kHz for a plate thickness of $\bar{\delta}_s/\bar{W} = 10^{-3}$ (see Figure 12b) for reference). From the colorbars we note that the predominant motion is actually parallel to the interface (Figure 14a)) with significant motion coupled in both the plate and near the interface in the fluid. The anti–symmetric mode is given in Figure 15, noting that in this case the magnitude of the motion is much more distributed in both directions with the predominant motion in the plate being perpendicular to the interface, which is expected due to the 'bending' nature of the anti–symmetric mode.

In Figure 16 we give direct comparisons of (the absolute value of) the particle displacements from Figs 14, 15 for $y \geq 0$ evaluated at $x = 0$ together with the equivalent results of a steel water-loaded plate. From Fig 16a) we first observe how indeed for the symmetric mode the parallel (to the interface) particle displacement is dominant over the perpendicular. For PVC we observe a fast decay within the fluid region, whereas the situation is very different for water–steel, where the majority of the motion (hence energy) lies in the fluid region with no decay observed. This

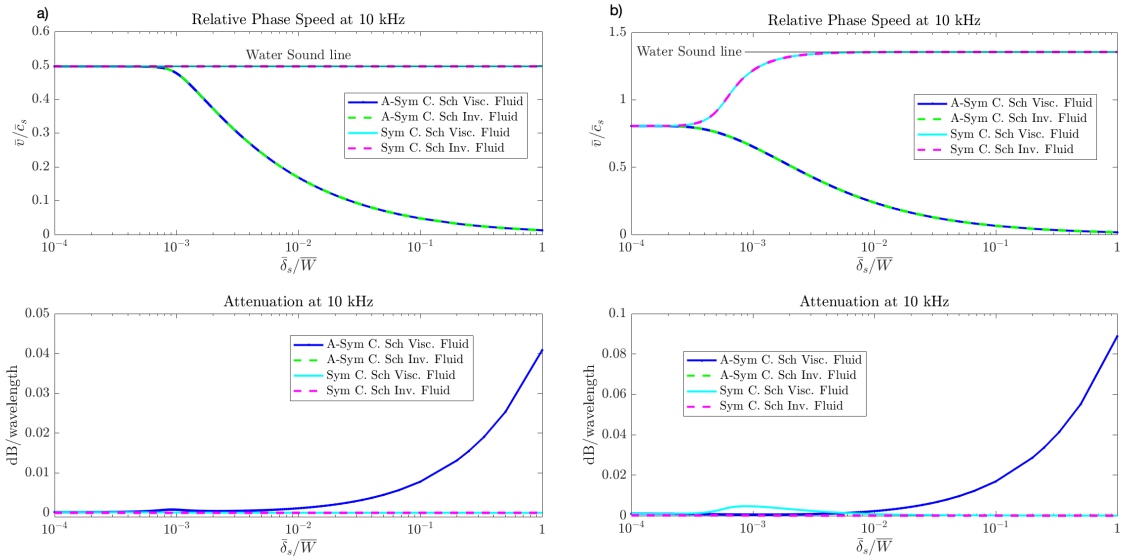


Figure 12: Relative phase speed/attenuation at 10 kHz for coupled Sc modes in water-loaded VE solid plates of decreasing width for: a) Steel, and b) PVC, whose material properties are in Table 1. The initial values (thick plate limit) are dictated by the Stoneley DE (3.4) and therefore the initial phase speeds are equivalent to those in Figure 6 (noting the change in non-dimensionalisation).

situation is in agreement with the half–space observations e.g. Figure 3, where we essentially have compressional waves at grazing incidence in the fluid region travelling at the sound speed (Fig 12a)), with little coupling in the plate region. A fairly similar situation is observed for the anti–symmetric mode Fig 16b) in water–PVC, noting the more rapid decay of the motion, whereas for water–steel we again observe a significantly larger magnitude of the horizontal particle displacement in the fluid region, although its decay is nevertheless noticed, in agreement with [23]. Note that the apparent discontinuities for $u_x$ at the plate interface $\bar{y} = \bar{L}$ are simply due to the extremely thin boundary layer regions (as in Fig 8a)) with the chosen parameters ($\bar{\delta}_s/\bar{W} = 10^{-3}$ at 10 kHz) which make them not visible at the provided $y$ scale.

### 4.4.3 Influence of stress relaxation

Finally, we want to pay attention to the effect of stress relaxation on the soft plate and observe the corresponding effects on the phase speed/attenuation of the coupled Scholte mode. As we have done in Sections 3.3.3, 4.3.3 we proceed by letting the Young's modulus of the plate $E_1(\omega)$ follow the SLSM whilst its Poisson's ratio $\nu_1$ remains constant, as in (3.10) (with subscripts in the moduli interchanged from '2' to '1') noting that $t_r = \bar{c}_s \bar{t}_r/\bar{L}$. In the illustrations below we also let $\bar{E}_\infty = 4.43$ GPa so that the rubbery phase limit of the PVC material corresponds to the (fixed) value from Table 1 (as we have did for the slits in Section 4.3.3).

In Figure 17 we give the phase speed/attenuation of the symmetric and anti–symmetric coupled Sc mode as a function of plate thickness (as in Fig 12) with fixed Deborah numbers $\omega t_r = 0.1, 1, 50$ so that we cover the rubbery and glassy phases, as well as glass transition. Furthermore, in this figure we have chosen a moderate value of the ratio $\bar{E}_0/\bar{E}_\infty = 1.58$, see Figure 4b). For the anti–

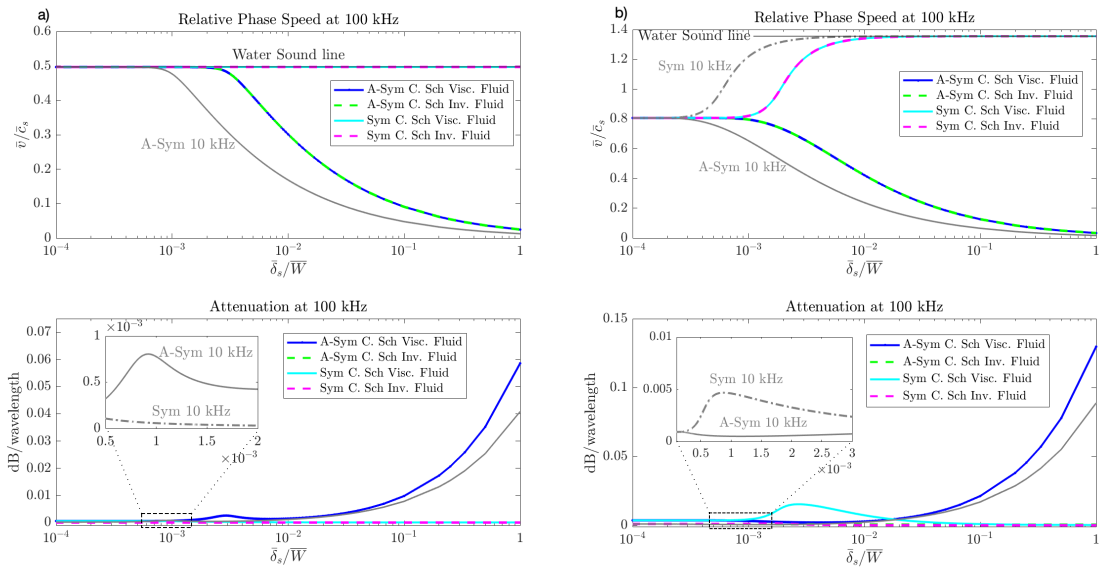


Figure 13: Relative phase speed/attenuation at 100 kHz for coupled Sc modes in water-loaded VE solid plates of decreasing width for: a) Steel, and b) PVC, whose material properties are in Table 1. The curves in grey correspond to the Sym/A-Sym Coupled Sc mode for viscous water at 10 kHz, as in Figure 12. For clarity purposes, the inset figures in attenuation only contain the grey curves. Except for the Sym mode in a), strong dispersion in phase speed is noted for most plate thicknesses in both media.

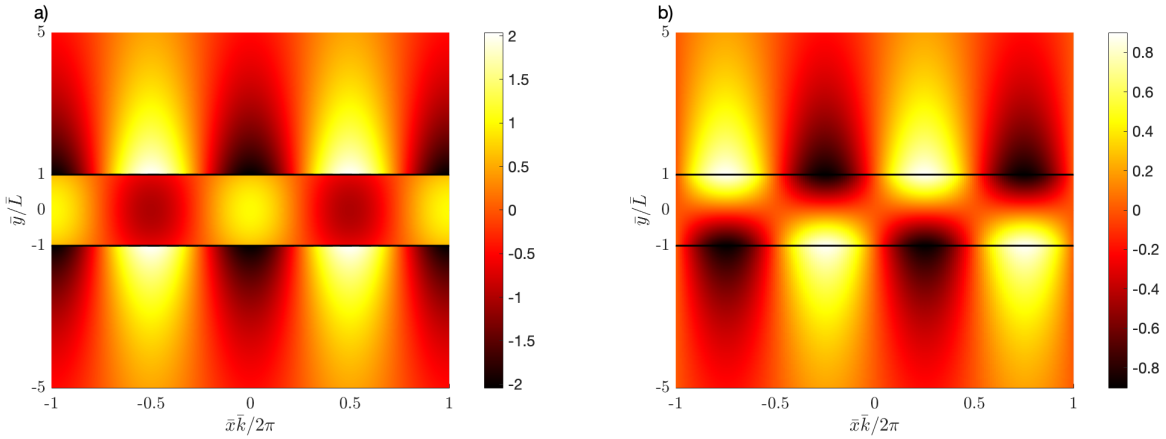


Figure 14: Real part of the displacement fields for the symmetric coupled Sc mode propagating in a PVC plate immersed in water at 10 kHz, for a plate thickness of $\bar{\delta}_s/\bar{W} = 10^{-3}$ with values from Table 1. a) represents the horizontal particle displacement $\mathrm{Re}\{u_x(x,y)\}$, and b) the vertical displacement $\mathrm{Re}\{u_y(x,y)\}$. The plots have been normalized such that $u_x(y = x = 0) = 1$, and different lengthscales are used for the $x$ and $y$ directions with the black lines representing the plate boundaries. The difference in the values of the colorbar show that the predominant motion is parallel to the interface.

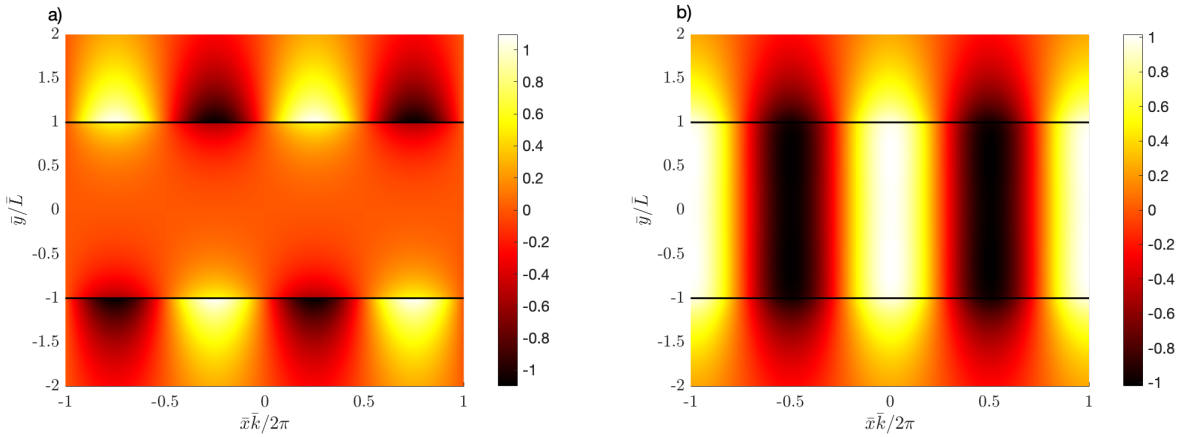


Figure 15: Real part of the displacement fields for the anti–symmetric coupled Sc mode propagating in a PVC plate immersed in water at 10 kHz , for a plate thickness of $\bar{\delta}_s/\bar{W} = 10^{-3}$ with values from Table 1. a) represents the horizontal particle displacement $\mathrm{Re}\{u_x(x,y)\}$, and b) the vertical displacement $\mathrm{Re}\{u_y(x,y)\}$. The plots have been normalized such that $u_y(y = x = 0) = 1$, and different lengthscales are used for the $x$ and $y$ directions with the black lines representing the plate boundaries.

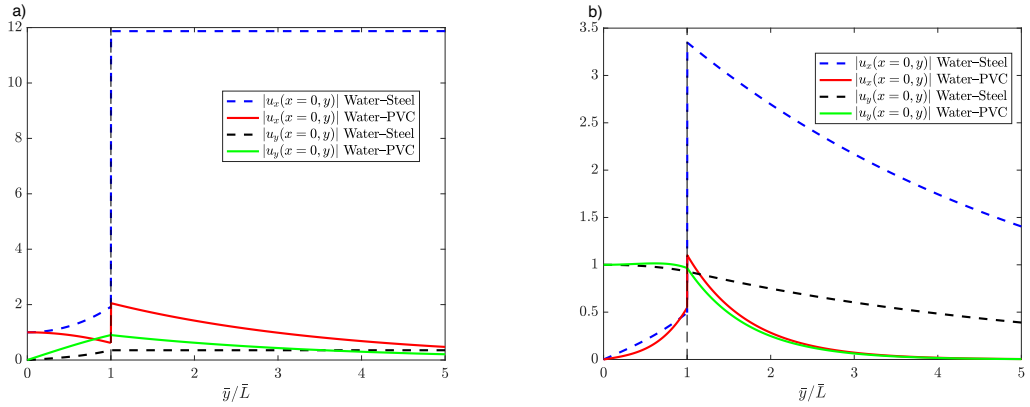


Figure 16: Comparisons between the magnitude of the components of the displacement fields of steel/PVC plates loaded with water at at 10 kHz for the sym. coupled Sc mode (a), and the anti–sym. coupled Sc mode (b) normalized in each case s.t. the displacement at the center of the plate is 1. The plate thickness is $\bar{\delta}_s/\bar{W} = 10^{-3}$ with values from Table 1. The apparent discontinuities for $u_x$ at the plate interface $y = 1$ are simply due to the thinness of the boundary layer region with the large $y$ scale employed.

symmetric mode (Figure 17a)) we observe how the initial phase speed values dictated by the Stoneley DE (3.4) become higher when the material is in the glassy phase, which then tend to zero in the thin plate limit following the observations in Figure 12. In terms of attenuation, we first observe the remarkably higher values for $\omega t_r = 0.1, 1$ (at all plate widths) when compared to the KVM results from Figure 12. For the anti–symmetric mode (Figure 17a)) we observe that the attenuation (per wavelength) approaches non-zero values (except for $\omega t_r \gg 1$) in the thin plate limit. With regards to the symmetric mode (Figure 17b)) we first note that the initial behaviour in both phase speed and attenuation is identical to that of the anti–symmetric mode following our discussion above. As the plate width decreases, the mode first enters the dispersive region and continues to asymptote towards the fluid's phase speed $\bar{v}/\bar{c}_s = 1.35$ following the observations from Figure 12. When it comes to the attenuation, the global maximum discussed above become significantly enhanced in the dispersive region (particularly for $\omega t_r \approx 1$), after which it monotonically decreases towards zero as the root approaches the fluid's (constant) bulk mode.

To our surprise, we have not been able to find discussions about this feature in the existing literature. It is worth stressing that this global maximum for the symmetric coupled Sc only arises when the mode's phase speed is dispersive which (for a fixed fluid) requires soft media, so that $\rho_s \approx 1$. For this reason we did not observe it for water-loaded steel plates in Figure 12a), which is where most of the literature has been centred [3]. Some further tests (not shown) confirmed that the inclusion of fluid viscosity has little influence on the presence of this maximum, so that solutions to (4.6) (corresponding to $\eta_{\mu_2} = 0$) accurately capture this global maximum (as expected given the little magnitude of boundary layer attenuation in Figure 12). We believe this phenomenon may be related to a critical point in the mode's group velocity, but this is yet to confirm with further analysis.

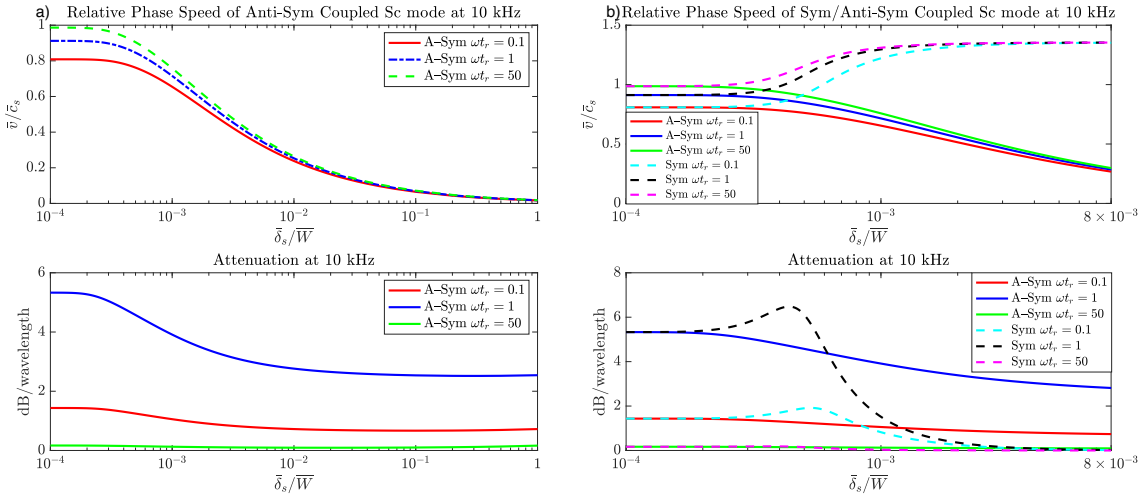


Figure 17: Relative phase speed/attenuation at 10 kHz for coupled Sc modes in water-loaded VE PVC plates of decreasing width according to the SLSM with $\bar{E}_0/\bar{E}_\infty = 1.58$, whilst keeping the Deborah number fixed (and in all cases $\bar{c}_s = 1100$ m/s). The fluid is assumed to be viscous so that all the curves correspond to roots of (4.2) and (4.4). In a) we only show the anti–symmetric mode for a very wide range of plate widths, whereas in b) we also include the symmetric mode for plate thicknesses in the region of interest. In particular, we note the enhancement of the global attenuation maxima for the symmetric mode which subsequently tends to zero as the mode becomes non-dispersive.

# 5 Conclusions

This paper has been focused around the influence of viscosity in some of the principal modes of propagation in two physical systems, namely fluid-filled slits embedded in infinite viscoelastic solids, and fluid-loaded viscoelastic plates, where the fluid considered is water. These two settings are connected by the fact that the respective waves in the short wavelength limit (with respect to channel/plate width) are governed by the same dispersion equation, namely the Scholte-Stoneley DE which was therefore analysed in detail first. Furthermore, the direct correspondence between the governing equations for visco-acoustic fluids and (visco)elasticity discussed in [1] is used in order to obtain generalised dispersion relations for symmetric and anti–symmetric modes that can govern the two specific set-ups of interest when taking the appropriate limits, which is a particularly convenient detail of this study.

For fluid–filled channels, the results are presented as an extension of an earlier work by some of the present authors, namely [2]. We firstly show how the consideration of soft media requires paying more attention to the way the roots are initially found, as a result of the Scholte mode's phase speed reduction (from the fluid sound line) in water-(soft) solid interfaces. We then emphasise how viscoelastic mechanisms in the solid can affect the overall attenuation at different frequencies and channel widths, for both the commonly used Kelvin-Voigt model (KVM) and the standard linear solid model (SLSM), which incorporates stress relaxation. It has been shown how stress relaxation can greatly affect the phase speed and attenuation of the mode, and in particular the ability to damp energy if the mode can be excited around the glass transition of the material which is characterized by a Deborah number of one, i.e. $\omega t_r = 1$.

For water-loaded viscoelastic plates, much of the work in this article has been inspired by the recent study [3], which we refer to multiple times in this paper. Utilizing the same root finding technique as for the channels, where the initial value is based on the Scholte-Stoneley DE behaviour, the dispersion of the phase speed of both the symmetric and anti–symmetric modes as a function of plate thickness is analysed, as well the associated displacement fields. We originally observe very little dissipation compared to the slit case as a result of the boundary layers being localized on the exterior sides of the plate and therefore never interacting regardless of the thinness of the plate. Nevertheless, the presence of a global maximum in the attenuation of the symmetric coupled Scholte mode is noticed for the soft solid only, indicating that it is closely linked to the dispersion in phase speed, which is not observed for hard water-solid interfaces. To the knowledge of the authors this feature has not yet been reported in the literature, and therefore we believe that it requires further analysis in order to give truly physical explanation, but some early observations are noticed. The attenuation increases significantly for both modes when stress relaxation is included in the soft plate, and in the thin-plate limit the attenuation of anti–symmetric modes tends to constant non-zero values for each $\omega t_r$, whereas the dissipation of the symmetric mode becomes zero as soon as the phase speed becomes constant. Nevertheless, the global maximum in attenuation observed previously is largely enhanced, particularly around glass transition. It is believed that this global maximum should be able to be demonstrated experimentally following the work in [3] and perhaps even be interesting to the non-destructive testing community for possible applications.

More generally, we find that although the widely used KVM (even with varying viscosity coefficient to match experimental results) can accurately predict the loss at particular frequencies as shown in e.g. [13], with such models the dispersion of the real parts of these elastic moduli (and hence phase speed of the associated modes) cannot be captured. We show this can be crucially important, particularly at frequencies near glass transition. We further note that the SLSM used here to capture stress relaxation, namely Prony series with a single relaxation time, is the simplest

model that captures long time solid-like 'glassy' behavior and generally, the VE behavior of polymers is much more complex [41, 16]. Furthermore, the relaxation results are based around a PVC sample with $\bar{E}_\infty = 4.43$ GPa, such that the half-space Scholte mode propagates at a phase speed approximately 60% of that of water and is therefore considered soft in this context, especially when compared to the steel sample analysed here, for which the Scholte mode propagates essentially at the speed of sound of water. Nevertheless, the amplitude ratio $\bar{E}_0/\bar{E}_\infty$ is well known to become particularly large for significantly softer media, although in terms of practicality this is offset by the fact that in this regime the Scholte mode is likely to be much more difficult to excite. These results motivate the need for further experimental results in the frequencies of interest in order to be able to make sure under which conditions these mechanisms can be exploited as well as relevant data for relaxation times short/large range moduli which we hope to obtain soon.

# REFERENCES

[1] E García Neefjes, D Nigro, AL Gower, RC Assier, V Pinfield, and WJ Parnell. A unified framework for linear thermo-visco-elastic wave propagation including the effects of stress relaxation. *(To be submitted)*, 2021.

[2] PA Cotterill, D Nigro, ID Abrahams, E Garcia-Neefjes, and WJ Parnell. Thermo-viscous damping of acoustic waves in narrow channels: A comparison of effects in air and water. *The Journal of the Acoustical Society of America*, 144(6):3421–3436, 2018.

[3] BM Staples, TJ Graham, AP Hibbins, and JR Sambles. Coupled Scholte modes supported by soft elastic plates in water. *Physical Review E*, 103(6):063002, 2021.

[4] GP Ward, RK Lovelock, ARJ Murray, AP Hibbins, JR Sambles, and JD Smith. Boundary-layer effects on acoustic transmission through narrow slit cavities. *Physical review letters*, 115(4):044302, 2015.

[5] G Kirchhoff. Ueber den einfluss der wärmeleitung in einem gase auf die schallbewegung. *Annalen der Physik*, 210(6):177–193, 1868.

[6] M Bruneau. *Fundamentals of acoustics*. John Wiley & Sons, 2013.

[7] Q Qi. Attenuated leaky Rayleigh waves. *The Journal of the Acoustical Society of America*, 95(6):3222–3231, 1994.

[8] VA Gusev and PA Simonova. Effect of shear components of the acoustic field in the viscous liquid on the structure of the Stoneley wave at the interface between the liquid and elastic half-spaces. *Physics of Wave Phenomena*, 23(4):268–272, 2015.

[9] J Zhu, JS Popovics, and F Schubert. Leaky Rayleigh and Scholte waves at the fluid–solid interface subjected to transient point loading. *The Journal of the Acoustical Society of America*, 116(4):2101–2110, 2004.

[10] N Favretto-Anrès. Theoretical study of the Stoneley-Scholte wave at the interface between an ideal fluid and a viscoelastic solid. *Acta Acustica united with Acustica*, 82(6):829–838, 1996.

[11] C Glorieux, K Van de Rostyne, K Nelson, W Gao, W Lauriks, and J Thoen. On the character of acoustic waves at the interface between hard and soft solids and liquids. *The Journal of the Acoustical Society of America*, 110(3):1299–1306, 2001.

[12] VG Mozhaev and M Weihnacht. Subsonic leaky Rayleigh waves at liquid–solid interfaces. *Ultrasonics*, 40(1-8):927–933, 2002.

[13] N Favretto-Anrès and G Rabau. Excitation of the Stoneley–Scholte wave at the boundary between an ideal fluid and a viscoelastic solid. *Journal of sound and vibration*, 203(2):193–208, 1997.

[14] N Favretto-Anres and JP Sessarego. Identification of shear wave parameters of viscoelastic solids by laboratory measurements of Stoneley-Scholte waves. *Acta Acustica United with Acustica*, 85(4):505–516, 1999.

[15] M Zajac, H Kahl, B Schade, T Rödel, M Dionisio, and M Beiner. Relaxation behavior of polyurethane networks with different composition and crosslinking density. *Polymer*, 111:83–90, 2017.

[16] Y Liao and V Wells. Estimation of complex modulus using wave coefficients. *Journal of Sound and Vibration*, 295(1-2):165–193, 2006.

[17] CY Hui and A Jagota. Effect of surface tension on the relaxation of a viscoelastic half-space perturbed by a point load. *Journal of Polymer Science Part B: Polymer Physics*, 54(2):274–280, 2016.

[18] MFM Osborne and SD Hart. Transmission, reflection, and guiding of an exponential pulse by a steel plate in water. i. theory. *The Journal of the Acoustical Society of America*, 17(1):1–18, 1945.

[19] A Schoch. Der schalldurchgang durch platten. *Acta Acustica united with Acustica*, 2(1):1–17, 1952.

[20] Z Zhu and J Wu. The propagation of Lamb waves in a plate bordered with a viscous liquid. *The Journal of the Acoustical Society of America*, 98(2):1057–1064, 1995.

[21] J Wu and Z Zhu. An alternative approach for solving attenuated leaky Rayleigh waves. *The Journal of the Acoustical Society of America*, 97(5):3191–3193, 1995.

[22] AH Nayfeh and PB Nagy. Excess attenuation of leaky Lamb waves due to viscous fluid loading. *The Journal of the Acoustical Society of America*, 101(5):2649–2658, 1997.

[23] FB Cegla, P Cawley, and MJS Lowe. Material property measurement using the quasi-Scholte mode—a waveguide sensor. *The Journal of the Acoustical Society of America*, 117(3):1098–1107, 2005.

[24] X Xu, J Goossens, G Shkerdin, and C Glorieux. Effect of loading a plate with different liquids on the propagation of lamb-like waves studied by laser ultrasonics. *IEEE transactions on ultrasonics, ferroelectrics, and frequency control*, 55(3):675–685, 2008.

[25] R Christensen. *Theory of viscoelasticity: an introduction*. Elsevier, 2012.

[26] NW Tschoegl, WG Knauss, and I Emri. Poisson's ratio in linear viscoelasticity–a critical review. *Mechanics of Time-Dependent Materials*, 6(1):3–51, 2002.

[27] RD Borcherdt. *Viscoelastic waves in layered media*. Cambridge University Press, 2009.

[28] R Stoneley. Elastic waves at the surface of separation of two solids. *Proceedings of the Royal Society of London. Series A, Containing Papers of a Mathematical and Physical Character*, 106(738):416–428, 1924.

[29] L Rayleigh. On waves propagated along the plane surface of an elastic solid. *Proceedings of the London mathematical Society*, 1(1):4–11, 1885.

[30] CT Schröder and WR Scott Jr. On the complex conjugate roots of the Rayleigh equation: The leaky surface wave. *The Journal of the Acoustical Society of America*, 110(6):2867–2877, 2001.

[31] JG Harris and JD Achenbach. Comment on "on the complex conjugate roots of the Rayleigh equation: The leaky surface wave"[j. acoust. soc. am. 110, 2867 (2001)](l). *The Journal of the Acoustical Society of America*, 112(5):1747–1748, 2002.

[32] AD Pierce et al. *Acoustics: an introduction to its physical principles and applications*, volume 678. McGraw-Hill New York, 1981.

[33] MM Volkenshtein and VM Levin. Structure of a Stoneley wave at an interface between a viscous-fluid and a solid. *SOVIET PHYSICS ACOUSTICS*, 34(4):351–355, 1988.

[34] PB Nagy and AH Nayfeh. Viscosity-induced attenuation of longitudinal guided waves in fluid-loaded rods. *The Journal of the Acoustical Society of America*, 100(3):1501–1508, 1996.

[35] SC Hunter. *Mechanics of continuous media*. Halsted Press, 1976.

[36] N Obaid, MT Kortschot, and M Sain. Understanding the stress relaxation behavior of polymers reinforced with short elastic fibers. *Materials*, 10(5):472, 2017.

[37] T Chen. Determining a prony series for a viscoelastic material from time varying strain data, 21p. *NASA*, 2000.

[38] WJ Parnell and R De Pascalis. Soft metamaterials with dynamic viscoelastic functionality tuned by pre-deformation. *Philosophical Transactions of the Royal Society A*, 377(2144):20180072, 2019.

[39] SI Rokhlin, DE Chimenti, and AH Nayfeh. On the topology of the complex wave spectrum in a fluid-coupled elastic layer. *The Journal of the Acoustical Society of America*, 85(3):1074–1080, 1989.

[40] X Jia. Modal analysis of Lamb wave generation in elastic plates by liquid wedge transducers. *The Journal of the Acoustical Society of America*, 101(2):834–842, 1997.

[41] WN Sharpe. *Springer handbook of experimental solid mechanics*. Springer Science & Business Media, 2008.

# Chapter 5

# Conclusions and further work

### Summary

This thesis has been focused around the modelling of viscous and thermal dissipative effects in the propagation of linear acoustic and elastic waves in a number of different physical set-ups consisting of (homogeneous) continua ranging from fluids in the form of gases and liquids like air and water, to hard solids such as metals, to softer solid media such as rubbery materials and plastics.

Our first contribution to the existing literature (Chapter 2) is centred around a canonical problem consisting of the propagation of natural modes in a single fluid-filled slit, where the focus lies on viscous and thermal losses through boundary layers and in particular the differences when the slit is occupied by air or water. For the in-air problem, we are able to give a fundamental theoretical footing to some experimental realisations from Ward et al. [2015], and in particular show that the boundary layer parameter used therein is an underestimate to the true extent of this region and Stokes's boundary layer parameter is a better estimate. This result helps explain the unexpected observation discussed in Ward et al. [2015] with regards to the specific channel widths at which losses become dominant. For the in-water problem, we find thermal dissipation to be negligible (at the temperatures considered in this study) as a result of its low thermal expansion coefficient, but illustrated the importance of fluid-structure interaction (FSI) when the slits are within standard hard materials such as steel. We believe the magnitude of the reduction in phase speed for decreasing channel

widths is of physical significance, but we note that the dissipation nevertheless is still only due to the boundary layers since the steel considered is perfectly elastic so that it cannot dissipate energy and further although it causes the energy to be redistributed along the slit, there is no radiation loss into the solid (as expected since even for water, steel is highly supersonic). The possibility to analyse some of these extra physical mechanisms resulted in motivation for the authors to consider softer solid media. As outlined in Section 2.3, early results showed that even with the purely elastic model considered in the paper, the obtained behaviour was so different than for hard solids, that we acknowledged that the extension of the parameter space into softer solid media needed a more in-depth discussion, especially if we want to discuss visco-elastic effects. This discussion is continued further in Chapter 4, nevertheless prior to the development of this chapter, we realised that it could be beneficial to devote some time to generalising the theories that we had employed so far, which eventually led to Chapter 3.

In Chapter 3 we focus on the development of a framework for thermo-visco-elastic (TVE) continua. It is noted that previous related works have either used approximate 'local' TVE theories (that do not include stress relaxation) such as Deschamps and Cheng [1989] for specific problems, or conversely stated general equations without providing detail into how these can be applied to dynamic problems of physical interest [Christensen and Naghdi, 1967]. In this paper, we focus on developing a theory that is readily available for wave-propagation type problems. The resulting three free-space modes propagating in this media are analysed in detail, and in particular we provide useful approximations to the thermo-compressional wavenumbers that highly simplify the original expressions which are tested for solids and fluids. Furthermore, the simple connection between TVE and TVA as well as other physically relevant theories is demonstrated. In particular, we are able to show that with our framework a general TVA fluid-solid boundary as in Figure 1.12 can indeed be generalised to that of Figure 1.13, which allows us to consider the reflection/transmission of many more media under the same equations. This is done specifically for two TVE half-spaces under incident plane wave forcing, and results involving materials as diverse as air, water, steel and rubber are given. In particular, some results from Borcherdt [2009]

for water-steel are extended to include the presence of thermal effects, although they are shown to be negligible as for the slits in Chapter 2. The extra dispersive properties upon reflection/transmission provided by stress relaxation are discussed for hypothetical rubbery-type media.

Finally, Chapter 4 is devoted to an analysis of viscous dissipation of some of the principal modes of propagation in two different physical set-ups involving fluid-solid interfaces: water-filled slits within semi-infinite viscoelastic solids and water-loaded viscoelastic plates. Using our previously developed framework, we show that the equivalence between the equations governing linear viscoelastic solids and visco-acoustic fluids nevertheless implies that these two systems can in fact be governed by the same dispersion equations (for symmetric/anti-symmetric modes), which then become tailored to each particular problem when specific limits of the material parameters are considered. Furthermore, for slits/plates much larger than the characteristic mode's wavelength, the associated dispersion in these two physically different problems becomes governed by the same equation, namely the Scholte-Stoneley DE for fluid-solid half-spaces. The first part of the paper is therefore devoted to the study of this canonical problem, where both Scholte-Stoneley and Leaky-Rayleigh modes are analysed in detail. In terms of material parameters, the fluid considered is water whereas results for both steel and PVC are provided with the intention to cover both hard and soft solids, and in particular illustrate the effect of their intrinsic differences on the properties of the respective modes. Viscoelastic losses are initially modelled with a KVM, and consequently with the SLSM which allows us to bring special attention to the influence of stress relaxation.

The discussion for the fluid-filled slits set-up is given as an extension of Cotterill et al. [2018] provided in Section 2.2, taking into account the further comments from Section 2.3. It is shown how the significant reduction of the Scholte mode's phase speed for soft solid-water interfaces requires paying more attention to the initial value used in the root finding algorithm, as opposed to hard solids for which the the Scholte mode propagates essentially at the speed of sound. The dispersion on phase speed and attenuation is discussed thoroughly and the extra possibilities for wave manipulation resulting from operating near glass transition $\omega t_r = 1$ are noted.

Conveniently, we are able to use the same root finding technique to the problem of water-loaded plates. The dispersion of both symmetric and anti-symmetric modes is discussed as a function of relative plate thickness. In particular, we observe that the symmetric coupled plate-Scholte mode becomes dispersive in soft solids, as opposed to hard solids such as metals for which the mode propagates at the constant sound speed. Coincidentally, we note the dispersion of the symmetric coupled plate-Scholte mode was studied (in the absence of dissipation) in the very recent work Staples et al. [2021], and verified experimentally. We make use of our framework in order to observe whether any notable consequences may arise when losses are taken into account. Although the viscosity due to the fluid is minimal due to the boundary layers being located in the regions exterior to the plate (as opposed to the fluid-filled slits), we show that viscoelastic losses in the soft plate can be significant, especially when the SLSM is employed and it is operated around glass transition. In particular, our calculations predict a global maximum in the attenuation (as a function of plate thickness) of the symmetric coupled plate-Scholte mode in the dispersive region which we believe may be of physical interest, but needs further investigations which we hope we may conduct in the near future.

**Future work**

There are several possible extensions that can be conducted as followups to the work that has been presented in this thesis, some of which have been pointed out in the conclusions to the separate papers provided in each chapter.

A straightforward extension to our setting for the slit/plate analysis in Chapters 2, 4 would be to replace the unboundedness of the exterior medium by instead applying periodicity conditions, so that the canonical problem considered in this thesis would constitute the unit cell of an infinite array of slits/plates. This naturally introduces an extra lengthscale in the problem, and can give rise to additional interesting physical effects, see e.g. Brandão et al. [2020]. It would be of high interest to further understand the partition of energy between the Scholte-type modes that have mainly been considered here (for both the slits and plates), and the presence of other modes such as Leaky Lamb modes in the case of water-loaded hard plates, and in particular how these

change depending on the type of solid medium and the plate/slit thickness. Analytically, this requires the consideration of the forced-type scattering problem where the governing equations become inhomogeneous and significantly more complex to solve, generally requiring specific techniques. Additional experimental realisations are necessary in order to validate many of the novel results introduced here for both coupled duct-Scholte and coupled plate-Scholte modes.

The problems proposed in this thesis have only involved planar geometries and therefore have been described with Cartesian coordinates, but the extension to other (separable) geometries is direct, since as we have seen the governing equations for linear TVE reduce down to three Helmholtz equations which couple in the boundaries only via expressions involving standard linear operators. We would particularly like to apply the theory to problems involving resonances in elastic systems, in order to be able to assess the impact of thermal and viscoelastic damping in the resonant frequencies and associated amplitudes. A key step for this would be to analyse the possibilities to implement the method of matched asymptotic expansions to particular problems in this generalised setting.

It would be of extreme utility to obtain more realistic data about relaxation times of common viscoelastic materials, and general frequency characterization in order to be able to better understand the parameter space (in both temperature and frequency) in which stress relaxation could be particularly exploited and under what circumstances. Analysis on how these effects are manifested in the time domain is also needed and would be highly beneficial. It would also be useful to identify particular media for which both thermal and viscous effects are important since we often found that highly thermoelastic materials (such as certain metals) often dissipate little energy due to viscosity, whereas for standard temperatures viscoelastic media often dissipate little energy due to thermal damping (as we found for many polymers). On the other hand for fluids we observed that "light" media such as gases which have strong thermal coupling do not generally need FSI considerations (as we have seen here for air), whereas liquids for which FSI is important in standard interfaces can be described accurately without thermal effects (as we have seen for water-metal interfaces). More generally, it is clear that the large parameter space involved in the TVE model allows for the consideration of a very wide range of media, and we hope some of the results

in this thesis will motivate fellow researchers into conducting some of these studies.

# Bibliography


J Achenbach. *Wave propagation in elastic solids*. Elsevier, 2012.

AL Gower (GitHub). Linear thermo-visco-elasticity. URL https://github.com/arturgower/LinearThermoViscoElasticity.

K Attenborough. Acoustical characteristics of rigid fibrous absorbents and granular materials. *the Journal of the Acoustical Society of America*, 73(3):785–799, 1983.

WM Beltman. Viscothermal wave propagation including acousto-elastic interaction, part i: theory. *Journal of Sound and Vibration*, 227(3):555–586, 1999.

LL Beranek. Acoustic impedance of porous materials. *The Journal of the Acoustical Society of America*, 13(3):248–260, 1942.

MA Biot. Thermoelasticity and irreversible thermodynamics. *Journal of Applied Physics*, 27(3):240–253, 1956.

DR Bland. *The theory of linear viscoelasticity*. Courier Dover Publications, 2016.

BA Boley and JH Weiner. *Theory of thermal stresses*. Courier Corporation, 2012.

L Boltzmann. Zur theorie der Elastischen Nachwirkung. *Sitzungsberichte Kaiserliche Akademie Wissenhaft Wien Mathematische-Naturwissenhaft*, (70):275–306, 1874.

RD Borcherdt. Energy and plane waves in linear viscoelastic media. *Journal of Geophysical Research*, 78(14):2442–2453, 1973.

RD Borcherdt. *Viscoelastic waves in layered media*. Cambridge University Press, 2009.

R Bossart, N Joly, and M Bruneau. Hybrid numerical and analytical solutions for acoustic boundary problems in thermo-viscous fluids. *Journal of Sound and Vibration*, 263(1):69–84, 2003.

R Brandão, JR Holley, and O Schnitzer. Boundary-layer effects on electromagnetic and acoustic extraordinary transmission through narrow slits. *Proceedings of the Royal Society A*, 476(2242):20200444, 2020.

AM Bruneau, M Bruneau, PH Herzog, and J Kergomard. Boundary layer attenuation of higher order modes in waveguides. *Journal of Sound and Vibration*, 119(1):15–27, 1987.

M Bruneau. *Fundamentals of acoustics*. ISTE Ltd., London, 2006.

M Bruneau, PH Herzog, J Kergomard, and JD Polack. General formulation of the dispersion equation in bounded visco-thermal fluid, and application to some simple geometries. *Wave Motion*, 11(5):441–451, 1989.

T Chen. Determining a Prony series for a viscoelastic material from time varying strain data, 21p. *NASA*, 2000.

RM Christensen. *Theory of viscoelasticity: an introduction*. Elsevier, 2012.

RM Christensen and PM Naghdi. Linear non-isothermal viscoelastic solids. *Acta Mechanica*, 3(1):1–12, 1967.

BD Coleman and W Noll. The thermodynamics of elastic materials with heat conduction and viscosity. *Archive for Rational Mechanics and Analysis*, 13(1):167–178, 1963.

PA Cotterill, D Nigro, ID Abrahams, E García Neefjes, and WJ Parnell. Thermoviscous damping of acoustic waves in narrow channels: A comparison of effects in air and water. *The Journal of the Acoustical Society of America*, 144(6):3421–3436, 2018.

R Courant. *Differential and Integral Calculus, Volume 2*, volume 2. John Wiley & Sons, 2011.

V Cutanda-Henríquez and PM Juhl. An axisymmetric boundary element formulation of sound wave propagation in fluids including viscous and thermal losses. *The Journal of the Acoustical Society of America*, 134(5):3409–3418, 2013.

V Cutanda Henríquez, VM García-Chocano, and J Sánchez-Dehesa. Viscothermal losses in double-negative acoustic metamaterials. *Physical Review Applied*, 8(1): 014029, 2017.

H Deresiewicz. Plane waves in a thermoelastic solid. *The Journal of the Acoustical Society of America*, 29(2):204–209, 1957.

M Deschamps and C Cheng. Liquid-thermoviscoelastic solids interface. *Ultrasonics*, 27(5):308–313, 1989.

N Favretto-Anrès. Theoretical study of the Stoneley-Scholte wave at the interface between an ideal fluid and a viscoelastic solid. *Acta Acustica United with Acustica*, 82(6):829–838, 1996.

AA Fernández-Marín, N Jiménez, JP Groby, J Sánchez-Dehesa, and V Romero-García. Aerogel-based metasurfaces for perfect acoustic energy absorption. *Applied Physics Letters*, 115(6):061901, 2019.

R Fleury and A Alù. Extraordinary sound transmission through density-near-zero ultranarrow channels. *Physical Review Letters*, 111(5):055501, 2013.

NJRK Gerard and Y Jing. Loss in acoustic metasurfaces: a blessing in disguise. *MRS Communications*, 10(1):32–41, 2020.

R Graciá-Salgado, VM García-Chocano, D Torrent, and J Sánchez-Dehesa. Negative mass density and $\rho$-near-zero quasi-two-dimensional metamaterials: Design and applications. *Physical Review B*, 88(22):224305, 2013.

KF Graff. *Wave motion in elastic solids*. Courier Corporation, 2012.

JG Harris. *Linear elastic waves*. Cambridge University Press, 2001.

JG Harris and JD Achenbach. Comment on "on the complex conjugate roots of the Rayleigh equation: The leaky surface wave". *The Journal of the Acoustical Society of America*, 112(5):1747–1748, 2002.

SC Hunter. *Mechanics of continuous media*. Halsted Press, 1976.

SG Jennings. The mean free path in air. *Journal of Aerosol Science*, 19(2):159–166, 1988.

WR Kampinga, YH Wijnant, and A de Boer. An efficient finite element model for viscothermal acoustics. *Acta Acustica United with Acustica*, 97(4):618–631, 2011.

JT Karlsen and H Bruus. Forces acting on a small particle in an acoustical field in a thermoviscous fluid. *Physical Review E*, 92(4):043010, 2015.

G Kirchhoff. Ueber den einfluss der wärmeleitung in einem gase auf die schallbewegung. *Annalen der Physik*, 210(6):177–193, 1868.

RS Lakes. *Viscoelastic solids*. CRC Press, 2017.

LD Landau and EM Lifshitz. *Fluid mechanics*. Pergamon Press, 1959.

SH Lee, CM Park, YM Seo, ZG Wang, and CK Kim. Composite acoustic medium with simultaneously negative density and modulus. *Physical Review Letters*, 104(5): 054301, 2010.

F Lemoult, N Kaina, M Fink, and G Lerosey. Soda cans metamaterial: a subwavelength-scaled phononic crystal. *Crystals*, 6(7):82, 2016.

Y Li, C Shen, Y Xie, J Li, W Wang, SA Cummer, and Y Jing. Tunable asymmetric transmission via lossy acoustic metasurfaces. *Physical Review Letters*, 119(3): 035501, 2017.

Y Liao and V Wells. Estimation of complex modulus using wave coefficients. *Journal of Sound and Vibration*, 295(1-2):165–193, 2006.

AEH Love. *A treatise on the mathematical theory of elasticity*. Cambridge University Press, 2013.

VA Lubarda. On thermodynamic potentials in linear thermoelasticity. *International Journal of Solids and Structures*, 41(26):7377–7398, 2004.

G Ma and P Sheng. Acoustic metamaterials: From local resonances to broad horizons. *Science Advances*, 2(2):e1501595, 2016.

JE Marsden and TJR Hughes. *Mathematical foundations of elasticity*. Dover, 1994.

H Meng, J Wen, H Zhao, and X Wen. Optimization of locally resonant acoustic metamaterials on underwater sound absorption characteristics. *Journal of Sound and Vibration*, 331(20):4406–4416, 2012.

M Molerón, M Serra-Garcia, and C Daraio. Visco-thermal effects in acoustic metamaterials: from total transmission to total reflection and high absorption. *New Journal of Physics*, 18(3):033003, 2016.

PM Morse and KU Ingard. *Theoretical acoustics*. Princeton University Press, 1986.

W Nowacki. *Thermoelasticity*. Elsevier, 2013.

R Opdam, D de Vries, and M Vorländer. Locally or non-locally reacting boundaries: Does it make a significant acoustic difference? *Building Acoustics*, 21(2):117–124, 2014.

WJ Parnell. *Homogenization techniques for wave propagation in composite materials*. The University of Manchester, Ph.D thesis, 2004.

AD Pierce et al. *Acoustics: an introduction to its physical principles and applications*. McGraw-Hill New York, 1981.

L Rayleigh. *The theory of sound*. Macmillan, 1896.

SW Rienstra and A Hirschberg. *An introduction to acoustics*. Technical report, Eindhoven University of Technology, 2004.

V Romero-García, G Theocharis, O Richoux, A Merkel, V Tournat, and V Pagneux. Perfect and broadband acoustic absorption by critically coupled sub-wavelength resonators. *Scientific reports*, 6(1):1–8, 2016.

RW Scharstein and AMJ Davis. Acoustic scattering by a rigid elliptic cylinder in a slightly viscous medium. *The Journal of the Acoustical Society of America*, 121(6): 3300–3310, 2007.

CT Schröder and WR Scott Jr. On the complex conjugate roots of the Rayleigh equation: The leaky surface wave. *The Journal of the Acoustical Society of America*, 110(6):2867–2877, 2001.

AH Shapiro. *Shape and flow: The fluid dynamics of drag.* Anchor Books, 1961.

GS Sharma, A Skvortsov, I MacGillivray, and N Kessissoglou. Sound absorption by rubber coatings with periodic voids and hard inclusions. *Applied Acoustics*, 143: 200–210, 2019.

IS Sokolnikoff. *Mathematical theory of elasticity.* McGraw-Hill, 1956.

A Sommerfeld. *Partial differential equations in physics.* Academic Press, 1949.

BM Staples, TJ Graham, AP Hibbins, and JR Sambles. Coupled Scholte modes supported by soft elastic plates in water. *Physical Review E*, 103(6):063002, 2021.

EM Stein and G Weiss. Introduction to Fourier analysis on Euclidean spaces. *Princeton Mathematical Series*, 32, 1971.

MR Stinson. The propagation of plane sound waves in narrow and wide circular tubes, and generalization to uniform tubes of arbitrary cross-sectional shape. *The Journal of the Acoustical Society of America*, 89(2):550–558, 1991.

GG Stokes. An examination of the possible effect of the radiation of heat on the propagation of sound. *Phil. Mag*, 1(4):305–317, 1851.

H Tijdeman. On the propagation of sound waves in cylindrical tubes. *Journal of Sound and Vibration*, 39(1):1–33, 1975.

GP Ward, RK Lovelock, ARJ Murray, AP Hibbins, JR Sambles, and JD Smith. Boundary-layer effects on acoustic transmission through narrow slit cavities. *Physical Review Letters*, 115(4):044302, 2015.

E Wegert. *Visual complex functions: an introduction with phase portraits.* Springer Science & Business Media, 2012.

DE Weston. Thermoviscous regions for the principal and higher sound propagation modes in tubes. *The Journal of the Acoustical Society of America*, 68(1):359–361, 1980.

AH Wilson. *Thermodynamics and statistical mechanics.* Cambridge University Press, 1960.

TY Wu. Small perturbations in the unsteady flow of a compressible viscous and heat-conducting fluid. *Journal of Mathematics and Physics*, 35(1-4):13–27, 1956.

Z Yang, J Mei, M Yang, NH Chan, and P Sheng. Membrane-type acoustic metamaterial with negative dynamic mass. *Physical Review Letters*, 101(20):204301, 2008.

C Zwikker and CW Kosten. *Sound absorbing materials*. Elsevier publishing company, 1949.

# Appendix A

# TVA physical constants for air and water

For completeness and in order to facilitate reproducibility, here we simply list the air/water TVA material parameters employed in some of the figures from Chapter 1.

| TVA Parameters | | | | |
|---|---|---|---|---|
| Parameter | Unit | Symbol | Water (10°C) | Air (27°C) |
| Adiabatic speed of sound | m/s | $\bar{c}_{\mathrm{A}}$ | 1490 | 343 |
| Density | kg/m$^3$ | $\bar{\rho}_0$ | 1000 | 1.19 |
| Dynamic shear viscosity | kg/m·s | $\bar{\eta}$ | $1.002\times10^{-3}$ | $1.846\times10^{-5}$ |
| Dynamic bulk viscosity | kg/m·s | $\bar{\eta}_K$ | $3.006\times10^{-3}$ | $1.108\times10^{-5}$ |
| Thermal conductivity | W/m·K | $\bar{\mathcal{K}}$ | 0.597 | $2.624\times10^{-2}$ |
| Specific heat at constant pressure | J/kg·K | $\bar{c}_p$ | 4192 | 1005 |
| Ambient temperature | K | $\bar{T}_0$ | 283.16 | 300 |
| Coefficient of thermal expansion | 1/K | $\bar{\alpha}$ | $8.822\times10^{-5}$ | 1/300 |

Table A.1: Thermo-viscous parameters (assumed to be independent of frequency) for both air and water, as taken from Section 2.2 taken from various sources.